Theoretical, numerical and experimental study of DC and AC electric arcs

Marina Lisnyak

Centre Val de Loire UNIVERSITÉ
Spirit of the Loire Valley

UNIVERSITÉ D'ORLÉANS

UNIVERSITE D'ORLEANS

ÉCOLE DOCTORALE ÉNERGIE – MATÉRIAUX

Laboratoire GREMI – Groupe de Recherche sur l'Énergétique des Milieux Ionisés

Thèse présentée par :

Marina LISNYAK

soutenue le : **20 Avril 2018**

pour obtenir le grade de : **Docteur de l'Université d'Orléans**

Discipline / Spécialité : **Physique des gaz et des plasmas**

THEORETICAL, NUMERICAL AND EXPERIMENTAL STUDY OF DC AND AC ELECTRIC ARCS

Modélisation et expérimentation d'arcs de défaut se propageant sur des barres de distribution électrique dédiées aux applications aéronautiques

Thèse dirigée par :

Jean-Marc BAUCHIRE	Professeur, Université d'Orléans, France

RAPPORTEURS :

Laurent FULCHERI	Directeur de Recherche, MINES ParisTech, France
Armelle VARDELLE	Professeure, Université de Limoges, France

JURY :

Mikhail BENILOV	Professeur, Université de Madère, Portugal
Pascal BRAULT	Directeur de Recherche CNRS, France
Moussa CHNANI	Ingénieur expert, Zodiac Aero Electric, France
Yann CRESSAULT	Maître de conférences, Université Paul Sabatier, France

Посвящается моей маме ...

Acknowledgments

This work would not be possible without the financial support of the industrial group Zodiac Aerospace and its department Zodiac Aero Electric. I would like to express my special appreciation to Zodiac Aerospace and thanks.
I gratefully acknowledge the direction of the GREMI laboratory to provide me a great chance to prepare this work.
I would like thanks to my advisor Prof. Jean-Marc Bauchire, to give me your trust and freedom to conduct the research of this work. It was a real pleasure to share scientific knowledge as well as extraordinary human qualities. Thank you for encouraging my research and for allowing me to grow as a research scientist.
Each of the members of my Dissertation Committee has provided me extensive personal and guidance and taught me a great deal about both scientific research and life in general. I also want to thank you for letting my defense be an enjoyable moment, and for your brilliant comments and suggestions, thanks to you. I would also like to thank to Prof. Armelle Vardele and Prof. Laurent Fulcheri for being referees of my work and giving relevant comments to my thesis and fruitful conversation during the defense. I would like to thank Prof. Pascal Brault, the chairman of the committee and the colleague who daily inspired me for the research. I am very grateful to Dr. Yann Cressault for his support and assistance for this work as well as extensive investigation of the manuscript.
My special thanks go to Prof. Mikhail Benilov for his guidance, for all the invested time in the work we prepared together, and the scientific maturity and confidence I received during the work together. In addition, I acknowledge the very interesting scientific discussions, and critical comments on this written work.
A special mention goes to the "GREMIsts" for all the funny and great moments we had together, for all our fruitful discussions and for bringing me up during the most difficult situations. I really enjoyed spending the time and sharing emotions with you! Some of you became very close friends and gave me most of the support to make this step until the defense. Thank you for being near and encourage me in any situation I have had. I will miss all of you and the great moments we had together!
The great experience I have had in collaboration with Madeira University would not be possible without the full support of all the group of Prof. Benilov. I would like to thank each member

of the group for their kindness, honesty and scientific discussions we have had.
Nobody has been more important to me in the pursuit of this project than the members of my family. I would like to thank my *Mum* whose love and guidance are with me in whatever I pursue. Thank you for the selfless love, care, pain and sacrifice you did to shape my life. Most importantly, I wish to thank my loving and supportive husband, Sylvain. This work would not be possible without your help, support and encouragement. Words can not express how grateful I am to my parents-in-law for all you have made on my behalf.

To my mother who taught me common sense and to be who I am, and my husband who handles the consequences ...

Contents

Nomenclature

Physics Constants

c	Speed of light in a vacuum	$299\,792\,458\,\mathrm{m/s}$
e	Elementary charge	$1.602\,176\,62 \times 10^{-19}\,\mathrm{C}$
k_B	Boltzmann constant	$1.380\,648\,52 \times 10^{-23}\,\mathrm{J/K}$
m_e	Electron mass	$9.109\,383\,56 \times 10^{-31}\,\mathrm{kg}$

Physical quantities

δE_Z	Lowering of the ionization energy	J
ϵ	Internal energy per unit volume	$\mathrm{J/m^3}$
ϵ_N	Net emission coefficient	$\mathrm{W/(m^3 \cdot sr)}$
λ	Plasma thermal conductivity	$\mathrm{W/(m \cdot K)}$
λ_e	Electron thermal conductivity	$\mathrm{W/(m \cdot K)}$
λ_h	Heavy particles thermal conductivity	$\mathrm{W/(m \cdot K)}$
λ_s	Thermal conductivity of the electrode material	$\mathrm{W/(m \cdot K)}$
μ	Plasma dynamic vicosity	$\mathrm{Pa \cdot s}$
μ_0	Vacuum permeability	$\mathrm{T \cdot m/A}$
ϕ	Electric potential	A
$\phi^{(LTE)}$	Electrostatic potential on LTE plasma side	V
$\phi^{(s)}$	Electrostatic potential on the cathode suface	V
ϕ_{a0}	Potential drop in near anode sheth layer	V
ρ	Plasma mass density	$\mathrm{kg/m^3}$

ρ_a	Mass density of element a	$\mathrm{kg/m^3}$
ρ_s	Mass density of the electrodes materials a	$\mathrm{kg/m^3}$
σ	Plasma electrical conductivity	S/m
σ_s	Electrical conductivity of the electrodes material	S/m
$\mathbf{A}$	Vector potential	$\mathrm{V \cdot s/m}$
$\mathbf{B}$	Magnetic flux density	T
$\mathbf{E}$	Electric field	V/m
$\mathbf{F}_a$	Force acting on the component a	N
$\mathbf{F}_L$	Lorentz force	$\mathrm{N/m^3}$
$\mathbf{F}_{vis}$	Volumic viscous forces	$\mathrm{N/m^3}$
$\mathbf{j}$	Current density	$\mathrm{A/m^2}$
$\mathbf{n}$	Normal to the boundary vector directed externally	1
$\mathbf{n}_l$	Vector along the streamline	1
$\mathbf{q}$	Energy flux	$\mathrm{W/m^2}$
$\mathbf{r}$	Coordinate vector	m
$\mathbf{R}_e$	Friction forces between electrons and heavy particles	N
$\mathbf{V}$	Average (mean) plasma velocity	m/s
$\mathbf{V}_a$	Average (mean) velocity of element a	m/s
$\mathbf{v}_a$	Velocity of element a	m/s
Re	Reynolds number	1
$\widehat{\pi}$	Plasma viscous tensor	$\mathrm{kg/m^3}$
$\widehat{\pi}_a$	Viscous tensor of element a	$\mathrm{kg/m^3}$
A_f	Work function of the electrode material	eV
C_a	Collision integral of element a	

C_e	Average thermal speed of electrons	m/s
C_{p_s}	Specific heat of the electrodes materials	$\mathrm{J/(kg \cdot K)}$
C_p	Specific heat of the plasma with constant pressure	$\mathrm{J/(kg \cdot K)}$
E_Z	Ionization energy	J
$f_a(t, \mathbf{r}, \mathbf{v})$	Distribution function for element a	
H	Enthalpy per unit volume	$\mathrm{J/m^3}$
h	Interelectrode gap	mm
I	Arc current intensity	A
j_{em}	Electron emission current density	$\mathrm{A/m^2}$
j_e	Electron current	$\mathrm{A/m^2}$
j_i	Ion current density	$\mathrm{A/m^2}$
j_n	Normal to the electrode component of the current density	$\mathrm{A/m^2}$
k_T	Thermal diffusion ratio	1
L	The cathode length	mm
m_a	Mass of a single particle a	kg
m_i	Ion mass	kg
n_a	Density of element a	$\mathrm{1/m^3}$
$n_{e_{Saha}}$	Electron density according to Saha equilibrium	$\mathrm{1/m^3}$
n_e	Electron density	$\mathrm{1/m^3}$
n_i	Ion density	$\mathrm{1/m^3}$
p	Plasma pressure	Pa
p_a	Pressure of element a	Pa
$q^{(rad)}$	Density of energy flux removed from the electrode surface by radiation into the plasma	$\mathrm{W/m^2}$
Q_a	Partial function of element a	

q_a	Energy flux to the anode	$\mathrm{W/m^2}$
q_e	Electron energy flux	$\mathrm{W/m^2}$
q_e	Ion energy flux	$\mathrm{W/m^2}$
Q_{JH}	Joule heating energy per unit volume	$\mathrm{W/m^3}$
Q_{rad}	Radiation losses per unit volume	$\mathrm{W/m^3}$
$q_w^{(LTE)}$	Energy flux normal component from LTE bulk plasma to the near-electrode layer	$\mathrm{W/m^2}$
$q_w^{(nl)}$	Energy flux normal component from the near-electrode layer to the cathode	$\mathrm{W/m^2}$
$q_w^{(s)}$	Energy flux normal component from the electrode surface	$\mathrm{W/m^2}$
s	Entropy per unit volume	$\mathrm{J/(K \cdot m^3)}$
T	LTE plasma temperature	K
t	Time	s
T_a	Temperature of element a	K
T_e	Electron temperature	K
T_h	Heavy particles temperature	K
T_w	Cathode surface temperature density	K
U_a	Anode voltage drop into the near-electrode layer	V
U_c	Cathode voltage drop into the near-electrode layer	V
U_h	Anode heating voltage	V
V_{arc}	Arc displacement velocity	m/s
W_{rad}	Radiative losses near electrode layer	$\mathrm{W/m^3}$
Z	Charge sign	1
z	Position in the gap; in figures, $z = 0$: *top* electrode; $z = h$: *bottom* electrode	mm

Abbreviations

2T	Two temperatures (arc model)

AC Alternating Current

AFCB Arc Fault Circuit Breakers

Al Aluminium

Ar Argon

CB Circuit Breaker

Cu Copper

DC Direct Current

FOD Foreign Object Debris

fps Frames per second

IL Ionization Layer

LTE Local Thermal Equilibrium

LVCB Low Voltage Circuit Breaker

MHD Magneto-HydroDynamic

NLTE Non-Local Thermal Equilibrium

SH Sheath layer

TN Thermal Non-equilibrium layer

TP Thermal Perturbation layer

Chapter 1

Introduction

1.1 Motivation

The continuously growing amount of information reporting issues, faults or problems in the aeronautical industry underscores the need to maintain the maximum level of safety. Accessibility to this information is often limited, however. The context of this work is directly related to aeronautical safety as it aims at supporting engineering development with basic research in physics. The study is devoted to the investigation of arc fault phenomena in the electrical network of aircraft.
Arc fault detection poses a strong challenge to the monitoring processes that collect all kinds of data from various sensors placed in the aircraft, a situation that may lead to a safety failure of the whole system. While the detection of arc faults is being continuously improved, the ignition of a fault arc remains a realistic hypothesis. Additional safety measures must therefore be developed to prevent its propagation and to switch it off as rapidly as possible. First, as it is important to define the place where the arc occurs in the aircraft, a brief description of the architecture of the power distribution systems in the aircraft is given below.
Generally, the power distribution system of an aircraft plays an essential role and is needed to distribute the electricity from the generators to all kinds of electrical equipment and to the commands to control the plane. There are two types of distribution systems in aircraft:

- busbar systems,
- wire and cables.

In most types of aircraft, the output of the generators is connected to one or more conductors before supplying additional equipment linked to the system. These main conductor lines are called *busbars* or *busses* and act as a distribution centre for the electric power. The electrical power distribution system is based on one or more busses. Their number varies as a function of the size and the complexity of the aircraft. Each power source can supply one or several busbar systems. A variety of electrical items (devices) are connected up to a bus with cables depending on its function. The buses are interconnected via circuit protection devices which are called

bus ties. Bus ties are switches or relays used to connect or disconnect buses from one another. They serve to isolate failed buses from the working ones and/or supply the electrical power to buses that have lost their original power source. Each engine-driven generator normally drives its own generator bus and high-current driven items are connected to these buses. Items such as fixed fire extinguishers and emergency lights are excluded from this system and are usually powered by a battery bus. In that way, they are powered for use even when no generator power is available.

In general, the busbar systems are robust and thoroughly designed to prevent any internal bus crossing. However, with time, the vibrations which take place during flight can cause an arc fault to be initiated between busses. Another source of arc faults is so-called *foreign object debris* (FOD). A FOD may appear in the distribution network for different reasons, for instance a screw falling because of vibrations, fluid droplets due to a leakage... Figure 1.1 depicts the bus bar system after arcing.

Wires and cables conduct electrical power in its various forms and quantities to and between equipment. Various types of wire are used in the aircraft electrical system and often consist of a conductor made of copper or aluminium with specific fireproof isolation. Different wires are used depending on the load, their location within the aircraft and many other factors which are strictly specified and regulated by international normalization standards.

The average age of an aircraft in today's fleets is increasing. There are numerous issues pertaining to ageing aircraft, one of them being the condition of the wiring. Aircraft wiring can be subjected to moisture, vibration, or chafing and undergoes a broad range of temperature changes. While other parts of the aircraft are routinely inspected or rebuilt, the wiring tends to remain untouched, creating favourable conditions for electrical arc faults to take place. On

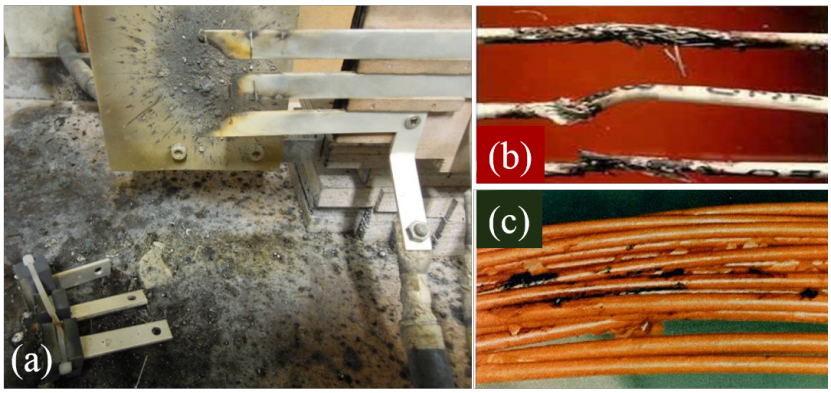

Figure 1.1: (a) The busbars [Zodiac AE 17]; (b)-(c) the wires after arcing in the distribution system of the aircraft [Team 04].

figure 1.1 one can see the danger of arcing in the cable system.

In both cases, busbars or wires, the appearance of an arc fault can be crucial and may degrade the aircraft safety. The existing electronics systems which are implemented in aircraft enable arcs to be detected, and protect the distribution system from the arc. Currently these devices called arc fault circuit breakers (AFCB) mainly rely on electronic components. They continuously analyse the current waveform in the network. In the event of a fault, the current in the circuit changes the typical behavior. The function of the AFCB is to identify this arc fault and then take action, such as disconnecting the part of the circuit where the arc occurs. Isolating the defective element in this way should provide stable conditions until the end of the aircraft operations. However, this system can be improved to achieve a shorter time reaction or to lower the level of damage. This will be particularly necessary in the near future with the next generation of aircraft relying more and more on electrical energy and thus more and more electronics. In such a context, the use of AFCBs based on electronic arc detection will be questionable. To achieve such improvements, it is necessary to investigate the physics of electric arcs in the conditions which are found in aircraft distribution networks. A better understanding of arc behavior in different operating conditions could help to detect, or better, to predict arc ignition. The present study investigates the new idea of arc detection and arc cut in response to this issue.
An electric arc is a combination of complex phenomena which involve many fundamental physical processes. In order to give a clearer picture of the arc physics applied in an aeronautical environment, we first review basic knowledge and state-of-the-art.

1.2 General characteristics of electric arcs

An electric arc, or arc discharge, is an electrical breakdown of a gas that produces an electrical discharge. The current usually passes through non-conductive media and creates a plasma which sustains the discharge. An arc discharge may be formed either during the separation of two electrical contacts with different electric potentials or in a spark breakdown of the gap between the two contacts. Initiation can also arise from the glow discharge when the current intensity is increased. This transition is characterized by a sharp drop in the electric potential at the cathode, resulting simultaneously in an increase in the current intensity. In comparison with other kinds of electrical discharges, electrical arcs are characterized by a relatively small cathode fall. For instance, the cathode voltage drop in a glow discharge is approximately in the order of 100 V or more while in short arc discharges (in the order of cm), it is only 10 V to 15 V. Such a small cathode voltage fall is the consequence of different cathode emission mechanisms. Emission of electrons from the cathode in a glow discharge takes place as a result of bombardment of the cathode with the ions accelerated in a strong near-cathode electric field. Additionally, a large quantity of electrons is produced by photo-emission at the cathode

surface exposed to energetic radiations coming from the ionized gas. In the case of electric arc discharges, the emission of electrons from the cathode is mainly due to the mechanism of auto-electronic (at a low cathode temperature) or thermoionic (at a high cathode temperature) emission or to both mechanisms. The arc discharges are driven with high current (from a couple of A to several kA), consequently, the typical current density is also high, usually in the order of $\sim 10^4$ A/cm^2 to 10^7 A/cm^2. The arc behaves as a conductive medium with, by definition, a low impedance and thus a relatively low arc voltage. In the case of short arcs, the voltage usually remains in a range below 100 V being in some cases a couple of V. The cathode temperature is an important point in the physics of arc discharges. It reaches several hundreds or thousands K with sometimes the formation of hot spots. Therefore, erosion and evaporation phenomena are important mechanisms taking place on the cathode surface, which motivates the use of refractory materials such as bulk cathodes for some industrial applications.
Depending on the processes taking place on the cathode and the gas pressure, it is possible to distinguish several types of arc discharges which are properly described in [Raizer 87]. More generally, arc discharges can be divided into *high-pressure* and *low-pressure* arc discharges. In reality, the elementary processes taking place in the plasma in high-pressure and low-pressure arcs are different. The plasma state of the electric arcs is discussed in greater detail below. A scheme of an arc discharge is shown on figure 1.2 (a). In the arc discharge, similar to the glow

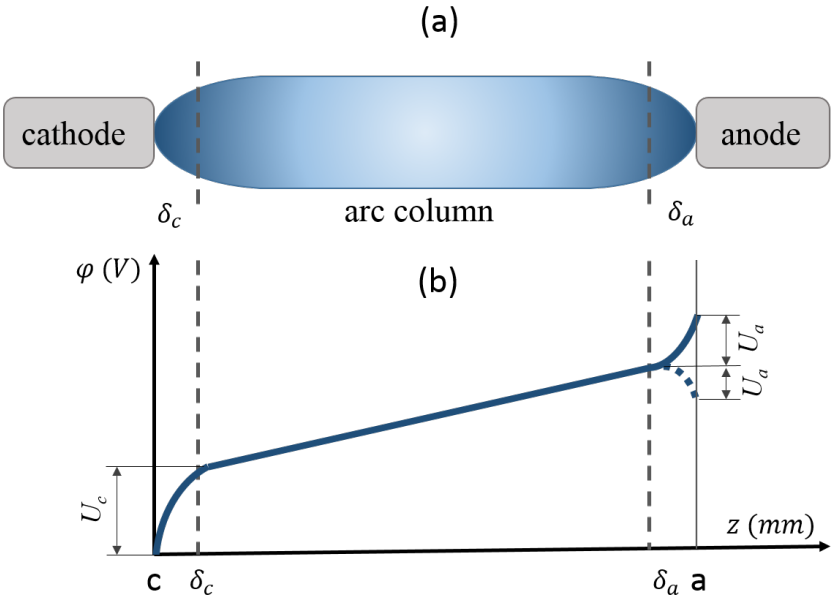

Figure 1.2: (a) Schematic of the electric arc. (b) Typical distribution of the electrostatic potential along the arc axis.

discharge, one can distinguish near-electrode zones (cathode δ_c and anode δ_a on figure 1.2) and

the arc column itself. The arc column occupies most of the space between the electrodes, while the near-electrode regions are narrow. The arc column is filamentary and homogeneous in the axial direction. Arc constriction is usually observed near the cathode and on the anode the attachment can be either confined or spread over the surface. The near-electrode jets, formed as a result of the axial gradient of magnetic pressure in the arc, play a significant role in forming the arc column itself.

The distribution of the potential along the arc column is uniform (figure 1.2 (b)), i.e. the strength of the electrical field is approximately constant. Normally, the extension of the arc length will linearly increase the total arc voltage. However, the effect of the external conditions (the gas flow, the magnetic field, the channel walls) may result in a large change along the length of the column. In the near-electrode regions with the length δ_c and δ_a, the potential rapidly changes as a result of the energy transfer between the arc column and the electrodes. There are potential falls: the negative cathode fall U_c and the anode one U_a, which can have different signs, either negative or positive. The near-electrode zones are very narrow and, according to reasonable estimations, has the order of several path lengths of the particles of $\sim$0.1 mm at atmospheric pressure. This means that the strength of the electrical field in the near-electrode region is very high. The strength of the electrical field in the arc column depends strongly on the diameter of the discharge channel, the current intensity, the type of gas, the flow regime and many other conditions. For instance, at atmospheric pressure, the channel diameter is about 10 mm and the current intensity 100 A. Typical ranges of the strength of the electric field for different gases are reported in table 1.1. The most important electrical characteristic of the

gas	Ar	He	H_2	N_2
electric field (V/cm)	5–8	15–20	30–50	10–15

Table 1.1: Typical electric field strength at atmospheric pressure arcs [Zhukov 07].

arc is the volt–ampere characteristic (VAC). The arc voltage is the sum of the cathode and anode falls and the arc column voltage. The shape of this characteristic curve determines the selection of the parameters of the power source for the arc and the electrical efficiency for its industrial applications. The VAC of free-burning electric arcs are usually falling. This means that with an increase in arc current, the arc voltage decreases [Finkelburg 61]. It occurs due to a decrease in the arc resistance with an increase in the current, resulting from an increase in the arc radius (the conductive radius). Consequently, the arc temperature will also rise. These factors lead to the increase in the arc conductance. The VAC of electric arcs with high currents can also grow and form a so-called *U-shape* VAC.

1.3 Fields of electric arc application

Depending on the discharge power, discharge pressure, or electrode geometry, there are several distinct applications of electric arcs. In some industrial devices the electric arc is the key-object. For example, electric arcs are used for plasma cutting and welding, plasma spraying, material processing, and arc furnaces. When current interruption occurs in a switching device, this will ignite an electric arc. An example of the electric arc in nature is lightning. On the diagram 1.3 are shown the most common applications of electric arcs according to their power. For many years, high intensity high pressure discharge lamps were one of the main applications

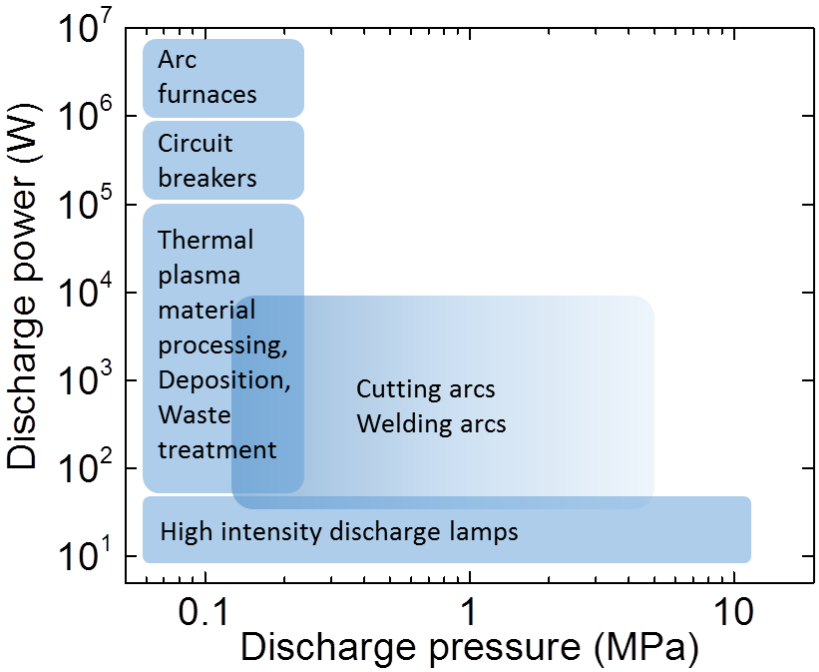

Figure 1.3: Classification of thermal plasmas for various applications depending on the power. Graph adapted from [Wendelstorf 00].

of electric arcs. Scientific research therefore focused on this area of investigation. However with the widespread availability of LED lamps on the market, this research topic shrank and has now almost vanished, and research interest shifted to other applications. As a result the experimental and theoretical research of the welding and cutting processes using electric arcs are well-developed nowadays. With the improvement in the interrupting capability of switching devices, research on the core of the electric arc is needed and research is therefore continuously growing in this direction. With the increasing interest in the use of nanoparticles for applications, it has been found that arc discharges can be used for their synthesis. Paradoxically, as electric arcs are the core of plasma torches they are of great interest to support current and future environmental challenges in the context of waste treatment.

1.4 Thermal plasmas

It is well-known that plasmas occur over a wide range of working conditions, so it is common to classify them in terms of electron temperatures and electron densities (figure 1.4) [Boulos 94]. This classification concerns some natural and man-made plasmas. The plasma produced by

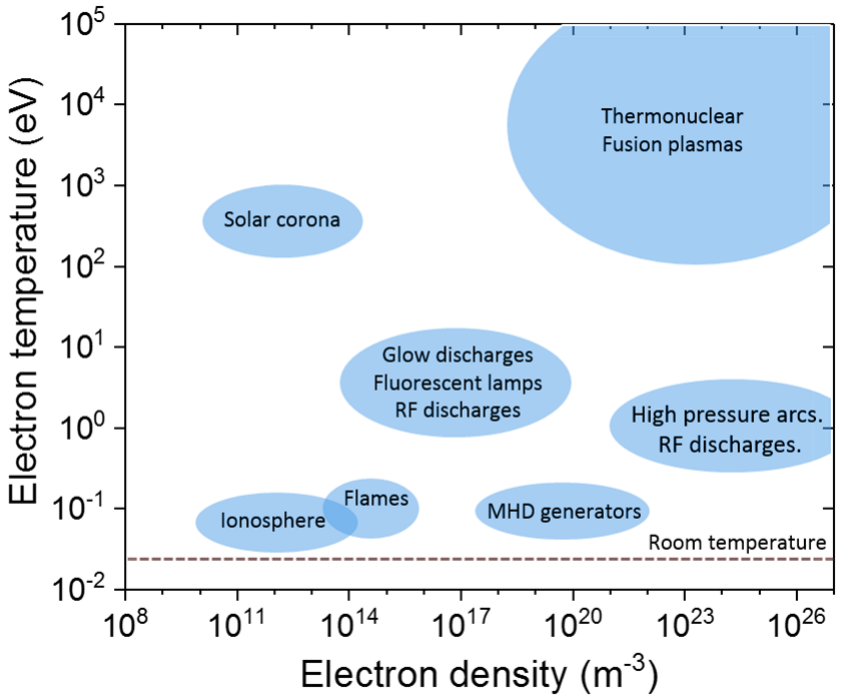

Figure 1.4: Classifications of plasmas adapted from [Boulos 94].

electric arcs belongs to the category of thermal plasmas. These plasmas have temperatures around $10^4\,\mathrm{K}$ with an electron density ranging from $10^{21}\,1/\mathrm{m}^3$ to $10^{26}\,1/\mathrm{m}^3$. In comparison, the well-known glow discharges are typically operated in a pressure range from $1 \times 10^{-4}\,\mathrm{kPa}$ to $1\,\mathrm{kPa}$ and have an electron temperature in the order of $1 \times 10^3\,\mathrm{K}$, while heavy particle temperatures remain unchanged. In order to establish a distinction between thermal and non-thermal plasmas, the definition of thermal equilibrium needs to be introduced. A full definition is given in chapter 2 but a short version will be formulated in the present section. Thermal equilibrium means the existence of kinetic, chemical and radiation equilibrium. The kinetic equilibrium can be realized by frequent collisions between all the particles. In this case the Maxwellian distribution function is realized. Within thermodynamic equilibrium the energy of each type of species distributed among all species according to the Boltzmann distribution and Saha equilibrium is established. Moreover, the radiation transport needs to be in equilibrium as well. Thermal equilibrium in such a description is idealized and never satisfied in reality. Hence, it is highly desirable to use laws of thermal equilibrium; at this point, the assumption

of local thermal equilibrium (LTE) can be introduced. In LTE the equilibrium is realized in all aspects except for radiation transport. In the plasma of high-pressure electric arcs, when the plasma is dense and hot enough to generate frequent collisions, the LTE assumption is justified. Therefore, the plasma is characterized by the temperature T of all the species. However, applying the LTE assumption in all the plasma regions of the electric arc is not justified. It can be achieved only in the arc column. In the near-electrode regions δ_c and δ_a (figure 1.2) thermal equilibrium is disturbed; moreover there is no quasi-neutrality. On the arc fringes, where the plasma temperature is low, the LTE is also disturbed. In low-pressure arcs, the existence of thermal equilibrium is questionable.

1.4.1 Theoretical approaches to thermal plasmas

A large number of applications of arc discharges are associated with the use of the arc column in which most of the thermal and radiant energy is generated. At atmospheric and higher pressures, the physical processes taking place in the arc column are important as well as the processes near the electrodes. Advanced knowledge has been achieved in understanding the physical processes taking place in the arc column plasma, and mathematical methods to describe electric arcs have been established and applied for many decades [Zhukov 07]. The two main directions of the theoretical description of electric arc plasmas are presented in this section. The differences between the two approaches are mostly in the degree of refinement with which the processes are described, the methods of examination, and the accuracy of the results.

First theoretical approach

The first approach is based on analytical methods. These models make rational simplifications of the problem so as to obtain explicit and adequate relationships between the main parameters of the discharge. Although this approach cannot be applied efficiently to describe individual details of the processes in electric discharges, the results are important both for determining the physical pattern of the plasma flows and for direct and immediate application and understanding arc behavior.

Two kinds of analytical models are currently used to investigate electric arcs. One is the so-called *block model* of electric arcs [Habedank 93, Thomas 15, Marković 13]. In the block model, the arc is described by a simple mathematical equation where the obtained relation refers to the arc conductance, which can be determined experimentally, for instance by measuring specific parameters such as the voltage and current of the arc. A black box model is very reliable for simulating occurrences in electric arc circuits in studies of electric networks. Although it is based on the model of physical conditions, it is just a mathematical model. The classical black box models are the *Cassie* model [Cassie 39] and the Mayr model. These models are

usually used to simulate switching devices. However, they do not describe the arc itself, but the electrical circuit where the arc occurs.
Another type of model is based on solving the Elenbaas-Heller equation [Heller 35, Fridman 07], which defines the radial temperature distribution in the arc column. These models are usually applied for stationary cylindrically symmetrical long arcs, i.e. the arc column is characterized by the formation of an axially homogeneous cylindrically symmetric arc column whose properties are not influenced by the electrodes. Using some simplifications, the analytical solution can be found. These models are used for wall-stabilized cascaded arcs with a superimposed laminar flow [Shaw 06, Kuiken 91, Liao 16].

Second theoretical approach

However, these approaches cannot be applied efficiently to describe individual details of the processes taking place in electric arcs. With the increase in computational power, it became more and more interesting to look for numerical solutions to the detailed description of electric arcs. Along these lines, a mathematical model has been established based in a general case for an arc column on a complicated non-linear system of equations of radiation magnetic gas dynamics with the appropriate boundary-value conditions. In a general case, it is described by a system of *magneto-hydrodynamic* equations (MHD), including the laws of conservation of mass, momentum and energy, and the equations of electrodynamics and radiation transfer. Sometimes such models are called fluid models of plasma. A general principles of the hydrodynamics models of the electric arc, the state of the art on present day is reported below. Fluid models describe the evolution of the moments of the Boltzmann equation for each species in the plasma, and provide direct measures of macroscopic flow properties, such as temperature and pressure. The simplest MHD models are a combination of one fluid with the assumption of LTE in the arc column [Hsu 83c, Gleizes 05]. Fluid models need to be supplied with thermodynamic properties and transport coefficients. The existence of thermal equilibrium in a thermal plasma means that the plasma composition and the transport coefficients can be calculated. Thorough reference studies have been published in this field [Murphy 14, Cressault 13b, Boulos 94, Devoto 66]. The energy balance in a thermal plasma is established by Joule heating of the gas by the current flowing through and by the radiation emitted by the plasma. It is therefore crucial for MHD models to take arc radiation into account. The radiative spectra of thermal plasmas are extremely wide. The highest spectral densities are mainly in the ultraviolet, the visible and the near infrared regions. To solve the radiation transport equation, several approaches have been developed. Commonly, the radiative transfer is taken as the difference between the total emission and the total absorption at any point and isotropically in the plasma. The most common method is the so-called Net Emission Coefficient (NEC) [Lowke 74, Nordborg 08, Cressault 15].

Models based on the MHD approach with the assumption of LTE are a powerful tool to investigate electrical arcs. This model can be adopted for different applications, where different geometries with the corresponding external conditions such as arc current, working gas, pressure... can be used. Below, the main numerical simulation results of electric arcs for different applications are shown.

Historically, the first numerical realization of the MHD approach was computed for so-called free-burning, or transferred, arcs by Hsu et al. [Hsu 83a]. Free-burning arcs have been inves-

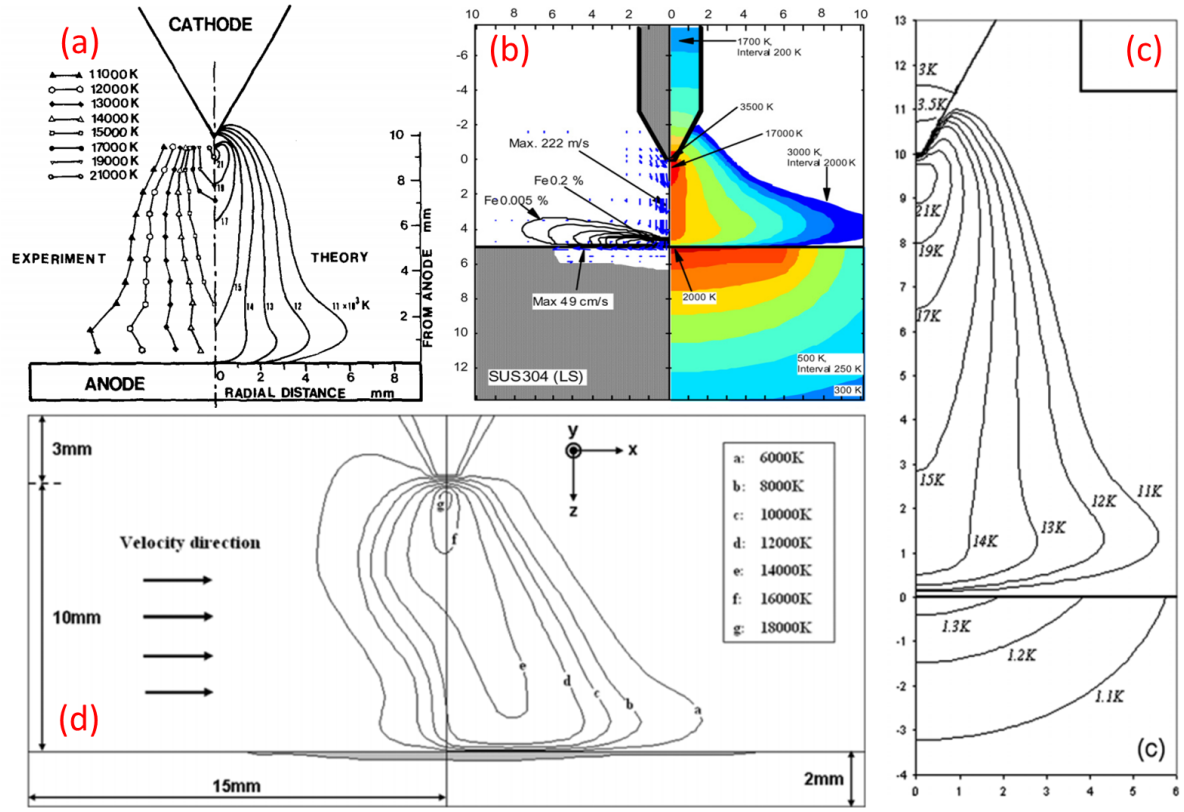

Figure 1.5: Examples of numerical simulations of free-burning electric arcs. DC current conditions, working gas is Ar. (a) Temperature isolines in the arc column experiment (left) and simulations (right), $I = 200\,\mathrm{A}$ [Hsu 83a]; (b) Evaporation rate of the iron anode material (left) and temperature distribution in the arc and the electrodes (right), $I = 150\,\mathrm{A}$, 20 s after ignition [Tanaka 10]; (c) Temperature isolines in the arc and copper anode $I = 200\,\mathrm{A}$ [Bini 06]; (d) Temperature isolines in the arc column, simulations are computed in 3D, where the inflow from the side has a velocity 20 m/s is introduced in order to disturb the arc symmetry [Lago 06].

tigated by many groups over the past decades. Several examples are depicted in figure 1.5. The geometry contains a refractory rod cathode placed in front of plane anode, usually made of copper or iron. The electrodes are surrounded with the gas, usually argon, which is free to move

due to electro-magnetic forces. Additional inlets are sometimes used from the top of the computational domain. The focus of these studies is on the arc column itself and the temperature distribution in the plasma. For the arc of 200 A, the temperature is about 21 000 K near the cathode tip and from 15 000 K up to 17 000 K within the arc column. The temperature then falls near the anode down to 13 000 K. The temperature isolines form the shape called *bell-shape*. The same cathode geometry is implemented in models [Hsu 83a, Bini 06, Lago 06, Gonzalez 02], while the current transfer from latter to the plasma is realized by applying the current density distribution on the surface just near by cathode. The latter was obtained from the experiment also reported in [Hsu 83a]. The distribution of the arc temperature in the column has led to research into determining the anode temperature. Therefore, some attempts to implement plasma-anode interaction in LTE models have been undertaken. This is accomplished by correcting the energy flux from the arc column to the anode or by introducing a non-equilibrium electron density near the electrodes in order to calculate non-equilibrium electrical conductivity [Morrow 93, Lowke 06]. Depending on the external conditions of the arc and on the anode, the anode can be heated and evaporated. The evaporation of anode material has been implemented in hydrodynamic models [Lago 04, Tanaka 10, Gonzalez 93]. As an example, on figure 1.5 (b) shows the rate of the iron evaporated from the anode surface after 20 s of arc - anode interaction with the current of 150 A. The processes taking place in the melting pool of the anode were investigated and movements of the melting anode material were reported in [Mougenot 13, Murphy 11]. Most of the simulations are usually done using an approximation of axial symmetry. However, the mathematical description is easily extended to complete 3D simulations restricted only by the computational capacity and time [Gonzalez 02, Franceries 05, Murphy 11, Tanaka 06]. Similar geometrical configurations presented for free burning arcs are commonly used to simulate welding arcs. Advanced research has been carried out on this topic in the last decade in studies of the arc behavior, weld-pool and droplets using numerical simulations [Haidar 96, Yongbing 02, Wang 03, Murphy 11]. The MHD models described above give a good estimation of the arc temperature and the arc column behavior, making it possible to estimate the processes taking place on the anode. However, efforts have been made to improve the physical description of the arc column especially in order to resolve near-electrode non-equilibrium layers. Improvements of LTE models are usually done with the aim of taking non-equilibrium effects into account. Thermal non-equilibrium can be taken into account by solving separately the electron and heavy particle temperatures, T_e and T_h respectively. Comparison between these studies and LTE results shows a relatively good agreement [Baeva 12, Baeva 16, Hsu 83c, Benilov 12, Li 07, Jenista 97].

Fluid models can be also used to describe plasma torches, which are used for many industrial applications, such as plasma spraying and particle and chemical synthesis. The plasma torch is a device that generates a directed flow of plasma from a stream of working fluid. Hydrody-

namic plasma models under the assumption of thermal equilibrium are reported in [Bauchire 97, Bauchire 99, Moreau 06, Baudry 05, Trelles 07, Colombo 08, Park 04]. These models give a good estimation of the arc temperature and the gas speed [Freton 03]. However, it is more difficult to predict the anode attachment behaviour, which moves on the anode surface during arcing. One of the complications which arises in these models is the time-dependent arc behavior which needs to be included. Moreover, to implement plasma-anode interaction correctly, one should consider non-equilibrium effects near the anode, which requires additional equations. Extending the system of equations to the non-equilibrium case significantly increases the calculation time. More recent models of plasma torches deal with so-called 2T plasma description [Trelles 08b, Trelles 08a, Trelles 13b], in which a specific approach to the electron and heavy particle energy conservation is proposed.
Plasma flows, particularly for industrially relevant applications, are complex phenomena and in some conditions the flow can produce shock waves or in most cases the flow velocity reaches its limit and becomes turbulent. Turbulence phenomena have also been investigated for plasma torch applications [Bauchire 97, Lincun 08, Trelles 14]. The implementation of different turbulence models can slightly change the flow behavior, but in most cases, it influences the energy transport. In sum, when in the Reynolds number range where turbulent flow is present, turbulent energy dissipation should be implemented in the arc model.
One of the phenomena which has attracted attention in many industries is electric arcs in low voltage circuit breakers (LVCB) [McBride 01, Brice 96, Guillot 01]. LVCB, like all CB, are made to interrupt the current flow after a fault has been detected. However, this class of devices operates in atmospheric pressure conditions. Electric arcs occur in the CB during contact switching. Several characteristic processes take place during interruption in a CB:

1. Separation of the electrodes (opening), ignition and elongation of the electric arc;
2. Electric arc propagation along the rail electrodes;
3. Disruption of the electric arc by the splitter plates.

Figure 1.6 illustrates the sequence of the arc occurring within a CB. The arc displacement between the electrodes is determined mainly by the Lorentz force acting on the arc in the axial direction. The Lorentz force caused by the superposition of the magnetic field of the rail electrodes and the magnetic field of the arc and current which passes through the arc.
Usually, studies concerning arc propagation in low voltage CBs focus on electrical aspects of the arc and do not propose a fine description of the arc plasma [McBride 01, Brice 96, Guillot 01]. However, numerical models of the arc itself are of great interest to predict its behavior in order to estimate the lifetime of the device and improve its capability. The number of studies on this topic is limited, however. The main trend over the last decade has

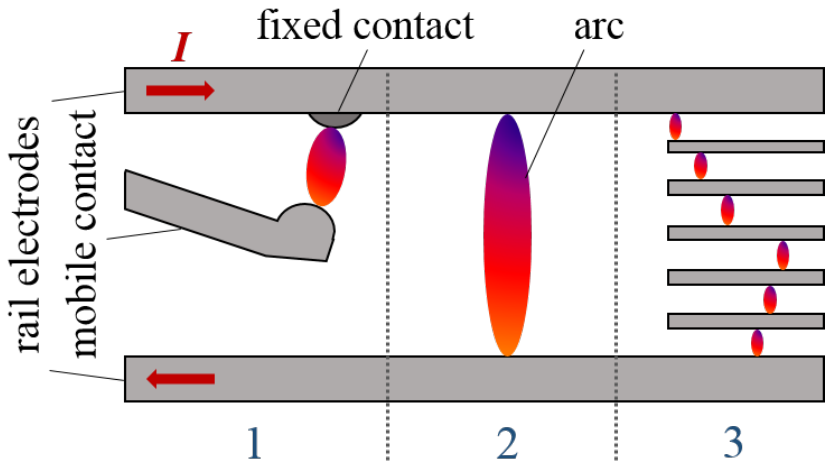

Figure 1.6: Schematic of the main steps of arc propagation in a low voltage CB.

been to use hydrodynamic models to describe arcing in CB applications. Starting with 2D hydrodynamic models of the electric arc [Domejean 97, Fiévet 97] and further extended to 3D [Lindmayer 02, Qiang 08, Wu 08b], numerical models have become more and more advanced [Swierczynski 04, Rondot 09a, Rondot 14, Quéméneur 15, Quéméneur 16]. Some examples of temperature distributions are shown in figure 1.7. In these models the mobile electrode opens and the arc initiates and propagates further along the electrodes. Unfortunately, most studies were conducted in different external conditions, making comparison difficult. In general, the mapping of the temperature distribution in the arc is similar from one work to another, i.e. there are cathode and anode jets one in front of the other, with the time they take to propagate along the rails. The plasma temperature is very similar to that of a free burning arc and remains in the range of 15 000 K to 20 000 K. The calculation results shown in figure 1.7 adopted a similar hydrodynamic approach for the arc column. However, a different concept of plasma electrode interaction is used. It is difficult to say which one is more correct, since there is no consensus on this topic. Last but not least, in such complex models, it is important to address the calculation of the magnetic field. Since the computational 3D domain of the gas should be large enough to resolve the magnetic field from the electrodes, in some studies [Freton 09] this field was calculated independently and applied as a condition. This literature review shows that a hydrodynamic description of the plasma is commonly used to describe electric arcs for different applications. The advantage of the hydrodynamic description is that it can be implemented with the mathematical description in commercial software such as ANSYS Fluent, Comsol Multiphysics and other software programmes. Thanks to the specifically optimized solvers used, simulations of these models can be run in a reasonable time. An added advantage is their flexibility, allowing different geometries and external conditions to be implemented, not

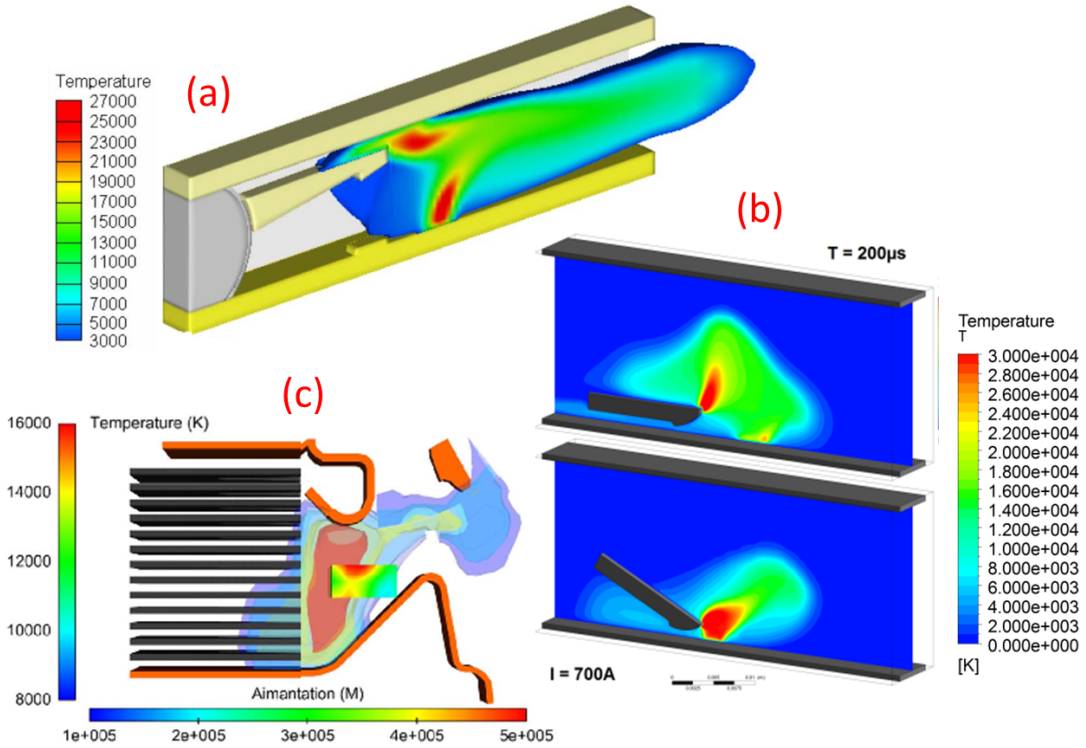

Figure 1.7: Three-dimensional temperature evolution of the arc plasma in air during the opening of the moving contact. (a) $I = 1.5\,\mathrm{kA}$, $t = 1.55\,\mathrm{ms}$ [Wu 08b]; (b) $I = 700\,\mathrm{A}$, $t = 200\,\mu\mathrm{s}$, for two mobile contact orientations [Quéméneur 17]; the arc temperature and the magnetization in the ferromagnetic plate, $I_{max} = 4.5kA$, $50\,\mathrm{Hz}$, $t = 200\,\mu\mathrm{s}$ [Rondot 14].

only symmetrical configurations.
However, the calculation results always need to be checked and validated. Otherwise, the distributions obtained using hydrodynamic plasma descriptions can be nothing more than CFD (color full display) pictures.

1.4.2 Experimental methods applied to thermal plasmas

Plasmas can be investigated by a wide variety of experimental methods [Lochte-Holtgreven 68], but only a few of them are applicable for thermal plasmas. For instance, using electrical probes can be problematic due to the high plasma temperature of the electric arcs. On the other hand, for thermal plasmas, when the assumption of LTE is valid, optical emission spectroscopy methods are highly attractive for plasma specification. In general, due to the intense radiation of thermal plasmas, the most commonly used methods of investigation are based on light collection, spectroscopy, video-spectroscopy, and high-speed video-imaging. We will briefly describe the capabilities and applicabilities of experimental methods for electric arc investigations.

Emission spectroscopy

This is a well-established technique which enables the plasma temperature to be determined from the intensity of the spectral lines, under the assumption of LTE. Particle densities can also be obtained by assuming Saha equilibrium. This method has been extensively applied to obtain the plasma temperature experimentally, particularly in the case of free burning or welding arcs [Hsu 83a, Haddad 84, Hiraoka 97, Valensi 10, Valensi 11]. More generally, without the assumption of thermal equilibrium, the temperature obtained with this method is the excitation temperature of the probed state. On the arc fringes and the electrodes, it has been shown that the excitation, rotational and electron temperatures are slightly different [Fauchais 97], proving the deviation from thermal equilibrium. In order to deduce the plasma temperature, the ratio of two spectral lines can also be used [Lochte-Holtgreven 68]. This method can be extended to video spectroscopy by using very narrow band optical filters to obtain a simultaneous 2D diagnostic of the arc temperature [Bachmann 13]. Based on the temperature distribution and assumption of Saha equilibrium, densities of species can be calculated, for example evaporation from the material during welding processes [Kozakov 13, Wilhelm 12]. This method can be adapted to measure both the composition and the plasma temperature for plasmas which contain more than one atomic element [Murphy 94]. Another possibility is to measure the electron temperature and electron density by analysing the line broadening [Griem 05]. One strong advantage is that this approach does not necessarily require the assumption of LTE. It can be done with commonly used hydrogen lines broadening or atomic lines [Brugeat 04], for example in [Valensi 10, Valensi 11] the Stark broadening of the iron line at 538.3 nm and the argon line at

696.5 nm. The electron density can also be obtained by spectroscopic measurements of the continuous background intensity [Bastiaans 85] which is a convenient method because it does not require a LTE state of the plasma. It has been used in an Ar plasma [Bott 66, Schnehage 82].

Absorption spectroscopy

The method of absorption spectroscopy is very sensitive due to its selectivity and is widely used to perform trace analysis [Kirkbright 82]. In the context of electrical arcs, it is used to measure chemical densities, in particular to quantify the material vaporised from the electrodes when the emission of the material is not intense [Veklich 13]. The advantage of this method is its high sensitivity to determine densities even in low amounts of material. However, the method is more complex than emission spectroscopy and requires close attention to the estimation of the plasma optical thickness. The application of absorption spectroscopy to low voltage circuit breakers in order to determine the density of copper vapor was reported in [Hong 02a, Hong 02b].

Laser scattering

Thomson scattering is a well-established diagnostic for the simultaneous measurement of the electron density and temperature. Thomson scattering has been used for thermal plasmas [Mendys 11, Dzierzega 06, Kühn-Kauffeldt 14, Snyder 93]. The advantage of the method is the high time resolution, which allows a temporal study of the discharge parameters to be performed. Additionally, Rayleigh scattering has been used for temperature measurements [Murphy 92]. The technique of laser induced fluorescence (LIF) is used infrequently in thermal plasmas, most likely due to the complexity of the method and the need to couple the two mechanisms of absorption and emission spectroscopy. However, it is a well-established technique to determine the densities, energies and kinetics of atoms and ions in plasmas. LIF diagnostics allow spatially and temporally resolved measurements of tungsten impurities eroded from the cathode of a free-burning argon arc as reported in [Kühn 02].

Probe

When applied to thermal plasma, this method concerns only the warm region in the fringes or the jet exiting a torch but not very close to the nozzle exit. Langmuir probes are a powerful tool to specify plasma properties in low temperature high pressure plasmas. However, for thermal plasmas this method can be problematic due to the high temperatures in the plasma core and the probe material needs to be highly heat-resistant. Moreover, the interpretation of the measured results is different to low temperature plasmas, where the ionization degree is low and ion current is negligible. Consequently only a few studies have attempted to characterize arc plasmas using Langmuir probes [Sanders 84, Fanara 01, Fanara 04].

Enthalpy probes are considered as a robust tool in thermal plasma diagnostics. The main advantages of this technique are its capability for direct and simultaneous measurement of temperature, velocity, and species concentration fields and temperatures measurements [Rahmane 95, Brossa 88]. The enthalpy probe technique is slightly less accurate than emission spectroscopic methods, but gives a good estimation of the plasma temperature. Plasma flow velocities have been determined using stagnation pressure measurements with enthalpy probes for plasma jets [Chen 94, Fincke 93].

Various Techniques

Nowadays, with the development of new technologies and the improvement in camera time resolution, a commonly used method to investigate electric arcs is high speed video imaging. This method is usually applied in addition to other methods to gather more information about the discharge simultaneously. It can, however, often be difficult to interpret the high speed imaging used to understand arc behaviour, or to interpret and quantify the signal. Some research is done with video spectroscopy, in which band filters are used to collect the light on the chosen wavelength [Rouffet 10]. The arc instabilities in plasma torches have been observed using high speed video cameras [Duan 02] and the near anode region [Yang 06], where the different positions of the anode attachment can be seen. The transition from a laminar to a turbulent plasma flow can also be investigated using video imaging [Huang 08]. High speed videos are often applied to low voltage circuit breakers to measure the arc displacement velocity. The cathode and anode attachments and the time evolution of their position can be obtained from the images and their speed evaluated [Zeller 01, Quéméneur 17, McBride 02].
Shadowgraphy or the Schlieren method can also be used to investigate electrical arcs in order to obtain information about the temperature, the turbulence of the fluid and the electron density [Pfender 91, Prevosto 10, Nagulin 15].

Electrical measurements

Electrical measurements, such as arc current and arc voltage, are often measured together with other techniques. These traditional methods are relatively simple to carry out. It is worth recalling, however, that these are the most stable and powerful methods to predict arc behavior. This overview of the most commonly used methods for the experimental study of electric arcs shows that there is a high potential to obtain plasma and flow properties, flow behavior, and electric characteristics of the arc. The above-mentioned methods are not an exhaustive list, and there are also some more exotic ones, but in most cases it is not necessary to conduct more sophisticated research.

1.5 Electrical arcs in the aeronautical context. Research issues of the work.

Despite the many applications of electric arcs, and the great number of methods for their investigation, not all the answers are available, leading perpetually to new questions. It has been already pointed out that the electric arc may occur inside the distribution network of the aircraft and it is of great interest to conduct research in this context, as the lack of accessible data makes the work more valuable. The literature review on the topic of electric arcs and thermal plasmas briefly presented above is considered as a starting point to approach the topic.
The arcs between busbars and in the wiring systems belong to the same phenomenon, that of electric arcs. However, their nature and properties are different, which means that detailed investigations require different methods to perform their characterization. This implies that different arc-protection mechanisms are needed. In this work, the problem of electric arc phenomena in the busbar system is addressed. The geometrical configuration of busbars is simple: they have a length of hundreds of mm and a thickness of several mm and are placed one in front of the other with a spacing of 5 mm to 10 mm. The power conditions of these distribution systems are three-phase configurations with a load of 115 V or 230 V with frequencies from about 400 Hz to 800 Hz (depending on the alternator rotation speed) or direct current with voltages of 24 V and 48 V. The busbars are arranged in such a way that under normal conditions, electric arcs do not occur. The electric arc appears when a fault occurs between busbars. Usually (it has not been observed otherwise) the electric fault is initiated by the presence of a FOD in the distribution system. Figure 1.8 shows the occurrence of an arc between the busbars. Then the

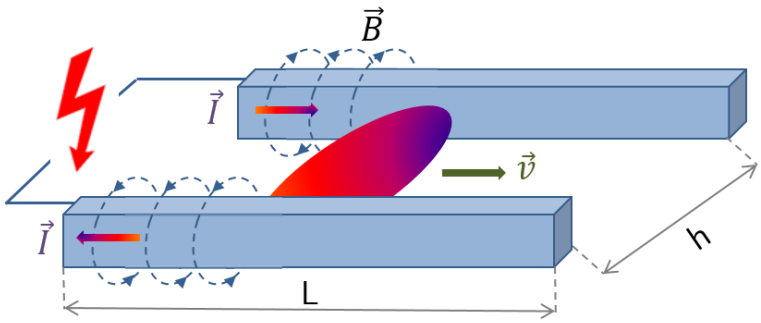

Figure 1.8: Schematic of the arc between busbars, due to electric fault.

electric fault takes place and the electric arc appears. However, the problem becomes more and more dangerous due to arc propagation along the electrodes caused by the Lorentz force. The Lorentz force is the result of the superposition of the magnetic fields induced by the current in the busbars and the arc induced magnetic field and the current passing through the arc. As arc

propagation can be problematic for the entire electrical network, it needs to be detected and disrupted in order to accomplish successful flight.
The difficulty in investigating electric arc propagation between the busbars is the variety of parameters which can be changed during the process. Depending on the moment when the electric arc takes place, the pressure can be different (depending on the altitude of the flight), as can the hydrometry, or the alternative current. The abundance of parameters which can change while the arc is taking place means that theoretical investigation and numerical simulations are preferable to experimental approaches. Numerical simulations are widely used to investigate electric arcs and the commonly adopted MHD approach provides an adequate description of the arc. Moreover, commercial software is capable of performing such simulations in a convenient manner. It therefore appeared reasonable to build a hydrodynamic model of the electric arc between busbar electrodes. In the present research, the commercial software COMSOL Multiphysics was chosen as a tool for the numerical exploration of the arc problem in order to solve the system of hydrodynamic equations.
An experimental study of the arc between busbars was conducted in this work. As arc propagation along the rails is similar to the simulation in low voltage circuit breakers, similar experimental techniques were adopted in this work. The experimental data were used to validate the theoretical model and to better understand the arc displacement.

1.6 Outline of the work

This work is structured in five chapters. This first chapter has introduced electric arc phenomena and given a brief state-of-the-art as a background to the experimental and theoretical investigations. The problem of electrical arcs in aeronautical applications is explicitly detailed. The need for theoretical and experimental research to solve the problem of electric arcs in aircraft and predict its behavior for different external conditions are the main motivations of this work.
The theoretical approach to describing electric arc plasmas is introduced in the second chapter. To establish the arc column model, the hydrodynamic approach under the assumption that the arc plasma is in LTE was chosen. Plasma-electrode interaction is one of the weak points in hydrodynamic models, since the equilibrium is disturbed near the electrodes. This problem is discussed in application to the cathode and anode. The novel approaches developed to match the arc column under the LTE assumption with the cathode and the anode are presented. The matching conditions are delivered with the law of energy conservation in the non-equilibrium near-electrode layers. The calculation results are validated with existing comprehensive numerical models which involve non-equilibrium effects and experimental data and show excellent agreement.

The experimental study of the electric arc between rail electrodes is presented in the chapter 3. Two geometrical configurations were used for different current conditions - pulsed and alternating current with frequencies used in aeronautical applications. High-speed video imaging was performed with a high temporal resolution in order to understand the possible mechanisms of arc displacement near the electrodes. The video imaging is supported with electrical measurements.

Using the theoretical model established and described in chapter 2, the full three-dimensional configuration of the arc model is performed. The latter is reviewed in chapter 4. The geometrical configurations of the electrodes correspond to the conditions of the experiment in order to validate the model. An attempt was made to analyze the arc displacement mechanisms and is discussed in detail.

Finally, in chapter 5 the general conclusions of this work are reported. Possibilities for improving the research and the model are proposed and discussed. The work is completed with a list of references and appendices containing additional data from the numerical particularities of the model.

Chapter 2

Arc simulations

Different approaches are used to describe plasmas theoretically and phenomenologically. The gas state can be characterized as a number of particles and their motion investigated using classical or quantum mechanics formalisms. On the other hand, kinetic theory can be used to describe the gas by introducing the concept of distribution function. With several assumptions, the plasma can be described as an ideal gas and its behaviour can be defined by a system of MHD equations. This approach is commonly used for modeling electric arcs and is favorable for numerical simulations. The remaining questions are: under which conditions can such an approach be used? Could kinetic theory be an alternative to hydrodynamic theory? In this chapter, the reader will find some information to answer these questions.

The system of hydrodynamic equations is described with the assumption of LTE in the arc column. In the vicinity of the electrodes, however, the LTE assumption is no longer valid. Moreover, the processes taking place on and near the electrodes are extremely important to establish the arc. In this chapter, significant efforts are made to describe plasma-electrode interaction. In order to avoid a complicated non-equilibrium formalism of the near-electrode plasma, the matching conditions between the electrodes and LTE plasma are defined. This is achieved by means of current and energy conservation in the non-equilibrium layers (both anode and cathode). This approach allows us to correctly implement physical phenomena in the layer and at the same time to avoid a cumbersome non-equilibrium plasma models in this region. Additionally, the numerical realization of the approach proposed in this chapter is relatively simple, and the calculation time is significantly reduced.

The numerical solution of the theoretical model of the arc column and its interaction with the electrodes was tested on the most common example, i.e. a refractory rod cathode and a flat copper anode in a wide range of arc currents. The simulation results were compared with other existing models and experimental data available in the literature.

2.1 Transport equations

The plasma state can be described with the distribution function $f_a(t, \mathbf{r}, \mathbf{v})$ for every species in the gas. The quantity $f_a(t, \mathbf{r}, \mathbf{v})d\mathbf{r}d\mathbf{v}$ describes the average density of the particles a at time moment t in the volume $d\mathbf{r}$ having a speed in the interval $d\mathbf{v}$, or in other words the probability of finding particle a with speed $\mathbf{v}$ near the point $\mathbf{r}$ at time t. The behavior of the plasma is defined by the Boltzmann equation which describes the evolution of the distribution function over time [Braginskii 65]:

$$\frac{\partial f_a}{\partial t} + \frac{\partial}{\partial x_b} v_b f_a + \frac{\partial}{\partial v_b}\left(\frac{F_{ab}}{m_a} f_a\right) = C_a, \tag{2.1}$$

where the summation is over the subscript b. The force $\mathbf{F}_a$ acting on the component a at position $\mathbf{r}$ with the velocity $\mathbf{v}$; m_a is the mass of the single particle a. For the charged particles in an electric field $\mathbf{E}$ and a magnetic field $\mathbf{B}$, the resulting force is given by:

$$\mathbf{F}_a = Ze \cdot \mathbf{E} + \frac{Ze}{c}\left(\mathbf{v} \times \mathbf{B}\right), \tag{2.2}$$

where Z is the charge sign, $Z = -1$ corresponds to electrons, $Z = 1$ corresponds to single charged ions, $Z = 2$ is double charged ions, ... The term C_a on the right hand side of equation 2.2 accounts for the changes in the distribution function due to collisions with other plasma components.

The distribution function gives the comprehensive behavior of each element of the plasma. However, it is more useful to deliver macroscopic parameters, such as particle density, average velocity and kinetic energy or temperature. Hence, for a particle of type a the following features are defined:

- the density,
$$n_a(t, \mathbf{r}) = \int f_a(t, \mathbf{r}, \mathbf{v}) d\mathbf{v} \tag{2.3}$$
- the average velocity,
$$\mathbf{V}_a(t, \mathbf{r}) = \frac{1}{n_a} \int \mathbf{v} f_a(t, \mathbf{r}, \mathbf{v}) d\mathbf{v} \tag{2.4}$$
- the average kinetic energy,
$$E_{kin} = \frac{m_a \langle v^2 \rangle}{2} \tag{2.5}$$
- the temperature,
$$T_a = \frac{m_a \langle v^2 \rangle}{3} \tag{2.6}$$
$$T_a(t, \mathbf{r}) = \frac{1}{n_a} \int \frac{m_a}{3} \left(\mathbf{v} - \mathbf{V}_a\right)^2 f_a\left(t, \mathbf{r}, \mathbf{v}\right) d\mathbf{v}. \tag{2.7}$$

In the case of a non-equilibrium plasma $n_a, \mathbf{V}_a$ and T_a are different for every sort of particles, making it cumbersome and complex to describe the plasma. However, in some cases the description can be simplified, as discussed below.

2.2 Thermal equilibrium in arc plasma

The distribution function contains information about the equilibrium state or the departure from equilibrium. Macroscopic phenomena are grouped on the left hand side of equation 2.1, while the elementary processes are considered on the right hand side. The most important elementary process is self-collision. For those species in which the frequency between like particles is high, a Maxwellian distribution will be established:

$$f_a = \frac{n_a}{(2\pi k_B T_a/m_a)^{3/2}} \cdot \exp\left(-\frac{m_a}{2k_B T_a}(\mathbf{v}-\mathbf{V}_a)^2\right) \tag{2.8}$$

In the non-equilibrium case the Maxwellian distribution function exists for all the plasma components: electrons, ions, atoms, molecules,etc. For thermal plasma the momentum and energy exchange between heavy particles is very effective. Thus one may assume that ions and atoms have the same translation distribution function, i.e. with the same temperature T_h and electrons characterized with T_e.
The maxwellization of the electrons is more complex and is discussed in [van der Mullen 90]. Inelastic collisions may disturb the maxwellization of the electron gas. The departure of the electron distribution function from equilibrium is described in detail in [van der Mullen 90] for an atomic plasma dominated by electron kinetics. To sum up, the maxwellization of the electron gas with the temperature T_e is assumed when e-e collisions are dominant, i.e. the characteristic relaxation time to establish the Maxwell distribution function is small enough. For thermal atmospheric plasmas, this time τ_{ee} is about 10^{-10} s [Mitchner 73]. The existence of maxwellization of the plasma species means that a hydrodynamic description of the plasma can be applied.
A state of thermal equilibrium is in fact very rare in plasma as the plasma must be uniform, the emission processes must be in equilibrium and the plasma thickness must be high enough [Lochte-Holtgreven 68]. In plasma physics a plasma state close to thermal equilibrium called the local thermal equilibrium (LTE) is often introduced. In this case plasma species are described with the Maxwell distribution function and $T = T_e = T_h$ and the Boltzmann distribution for excited states of heavy particles is valid with the temperature T. However, there is no radiation equilibrium: emission is not in equilibrium with absorption. LTE can usually be observed in plasmas where the particle density is high enough and elastic collisions are dominant.

The applicability of local thermal equilibrium in experimental spectroscopy is valid according to the criterion where the electron density [Griem 63] for an optically thin plasma should correspond to:

$$n_e \geq 10^{14} \cdot T_e^{1/2} \left(E_k - E_i\right)^3 [1/\mathrm{cm}^3], \tag{2.9}$$

where T_e and $E_k - E_i$ are in eV and $E_k - E_i$ corresponds to the biggest energy gap and, for most gases, corresponds to $E_2 - E_1$, where E_1 is a ground state and E_2 is the first excited state. For example, in the case of an argon plasma $E_2 - E_1 = 11.5\,\mathrm{eV}$, $T_e = 1\,\mathrm{eV}$, the electron density should be $n_e \geq 10^{17}/\mathrm{cm}^3$. Critical electron densities necessary for establishing LTE can also be found in [Numano 90] and give similar values.

2.3 Mathematical description of the arc bulk plasma

The conservation equations of macroscopic parameters for each plasma component can be obtained from 2.1 by multiplying it by the factors: $m_a, m_a\mathbf{V}_a, m_a v^2/2$ and integrating over the velocity space, giving a mass, momentum and energy conservation respectively for each plasma component.

$$\frac{\partial \rho_a}{\partial t} + \nabla \cdot (\rho_a \mathbf{V}_a) = 0, \tag{2.10}$$

where $\rho_a = n_a m_a$ is the mass density of species a.

$$\frac{\partial \rho_a \mathbf{V}_a}{\partial t} + \nabla \cdot (\rho_a \mathbf{V}_a \otimes \mathbf{V}_a) + \nabla p_a + \nabla \cdot \hat{\pi}_a + \frac{Ze\rho_a}{m_a}\left(E + \frac{1}{c}\mathbf{V}_a \times \mathbf{B}\right) = \mathbf{R}_a. \tag{2.11}$$

The pressure and viscous tensor p_a and $\hat{\pi}_a$ are defined in [Braginskii 65]. The fourth term on the left hand side of equation 2.11 describes the electro-magnetic force acting on the particles with a charge Z. The term on the right hand side is the friction momentum which gives the momentum exchange between different plasma components.

$$\frac{\partial \rho_a \langle v^2 \rangle / 2}{\partial t} + \nabla \cdot \frac{\rho_a \langle v^2 \mathbf{V}_a \rangle}{2} + Zen_a \left(\mathbf{E} \cdot \mathbf{V}_a\right) = Q_a, \tag{2.12}$$

where Q_a is a term which considers the energy exchange between the particles. The equations 2.11 - 2.12) are written in a conservative form, where on the left hand side there is conservation of the fluxes: mass, momentum, energy and on the right hand side are the source terms.

2.3.1 The continuity equation

The continuity equation of the whole plasma can be obtained from the species mass conservation equation. Summing the species equations over all the species gives the global mass balance in the plasma,

$$\frac{\partial \rho}{\partial t} + \nabla \cdot \rho \mathbf{V} = 0 \tag{2.13}$$

where $\rho = \sum n_a m_a$ is the plasma mass density and $\mathbf{V} = \frac{1}{\rho}\sum m_a n_a V_a$ is the average plasma velocity. The sum is taken over all the plasma components (electrons, atom, ions, molecules). The mass of the electrons is negligible in comparison with the mass of heavy particles, therefore it is valid to assume that ρ is the density of heavy particles and $\mathbf{V} = \mathbf{V}_h$. On the right hand side of equation 2.13 is zero due to the absence of net mass creation/destruction in chemical reactions.

2.3.2 The momentum equation

By summing the momentum equations for every species of the system 2.11 over all components assuming quasi neutrality of the plasma ($n_e = \sum Z n_i$, where the sum is taken over all the ions with their charges Z), one obtains the Navier-Stokes equation for the whole gas:

$$\frac{\partial \rho \mathbf{V}}{\partial t} + \nabla \cdot \rho \mathbf{V} \otimes \mathbf{V} = -\nabla p - \nabla \cdot \widehat{\pi} + \mathbf{j} \times \mathbf{B} \tag{2.14}$$

where p is the total plasma pressure and $p = \sum_a p_a = \sum n_a k_B T_a$; the viscous tensor $\widehat{\pi}$ expressed as: $\widehat{\pi}_{i,j} = -\mu\left[\left(\frac{\partial \mathbf{V}_i}{\partial x_j} + \frac{\partial \mathbf{V}_i}{\partial x_j}\right) - \frac{2}{3}\nabla \cdot \mathbf{V}\delta_{ij}\right]$, where μ is plasma viscosity. The global momentum balance is solved together with the mass balance in order to calculate the velocity field and the pressure. This approach is called a fluid plasma description and is commonly implemented in the case of thermal plasmas.

2.3.3 The energy equation

The energy equation of the plasma in the thermal equilibrium case is obtained as a sum of the energy conservation equations (2.12) for every species [Braginskii 65]:

$$\frac{\partial\left(\frac{\rho \mathbf{V}^2}{2} + \epsilon\right)}{\partial t} + \nabla \cdot \left(\rho \mathbf{V}\left(\frac{\mathbf{V}^2}{2} + H\right) + \mathbf{V} : \widehat{\pi} + \mathbf{q}\right) = Q_{JH} - Q_{rad}. \tag{2.15}$$

On the right hand side of equation 2.15 are the loss and gain energy terms due to particle interaction such as Joule heating $Q_{JH} = \mathbf{j} \cdot \mathbf{E}$ and radiation losses Q_{rad}. The first term on the left hand side of equation 2.15 is the energy of the system (kinetic and internal); the second term corresponds to the changes in energy flux: $\rho \mathbf{V}\left(\frac{\mathbf{V}^2}{2} + H\right)$ is the energy which describes the mass translation in space, where H is the heat function or in other words, the enthalpy of the system; term $\mathbf{V} : \widehat{\pi}$ gives the proportion of energy flux due to internal fluid friction and characterizes the energy dissipation due to viscous effects. Usually this term is negligible for plasmas and in further discussions is dropped. The other mechanisms of energy transfer which can be observed in plasma are considered in q, which can more generally be presented as:

$$\mathbf{q} = \sum_a \rho_a \langle v^2 \mathbf{V}_a \rangle / 2, \tag{2.16}$$

where the sum is taken over all the plasma components.
The energy conservation equation of the plasma 2.15 can commonly be written in terms of entropy s [Landau 69]. This involves taking heat functions into consideration: $d\epsilon = Tds - pdV = Tds - \frac{p}{\rho^2}d\rho$ and $dH = Tds + \frac{dp}{\rho}$ taking into account 2.14:

$$\rho T\left(\frac{\partial s}{\partial t} + \mathbf{V}\cdot\nabla s\right) = -\nabla\cdot\mathbf{q} + Q_{JH} - Q_{rad} \tag{2.17}$$

If the term on the right hand side of equation 2.17 is zero, the latter is the entropy conservation of the ideal gas. The equation 2.17 can be simplified if the gas velocity is lower than the speed of sound. Then the derivative of the pressure is negligible and depending on the thermodynamic properties can be disregarded as a function of pressure. However, the gas is still considered as compressible and the gas properties are a function of temperature. Indeed, for a constant pressure, while the density is a function of the temperature: $\frac{\partial s}{\partial t} = \left(\frac{\partial s}{\partial T}\right)_p \frac{\partial T}{\partial t}$ and $\nabla s = \left(\frac{\partial s}{\partial T}\right)_p \nabla T$. The value $C_p = T\left(\frac{\partial s}{\partial T}\right)_p$ is a specific heat function with a constant pressure. Equation 2.17 is transformed as:

$$\rho C_p\left(\frac{\partial T}{\partial t} + \mathbf{V}\cdot\nabla T\right) = -\nabla\cdot\mathbf{q} + Q_{JH} - Q_{rad} \tag{2.18}$$

The last term which has to be defined is the expression for the heat flux. Under the thermal equilibrium assumption the heat flux in the plasma can be described as:

$$\mathbf{q} = -\lambda\nabla T - \left(\frac{5}{2} + k_T\right)\frac{k_B T}{e}\mathbf{j} \tag{2.19}$$

where the heat flux includes the thermal conduction processes with thermal conductivity λ of the whole plasma; the effects of thermal diffusion due to arc current with k_T is the thermal diffusion ratio, $\mathbf{j}$ is the current density, which is defined below and the enthalpy of the electrons.

2.3.4 Current continuity equation

The total electric current of the plasma is:

$$\mathbf{j} = \sum_a Zen_a\mathbf{V}_a \tag{2.20}$$

where the sum is taken over all the plasma components a. In order to obtain the current density as a function of other plasma parameters, we multiply equation 2.11 by the factor Ze/m_a and find the sum over all the components a [Benoy 93] assuming that $m_e << m_i$:

$$\frac{m_e}{n_e e^2}\frac{\partial\mathbf{j}}{\partial t} - \mathbf{E} + \frac{1}{n_e e}(\mathbf{j}\times\mathbf{B}) - \frac{1}{n_e e}\nabla p_e + \frac{1}{n_e e}\mathbf{R}_e = 0. \tag{2.21}$$

Equation 2.21 is known as the generalized Ohm's law. The term $\mathbf{R}_e$ is a friction force which in most cases takes the interaction between electrons and heavy particles into account [Golant 77]:

$$\mathbf{R}_e = en_e\frac{\mathbf{J}}{\sigma_e} - \beta n_e k_B \nabla T,$$

where σ_e is the electron electrical conductivity, β is the numerical factor taking thermal diffusion into account. The most general case of Ohm's law is cumbersome and can be simplified for most cases. Only conduction due to electric field and thermal effects give the highest contribution to the whole current, therefore arc current is [Devoto 65]:

$$\mathbf{j} = \sigma\mathbf{E} + \frac{eD_e^T}{m_e T}\nabla T, \tag{2.22}$$

where D_e^T is the thermal diffusion coefficient [Devoto 65], σ is the plasma electrical conductivity and can be defined as $\sigma = \frac{e^2 n_e D_{ee}}{k_B T}$ and D_{ee} is the ordinary diffusion coefficient of electron-electron interaction. It is common to introduce a so-called thermal diffusion ratio k_T, which is $k_T = \frac{1}{m_e n_e}\frac{D_e^T}{D_{ee}}$.
The charge density $\rho_e = e(Zn_i - n_e)$ from equation 2.10 for the electron and ions, and the charge conservation is:

$$\frac{\partial \rho_e}{\partial t} + \nabla \cdot \mathbf{j} = 0 \tag{2.23}$$

Assuming quasi-neutrality of the plasma, then the current continuity equation is:

$$\nabla \cdot \mathbf{j} = 0 \tag{2.24}$$

2.3.5 Maxwell's equations

The magnetic field calculation can be established by introducing Maxwell's equations without introducing eddy currents:

$$\nabla \times \mathbf{B} = \mu_0 \mathbf{j} \tag{2.25}$$

where displacement currents are neglected.

$$\nabla \times \mathbf{E} = 0 \tag{2.26}$$

$$\nabla \cdot \mathbf{B} = 0 \tag{2.27}$$

Quite often the system of Maxwell equations is solved in terms of vector potential, which is defined as:

$$\nabla \times \mathbf{A} = \mathbf{B} \tag{2.28}$$

while Coulomb Gauge calibration is introduced for the vector potential.

2.3.6 Summary of the equations for the arc column description

As a summary, once again the system of the magneto-hydrodynamic equations in the case LTE is assumed, which is commonly used to describe thermal plasmas and which will be solved in this work, is:

$$\frac{\partial \rho}{\partial t} + \nabla \cdot \rho \mathbf{V} = 0, \tag{2.29}$$

$$\frac{\partial \rho \mathbf{V}}{\partial t} + \nabla \cdot \rho \mathbf{V} \otimes \mathbf{V} = -\nabla p + \nabla \cdot \mu \left(\nabla \mathbf{V} + \nabla \mathbf{V}^T \right) - \frac{2}{3} \nabla \left(\mu \nabla \cdot \mathbf{V} \right) + \mathbf{j} \times \mathbf{B}, \tag{2.30}$$

$$\rho C_p \left(\frac{\partial T}{\partial t} + \mathbf{V} \cdot \nabla T \right) + \nabla \cdot \left(-\lambda \nabla T - \left(\frac{5}{2} + k_T \right) \frac{k_B T}{e} \mathbf{j} \right) = \mathbf{j} \cdot \mathbf{E} - Q_{rad}, \tag{2.31}$$

$$\nabla \cdot \mathbf{j} = 0, \tag{2.32}$$

$$\mathbf{j} = \sigma \left(\mathbf{E} + k_T \frac{k_B}{e} \nabla T \right), \tag{2.33}$$

$$\nabla \times \mathbf{B} = \mu_0 \mathbf{j}, \tag{2.34}$$

$$\nabla \times \mathbf{A} = \mathbf{B}. \tag{2.35}$$

The equations of fluid motion are determined for the case of laminar flow and are valid when $Re = \frac{\rho V L}{\mu}$ is smaller than 1000, where L is the characteristic size of the discharge and Re_{max} does not exceed 100 in the case of a typical welding arc configuration. However, recent research in the simulation of plasma torches has shown that turbulence effects occur in thermal plasmas [Shigeta 16, ModirKhazeni 15].

This physical model can be applied for the largest part of the arc discharge. The model requires the additional computation of plasma composition, the functions of thermodynamic properties, and the transport coefficients.

2.3.7 Plasma properties and transport coefficients

Plasma composition, thermodynamic properties and transport coefficients of thermal plasmas vary strongly with temperature and are usually calculated for the case when LTE is established. In order to calculate the plasma composition, Saha-Eggert equations can be used for each plasma component [Lochte-Holtgreven 68]:

$$\frac{n_e n_Z}{n_{Z-1}} = \frac{2 Q_Z}{Q_{Z-1}} \exp \left(-\frac{E_Z - \delta E_Z}{k_B T} \right), \tag{2.36}$$

describing the ratio of the densities of the different ionization states by the Boltzmann term with the plasma temperature T. The function Q_Z is the partition function of each plasma component, E_Z is the ionization energy of ion Z and $\delta E_Z = \frac{Z e^2}{4\pi\epsilon_0 \lambda_D}$ is the lowering of the ionization function [Griem 63]. The calculation of particle densities requires knowledge of partial functions, which establish the link between the coordinates of microscopic systems and macroscopic

thermodynamic properties [Boulos 94]. Partition functions can be obtained from the electronic energy levels. While various studies can be drawn upon to define the right number of electronic levels, the difference between these various methods does not exceed 2 % [Murphy 14]. The Saha-Eggert system of equations needs to be completed with the Dalton law for the total plasma pressure: $p = \sum_Z n_Z k_B T + n_e k_B T$ and the plasma quasi-neutrality condition. The mass density results directly from the plasma composition by the relation $\rho = \sum_a m_a n_a$. The enthalpy per unit of mass of the system can be calculated according to [Cressault 04]:

$$H = \frac{k_B T}{\rho} \sum_a n_a \frac{d \ln(Q_a)}{d \ln(T)} + \frac{1}{\rho} \sum_a n_a \epsilon_a, \tag{2.37}$$

where the sum is taken over all the species considered in the plasma; ϵ_a is a reference energy [Cressault 04]. The specific heat using the enthalpy is:

$$C_p = \left(\frac{\partial H}{\partial T} \right)_p \tag{2.38}$$

The temperature dependence of C_p reflects the different ionization and dissociation processes within the plasma.

The transport coefficients (viscosity, thermal conductivity and electrical conductivity) were calculated using the Chapman-Enskog [Hirschfelder 64, Ferziger 73] method, applying the method of separation of electrons and heavy species derived by Devoto [Devoto 67]. The transport coefficients were approximated using Sonine polynomials. For this the interaction between particles within the plasma needs to be defined. The basic particle interactions (collisions) in the plasma are described by the particle number and collision integrals, which depend on the interaction potential. Usually only neutral-neutral interactions, ion-neutral interactions, neutral-ion interactions, and ion-ion interactions are taken into account [Murphy 14]. Electron-heavy particle interactions have little effect on the distribution function of the heavy particles and are therefore neglected in calculating the transport coefficients. Based on the definition of the collision integrals, transport parameters can be defined:

- the thermal conductivity of the whole plasma is $\lambda = \lambda_e + \lambda_h$ and was computed according to the second-order approximation of the Chapman–Enskog method,
- electrical conductivity is mainly defined by electron mobility and the electron density and was calculated according to the third order approximation of the Chapman–Enskog method [Devoto 65, Devoto 67, Devoto 66],
- viscosity is independent of electron properties ($\mu \approx \mu_h$) and was computed according to the first-order approximation of the Chapman–Enskog method [Cressault 04].

The thermodynamic functions and transport parameters have been calculated for many different plasmas and are widely accessible.

2.3.8 Radiation model

Because an arc plasma is highly luminous, radiation transport must be considered. Radiation losses generally have to be calculated as a function of wavelength, frequently extending into the far ultraviolet region of the spectrum. It is highly desirable to account for radiation losses in an approximate way in order to avoid the complexity of doing exact calculations of arc properties. To determine the transport of radiant energy the fundamental differential equation [Lowke 74, Modest 13] of the radiation needs to be solved for every wavelength. It needs to take into account absorption and emission, which in the case of LTE is connected with the Kirchhoff law. All the mechanisms of radiation emission and absorption must be considered: continuum radiation, line intensities and profiles, molecular bands.
The computation of the total radiation transfer is a complex task, since the radiation intensity diverges with the frequency. Therefore some assumptions need to be made in order to calculate radiation energy. In the case of a thermal plasma, the emission is usually calculated according to the net emission coefficient ϵ_N which consists in calculating the net radiation ('net' meaning the difference between emission and absorption, i.e. the divergence of the radiation intensity). The plasma is often considered as an isothermal sphere with the radius R_p ($R_p = 0$ where no absorption occurs within the plasma, i.e. the plasma is optically thin) with a uniform radiation intensity. According to [Gleizes 05], the radiation transfer equation can be simplified and the expression for the net emission coefficient is:

$$\epsilon_N = \int_0^{\inf} B_\nu K'_\nu \exp\left(-K'_\nu R_p\right) d\nu, \tag{2.39}$$

where B_ν is black body radiation, K'_ν is the absorption coefficient which considers spontaneous processes and the value of ϵ_N is obtained on the center of the cylinder. It was shown [Lowke 74] that this method of emission evaluation via net emission works well for plasmas with $T > 3500\,\mathrm{K}$ in atomic gases. The results of all the calculations [Cressault 13a] show that strong absorption occurs in the first millimeter of the plasma due to resonance line absorption. Recommendations concerning the choice of R_p are given in [Gleizes 92].
In order to determine the value of the radiation losses in the plasma in 2.31, the net emission coefficient is assumed used:

$$Q_{rad} = 4\pi\epsilon_N \tag{2.40}$$

The drawback with using the NEC is its limited applicability, as this method can reliably predict radiation losses only in the hottest regions of the plasma. It does not describe the radiation re-absorption in the colder regions and thus cannot evaluate the amount of radiation escaping from the plasma. In this work, this method was chosen as appropriate to describe the arc column. However, there are other methods: for example, the partial characteristics (PC) method, mean absorption coefficient method, and discrete ordinates method (DOM). Unlike

NEC, the PC method includes the calculation of radiation transfer in the absorbing parts and is able to predict the radiation escaping from the plasma. However, it requires a large database and in complex to implement, while the NEC is a widspread method that has been tabulated for most common plasmas.

2.4 Plasma-electrode interaction. Deviation from equilibrium in the arc.

As shown above, the method to describe the plasma behaviour of the electric arc is applicable if the plasma is in a state of LTE. Experimental research has shown that most of the arc plasma is dense, characterized by a high temperature, which establishes thermal equilibrium within the arc bulk. However, there are regions where the equilibrium is disturbed: the region near the electrodes and on the arc fringes.
Zones near the electrodes play an essential role, since they define current and energy transfer between metal and plasma, i.e. the plasma-electrode interaction. The term plasma-electrode interaction covers all the reactions taking place on the electrodes themselves and in their vicinity. The zones where the high gradients of plasma parameters occur and the plasma is no longer in LTE will be called the near-cathode and near-anode zones.
Different kinds of perturbations from the LTE plasma occur in the near-electrode layers. This allows one to divide the near-electrode perturbation region into a number of sub-regions with different physics [Benilov 08, Benilov 95b]. Figure 2.1 schematically depicts the sub-layer structure of the near-electrode zone. Each sub-layer is charcterized by its length, which in the case of the cathode and anode can be different.
In the LTE arc column Joule heating and radiative energy losses dominate over all the other (convective energy transport, enthalpy transport by diffusion fluxes of species and heat conduction) mechanisms of energy transport. In the layer just adjacent to the LTE arc column, this no longer holds and diffusion fluxes play an important role. Other contributions of energy dissipation therefore need to be considered. This layer, where the plasma is still in LTE, is called the thermal perturbation layer (TP). After the thermal perturbation layer, the near-electrode plasma is no longer in LTE. Three kinds of deviations from LTE occur near the electrode. The most important ones are pictured in figure 2.1:

- violation of thermal equilibrium, i.e. a divergence between T_e and T_h. This layer is called the thermal non-equilibrium layer (TN);
- violation of the ionization equilibrium, i.e. a deviation of the electron density n_e from the electron density $n_{e_{Saha}}$ predicted by the Saha equation for violation of quasi-neutrality. This layer is called the thermal ionization layer (IL);

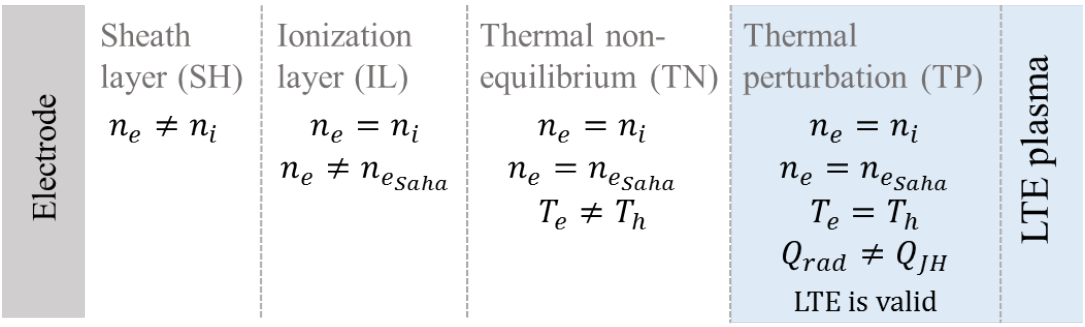

Figure 2.1: Sub-layer structure of the near-electrode zone.

- violation of quasi-neutrality. This layer is called the space-charge layer or sheath layer (SH).

Plasma-electrode interaction cannot be described in the same way near the cathode and the anode due to the different processes occurring on and near the electrodes [Benilov 08]. Therefore, it is reasonable to separate the description of plasma-cathode and plasma-anode interactions. In this chapter, the processes occurring near and on both electrodes are described and discussed; the current state of the art for both regions is also presented.
In spite of the complications which appear due to non-equilibrium effects near the electrodes, the main intention in this work to find a simple and at the same time reasonable description of these zones and match it with the theory of the LTE arc column. It is also of great interest to define the electrode temperatures.

2.5 Plasma-anode interaction

Recent reviews have reported on the processes occurring on the anode and in the near-anode plasma [Heberlein 09, Shkol'nik 11]. In these studies, the main principles operating in plasma-anode interaction, from the experimental point of view, are presented and a brief summary of theoretical research on the topic is also given. The theoretical description of the near anode region is well synthesized in [Almeida 09, Benilov 08]
The investigations by [Bron OB 75, Hartmann 01b, Hartmann 01a, Yang 06, Yang 07] show that there are different possibilities for the discharge in the near anode area. Usually the term anode "attachment" is used. There are two types of anode attachment: diffuse and constricted. In the case of diffuse attachment, the plasma propagates all along the anode surface, whereas for contracted attachment the plasma collapses near the anode and forms a single or several spots [Yang 06, Trelles 13a], called anode spots. The reason for this distinction between the two modes is the elementary processes which take place on the anode and in the near-anode region. In the case of diffuse attachment the main processes on the anode surface

are absorption-desorption and neutralization of the ions; evaporation of the anode material is negligible. Constricted attachment is considered as a more complicated case. In fact, the attachment can be single or multiple, i.e. when the current passes from one or several spots on the anode surface. Contraction of the arc near the anode leads to the formation of a new plasma jet which is directed from the anode surface to the plasma. In most cases constricted attachment is accompanied by strong anode evaporation and anode material sputtering.

The sub-layer structure was described above; for the anode it is explicitly given in [Shkol'nik 11, Dinulescu 80, Almeida 09]. The characteristic length of these layers depends on internal conditions: gas pressure, current density, working gas and etc. The following estimation is valid for atmospheric pressure and high-current density arcs: the sheath layer length is on the order of the Debye length $L_0 \sim 10^{-4}$ mm, while l_e, l_i on the order of 10^{-3} mm are the mean free path of electrons and ions; the ionization equilibrium length is $L_i \leq 0.1$ mm; the temperatures equalize within the distance $L_r \sim 1$ mm.

The near-anode zone is characterized by the voltage drop. Uncertainties exist due to the definition of the "anode fall": different authors use a different meaning and therefore obtain different values. However it is reasonable to define the anode fall as the difference between the anode potential and the potential of the arc column [Shkol'nik 11], denoted U_a. This is a complete value of the anode fall which is the sum of drops in the space charge layer and the ionization and thermal non-equilibrium layers, i.e. $U_a = \phi_{a0} + \triangle\phi$. Usually for the description of different anode attachment types, close attention is paid to the value of the anode fall [Amakawa 98, Jenista 97, Yang 07, Khrabry 17]. In order to obtain diffuse attachment a negative anode fall has to occur [Heberlein 09]. This is true for high current discharges but for low current discharges the physics of plasma-anode interaction is different. A positive anode fall is likely present in the diffuse attachment mode for low current discharges [Raizer 87, Khrabry 17]. In the well-known case of a welding arc with a flat and quite large anode, the anode fall is negative or close to zero.

It is important to recall that in the zone near the anode the temperature and particle density gradients are higher than in the column. When the temperature and particle density gradients increase, the charged particles start to move due to the diffusion mechanism (thermal diffusion, for example). At some distance from the anode, the diffusion mechanism exceeds the electric field influence and the ions move back in the direction of the anode, reducing the electron flow to the anode. In the space-charge layer, a positive space charge appears and a potential drop occurs ϕ_{a0}, which restricts the electron flow to the anode surface, and only electrons with a velocity greater than $\sqrt{\frac{2e\phi_{a0}}{m_e}}$ can reach the anode surface. Therefore the drop in the space charge layer restricts the arc current. It may be claimed that the anode drop controls the arc current.

The discussion above does not take the hydrodynamic behavior of the plasma near the anode

into consideration. Hydrodynamic effects are also important, however, and have to be considered as shown in [Hartmann 01b]. If the direction normal to the anode flow is considered, a reduction in the plasma flow towards the anode, for example by increasing the length of the arc and reducing any parallel flow (if it is imposed), will reduce the convective transport towards to the anode. Temperature gradients and as a result constriction and a positive anode fall will occur [Hartmann 01a, Jenista 97]. The dependence of the anode attachment on the plasma gas flow is well described in [Hartmann 01b], where a different inflow of the Ar gas for a transferred arc is imposed in order to obtain different attachment modes.
The situation changes when the plasma flow is not perpendicular to the anode, for example in the case of plasma torches, where the flow is parallel to the anode. A set of experiments with a rod anode and two parallel plates as an anode is presented in [Eckert 67] showing that constricted attachment will more likely appear. Moreover, if the superimposed flow rate reaches a critical value, the anode attachment becomes unstable and starts to move along the anode downstream. Once the voltage drop along the anode layer achieves a certain value, an upstream breakdown (*restrike*) takes place. Therefore, there are significant differences in anode attachment behavior depending on the hydrodynamic flow.

2.5.1 Modelling of the near-anode layer

As already mentioned, the structure of the near electrode layer is complex. Experimental investigations are complicated with such small distances, and experiments are mainly designed to predict the anode temperature, not the structure of the plasma layer nearby. Thus it is common to find only a theoretical description of this region. A limited number of studies give a theoretical description of the anode sub-layer structure [Almeida 09, Nazarenko 89, Nemchinskii 77], and these models are one dimensional and stationary. Convection effects are excluded from the observations as are evaporation and sputtering of the anode material. Such models are usually called unified models of the near-electrode layer and include non-equilibrium effects for the complete layer length. Thermal non-equilibrium effects, deviation from quasi-neutrality and ionization equilibrium have to be considered in the model. Therefore, for a unified layer modeling, the system of equations should contain:

- Temperatures of the electrons and heavy particles;
- Electron and ion densities;
- Current conservation of electrons and ions;
- Gas-kinetic pressure of the plasma;
- Description of the ionization-recombination processes;

- Poisson's equation for the space charge zone.

These calculations have been made in Ar [Yang 07, Dinulescu 80, Nazarenko 89, Nazarenko I 00] and He [Nemchinskii 77] in atmospheric pressure conditions and for higher pressures in Hg and Xe [Almeida 09]. With the exception of [Almeida 09], these studies adopt a two-layer approach to the anode layer description. The equations are solved separately in the sheath layer with deviation from quasi-neutrality and the rest of the plasma layer. A simplified picture of such an approach is presented on figure 2.2: the space-charge layer (I) adjacent to the anode, where quasi-neutrality is disturbed, and the rest where no thermal or ionization equilibrium exists (II). At the end of layer (II), the temperature $T_e = T_h$ and is equal to the LTE plasma temperature T, which is defined in the arc column. The solution has been matched according to Langmuir probe theory [Langmuir 29] between the sheath and the rest of the near-anode layer. The additional conditions for a potential drop in the sheath layer were defined in [Dinulescu 80]: $\phi_{a0} = -\frac{k_B T_e}{e} \ln\left(\frac{e n_{ea} C_e}{4j}\right)$, where n_{ea} is the electron density at the interface between layers, C_e is the average thermal speed of the electrons $C_e = \sqrt{\frac{8 k_B T_e}{\pi m_e}}$ and j is the current density in the layer which is constant in the model, and $\frac{1}{4} e n_{ea} C_e$ is a random current. The sign of the potential drop is defined by the relation between the actual current density j and a random current density and is negative when the random current is higher than the actual current.
Each of the above-mentioned studies gives slightly different values of the potential drop. For example, in [Nemchinskii 77] for Ar and He plasma current densities of 325 A/cm^2 and 550 A/cm^2, the value of the potential drop is positive. For gase He the authors attribute the positive value of ϕ_a to the dissociation processes in He. In [Dinulescu 80] for current densities ranging from 600 A/cm^2 to 3 kA/cm^2 in Ar, the potential drop was found to be in the range -2.7 V to -1.8 V. More detailed analysis of the processes in the near-electrode layer is presented in [Nazarenko 89, Nazarenko I 00]. On figure 2.3, at some distance from the anode ion current, the sign of the ion current changes, therefore the ions start to move towards the anode surface. The potential in layer (II) grows in the anode direction until reaching its maximum and then begins to fall in the anode direction, finally becoming negative. In the arc column plasma the electrons move due to the electric field. At some distance from the anode, the diffusion mechanism has a significant impact on the current transfer within the near-anode layer. For this reason, the electric field may change sign. The sign of the electric field changes, which prevents the electrons from moving towards the anode, while the ions start to move to the anode, thus the electric potential starts to decrease.
Temperature non-equilibrium effects in the layer are also important. An example can be seen on figure 2.3 where the temperature of the heavy particles drops down to the anode temperature, while the electron temperature does not fall so fast.
In [Nemchinsky 94] the case of the near-anode plasma layer for a spherical anode was simulated

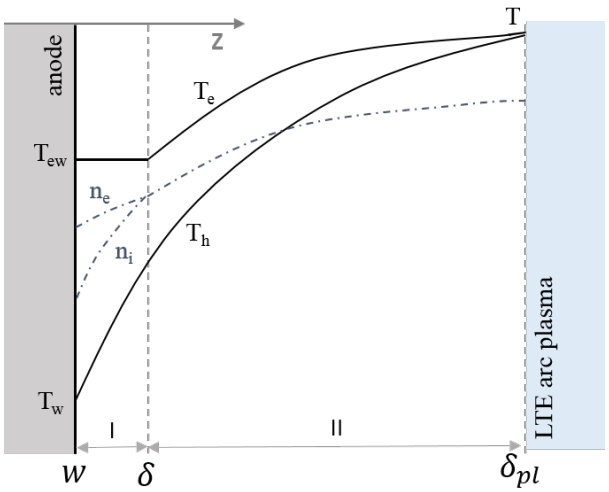

Figure 2.2: Schematic structure of the near-anode layer for high pressure electric arcs.

(Ar, $I = 200\,\mathrm{A}$). Interesting results were obtained: for a small anode radius $R = 0.57\,\mathrm{mm}$ the highest electron temperature occurred adjacent to the anode in comparison to the results obtained with an anode $R = 1.20\,\mathrm{mm}$ with the same current intensity. In the case of the small anode, the potential fall in the anode layer became positive. However on increasing the anode radius, the anode fall became negative.

The models discussed above allow us to understand the processes within the near-anode layer. These models are complex in that the sheath and the rest of the sub-layer structure are considered separately. Important changes were made in [Almeida 09] where the near-cathode layer description [Almeida 08] was adapted to describe the anode region in higher pressure arcs. The entire near-electrode region was considered, i.e. it was not divided into sub-layers. The structure of the near-anode layer, which was discussed according to figure 2.1 was resolved. Unfortunately, the calculations were done only for high pressure arc discharges, which are beyond the scope of this work.

For most industrial applications, the focus is on establishing the complete model of electrodes, near-electrode layers and plasma column concurrently, in order to predict the plasma behavior and electrode heating simultaneously. Such models usually simplify the plasma description near the electrodes and often the significant contributions from these non-equilibrium zones are excluded. The first attempts to develop a model including the LTE arc description together with the cathode were by [Zhu 92, Morrow 93, Zhu 95], implementing both cathode and anode regions. These models were used to perform two dimensional simulations of the arc column, while the non-equilibrium layer was taken into account using a one dimensional description and included corrections of the equilibrium parameters with ambipolar diffusion effects. Thus, the non-equilibrium electron density estimated the electrical conductivity near

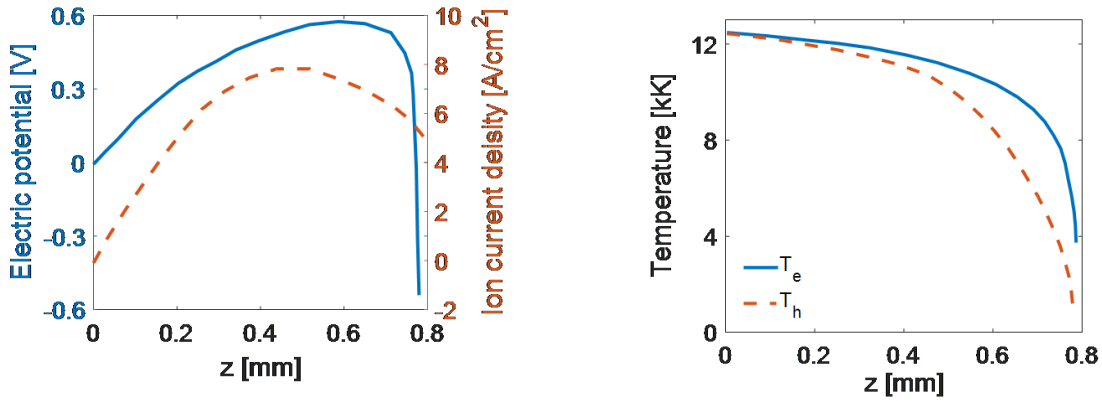

Figure 2.3: Left – Plasma potential and ion current density distribution in the anode layer. Right – Electron and heavy particle temperatures. $z = 0\,\text{mm}$ is the boundary between the LTE plasma and the near-anode layer. Ar, $p = 1\,\text{atm}$, $900\,\text{A/cm}^2$.

the electrode [Sansonnens 00], which in the case of an LTE arc near the electrode is small. Further development of this approach with slightly modified boundary conditions was used to define the anode temperature [Tanaka 06].

The first model of the arc bulk plasma and near-anode layer in the 2D axi-symmetrical case was proposed in [Jenista 97, Amakawa 98]. The near-anode layer was solved continuously up to the anode surface: the two-temperature MHD equations were solved in the arc plasma and in the electrode layer simultaneously. The ionization and recombination processes were included to resolve non-equilibrium effects. The deviation from thermal equilibrium was shown as well as the impact of diffusive currents. A positive value of the potential drop in the layer was obtained for currents 50 A, 100 A and 200 A. However, the space-charge layer was disregarded in these models, which can impact the value of the potential drop.

Complex one dimensional anode-layer models make the models very cumbersome and increase the calculation time drastically. Moreover they are difficult to extend to 2D and 3D cases. Over the last decade the aim has been to simplify the description of plasma-electrode interaction by disregarding non-equilibrium effects. The interaction between the LTE plasma and the anode is considered by means of energy and current transfer between the LTE plasma and the anode. With this approach, the anode temperature and the current transfer can be estimated [Bini 06, Masquere 07, Tanaka 03]. Using plasma-anode coupling, numerical simulations can be performed: for example, the material evaporation from the anode surface in 2D cases was estimated in [Gonzalez 93, Gonzalez 97, Murphy 09, Lago 04, Mougenot 13]. The limitations of these models come from the LTE arc column description which is expanded up to the anode surface, without additional processing.

This kind of numerical coupling requires paying particular attention to the heat transfer at the

arc-anode interface due to the low temperature adjacent to the anode. This low temperature near the anode gives a low electrical conductivity if thermal non-equilibrium is not taken into account. This can be overcome by taking into account electron diffusion in this region, which requires a separate continuity equation for electrons [Sansonnens 00]. A simpler approach is the LTE diffusion approximation [Lowke 06], in which the mesh size adjacent to the anode is chosen as approximately equal to the electron diffusion distance, an approach used in [Murphy 09]. In [Lago 04], the authors chose the near anode element size and imposed metal conductivity along this element.

2.5.2 Matching conditions of the LTE arc bulk and the anode

In this work, the attempt to establish a relation between the LTE arc column and the anode was done in a simple manner. The LTE arc description does not extend to the anode surface and the bulk plasma and the anode were solved separately. On the interface between them, matching conditions were applied according to the energy and current conservation. A schematic presentation of the anode-interface-LTE arc is shown on figure 2.4. The zero-dimensional interface

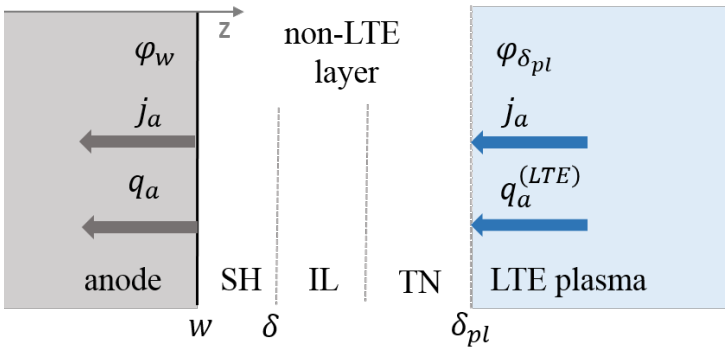

Figure 2.4: Schematic representation of the plasma-anode interface.

includes the non-LTE layer: the space-charge layer, the ionization and thermal non-equilibrium layers and ensures energy and current transfer between the anode and LTE arc column. In order to define the correct boundary conditions on the interface, a step by step reasoning was followed.

First, the energy transport was determined, using the system of equations for the near-cathode zone presented in [Almeida 08]. The model considers thermal and ionization equilibrium, while the plasma consists of electrons, atoms and ions. The energy conservation for the whole plasma near the anode, when thermal and ionization equilibrium are not satisfied, is expressed in equation (13) in [Almeida 08]:

$$\nabla \cdot \left(\frac{5k_B T_h}{2} \mathbf{J}_a + \frac{5k_B T_h}{2} \mathbf{J}_i + \left(\frac{5k_B T_e}{2} + A_i \right) \mathbf{J}_e + \mathbf{q}_e + \mathbf{q}_h \right) = \mathbf{j} \cdot \mathbf{E} - w_{rad}, \tag{2.41}$$

where $\mathbf{J}_a, \mathbf{J}_i, \mathbf{J}_e$ are the particle fluxes and $(\mathbf{J}_i - \mathbf{J}_e) = \mathbf{j}/e$. A_i is the ionization energy of the atoms (in eV); w_{rad} is the radiation losses in the non-equilibrium near-electrode layer. The energy fluxes of the electrons $\mathbf{q}_e$ and heavy particles $\mathbf{q}_h$ take into account conductivity and thermal diffusion. Multiplying the current continuity equation $\nabla \cdot (\mathbf{J}_i - \mathbf{J}_e) = 0$ by $(A_i - A_f)$, where A_f is the work function of the electrode (in eV), adding this result to 2.41 and considering $\nabla \cdot (\mathbf{J}_i + \mathbf{J}_a) = 0$, the energy conservation of the whole plasma is:

$$\nabla \cdot \left[(A_i - A_f)\, \mathbf{J}_i + \left(\frac{5k_B T_e}{2} + A_f \right) \mathbf{J}_e + \mathbf{q}_e + \mathbf{q}_h \right] = \mathbf{j} \cdot \mathbf{E} - w_{rad}. \tag{2.42}$$

Equation 2.42 is the energy conservation of all the species in the whole electrode layer. The energy flux is represented by the vector in the brackets on the left hand side of equation 2.42. Therefore, the energy flux from the plasma to the anode surface, taking into account the geometry of figure 2.2, is:

$$q_a = -\left[\left(\frac{5k_B T_e}{2} + A_f \right) J_e + q_e + (A_i - A_f)\, J_i + q_h \right]_w. \tag{2.43}$$

The index w shows that the heat flux is calculated on the anode boundary. The heat flux is determined by the electron and ion fluxes, respectively q_e and q_h.

Previously it was mentioned that ion current plays an important role in the near-anode layer. However, its value is still much smaller than the electron current $J_e >> J_i$. Let's assume that the arc current in the near anode layer is defined by the electron current, then equation 2.42 can be rewritten as:

$$\nabla \cdot \left[\left(\frac{5k_B T_e}{2} + A_f \right) \mathbf{J}_e + \mathbf{q}_e + \mathbf{q}_h \right] = \mathbf{j} \cdot \mathbf{E} - w_{rad}. \tag{2.44}$$

Rewriting 2.44 in a one dimensional approximation according to the geometry on figure 2.4, we obtain:

$$\frac{d}{dz} \left[\left(\frac{5k_B T_e}{2} + A_f \right) \frac{j}{e} - q_e - q_h \right] = jE_z - w_{rad}, \tag{2.45}$$

where $j = j_z$ to shorten the expression. Then, the heat flux to the anode is:

$$q_a = \left[\frac{j}{e} \left(\frac{5k_B T_e}{2} + A_f \right) - q_e - q_h \right]_w, \tag{2.46}$$

where the values of all the variables should be taken on the anode surface w. The current density j is the current density in the anode layer 2.4 and corresponds to j_a.

Let's proceed with the energy balance of the plasma in the anode layer assuming that the current density $j = j_a = const$ in the layer. Integrating equation 2.45 along the anode layer, i.e. from $z = \delta_{pl}$ the boundary with the LTE arc column to the anode surface boundary $z = w$ (figure 2.4) gives:

$$\left[\left(\frac{5k_B T_e}{2} + A_f \right) \frac{j}{e} - q_e - q_h \right]_w - \left[\left(\frac{5k_B T_e}{2} + A_f \right) \frac{j}{e} - q_e - q_h \right]_{\delta_{pl}} = -j \left(\phi_w - \phi_{\delta_{pl}} \right) - \int_{\delta_{pl}}^{w} w_{rad} dz \tag{2.47}$$

The first term on the left hand side in parentheses is just the flux to the anode defined by 2.46. The second term in the parentheses is the energy delivered from the LTE plasma to the non-equilibrium layer $q_a^{(LTE)}$. The first term on the right hand side in the parentheses is a voltage drop within the near-anode layer U_a. The term $W_{rad} = \int_{\delta_{pl}}^{w} w_{rad} dz$ is the power lost by the electrons inside the layer through radiation.
A simple expression for the heat fluxes considers a thermal conductivity and $\mathbf{q}_e = -\lambda_e \nabla T_e$ and for heavy particles $\mathbf{q}_h = -\lambda_h \nabla T_h$. On the boundary δ_{pl} the temperatures are equal $T_e = T_h$ and the gradients $\frac{dT_e}{dz} \simeq \frac{dT_h}{dz} \simeq 0$. Therefore, from equations 2.47 and 2.45 the flux to the anode is:

$$q_a = \left(\frac{5}{2} k_B T_{e_{\delta_{pl}}} + A_f \right) \frac{j}{e} + jU_a - W_{rad}. \tag{2.48}$$

The expression 2.48 gives an estimation of the energy flux delivered to the anode from the non-equilibrium anode layer. The value of the electron temperature $T_{e_{\delta_{pl}}}$ is taken on the external boundary of the thermal non-equilibrium layer. This expression of the energy flux to the anode can be used to calculate the anode heating and can be applied as a boundary condition on the anode surface excluding radiation losses from the surface.

The boundary conditions on the LTE-plasma - anode interface

The anode non-equilibrium layer is disregarded and the LTE column directly matched with the solid anode by means of a zero-dimensional interface. In this formulation, the temperature has a discontinuity; the electrostatic potential also has a discontinuity with a pre-defined value U_a. Since the energy and current conservation equations are elliptical, four kinds of conditions need to be introduced on each side of the interface, i.e. on w and on δ_{pl} (figure 2.4):

- On the LTE column side (δ_{pl}). The normal component of the conductive heat flux equals zero, i.e. $-\lambda \frac{\partial T}{\partial n} = 0$. Current continuity is established, i.e. $j_a = j_n$, where j_n is a normal component of the arc current from the LTE solution.

- On the anode side (w). The heating of the anode by the plasma is taken into account according to 2.48, where the value of $T_{e_{\delta_{pl}}}$ is taken on the LTE plasma side. The radiation losses from the material according to the expression $\epsilon \sigma_{SB} T_a^4$ are considered, where $\sigma_{SB} = 5.67 \cdot 10^{-8}\,\mathrm{W \cdot m^{-2} \cdot K^{-4}}$ is the Stefan–Boltzmann constant, ϵ is the emanation coefficient and T_a is the anode temperature. Current continuity is established, i.e. $j_a = j_n$, where j_n is the current density normal to the electrode surface.

This approach makes it possible to calculate the anode heating without implementing the sub-layer model and plasma non-equilibrium. One of the advantages of using this method is that it avoids temperature gradients between the arc column and the anode. Therefore no dramatic changes occur in the electrical conductivity near the relatively cold anode, as has been observed

in the models [Lago 04, Bini 06]. Last but not least, the value of the near-anode voltage drop U_a is unknown. It has been estimated from complicated models [Almeida 09, Khrabry 17] for high pressure arcs in Hg and Xe and was found to range from -1 to +1 V for different arc current densities. However, experimentally it is difficult to measure the value of the anode fall. According to the existing data, the anode fall can be either positive or negative and does not exceed several volts$(1-2V)$. Therefore, in the present work, a value of 0 V was chosen for the anode voltage drop. This assumption has no impact on the plasma side but has an influence on the anode heating. However, in comparison with the first and second terms on the left hand side of equation 2.48 which make the main contribution to anode heating, the impact of the anode voltage drop is small. The radiation losses in the layer can be estimated according to formula (11) in [Almeida 09]. The evaporation of the anode material is not considered in the present work.

Recent results [Almeida 17] using the unified anode model showed the important relation between anode heating voltage and arc current density. Hence, the anode heating voltage according to [Almeida 09] is:

$$U_h = \left(\frac{5}{2}k_B T_e + A_f\right)\frac{1}{e} + U_a - \triangle U_{rad}, \tag{2.49}$$

where $\triangle U_{rad} = W_{rad}/|\mathbf{j}|$ and T_e is taken on the anode surface. In [Almeida 17] it was shown that for a wide range of parameters (gas nature, gas pressure) the anode heating voltage is constant and $U_h = 6.1\,\mathrm{V}$. Knowing the value of U_h one can estimate the value of q_a on the anode surface with the simple expression $q_a = U_h j$.

This method was applied in the present work. The calculations were done using two methods according to 2.48 and with respect to 2.49 and will be shown below.

2.6 Plasma-cathode interaction

Plasma-cathode interaction has been extensively investigated for many years in the HID lamp industry, where the high pressure low current[Benilov 02a, Neumann 87, Lister 04, Benilov 08] discharge and its interaction with the cathode is a key point. Since the replacement of these lamps with other light sources, work on plasma-cathode interaction has mainly focused on welding and cutting processes.

It is important to describe plasma-cathode processes correctly, since they define current transfer from the electrode to the arc. Experimental investigation of the near-cathode layer is a challenging task, however, due to its small size [Dabringhausen 02, Luhmann 02, Redwitz 05]. Theoretical models are therefore of great interest. Many efforts have been made to understand the processes taking place on the cathode and in the layer. Theoretically and experimentally, the existence of two modes of arc attachment on the cathode has been predicted: diffuse and

spot (or multispot) attachment [Dabringhausen 05a, Dabringhausen 05b]. In the spot mode the diameter of the arc attachment is much smaller than the cathode diameter. The diffuse mode is characterized by a much larger attachment area whose diameter is of the same order of magnitude as the cathode diameter. This type of attachment can exist in stationary and dynamic modes [Bötticher 01, Benilov 03]. Theoretically the spot structure has been obtained first by introducing so called non-linear surface heating of the cathode by [Bade 63] and continued by [Benilov 95a] and [Bötticher 00, Bötticher 01]. In these works, the plasma boundary layer model is used as a boundary condition for the cathode heat conduction problem, thus allowing the decoupling from the bulk plasma. For higher current arc discharges, a similar structure on the cathode was observed in [Mitrofanov 07]. It was found that the transition between the modes takes place due to instabilities and can be explained with bifurcation theory [Benilov 06, Benilov 03], which makes it different from the anode where the attachment type is defined by the processes near the anode. The diffuse mode exists at all currents and its current voltage characteristic (CVC) has two branches, one falling and the other rising, separated by a point of minimum. There are values of the current when any mode (central spot, edge spots and etc.) appears on the cathode surface. This transition between modes on the cathode is well known in nonlinear theory and can be described using bifurcation theory.
In order to illustrate the complexity of experimental investigation, we introduce the characteristic lengths of each non-equilibrium layer in the case of the cathode. A detailed description of these lengths is presented in [Benilov 95a] in the case of a high pressure discharge. The deviations can be characterized by the following length scales, respectively: the length of electron energy relaxation for the thermal non-equilibrium layer; the ionization length for the ionization layer; the Debye length for the space-charge layer figure 2.1. Estimations [Benilov 95a] of these scales can be obtained from numerical simulation, for example in the case of a pressure of $1atm$, on figure 5 for argon and on figure 3 for mercury [Almeida 08]. Therefore the electron energy relaxation is $L_r \sim 0.1$ mm, the ionization length is $L_i \sim 10^{-2}$ mm and the Debye length is $L_0 \sim 10^{-4}$ mm. From the previously estimated characteristic lengths of the sub-layers for the anode, one can conclude that the near-cathode layer is narrower.

2.6.1 Modelling of the near-cathode layer

In comparison to the anode where emitting mechanisms from the anode surface are negligible, thermionic emission amplified by the Schottky effect is a key mechanism of electron emission on the cathode for electric arcs [Benilov 02b]. The electron emission produces a cooling effect on the cathode. In order to maintain a sufficient cathode temperature for emission, the cathode needs to be heated by another mechanism. This mechanism is the heating of the cathode by ions coming from the plasma and accelerated in the space-charge sheath. Therefore ion current

is no longer negligible [Benilov 95b]. A considerable electrical power must be deposited in the space-charge sheath in order to sustain current on a cathode. Thus, the space-charge sheath plays an extremely active role at the cathode, in contrast to what happens on the anode. In conclusion, the ion current is not negligible near the cathode, and energy deposition in the space charge and ionization layers plays a significant role. In other words, the voltage drop near the cathode should be high enough to sustain the processes near the electrode.

In order to introduce plasma-cathode interaction, as for the anode, the full system of non-equilibrium equations needs to be considered, which can deviate from ionization equilibrium and quasi-neutrality. The most advanced model is that of [Almeida 08]. It takes into account three plasma components (electrons, atoms, ions) without dividing it into sub-layers, and solves the hydrodynamic equations in the layer. Calculations were done in the current range $10^6 - 10^8$ A/m^2 and high pressures (up to 100 bars) in atomic gases. For molecular gases and low currents a similar 1D approach was used in [Benilov 95a].

The theory developed in [Morrow 93, Sansonnens 00, Zhu 92, Zhu 95, Lowke 97] provides a description of the arc column and its matching with the electrodes. The cathode and arc column are treated together. However, in the near cathode region, non-equilibrium effects were taken into account to improve the electrical conductivity of the plasma. By implementing ambipolar diffusion near the electrodes the authors achieved higher electrical conductivities in this region. Moreover additional conditions for the numerical mesh size were imposed near the electrodes. Boundary conditions for the current density distribution on the cathode are specified in [Lowke 97] which takes only emission current and ion current into account.

A two-dimensional modeling of high-pressure arc plasmas without the assumptions of thermal or ionization equilibrium was performed in [Amakawa 98, Haidar 99]. However, the assumption of quasi-neutrality is more difficult to relax since this amounts to solving the Poisson equation in the whole near cathode region, including its outer part where the density of the charged particles and the degree of quasi-neutrality are quite high. As already mentioned, most of the energy near the cathode is deposited in the space-charge and ionization layers. Therefore a model of a near-cathode layer in a high-pressure arc discharge must include descriptions of the ionization layer and the near-cathode space-charge sheath, with some procedure for matching the solutions describing these two zones, while the temperature deviation in the layer has no strong impact [Benilov 08]. Numerical studies of the ionization layer accounting for the variability of heavy-particle and electron temperatures were carried out in [Hsu 83b, Rethfeld 96]. The attempt to match a diffusion solution for the ionization layer with a collisionless solution for the sheath, where the ions were assumed to leave the ionization layer and enter the sheath with a mean thermal velocity $\sqrt{3k_BT_h/2m_i}$ in [Hsu 83b] and the Bohm velocity $\sqrt{k_BT_e/m_i}$, is unjustified.

There are a huge number of studies in which the cathode layer is described by means of energy

and current conservation, separately from the arc plasma. Among these models, three consider a collisionless space-charge sheath: the model formulated by Benilov in [Benilov 95b] and modified in [Benilov 02b, Benilov 05], the models [Schmitz 02, Schmitz 01] and the model [Lichtenberg 05]. The model [Benilov 95b, Benilov 02b] is based on the multifluid solution for the ionization layer [Benilov 98], which accounts for inertia and the momentum exchange due to volume reactions. The model [Schmitz 02, Schmitz 01] assumes that the ionization length is much bigger than the ion mean free path, and consequently employs a diffusion solution, therefore no inertia and no momentum exchange are considered. The model [Lichtenberg 05] was formulated with similar criteria for the ionization length. There, an attempt was made to expand the range of applicability of the solution for the ionization layer by taking into account the momentum exchange due to volume reactions, although inertia was not included. In the model [Benilov 95b, Benilov 02b] no restrictions were imposed on the value of the ionization length. Thus, the matching of solutions for the ionization layer and for the space-charge sheath in the models proposed by [Benilov 98] and [Schmitz 02, Lichtenberg 05] occurs through the intermediate Knudsen layer; however, descriptions of the Knudsen layer differ. In spite of several differences in the description, the results of these three models are quantitatively similar, and the numerical differences are not great, especially at not too high near-cathode voltages. The recent study [Benilov 16] showed that a unified model of the non-equilibrium layer [Almeida 08] and the model where the near-cathode layer is modeled by means of ionization and space-charge [Benilov 95b, Benilov 02b] together with a complete arc simulation [Baeva 16] which considers all the non-equilibrium in the arc and near the electrodes, are generally in agreement, and in some cases the agreement is even surprisingly good. It follows that the predicted integral characteristics of the plasma–cathode interaction are not strongly affected by details of the model provided that in the simpler models [Benilov 95b, Benilov 02b] an accurate physical description is given.

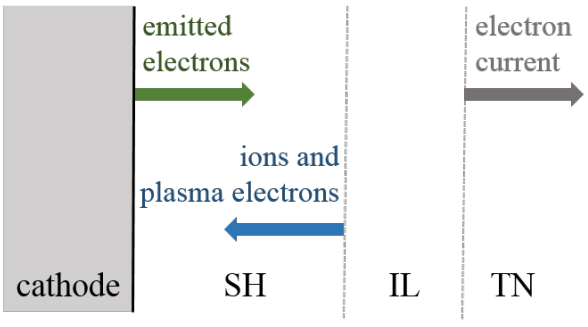

Figure 2.5: Schematic structure of the near-cathode layer for high pressure electric arcs.

Let's briefly describe the model of the near-cathode layer [Benilov 95b, Benilov 02b]. The most

important regions of the near-cathode layer are the ionization layer, in which the ion flux to the cathode surface is formed, and the space-charge sheath, in which ions going to the cathode and electrons emitted from the cathode are accelerated. A schematic description is presented on figure 2.5. Current transfer along the sheath and ionization layers is locally one dimensional and defined by the cathode temperature T_w and voltage U_c applied in the ionization and sheath layers. The voltage drop in the thermal non-equilibrium layer is on the order of tenths of a volt and can be neglected. Input parameters for the model are gas species, the pressure p of the plasma, work function of the cathode material, T_w and U_c. Output data are all the local parameters of the near-cathode layer: electron temperature T_e, ion current j_i, current of plasma electrons j_e, emission current j_{em}, total current from the plasma to the cathode j and heat flux from the plasma to the cathode q.

2.6.2 Matching conditions of the LTE arc bulk and the cathode

The formulation of these boundary conditions depends on the description of the bulk plasma used; see discussion in [Benilov 16] and references therein. If the bulk plasma is described by means of a fully non-equilibrium (NLTE) model, i.e. takes into account deviations from ionization equilibrium and equilibrium between electron and heavy-particle temperatures while assuming quasi-neutrality, then the boundary conditions must describe the near-electrode space-charge sheath. Such work has been done recently, but requires extensive computational resources [Baeva 16]. If the bulk plasma is described by means of a 2T model and takes into account the temperature non-equilibrium, but assumes ionization equilibrium and quasi-neutrality, then the boundary conditions must describe the space-charge sheath and the adjacent layer of quasi-neutral plasma where deviations from ionization equilibrium are located (the so-called ionization layer). This matching was done in [Benilov 12, Li 07].

The aim in the present work is to find the correct boundary conditions to match the LTE arc column with the cathode in a similar way as has been done for the non-equilibrium model [Baeva 16]. The importance of this subject has long been recognized and many attempts have been made; e.g. [Cayla 08, Gonzalez 09, Zhu 92, Lowke 06, Morrow 93, Sansonnens 00, Alaya 15, Shirvan 16]. However, there is still no universally accepted approach. The uncertainty of these studies is that many researchers do not consider the physics of plasma-electrode interaction and employ the LTE equations right up to the electrode surfaces. One of the problems of this approach is an unrealistically high resistance of the near-electrode plasma, which requires additional treatment, for example, numerical cut-off, as was done and discussed in [Benilov 12].

A joint self-consistent numerical modelling of the LTE bulk plasma and the cathode was achieved on the basis of the energy balance in the near-cathode non-equilibrium plasma layer [Lisnyak 17],

using a numerical model of the space-charge sheath and the ionization layer.

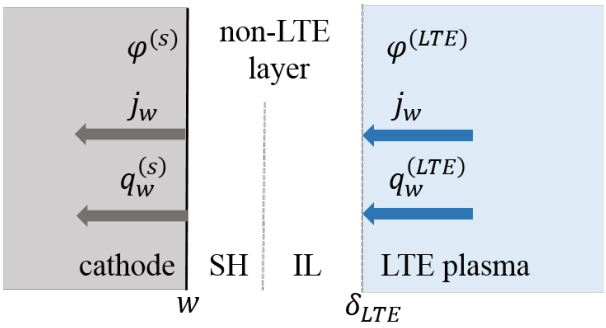

Figure 2.6: Schematic representation of the plasma-cathode interface.

The bulk LTE plasma is separated from each of the electrodes by a near-electrode plasma layer where deviations from LTE are localized figure 2.6. Similar to the plasma-anode interaction described above, no non-equilibrium layers are assumed in the model and the relevant physics of plasma-cathode interaction is taken into account through boundary conditions on the interfaces between the bulk LTE plasma and the electrodes.

Distributions of the temperature and electrostatic potential in the LTE bulk and in the electrodes are governed by elliptic differential equations, hence, two electric and two thermal boundary conditions are required at each interface. The electrostatic potential is discontinuous at the interface:

$$\phi^{(s)} - \phi^{(LTE)} = U_c, \tag{2.50}$$

where the superscripts LTE and s denote values on the LTE plasma side of the interface and on the electrode side respectively, and U_c is the near-electrode voltage drop, which in the general case varies along the electrode surface.

The appropriate boundary condition is the energy balance equation in the near-electrode layer:

$$q_w^{(nl)} - q_w^{(LTE)} = j_w U_c - j_w \frac{A_f}{e} \tag{2.51}$$

Here $q_w^{(LTE)}$ and $q_w^{(nl)}$ are the normal component of the energy fluxes from the LTE bulk plasma to the near-electrode layer and from the near-electrode layer to the electrode surface, respectively, and A_f is the work function of the electrode material. The first term on the right-hand side of equation 2.51 represents the electric power per unit area of the near-electrode layer deposited by the arc power supply. The second term accounts for the energy necessary for extracting the electrons from metal. Contributions of radiation emission and absorption in the near-electrode layer to the energy balance of the layer are neglected.

The energy flux $q_w^{(nl)}$ does not coincide with $q_w^{(s)}$ the normal component of the energy flux removed from the electrode surface by thermal conduction in the solid. In fact, $q_w^{(nl)} = q_w^{(s)} + q^{(rad)}$,

where $q^{(rad)}$ is the density of net energy flux removed from the electrode surface by radiation in the plasma.
The current transfer across the near-cathode layer is locally one dimensional and governed by local values of the cathode surface temperature T_w and near-cathode voltage drop U_c. (In principle, j_w may be considered as a control parameter instead of U_c, however this would be less convenient.) After the 1D current transfer across the near-cathode layer has been computed, one obtains the densities of energy flux and electric current, directed from the near-cathode layer to the cathode surface, as functions of T_w and U_c. Let us designate these functions $f_1(T_w, U_c)$ and $f_2(T_w, U_c)$, respectively. Then one can formulate the two lacking boundary conditions as:

$$q_w^{(nl)} = f_1(T_w, U_c), j_w = f_2(T_w, U_c) \tag{2.52}$$

A model of 1D current transfer across the near-cathode layer needs to be used in order to evaluate the functions $f_1(T_w, U_c)$ and $f_2(T_w, U_c)$. In this work, the functions $f_1(T_w, U_c)$ and $f_2(T_w, U_c)$ are computed by means of the model [Benilov 02b]. Note that the recent comparison by [Benilov 16] has shown that the results given by this model agree in a wide arc current range with results given by the more complex model [Baeva 16].

The boundary conditions on the LTE-plasma - cathode interface

The temperature and the electrostatic potential have discontinuity along the interface. Since the energy and current conservation equations are elliptical, four kinds of conditions needs to be introduced on each side of the interface, i.e. on w and on δ_{LTE} (figure 2.6):

- On the LTE arc column side (δ_{LTE}). The normal component of the energy flux is delivered according to 2.51, where the functions $f_1(T_w, U_c)$ and $f_2(T_w, U_c)$ are known with respect to U_c. Continuity of the current is established, i.e. $j_w = f_2(T_w, U_c)$.

- On the cathode side (w). The heating of the cathode by the plasma is taken into account according to $q_w^{(s)}$, Current continuity is established, i.e. $j_w = f_2(T_w, U_c)$.

It should be remembered that in this work it is the diffuse mode of cathode attachment that is considered. New results obtained for both attachment types are reported in [Chen 16b, Chen 16a].

2.7 The electrodes

The processes taking place in the electrodes during arc ignition are also important and have been investigated experimentally and theoretically. The main interest of these investigations is to determine the electrode temperature in order to estimate electrode wear.

In this work, only current transfer and heating of the electrodes were considered. The effect of melting, the Maragoni effect and other effects are neglected. The heat conduction and current continuity equations are solved in the electrodes:

$$\rho_s C_{p_s} \frac{\partial T}{\partial t} - \nabla \cdot \lambda_s \nabla T = \sigma_s \mathbf{E}^2, \tag{2.53}$$

$$\nabla \cdot \mathbf{j} = 0. \tag{2.54}$$

Here σ_s and λ_s are the electrical and thermal conductivities of the electrode material. The current density $\mathbf{j}$ in the metal electrodes is $\mathbf{j} = \sigma_s \mathbf{E}$.

2.8 Numerical simulation of the electric arc

A self-consistent mathematical model of the complete arc which includes its interaction with the electrodes was developed. Here, the numerical solution of this model is shown for the simple (in terms of geometry and computation time) discharge configuration, which is similar to the well-known welding arc configuration, i.e. a tungsten rod cathode and a flat water-cooled copper anode. This discharge geometry can be considered axially symmetric. A schematic view of the computation domain is shown on figure 2.7. The arc discharge is powered with direct current and ignites in argon at atmospheric pressure. Argon was chosen for the simulations for several reasons:

- The numerical realization is simpler, since thermodynamic functions and transport coefficients are smooth functions in comparison with molecular gases including air. Hence, the system of MHD equations can be solved more rapidly and the numerical stability is enhanced.

- In order to compare computation results with other work and experimental data, which are mainly in argon, due to its industrial use in applications such as welding.

The necessary plasma properties and transport coefficients are taken from [Devoto 73, Cressault 13b]. The radiation losses are from [Cressault 13a] for the arc radius $R_p = 5mm$. Data on thermal conductivity of tungsten and copper are taken from [Touloukian 70] and the electrical conductivity is evaluated in terms of thermal conductivity with the use of the Wiedemann-Franz law. The emissivity terms of tungsten and copper are taken from [Yih 79] and [Window 81], respectively.
The commercial software COMSOL Multiphysics (version 5.2) was used for the numerical calculations. The so-called “Heat transfer in solids” and “Electrical currents” modules were used to solve the equations in the electrode domains. The “Equilibrium DC Discharge” module was used to compute the bulk LTE plasma. The stationary fully coupled solver with direct

computation based on MUMPS (MUltifrontal Massively Parallel Sparse solver) was used. The relative tolerance was set at 1×10^{-3}. The number of degrees of freedom solved for was relatively small (around 1×10^4 including the bulk plasma domain and the electrodes). With this set of parameters, the code is considered optimized and fast.

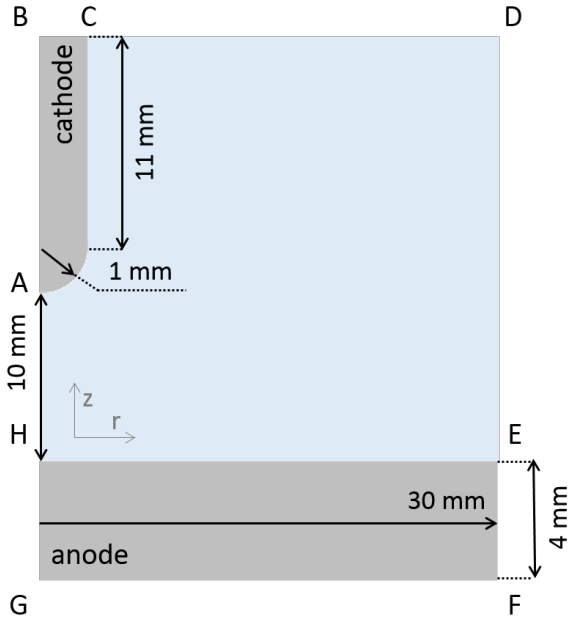

Figure 2.7: Details of the computational domain.

2.8.1 Computation domain and boundary conditions

Two slightly different axially symmetric geometries were considered in this work. Geometry 1, which corresponds to the conditions of the experiment in [Mitrofanov 07], is shown on figure 2.7. The cathode is a tungsten rod with a length of 12 mm with a hemispherical tip of 1 mm radius and a flat copper anode with a radius of 15 mm. A schematic view of the calculation domain is depicted on figure 2.7.

Geometry 2 corresponds to the conditions of the experiment reported in [Hsu 83a]: the cathode is a rod made of thoriated tungsten with a radius of 1.6 mm and a conical tip with an angle of 60 °. Different cathode lengths in the range from 10 mm to 20 mm were investigated. In both geometries, the anode is flat, made of copper, and has a diameter of 60 mm. The gap between the cathode and the anode is 10 mm.

In the case of the arc with direct current, the problem can be simplified and stationary solutions of the MHD system 2.29 and 2.35 need to be obtained in the computational domain ACDEH. This system can be solved numerically by putting the time derivatives to 0, i.e. $\partial/\partial t = 0$. The

same approach was used to obtain the stationary solution within the electrodes, in the computational domains ABC and HEFG for the cathode and for the anode respectively, according to equations 2.53 and 2.54.

Boundary conditions

- The matching conditions formulated on the cathode and on the anode side as well as for the no-slip conditions for the mean mass velocity are applied on the boundaries AC and EH.
- The temperature on the external boundaries of the calculation domain (plasma with the electrodes) is set at 300 K.
- The normal component of the current density vanishes on CDE.
- The electrostatic potential is null on EFG. An arbitrary constant value of the potential may be assumed at the cathode base BC. In principle, this value may be considered as a prescribed control parameter (the arc voltage with the opposite sign). However, we will consider the arc current I as a control parameter and the value of the potential at the cathode base as a parameter to be computed.
- On CD, the no-slip condition is applied. On DE, the normal stress vanishes.
- Magnetic isolation $\mathbf{n} \times \mathbf{A}$ is applied on the plasma domain boundaries, where $\mathbf{n}$ is normal to the boundary vector directed externally.

2.8.2 The work-flow

Extensive numerical work has shown that the voltage drop in the near-cathode layer is approximately the same at all points of the cathode surface inside the arc attachment [Benilov 05]. This may be exploited in order to simplify the work-flow: if U_c is assumed constant, then the problem in the cathode is decoupled from the rest of the equations and may be solved independently.
The numerical simulation procedure comprises several steps. In the first step, the functions $f_1(T_w, U_c)$ and $f_2(T_w, U_c)$ are evaluated by means of the model introduced in [Benilov 02b]. In the second step, equations 2.53 and 2.54 are solved in the cathode with the above-described boundary conditions for the current chosen accordingly. The additional condition, which governs the near-cathode voltage U_c, is the arc current, evaluated as the integral of the function f_2 over the cathode surface and takes the prescribed value I. Once solved for a given value of I, one obtains the temperature distributions and (to the accuracy of an additive constant) the electrostatic potential in the cathode. In particular, one will know the distributions of $q_w^{(s)}$ and

j_w over the cathode surface for I. The above-described calculation procedure of the cathodic part of the arc coincides with the so-called model of non-linear surface heating [Benilov 08] and references therein.
Thus, at this stage, one knows j_w on the plasma-cathode interface AC as a function of position, and $q_w^{(LTE)}$ may be evaluated from equation 2.51. In the third step, the system of MHD equations is solved within the bulk plasma together with equations 2.53 and 2.54 in the anode. The latter is performed using a known distribution of $q_w^{(LTE)}$ and j_w on the plasma-cathode interface AC as boundary conditions for equations 2.31 and 2.32. On the anode side, the condition 2.48 is applied and the current continuity on the interface is realized.
The solution is complete for the arc current I being considered. Note that equation 2.50 is satisfied only at one point of the cathode surface (on the axis of symmetry). This is a compromise to simplify the procedure, assuming U_c constant. However, the modeling results show that $\phi^{(LTE)}$ does not vary significantly on the cathode surface inside the arc attachment; the voltage drop inside the cathode is small, meaning that $\phi^{(s)}$ varies slightly as well. Hence, the residual in equation 2.50 is within the tolerance limits. On the anode side, the condition 2.48 or 2.49 is applied with corresponding boundary conditions. The default condition is 2.48 if not mentioned otherwise.

2.8.3 Calculation results

The system of equations with boundary conditions and matching expressions on the cathode and anode interfaces was solved numerically for a wide range of currents for a stationary case. Examples of computation results are shown on figures 2.8 and 2.9, where the arc column and electrode temperatures are plotted in the whole computation domain for currents of 100 A and 200 A. The first difference with conventional LTE models [Bini 06, Li 07, Lago 04] is that the temperatures between the LTE arc column and the electrodes are discontinuous: the plasma temperature does not drop down to the electrode temperatures on the electrode surfaces. This is a distinctive and important feature of this model which is due to the accurate matching conditions between the LTE arc column and the electrodes.
The temperature distribution in the arc column is typical: the maximum is near the cathode tip, then the temperature drops in the direction of the anode. The temperature iso-lines form a so-called bell-shape structure [Hsu 83a, Gleizes 05]. The cathode reaches its melting temperature at the tip although the anode heating is not strong due to its external cooling.
Ending this very brief description of the calculation results, let's proceed with a thorough description of each domain: LTE bulk plasma and the electrodes: the cathode and the anode.

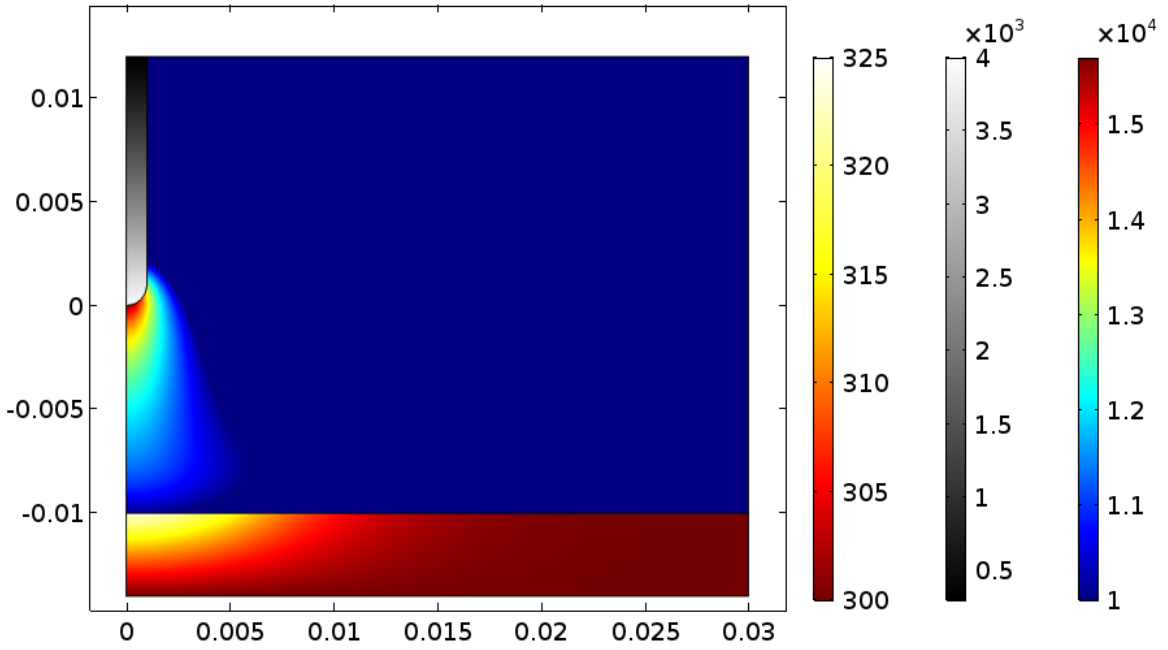

Figure 2.8: Temperature distributions in the LTE arc and the electrodes (in K); $I = 100\,\mathrm{A}$, 1 atm argon, tungsten cathode, copper anode.

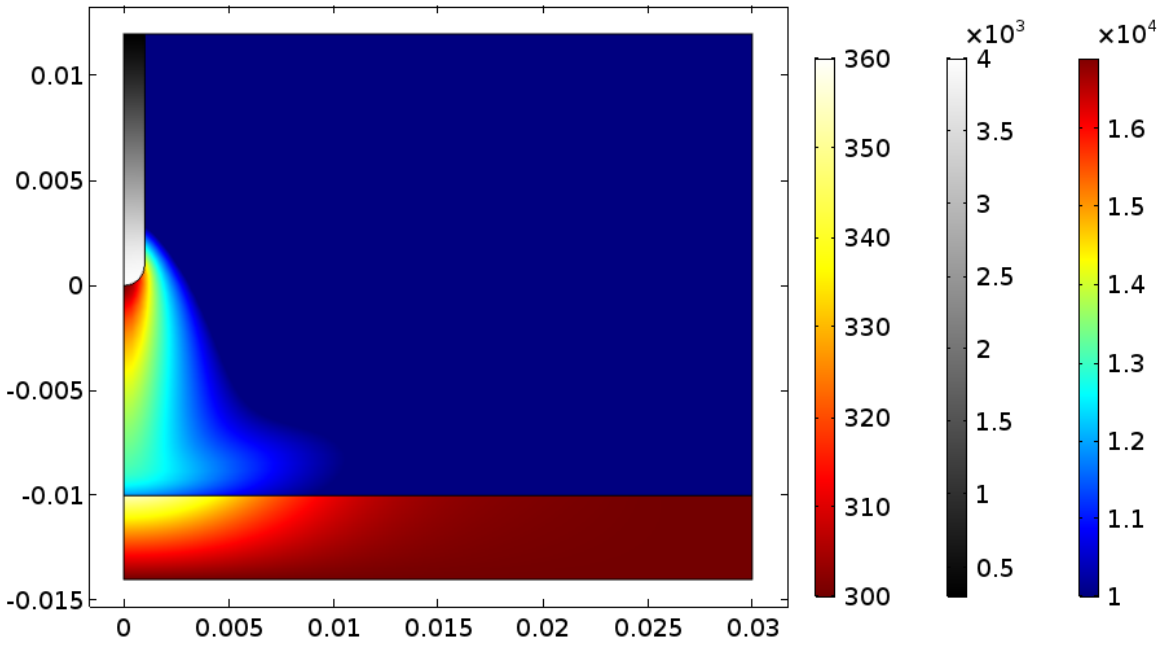

Figure 2.9: Temperature distributions in the LTE arc and the electrodes (in K); $I = 200\,\mathrm{A}$, 1 atm argon, tungsten cathode, copper anode.

2.8.4 Results within the LTE arc column

Figures 2.8 and 2.9 show the arc dimensions and temperature. Detailed discussions about the arc column behavior and comparisons of the calculation results with other studies will also be given below.

The impact of the thermal diffusion current in the arc column

According to the expressions 2.19 and 2.33 for the energy flux and arc current density respectively, the effect of thermal diffusion is taken into account with the term k_T, the thermal diffusion ratio. The effect of thermal diffusion is usually discussed in models of the near-electrode layers and is neglected in the arc column. Here, in contrast, this effect is discussed with respect to the arc column.
In the usual case, when thermal diffusion is not considered, the energy flux and the arc current density are expressed as:

$$\mathbf{q} = -\lambda \nabla T - \frac{5}{2}\frac{k_B T}{e}\mathbf{j} \tag{2.55}$$

$$\mathbf{j} = \sigma \mathbf{E} \tag{2.56}$$

The current density distributions along the arc axis are shown on figure 2.10(a) for arc current values of 100 A and 200 A. Plotted with different line styles, each contribution to the arc current density from equation 2.33 is shown:

- the induced currents, $\sigma\mathbf{E}$ (first term),
- the thermal diffusion currents, $\sigma k_T \frac{k_B}{e} \nabla T$ (second term),
- the total current according to equation 2.33.

The calculation results for the case without thermal diffusion, i.e. according to equations 2.55 and 2.56, are shown in figure 2.10 with solid lines. One can see that the thermal diffusion currents are low and appear mainly near the cathode ($z = 0\,\text{mm}$) and near the anode ($z = 10\,\text{mm}$). Thus, the main contribution comes from the induced currents.
In the case without thermal diffusion, the electrical conductivity is higher (figure 2.10 (b)) for both current conditions, 100 A and 200 A. However, the plasma temperature still remains higher for the case when thermal diffusion is not included, as shown in figure 2.11. The reason for this is the existence of thermal diffusion in the expression for heat flux (equation 2.19), which makes the arc radius wider (figure 2.11 (b)). The impact of thermal diffusion has no significant impact in the arc column. However, it is included in this work for a more accurate description. Further results and discussions on this chapter are based on the model which takes thermal diffusion into account.

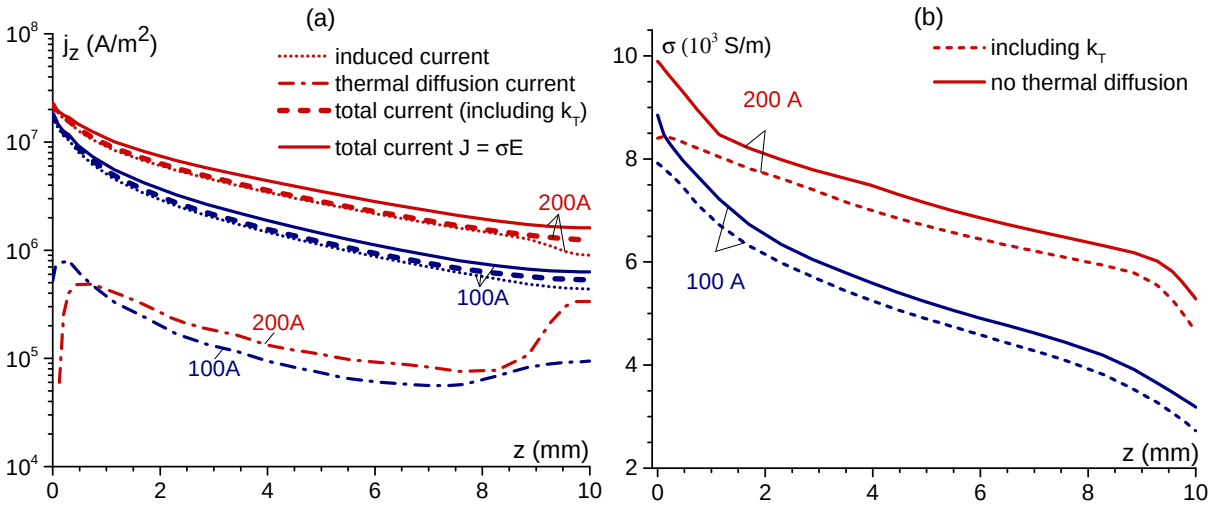

Figure 2.10: Distributions along the arc axis: (a) axial component of current density; (b) electrical conductivity. $I = 100\,\mathrm{A}$ and $I = 200\,\mathrm{A}$.

Analysis of the gas behavior within the arc column

In general, the gas behavior within the arc is poorly analyzed compared to the temperature field. As a matter of fact, there are no experimental investigations which give an estimation of the gas speed within the arc while only qualitative pictures of the gas flow can be found in the literature. In order to better understand the gas behavior in the arc bulk, two geometries are considered:

- the geometry with a hemispherical tip (geometry 1),
- the geometry with a sharp tip (geometry 2, with a cathode length of 16 mm).

The analysis of the forces distributed along a streamline can help understand the mechanisms of gas flow in arcs. According to the definition, streamlines are the curves that are instantaneously tangent to the velocity vector of the flow. Since the velocity at any point in the flow has a single value (the flow cannot go in more than one direction at the same time), streamlines cannot cross, except at points where the magnitude of the velocity is null.
The momentum balance in the stationary case can be written as:

$$\rho \mathbf{V} \cdot \nabla \mathbf{V} = -\nabla p + \mathbf{F}_{vis} + \mathbf{F}_L, \tag{2.57}$$

where $\mathbf{F}_{vis} = -\nabla \cdot \hat{\pi}$ is the viscous force and F_L is the Lorentz force. Let's multiply this equation by the unit vector along the streamline $\mathbf{n}_l = \frac{\mathbf{V}}{|\mathbf{V}|}$ and take into account that,

$$\mathbf{n}_l \cdot (\mathbf{V} \cdot \nabla \mathbf{V}) = \frac{d}{dl}\left(\frac{V^2}{2}\right), \tag{2.58}$$

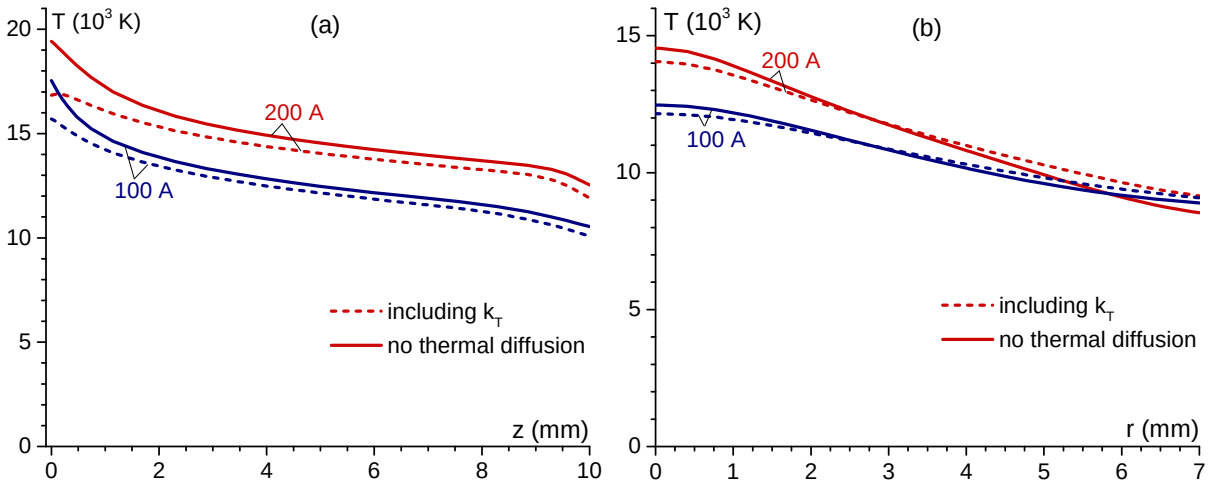

Figure 2.11: Temperature distributions in the arc column: (a) axial; (b) radial on $z = 5\,\mathrm{mm}$ for $I = 100\,\mathrm{A}$ and $200\,\mathrm{A}$.

where $\frac{d}{dl}$ is the directional derivative along the streamline. The value $\frac{\mathbf{V}^2}{2}$ is the kinetic energy per unit of the mass. Considering $\mathbf{n}_l \cdot \nabla p = \frac{dp}{dl}$, the equation is written:

$$\frac{d}{dl}\left(\frac{\mathbf{V}^2}{2}\right) = \frac{1}{\rho}\left(-\frac{dp}{dl} + \mathbf{n}_l \cdot (\mathbf{F}_{vis} + \mathbf{F}_L)\right). \tag{2.59}$$

In this way equation 2.59 shows the projection of the momentum conservation equation on the streamline, making it easier to interpret the phenomena. Hence, the left hand side of equation 2.59 describes the changes in the kinetic energy along the streamline of a unit of mass. The right hand side accounts for the work done on a unit of mass on a unit of length. The latter consists of the potential energy due to the pressure difference (further called *pressure force*), the work of the acting force (in the present case the Lorentz force) and the viscous forces.
Further, two geometries are considered. For each of them the streamline passing near the cathode tip and close to the arc axis is chosen as shown in figure 2.12. Particular portions of the streamline were identified according to the behavior of the fluid and numbered from 1 to 4:

- 1 – 2 is the acceleration distance,
- 2 – 3 is the distance of deceleration,
- 3 – 4 is the outflow.

Before describing the distribution of forces along the streamline, it is interesting to show the plasma temperature and velocity ($|\mathbf{V}|$) distributions along the streamlines (figure 2.13). On the first part of the streamline 1 – 2, the gas passing near the electrode tip is heated by Joule heating and accelerates due to the acting forces. On the next interval, 2 – 3, in the arc column,

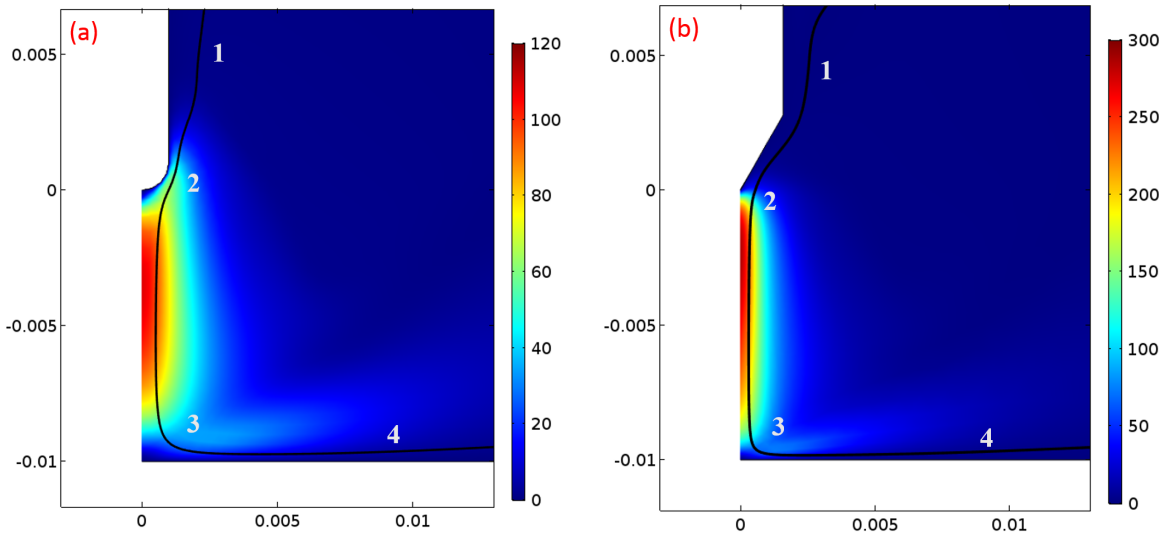

(a) geometry 1.

(b) geometry 2 with $h = 16\,\mathrm{mm}$.

Figure 2.12: Velocity magnitude in the arc column (in m/s), with assigned streamline; $I = 200\,\mathrm{A}$.

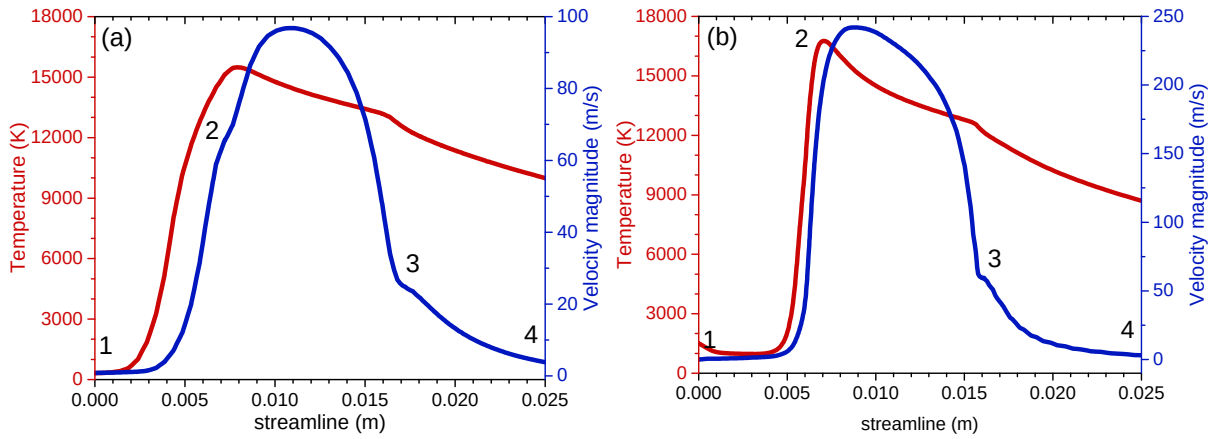

Figure 2.13: Temperature and velocity distributions along the streamline drawn in figure 2.12. $I = 200\,\mathrm{A}$.

the velocity and the temperature slowly decrease. As a matter of fact, the gas velocity changes significantly near the anode surface. On the interval 3 – 4, the temperature continues to decrease and the velocity changes its direction: this is the so-called outflow region.
In case of geometry 2 with the sharp cathode tip, the gas velocity is higher in the arc. This acceleration can be attributed to two factors: the current density is “focused” on the sharp cathode tip instead of on the rounded cathode tip. The second reason is that the sharp cathode has a geometry profile which matches better with the flow than the rounded one. In order to better understand this effect, the distribution of the forces along the streamline is analyzed and discussed below.
The distribution of the forces projection on the streamline was obtained according to the relation 2.59 for two streamlines from figure 2.12 The results are presented on figure 2.14. All the

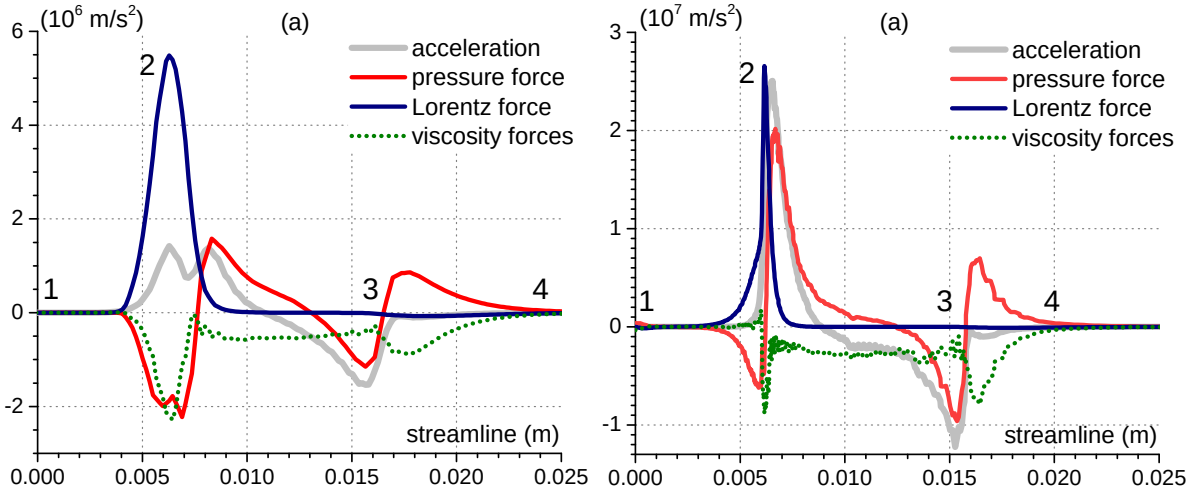

(a) geometry 1. (b) geometry 2.

Figure 2.14: Forces and gas acceleration for the unit of mass distributions along streamline; $I = 200\,\mathrm{A}$.

components of equation 2.59 are shown with respect to the unit of mass:

- gas acceleration,
- the pressure force,
- the Lorentz force,
- the viscous forces.

There is a similar behavior of the acting forces in both geometries. Generalizing the results from figure 2.14 (a) and (b), on the interval 1 – 2 the Lorentz force is the main "driving" force which

accelerates the gas. In the arc column (region 2 – 3), the gas decelerates, i.e. the acceleration becomes negative. In the last interval 3 – 4, the gas flows without any significant acceleration, and the pressure forces are slightly higher than the viscous ones.
The main difference between the distribution of the forces in the two geometries is in the region 1 – 2. In the geometry with the hemispherical cathode, the Lorentz force acts over a longer distance than in the case of the sharp geometry. This is due to the cathode distribution on the cathode side. However, in the interval 1 – 2 the hydrodynamic forces (pressure gradient and viscous forces) act against the gas acceleration, as shown in figure 2.14 (a)). In figure 2.14 (b), it can be seen that on 1 – 2 the gas accelerates mainly due to the Lorentz force while the friction is negligible. Consequently, two parameters were identified as playing a significant role in the arc behavior: the current density distribution along the cathode and a better streamlined geometry.
In the arc column (region 2 – 3) the gas is accelerated by the pressure gradient while the viscous effects decelerates the gas faster. Near the anode region the pressure gradient and the viscous forces are compensated due to the non-slip conditions inducing a low deceleration of the gas.

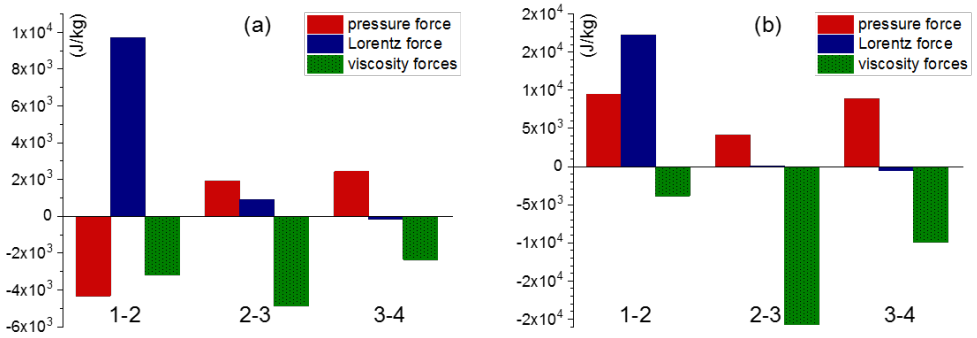

Figure 2.15: Work on the unit of mass (J/kg) on different portions of the streamlines depending on the force. (a) geometry 1, (b) geometry 2; $I = 200$ A.

By integrating the forces along the streamline (in fact, parts of the streamline), one can obtain the effective work produced on the chosen path. In the present case, the integration is made over the intervals 1 – 2, 2 – 3 and 3 – 4. The calculations were done for two streamlines and the outcomes are presented on figure 2.15, where the work is considered on the unit of mass, i.e. (J/kg). The interval where the work is positive, i.e. portion 1 – 2, corresponds to the acceleration zone. The main contribution is made by the Lorentz force near the cathode tip and by the pressure gradient below the cathode tip. Along the intervals 2 – 3 and 3 – 4, viscous energy dissipation plays a significant role and decelerates the gas which then leaves the

calculation domain. Relatively speaking, the results on figures 2.15 (a) and (b) have a similar trend, except the region 1 – 2 for the pressure forces. The negative impact of the pressure forces for the cathode with a hemispherical tip is due to poor streamlining and forming of the region in front of the tip where the gas stagnates. This analysis allows one to understand more accurately the gas behavior due to the contribution of each force on different parts of the streamline.

Arc properties: comparison of the results with other studies and experimental data

The aim of this part is to give insight into the arc bulk and at the same time compare the results given by this model with others found in the literature involving different approaches, for instance a so-called two temperature (2T) model [Li 07] and a non-LTE model [Baeva 16] (NLTE). The comparison will be extended to experimental data when possible. As mentioned above, in the framework of this work (as well as the approach [Li 07]) the cathodic part of the arc is described by a model of nonlinear surface heating and these results are presented below. Distributions along the arc axis of the plasma temperature T computed in this work and of the heavy-particle and electron temperatures T_h and T_e, given by the 2T and the NLTE models, are presented in figure 2.16 for currents of 20 A, 100 A and 200 A. Details of the distributions in

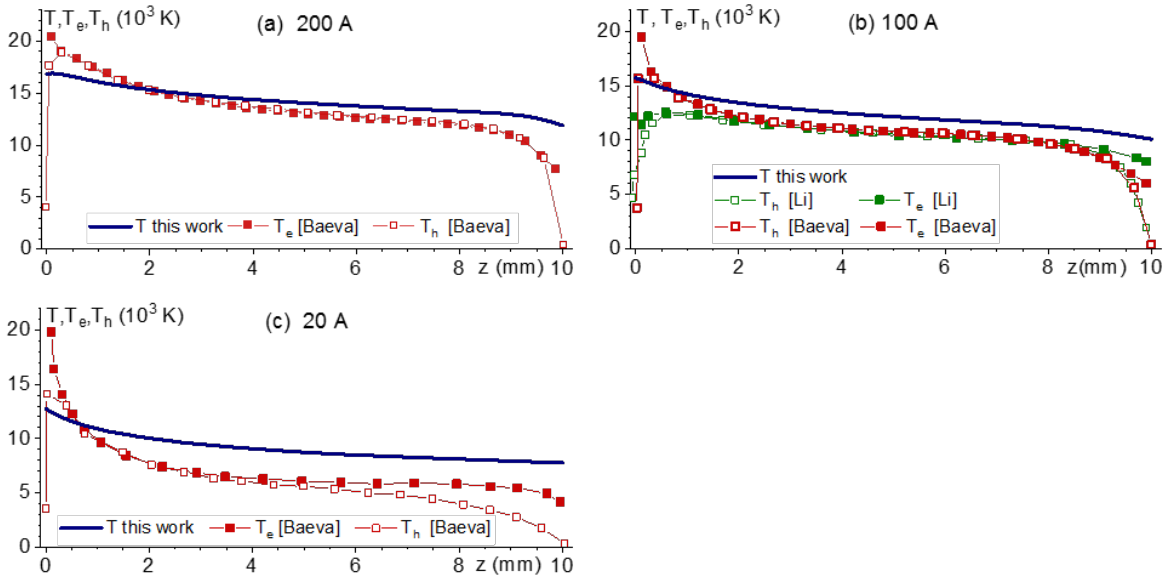

Figure 2.16: Temperature distributions given by different models along the arc axis for different currents.

the vicinity of the cathode are shown in figure 2.17. A reasonable agreement is found in the arc bulk for $I = 100$ A and $I = 200$ A. Some differences are noticed for the case of $I = 20$ A, where the deviations from LTE in the bulk become significant. On the other hand, there are indicative

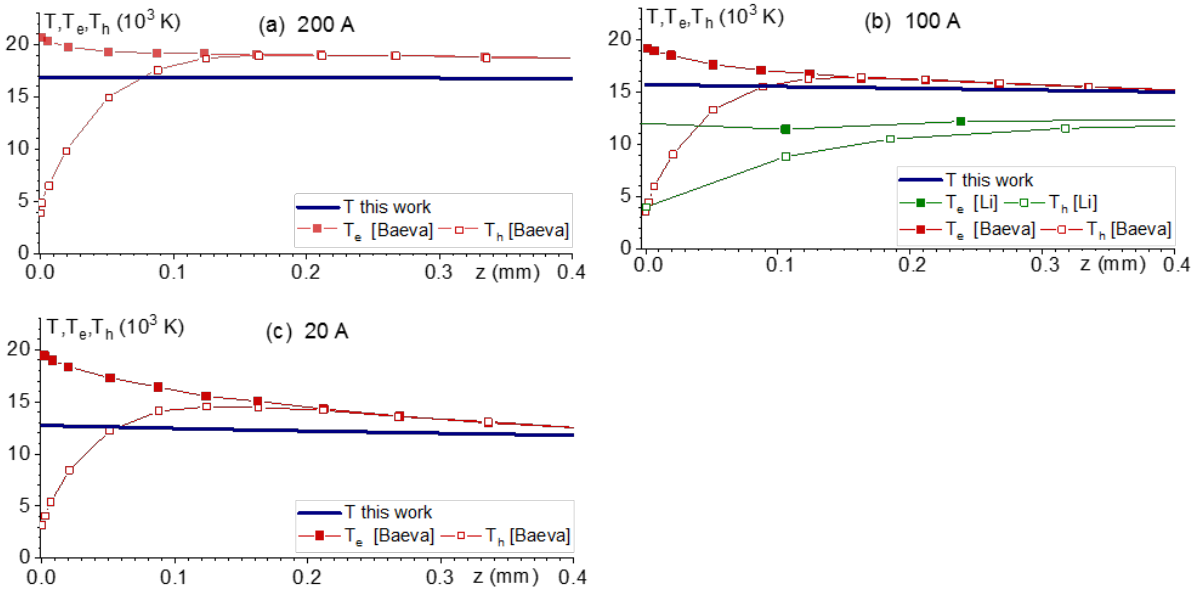

Figure 2.17: Details of temperature distributions given by different models on the arc axis in the vicinity of the cathode for different currents.

deviations between T and T_h near the electrodes. This is the key point of the proposed approach: the fast decrease of the heavy-particle temperature in the near-electrode regions is described not by a solution of the LTE bulk equations but rather through the boundary conditions on the interfaces between the LTE plasma and the electrodes. Temperature distributions in the radial direction at 0.2 mm from the cathode tip and in the midplane (5 mm) of the arc are shown in figure 2.18 for the arc current of 200 A. Again, the agreement is reasonably good. More radial distributions for different currents near the cathode and on the midplane are presented in figure 2.19. In the model developed in this work, the total arc voltage is obtained by adding up the voltage drop inside the electrodes, the voltage drop in the LTE arc bulk, and the near-cathode voltage drop U_c. The current-voltage characteristic (CVC) of the arc, evaluated in this way for a wide current range, is shown in figure 2.20. Note that the voltage drop inside the electrodes is negligible in these conditions. Also shown are data from the NLTE and 2T models, as well as the data from the experiment by [Mitrofanov 07] referring to the diffuse cathode arc attachment. The CVCs given by the NLTE and 2T models and the model proposed in this work agree with each other and with the experiment reasonably well in the whole range of arc currents from 20 A to 175 A.

Also shown in figure 2.20 is the CVC evaluated in the framework of the conventional LTE model, i.e. without accounting for the near-electrode layers. This CVC differs from the ones given by all the other theoretical models and the experimental one: the arc voltage monotonically increases for all currents. Comparing with the model used here, one can conclude that this difference

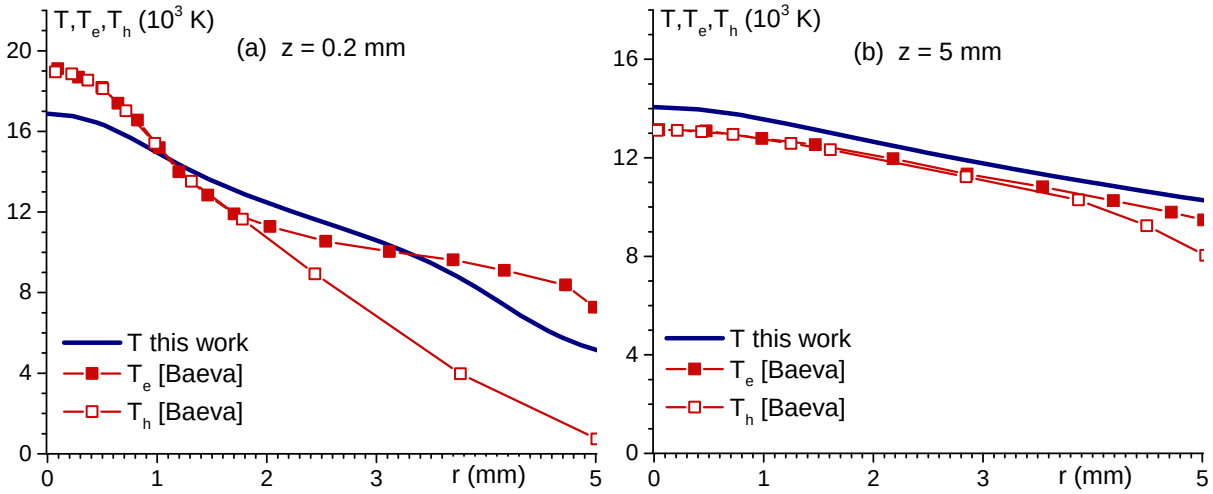

Figure 2.18: Radial temperature distributions in the arc column at different distances from the cathode tip. $I = 200\,\mathrm{A}$.

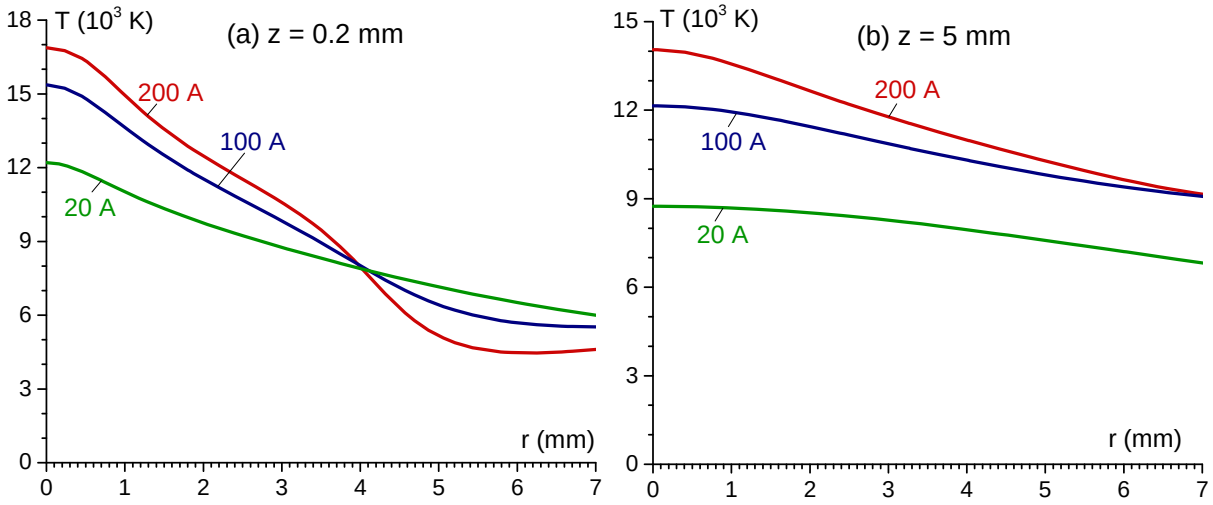

Figure 2.19: Radial temperature distributions in the arc column at different distances from the cathode tip. $I = 20\,\mathrm{A}$, $100\,\mathrm{A}$ and $200\,\mathrm{A}$.

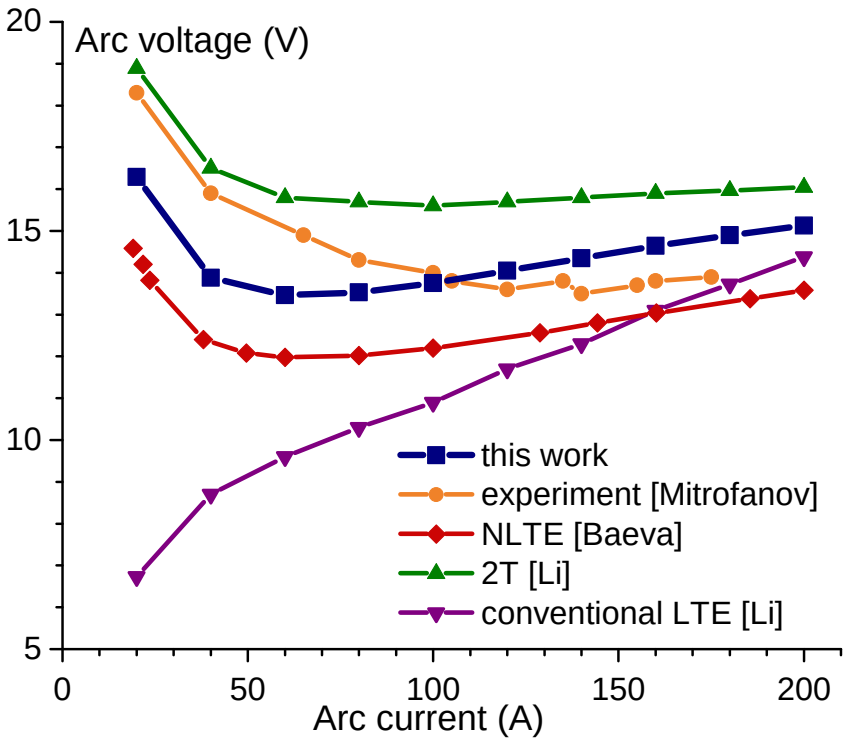

Figure 2.20: Arc voltage evaluated by means of different models and experimental data.

stems from the neglect of the near-electrode layers in the conventional LTE model, rather than from the mere fact that deviations from LTE become more pronounced as the current decreases. Another difference between the model proposed in this work and the conventional LTE model is that the former does not require any cut-off in evaluation of the resistance of the near-electrode plasma and therefore poses no limitations on the step of the numerical mesh near the electrodes.

2.8.5 Results on the electrodes: cathode and anode

The cathode

As previously described, the cathode heating was calculated according to [Benilov 02b] and the diffuse mode of cathode attachment was chosen. The cathode temperature and current density distribution along the cathode are shown on figure 2.21. Here, s is the distance measured along the generatrix of the cathode surface from the center of the tip (i.e. from point A in figure 2.7). The vertical dashed line designates the end of the spherical tip. Maxima of the cathode temperature for the total arc currents are near the axis on the cathode tip. The vertical line at $s = 1.5\,\mathrm{mm}$ shows the end of the rounded part of the cathode tip. It can be seen that the main current is focused on this rounded cathode zone.

The distribution of the electrostatic potential in the LTE arc column evaluated at the plasma-

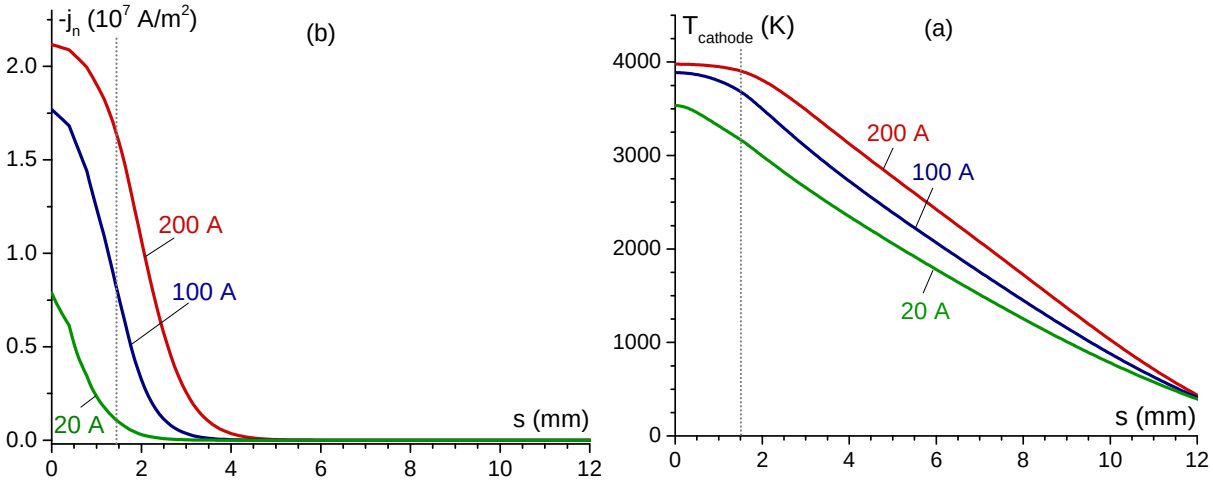

Figure 2.21: Distributions of the current density normal component (a) and the surface temperature (b) along the cathode surface given by different anode approaches.

cathode interface is shown in figure 2.22. The variation of the potential $\phi^{(LTE)}(s)$ in the region

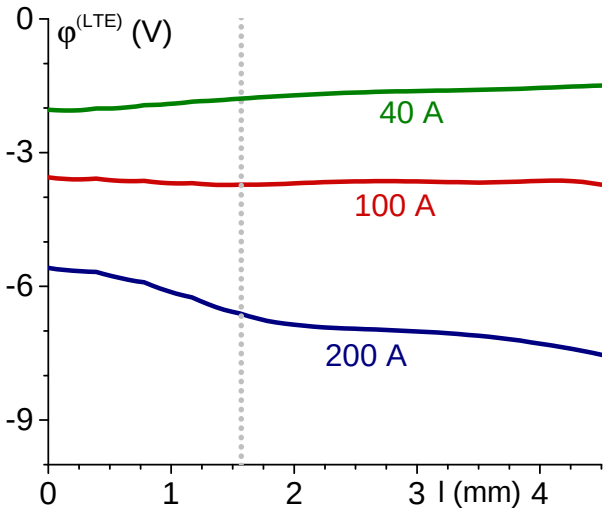

Figure 2.22: Distribution of electrostatic potential in the LTE arc column evaluated at the plasma-cathode interface.

$s < 4\,\text{mm}$, where the arc is attached to the cathode, is not large. Consequently, the voltage drop in the near-cathode layer does not change much from one point of the arc attachment to the other. This supports the corresponding assumption made in order to simplify the work-flow and to avoid more complex computations such as [Baeva 16, Chen 16b].

The anode

One of the critical parts of the calculation is to define the anode temperature. It is important for several reasons. Firstly, the overheating zones must be identified. Secondly, in this section two approaches for the plasma-anode interaction are considered and compared with computed results of the comprehensive models. It has already been shown that there is a temperature difference between the plasma temperature near the anode and the anode temperature. This temperature discontinuity is defined by matching conditions on the interface. Consequently, two approaches are considered:

- The energy flux from the LTE plasma to the anode corresponds to the expression 2.48 and on the plasma side the condition $\frac{\partial T}{\partial \mathbf{n}} = 0$ is valid.
- The energy flux from the LTE plasma to the anode is $q_a = U_h j_n$, where U_h is the anode heating voltage 6.1 V according to [Almeida 17].

The plasma temperature near the anode for these two approaches is shown on figure 2.23. The deviation between temperatures for both approaches takes place 1 mm from the anode

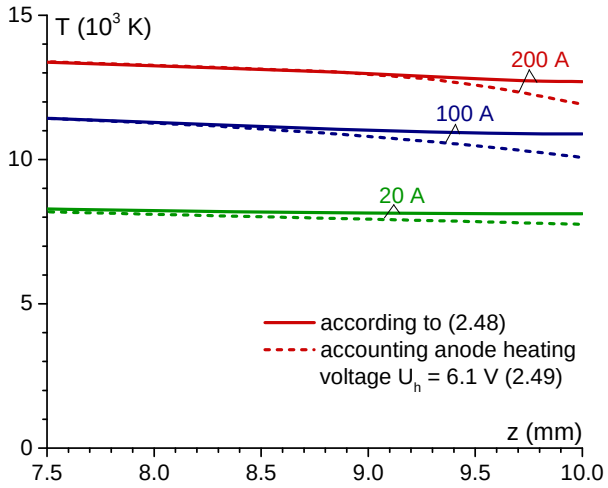

Figure 2.23: Distributions of the plasma temperature near the anode along the arc axis for two different approaches taking plasma-anode interaction into account.

surface. Moreover, the temperature difference is less than 1000 K, therefore the values of the current densities on the anode surface plotted on graph 2.24 are very similar. Additionally, these conditions have no influence on the arc column voltage. Distributions along the anode surface of the axial current density and the anode surface temperature computed in this work are compared with those given by the NLTE model in figure 2.24 for arc currents $I = 20$ A, 100 A and 200 A. The temperature of the anode surface does not exceed 360 K, even for an arc current of 200 A, due to intensive external cooling. To conclude, the agreement between the

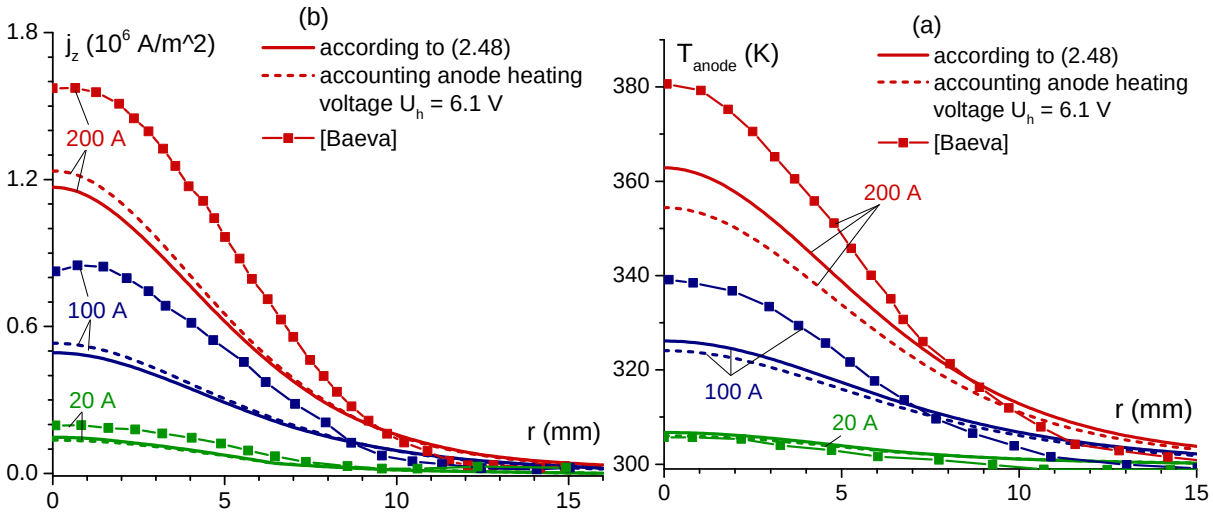

Figure 2.24: Distributions of the current density (a) and the surface temperature (b) along the anode surface for by different implementation of the anode.

two models is good. The difference in the calculation results between the two methods and the comparison with the comprehensive model validate the arc-anode description.

2.8.6 Other aspects. Thoriated-tungsten cathode with a conical tip

It has been shown that the model works well for the geometry with hemispherical cathode tip. On the one hand, it gives a good agreement with more comprehensive non-equilibrium models and, on the other hand, a good agreement with experimental investigations found in the literature. It is of great interest to perform simulations with geometry 2 (previously introduced) which is commonly used for the investigation of welding processes [Hsu 83a, Lowke 97] and where many experimental studies have been reported. Here the cathode is conical. However, the drawback in this case is the cathode geometry which is not precisely described. For instance, the dimensions of the cathode assembly are not documented. However, in order to establish plasma-cathode interaction correctly, one needs to know the complete cathode geometry. The model of nonlinear surface heating requires knowledge of the cathode dimensions and geometry to define the current density and the energy flux.
Since the exact cathode geometry was not detailed in [Hsu 83a], calculations for the experimental conditions in the latter reference were performed for several variants of shapes with the arc current values of $I = 100\,\mathrm{A}$ and $I = 200\,\mathrm{A}$. Several geometrical modifications were considered and are depicted in figure 2.25.

- The cathode tip is sharp, the length of the cathode changes ranging from 10 mm to 20 mm.
- The cathode has a fixed length, although the cathode tip is not sharp, while the gap stays

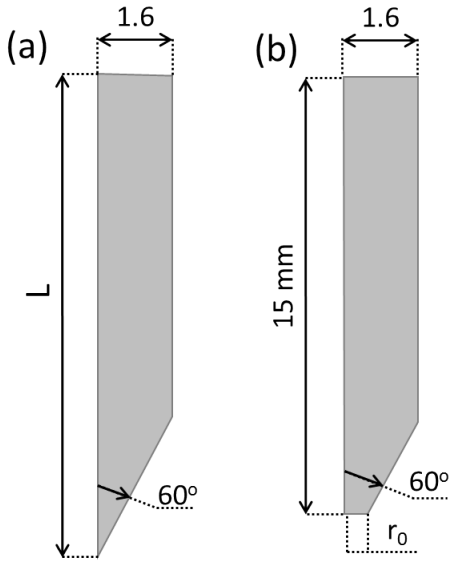

Figure 2.25: Schematics of different cathode geometries. (a) with a sharp tip, (b) with a plateau on the tip.

fixed to 10 mm. This situation usually occurs during the experiment after operating the arc for a certain time.

The calculation results for $I = 200$ A and two lengths 10 mm and 15 mm are shown in figure 2.26, where the temperatures of the arc and the electrodes are plotted on the same scale. The overheating of the plasma with the short cathode can be observed. The more intensive arc heating, especially near the cathode in the case of the short (10 mm) electrode, is due to the current density distribution on the tip (figure 2.27 (a)). Moreover, the arc is more constricted on the cathode tip for the shortest cathode.
The vertical line on figure 2.27 corresponds to the end of the conical part of the cathode. One can see that the main part of the current passes through a very narrow region on the cathode. The cathode surface temperature is presented on figure 2.27 (b) showing that the heating of the tip is more intense for a short cathode.
Regarding the current density, it was found to drop faster within the cathode gap of $L = 10$ mm, as shown on figure 2.28 (a). In this configuration, near the anode, the current density is also lower than in the other case. The arc radius is wider in this case (figure 2.28 (b)). This may be due to a hydrodynamic effect of the better cathode cooling for the longest cathode. In order to evaluate the impact of the hydrodynamic forces, the distribution of the forces along the streamlines are shown on figure 2.29. For both the selected cases, the streamlines pass in the vicinity of the cathode and on the arc axis, as shown in figure 2.12 (b). For clarity, on figure 2.29 for its better understanding, the results are shifted along the abscissa axis. It can

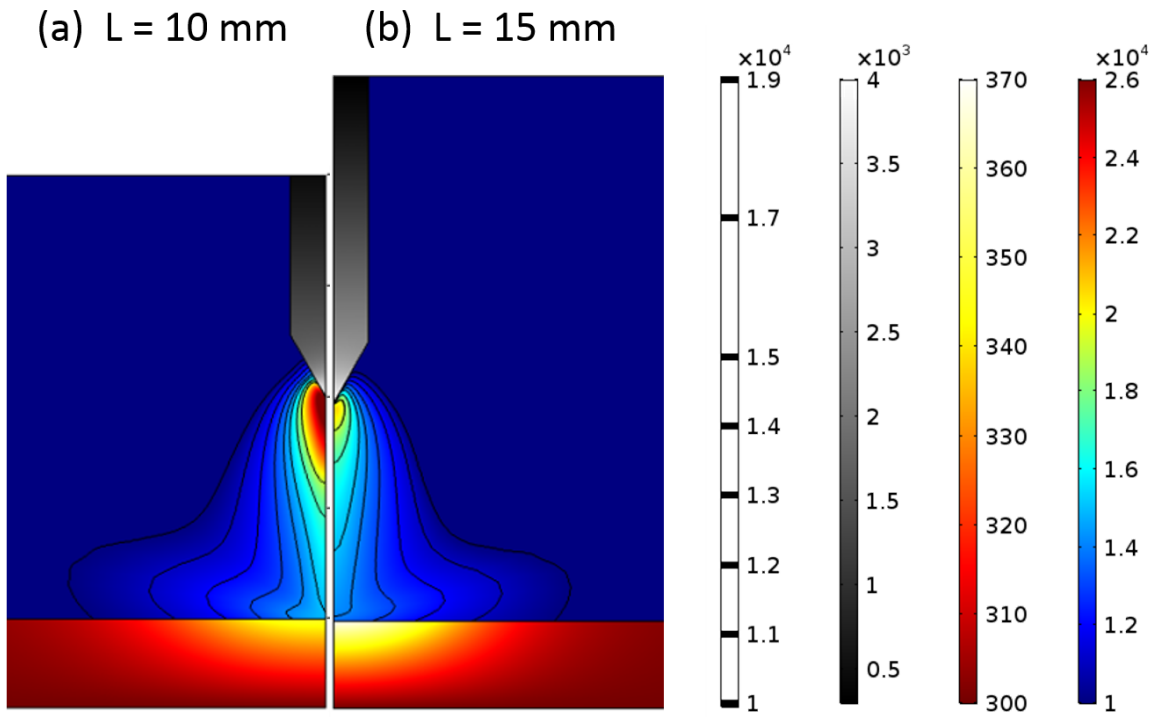

Figure 2.26: Temperature distributions in the LTE arc and the electrodes (in K); (a) $L = 10\,\text{mm}$; (b) $L = 15\,\text{mm}$. $I = 200\,\text{A}$, 1 atm argon, thoriated-tungsten cathode, copper anode.

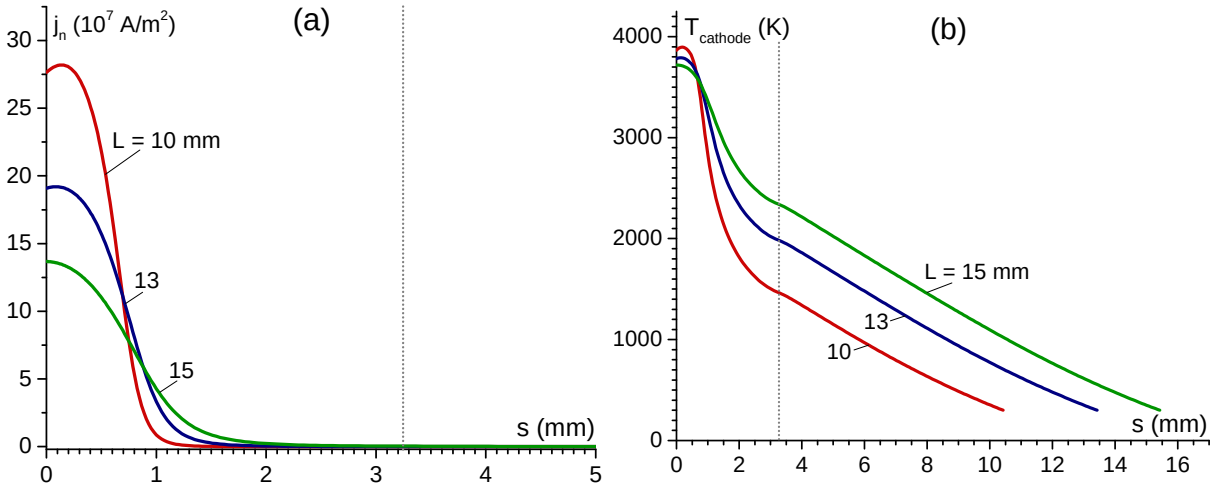

Figure 2.27: Distributions of the of the current density normal component (a) and the surface temperature (b) along the cathode surface for different cathode lengths; $I = 200\,\text{A}$.

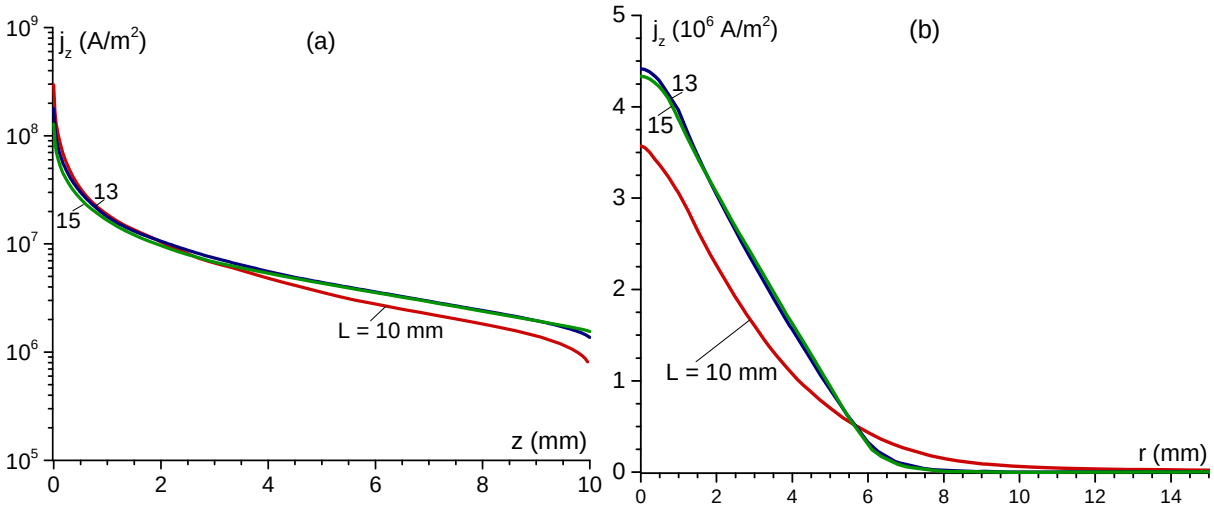

Figure 2.28: Axial component of the current density along the axis (a) and the radius with $z = 5$ mm (b); $I = 200$ A.

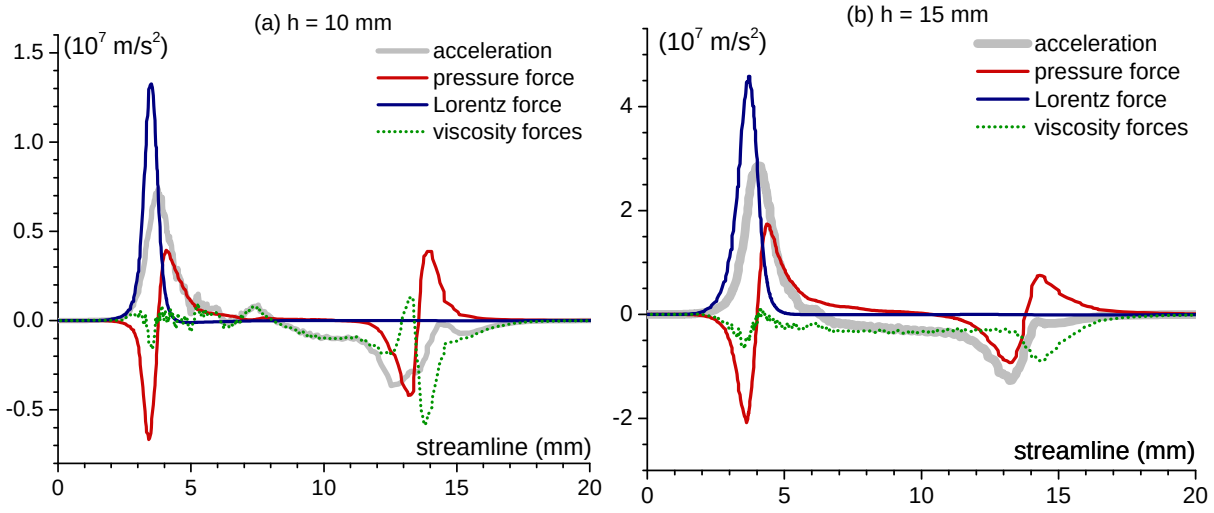

Figure 2.29: Forces and gas acceleration for the unit of mass distributions along streamlines for different cathode lengths; $I = 200$ A.

be seen that on the first 5 mm of the streamline, the gas accelerates in the same manner due to the Lorentz force. The ratio of the Lorentz force and pressure force is similar for both cases. Therefore, the effect of the geometry on the arc hydrodynamics is negligible.

Such drastic changes in the arc behavior due to different cathode geometries occur due to the complexity of the arc nature. The cathode geometry also has an impact on the anode heating. The anode temperature calculated using the proper anode heating voltage is presented on figure 2.30 together with the current density on the anode surface. As a result, it is important

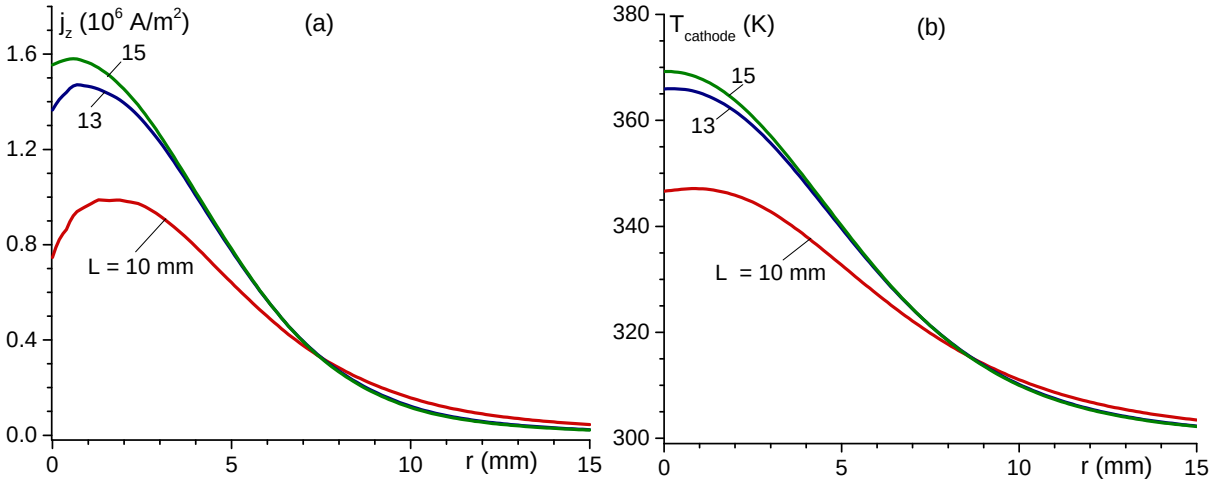

Figure 2.30: Distributions of the current density normal component (a) and the surface temperature (b) on the anode surface for different cathode lengths; $I = 200\,\mathrm{A}$.

to consider the conditions applied on the cathode side as well as the effect of arc column and the anode heating.

The temperature distributions on the arc axis are shown in figure 2.31 for cathode lengths L ranging from 10 mm to 20 mm. One can see that an increase in L causes an appreciable decrease in the plasma temperature near the cathode tip. Again, the higher thermal resistance of the cathode is favorable for wider attachments of the arc to the cathode, an effect that is well known to designers of arc lamps. Hence, an increase in L causes a decrease in the current density at the cathode tip and, consequently, lower plasma temperatures near the tip.

Results of computations for a cathode with a flat front, i.e. a plateau at the conical tip of the cathode, are shown in figure 2.32. Here r_0 is the radius of the plateau; note that $r_0 = 0\,\mathrm{mm}$ corresponds to the sharp conical tip which figure 2.31 refers to. The cathode length was 15 mm in these calculations. An increase in r_0 causes a decrease in the plasma temperature near the tip, which is again a consequence of a decrease in the current density at the cathode surface.

Last but not least, it is interesting to observe the arc voltage for the case of the different cathode length and tip shapes. In figure 2.33 the arc voltages are presented for all the calculated cases.

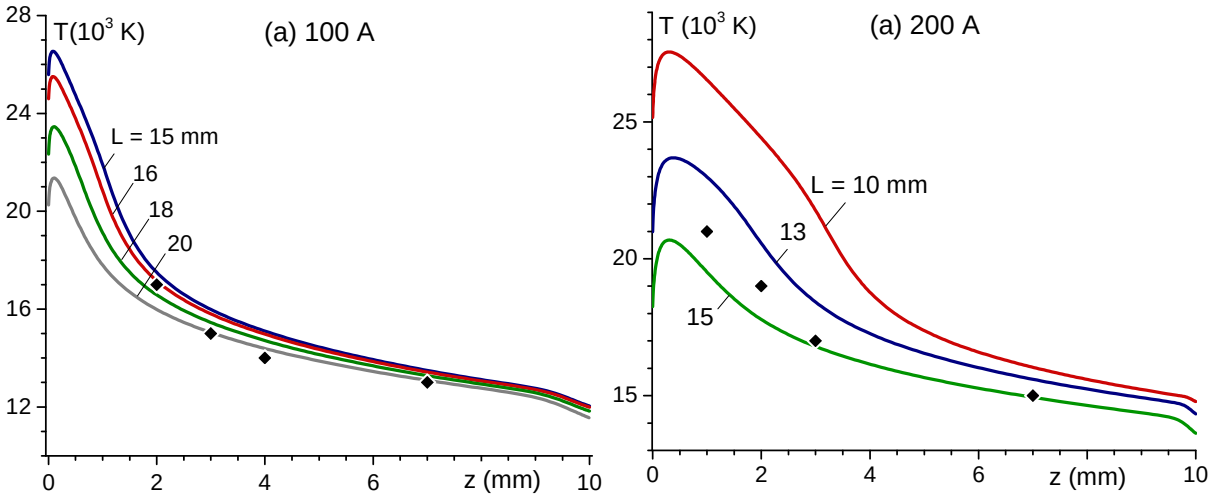

Figure 2.31: Computed temperature distributions along the arc axis for cathodes of different lengths (lines). Currents 100 and 200 A. Experimental data from [Hsu] (Diamonds).

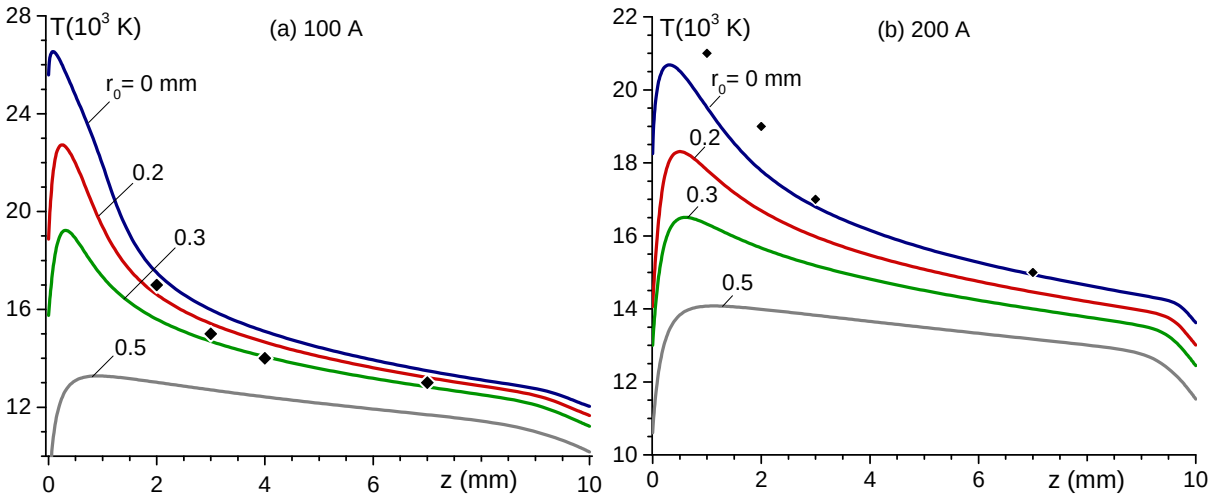

Figure 2.32: Computed distributions of temperature along the arc axis for cathodes with different plateau radii (lines). Current 100 and 200 A, $L = 15$ mm. Experimental data from [Hsu] (Diamonds).

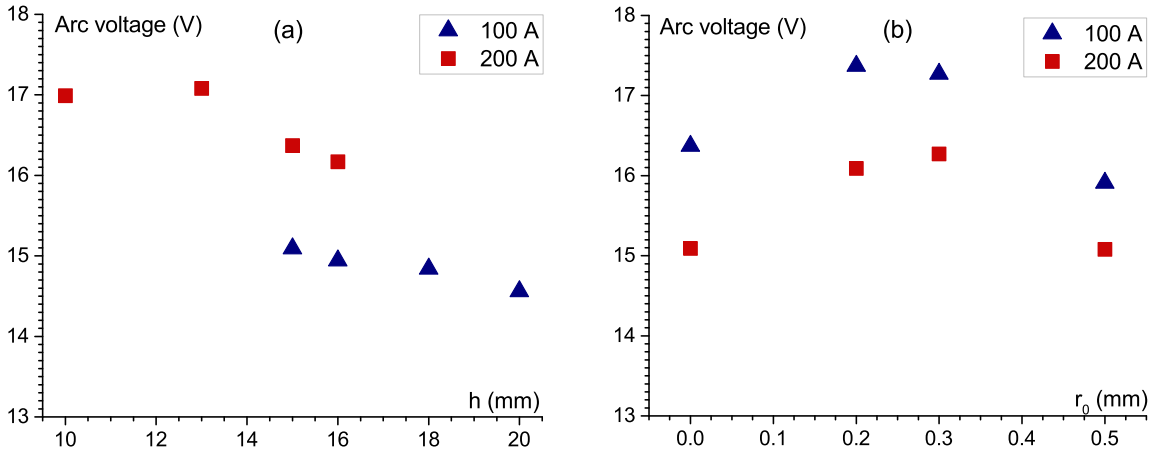

Figure 2.33: Comparison of computed arc voltages for different cathode lengths (a) and radius (b) in cases of $I = 100\,\mathrm{A}$ and $I = 200\,\mathrm{A}$.

It can be seen that changing the arc length does not have a drastic influence on the arc voltage. The same conclusion can be drawn for the case of the cathode with different plateau sizes. Consequently, the arc voltage variation is not sensitive to the morphological changes of the arc. Thus, the modeling has revealed a significant impact produced by the shape of the cathode geometry over the distribution of the current density along the cathode surface and therefore over the plasma temperature, while the arc voltage is not sensitive to changes in the cathode shape. Therefore, the experimental studies usually conducted to measure only the arc voltage will give no information about arc behavior. This highlights an interesting and potentially important effect that deserves further detailed experimental investigations.

2.9 Conclusions

This chapter has given an overview of the problem faced in the theoretical description of an electric arc and its numerical realization. A theoretical justification of the applicability of the MHD equations has been given as a particular case of the Boltzmann equations. The existence of thermal equilibrium in plasmas has been discussed, and the limitations of its applicability defined; in the case of an arc column plasma it can be concluded that the assumption of describing the plasma in LTE is valid.

The deviation from equilibrium (thermal, ionization and quasi-neutrality) occurs near the cathode and anode and on the arc fringes. The near-electrode zones and plasma interaction with them are very important to establish the arc correctly. Close attention must therefore be paid to the accurate description of these zones. Models of the near-electrode layers are complex and require more data; moreover, their numerical realization is computationally expensive. It is therefore interesting to avoid complex non-equilibrium models of plasma-electrode interaction,

while at the same time accounting for it correctly. One needs to find a valid approach to match the LTE model of the bulk plasma with the electrodes that reasonably accurately reflects the physics of plasma-electrode interaction. In this work, this matching was achieved by using energy balance equations in the non-equilibrium near-electrode layers that separate the LTE bulk plasma and the electrodes.

As an example, a numerical simulation of a free-burning arc in atmospheric pressure argon plasma has been reported in the current range from 20 A to 200 A. The simulation results have been compared with those given by the (more sophisticated) 2T and NLTE models and with the experimental data available in the literature. The agreement in the arc bulk is reasonably good for arc currents of 100 A or higher and starts to deviate for lower currents, where deviations from LTE in the bulk become significant. On the other hand, there are significant deviations between the plasma temperature given by the model proposed in this work and the heavy-particle temperature given by the 2T and NLTE models near the electrodes. This is the central point of the proposed approach: the fast decrease in the heavy-particle temperature in the near-electrode regions is described not by a solution of the LTE bulk equations but rather via the boundary conditions on the interfaces between the LTE plasma and the electrodes.

The arc voltage, given by the model developed in this PhD research, agrees reasonably well with the values obtained with the 2T and NLTE models and with the experiment in the whole range of arc currents from 20 A to 175 A, in contrast to the arc voltage given by the conventional LTE model (the one that disregards the near-electrode layers). Another difference between the model proposed here and the conventional LTE model is that the present model does not require a cut-off in the evaluation of the resistance of the near-electrode plasma and therefore poses no limitations on the step of numerical mesh near the electrodes.

The approach proposed in this work allows one to develop models that are physically justified and therefore applicable to a wide range of conditions, and that are also fast and robust. In particular, the simple 2D model reported in this work has predicted a strong effect produced by details of the cathode geometry over the distribution of the current density along the cathode surface and therefore over the plasma temperature. This is a result which seems to be interesting and potentially important and therefore should be verified in further numerical modeling and experimental investigations.

Chapter 3

Experimental study of electric arc displacement between rail electrodes

Experimental work involving electric arcs is probably the most intuitive approach to investigate arc properties. Nowadays, well-established methods exist to define different intrinsic properties of electric arcs and, in some cases, predict their behavior. In the particular case of arc propagation along or between rail electrodes, experimental investigations have often been conducted in the framework of low voltage circuit breakers. This is most likely the main reason for the scarcity of information available in the literature on the topic. Another reason is related to industrial purposes since private research has been actively conducted by the main actors on the market. This lack of open knowledge about arc displacement along electrodes means that dedicated experimental investigations need to be carried out.
Although this work focuses on the development of mathematical models describing the electric arc in aeronautical contexts, experimental investigations of arc displacement are mandatory in order to validate the simulation results. The need to run dedicated experimental investigations is twofold: - to reduce the number of assumptions by using the same geometrical and electrical conditions as those implemented in the model. - to understand the arc ignition phenomena, its propagation between the bars and the impact of internal conditions such as arc current, inter-electrode distance... The experiments were performed on two distinct platforms:

- In the GREMI laboratory where the electrode design is based on low voltage circuit breakers. The arc is initiated between the two electrodes and powered with an imposed current pulse of different amplitudes I_{max} ranging from 700 A to 2 kA.
- The experiments carried out under aeronautical conditions were performed on the platform located in the Zodiac Aero Electrics facility. Meant to be as close as possible to the real operating conditions in aircrafts, the setup includes bus-bar electrodes powered with alternating current maximum amplitudes I_{max} ranging from 500 A to 2 kA at 420 Hz or 760 Hz.

The purpose of this study is to investigate the typical behavior of the arc first in rather classical conditions and then the influence of the context-related conditions on the arc behavior.

The experimental protocol involves known methods and techniques to determine several arc parameters, which can be either set to the model or used to compare with simulation results, for instance the arc velocity, the arc voltage... The experimental results used to compare with the numerical simulation outcomes are mainly reported in the present chapter. Explicit comparisons with the simulation will be presented, analyzed and discussed in chapter 4.

3.1 State of the art

The detailed description of the physics of arc displacement is proposed in the next chapter, where the main mechanisms are given and discussed. In this section, the main achievements in the field of the experimental study of arc displacement between rail electrodes are reviewed.
Magnetically driven arcs are encountered in a variety of engineering applications including chemical reactors, arc flow control devices, plasma armature rail-guns and circuit breakers. Studying the structure and the motion of magnetically driven arcs is a complex task. The arc itself includes many phenomena. In this case, the arc is displaced along the electrodes, which makes its study even more challenging.
Arc displacement phenomena are mostly investigated by means of high-speed imaging. It is generally accepted that the arc can be identified and tracked as a high luminosity object (bright object) on high-speed camera images. The cathode and the anode attachments are the bright regions near the electrodes, where the arc column connects to the electrodes. Several hypotheses have been put forward with respect to high-speed imaging observations. Experimentally, the existence of a "single arc mode" with a single coherent arc column is observed by opposition with the transition to a "distributed arc mode" occurring at high currents. In the latter case, multiple arc columns exist simultaneously [Gray 15]. As well, the so-called *re-striking* of the arc is one of the typical features where hot gas and ablation of the material in the vicinity of the primary moving column provide conditions to produce additional breakdown [Ray 89, Koyama 93]. Generally, the main focus of such work is the arc motion, while other studies focus more on the arc column displacement or on the electrode attachments. Arc motion can be characterized either with a *smooth and continuous* movement of the arc roots over the electrode surface or with distinct jumps with "anchored" pauses as documented in [Velleaud 89, Velleaud 95].
One can find in the literature several opinions about arc displacement between electrodes. Intuitively, it is often reported that arc motion is driven by the arc column and that cathode attachment follows the arc column. Another point of view is that the arc follows the cathode attachment [Guile 57, Winsor 56, Secker 59]. Studies have been performed to investigate the tracks on the electrode surface after arcing. The authors report that the tracks were continuous in 90 % of cases and the rest were discontinuous under their experimental conditions. Different electrode materials (copper, aluminum, carbon, brass) with a different state of electrode surface

roughness (polished or unpolished) and different magnetic flux densities have been investigated. It has been found that for polished electrode surfaces the root displacement is likely discontinuous. Most of the experimental data are summarized in [Secker 59] where a description of the root behavior is given depending on the arc current, the electrode material, the electrode surface preparation, the inter-gap and the nature of the electrical circuit.
Another opinion reported in [Bobashev 10b, Bobashev 16] is that the arc is driven by the arc column and the roots "follow" the arc column displacement. The latter means where the hot conductive channel of the electric arc can be considered similar to the armature in a rail-gun and displaced continuously, while the arc attachments have their own behavior and have no impact on the arc displacement velocity. In these studies, experiments are performed in high current conditions and, as a result, the arc speeds have values around 100 m/s. Estimations of the arc propagation speed are given as well, where in comparison with a rail-gun with armature, the arc propagation velocity is limited by the drag forces [Zhukov 07].
In contrast to the specific attention paid to cathode attachment, anode attachment has been poorly investigated. The impact of the arc shape on its displacement is discussed in [Zeller 01] in great detail while the arc shape may be influenced by the specific gas flow conditions. Figure 3.1 presents a short summary of the results with different possible shapes of the arc column and near electrode zones. The investigations were carried out in different conditions for an arc in pulsed current conditions with a duration of 1.6 ms. The external magnetic field was included in the experiment. Interestingly, the so-called "arc nose" is proposed as a phenomenal

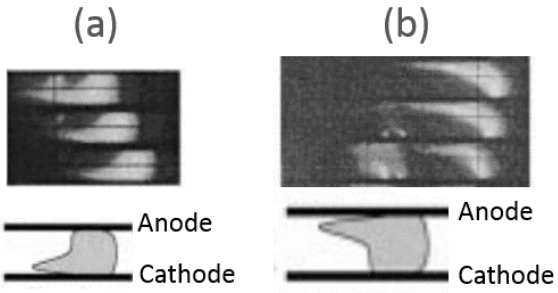

Figure 3.1: Images from high-speed video camera (33 000 frame 1/s) and arc schematic [Zeller 01]. (a) $h = 5$ mm, $I = 2$ kA, blast field 40 mT; (b) $h = 15$ mm, $I = 2$ kA, blast field 40 mT.

description for a specific, but reproducible, shape ahead of the arc [Zeller 01]. The authors, who first introduced this term, used it to refer to a specific feature observed randomly either near the cathode (figure 3.1 (a) or the anode 3.1 (b). According to [Zeller 01] and references therein, a good reproducibility was observed. The formation of several cathode spots (figure 3.1 (b)) is observed and a "forward jump" from the old spot position to the new one over time. If

the “nose” appears near the anode, several spots are observed near the cathode and vice-versa. In the study, it was shown that the cathode and anode roots can displace continuously or with jumps without a clear correlation. In another study [Teste 95], it was shown that the cathode attachment moves continuously, while the anode one experiences significant jumps.
To sum up, in spite of the number of studies on arc displacement, there is currently no commonly accepted opinion about the mechanism of arc motion. Either the velocity of the arc is dominated by the balance of electromagnetic and aerodynamic forces on the arc column or governed by the behavior of the arc roots. In addition, the role of anode attachment has not been clearly elucidated yet and its contribution may not be negligible as hinted in most of the studies cited.
The techniques used to investigate arcs in most studies involve high-speed imaging, measurement of the arc voltage together with monitoring of the arc current. The same protocol was used to conduct the present experimental investigation. The arc voltage consists of the sum of the cathode and the anode voltage drops with the arc column voltage. Increasing the distance between the electrodes will increase the arc voltage however, since the arc column is longer. During the arc displacement it was observed that when one of the attachments (cathode or anode) is further than another, the arc looks tilted [Zeller 01] and, therefore, the arc becomes longer. Elongation of the arc column will increase the arc voltage. It is reported that, if arc stretching is observed, shortly afterwards one of the attachments will make a "jump". This "jump" leads to the stabilization of the arc voltage [McBride 02]. Thus, a correlation must exist between the arc voltage and the arc displacement.
A review of experimental studies dealing with electric arcs in LVCB was published in [McBride 01]. General mechanisms are reported such as the appearance of the electric arc. In spite of widespread interest in arc investigations, there is no generally accepted description of the arc behavior between rails, leaving room for more experiments, investigations and discussions. This is one of the main motivations of the present study.

3.2 Experimental setups

In this work two experimental setups were used to study the arc propagation along rail electrodes. They have several principal differences in order to satisfy several requirements. The experiments performed in the GREMI laboratory were conducted in order to understand general arc behaviors during propagation and to establish the method of choice for the investigation. In this setup, a pair of copper electrodes are mounted with a sufficient gap to distinguish the arc column distance between the electrodes. The arc is initiated after the separation of a mobile contact which opens synchronously with the current pulse. The second set of experiments was performed using the facilities of Zodiac Aero Electric, located in Niort, France. The experi-

mental conditions were chosen so as to be as close as possible to the real situation of a default arc occurring in the electrical network of an aircraft. The arc is initiated due to a FOD and propagates between the busbars. The complete power supply of an aircraft is coupled to the experimental bench. In this case, powering is achieved by imposing the voltage, while the arc current is defined by the intrinsic capability of the system.
These two setups made it possible to investigate the arc, predict its behavior and extend current knowledge to conditions not considered in other studies. Additionally, the aim of this experimental study is to compare with the results obtained from numerical simulations. It is important to note that for both experimental setups, the arc is ignited in *ambient air at atmospheric pressure* (1 atm).

3.2.1 GREMI's experimental setup

Two copper rail electrodes with a circular cross section of 6.0 mm diameter and 250 mm long are placed one in front of the other with a 20 mm gap. The power supply delivers an arbitrary positive half-period of a 50 Hz sine waveform current. The description of the experimental setup is given in [Hong 02a, Hong 05]. The electrical parameters and the high-speed imaging are recorded simultaneously:

- The current of the arc is imposed and measured using a Rogovski coil;
- The arc voltage is measured at the same time with a differential voltage probe Langlois DP25;
- The high-speed video camera Photron SA5 is used to record the arc dynamics. The images are used in order to define the arc displacement and its velocity.
- All the devices are synchronized with respect to the trigger signal of the rising edge of the current pulse.

3.2.2 Zodiac experimental setup

A three-phase electrode system, in which each electrode has a rectangular cross section of 3.0 mm × 8.0 mm and a length of 20 mm made of aluminum is used for the experiment. The electric arc is initiated between two phases. The electrode gap varies from 5 mm to 8 mm. The electrical parameters are recorded for a whole system, which contains the bus-bar electrodes, the generator (the same as that used in aircraft), about 35 m of cables and a command/synchronization table. The electrical parameters and the high-speed imaging are recorded simultaneously:

- Electrical measurements were performed using the Zodiac Aerospace facilities (Rogovski coil, differential voltage probe);

- The same high-speed video camera Photron SA5 was used to record the arc dynamics;
- The electric arc is initiated by imposing a metallic wire between the two phases;
- All the devices are synchronized with respect to the opening of the mobile contact.

3.3 Results

For the complete analysis of the electric measurements the current and the voltage waveforms were used. In order to evaluate the arc displacement velocity, each frame from the high speed video was post-processed with a specifically developed program. The position of the cathode and anode attachments were defined according to the maximum of the luminance in the vicinity of the electrode. Then, at each time step point, the position of both attachments was identified, allowing the experimental determination of the arc root velocities.

3.3.1 Experimental study with pulsed arc – GREMI laboratory

The experiments were carried out for different values of the peak current. Here, a few examples of the experimental results are shown, analyzed and discussed. In figure 3.2 two examples of the

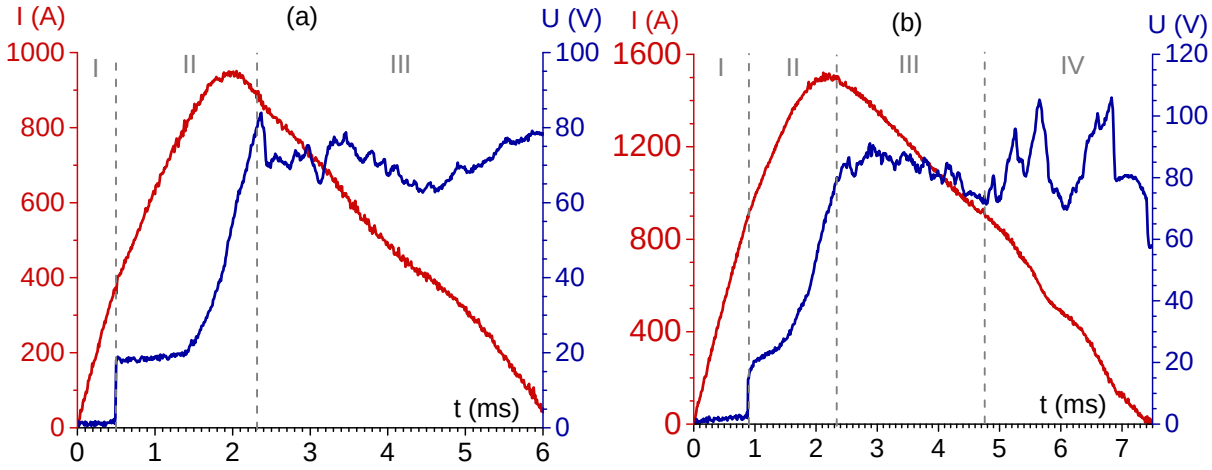

Figure 3.2: Temporal evolution of the arc current and arc voltage for two experimental conditions, (a) $I_{max} = 950\,\text{A}$ and (b) $I_{max} = 1.5\,\text{kA}$ at 1 atm.

arc current and voltage waveforms are reported. On both waveforms the maximum value of the current is reached 2 ms after the pulse ignition. Then, the current slowly decreases. During the entire period of the current pulse, a sequence of several phases occurs consecutively as depicted in figure 3.3: The typical sequence of events is:

i The mobile electrode is closed, the current flows though the mobile contact and one of the rails (in the present experiments, the anode).

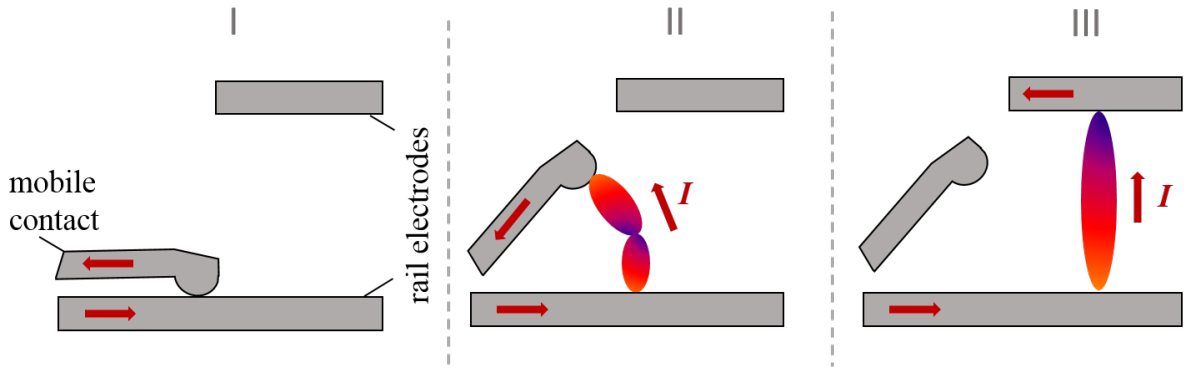

Figure 3.3: Schematic of the sequential arc initiation and propagation between the rail electrodes. (I) closed contacts; (II) opening of the contacts triggering the electric arc ignition and elongation; (III) arc propagation along the bus-bars.

ii Motion of the mobile contact triggering the arc ignition and elongation of the arc with its subsequent "jump" to the rails.

iii Existence of the arc between the rail electrodes, propagation along the electrodes, acceleration and speed stabilization.

iv Final burning of the arc at the edge of the electrode.

At time 0.5 ms after triggering, the mobile contact starts to open; the opening duration is about 1.5 ms (phase II). During opening, the electric arc is attached to the mobile contact and one rail, therefore the arc column elongates causing an increase in the arc voltage, as evidenced in figure 3.2. When the arc is long enough, a “jump” occurs onto the second rail electrode around 2.3 ms. Then, the displacement of the arc along the rail starts (phase III). The arc propagation along the electrodes was recorded with a high-speed video camera and a sequence of frames is shown for two different current conditions in figure 3.4 and figure 3.5. During arc propagation, the cathode and the anode attachments are observed (marked with (✳) and (✳) accordingly). Each of them forms the cathode and anode jets respectively. Each jet usually corresponds to the maximum luminance observed near the electrodes. To record the high-speed video, the frame rate was set at 9000 fps in order to track the continuous root displacement along each electrode. The cathode and the anode attachments move simultaneously in the same direction and no significant “jump” was observed. The *re-striking* of the arc during the experiment was never observed either. During the propagation phase, the arc voltage waveform is rather smooth with only small perturbations (phase III in figure 3.2). Once the arc has reached the end of the electrodes, it burns until the current returns to zero. During this time, instabilities arise on the arc voltage waveform (phase IV in figure 3.2 (b)).

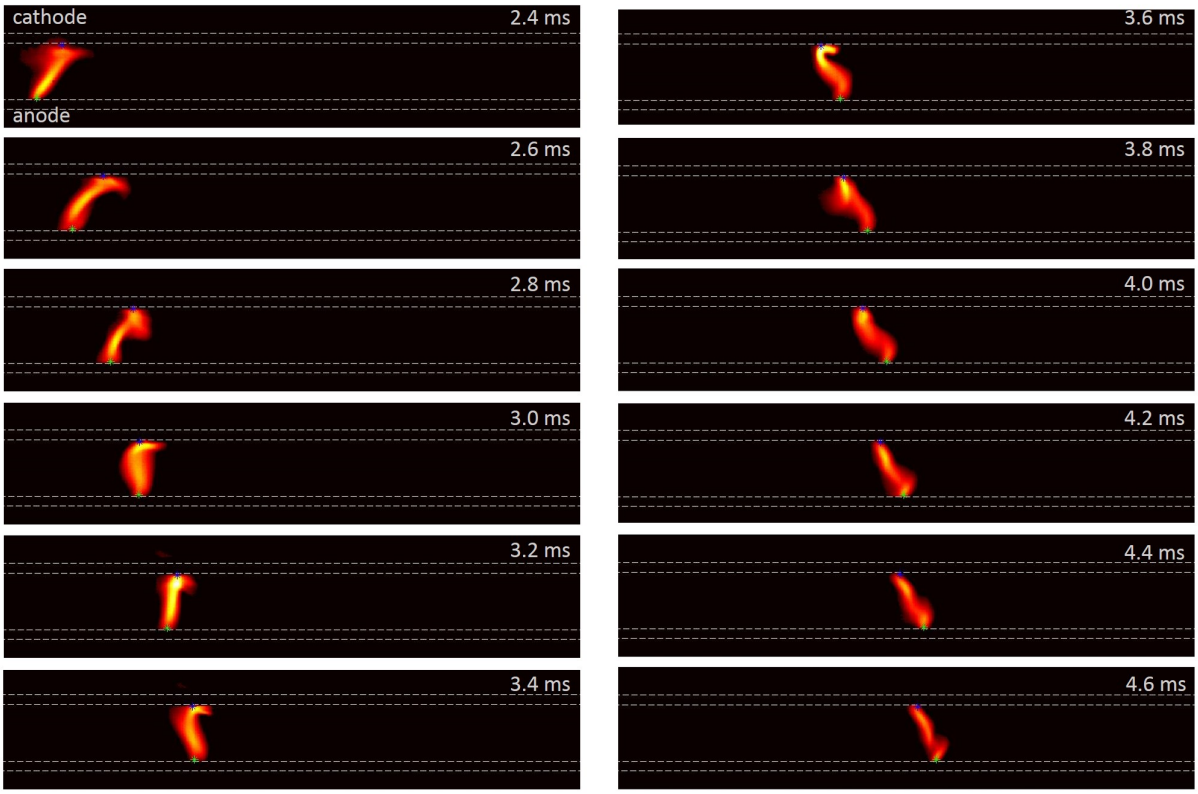

Figure 3.4: Sequence of images recorded by means of a high-speed video camera for a current pulse of $I_{max} = 800\,\text{A}$. On each frame, the blue (⚹) denotes the cathode attachment while the green (⚹) indicates the anode attachment.

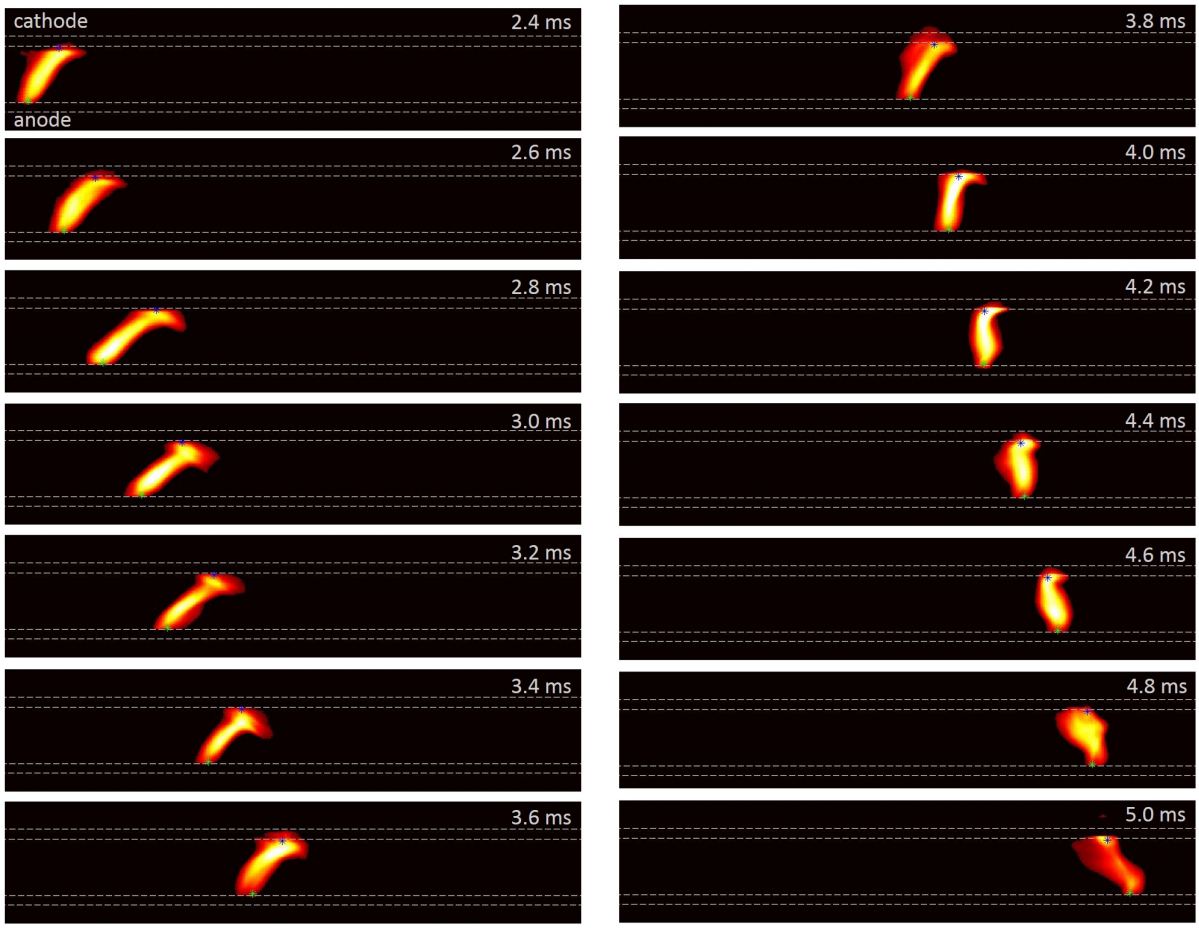

Figure 3.5: Sequence of images recorded by means of a high-speed video camera for a current pulse of $I_{max} = 1.5\,\mathrm{kA}$. On each frame, the blue (⚹) denotes the cathode attachment while the green (⚹) indicates the anode attachment.

The time evolutions of the position of each arc root along the electrodes are shown in figure 3.6 (a) for two current conditions (I_{max} = 800 A and I_{max} = 1.5 kA). The temporal

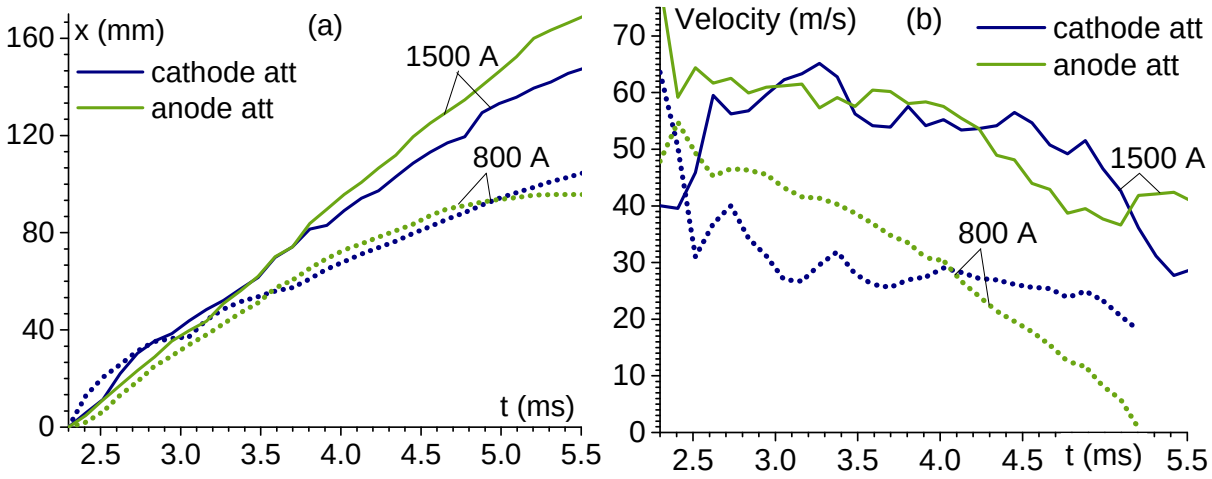

Figure 3.6: Time evolutions of the arc roots for two different current conditions I_{max} = 800 A and I_{max} = 1.5 kA at 1 atm. (a) Position of the cathode and anode roots along the electrode axis. (b) Velocity of each root along the electrode.

evolutions of the root velocities are also presented in figure 3.6 (b) with respect to the root position. It can be seen that the arc with the higher current has a higher propagation speed.
A number of experiments for different maximum peak current values were performed and analyzed. The results of this study are summarized in figure 3.7 and 3.8. The arc speeds for different current values are marked with the symbols in figure 3.7. The dependence between the arc speed and the arc current can be interpolated with a linear function $v_{arc} = 0.04I + 6.1$. In the investigated current range from 200 A to 2 kA this linear function can be used to define approximately the arc velocity. However, it is questionable whether it can be extended to a wider current range. The velocities of arcs operated with high current (2 kA) are below 100 m/s. This fact evidences that the arc speed matches the criterion $Ma < 0.3$ and that compressible effects can reasonably be neglected. Note that no sign of shock waves was observed ahead of the arc. Nevertheless, extrapolating the linear trend for a higher current range is doubtful due to the possible appearance of shock waves. Similar observations were reported in [Bobashev 10b, Bobashev 10a].
From the experimental data sets, the typical current–voltage characteristic was analyzed and is presented in figure 3.8. The current–voltage characteristic is linear for currents below 1 kA. For higher currents, the amplitude variation of the arc voltage for the same current value becomes higher and higher. This variation may be due to the arc displacement itself which induces some instabilities. Typically, this can happen when the cathode and the anode root displacements are not synchronized and the arc elongates. Amplitude variations of the arc voltage during prop-

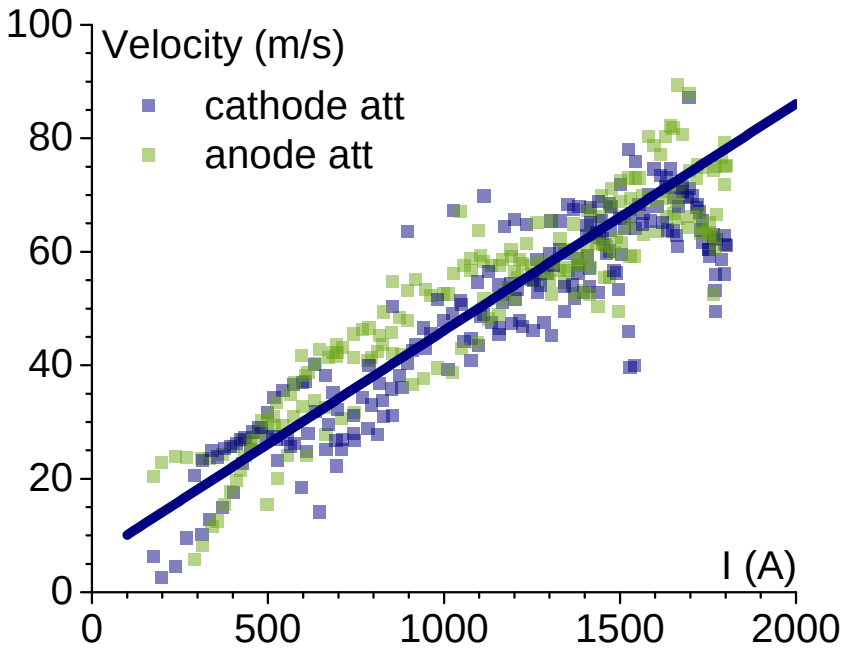

Figure 3.7: Arc displacement velocity versus the arc current. The linear regression obeys the formula $v_{arc} = 0.04 \cdot I + 6.1$.

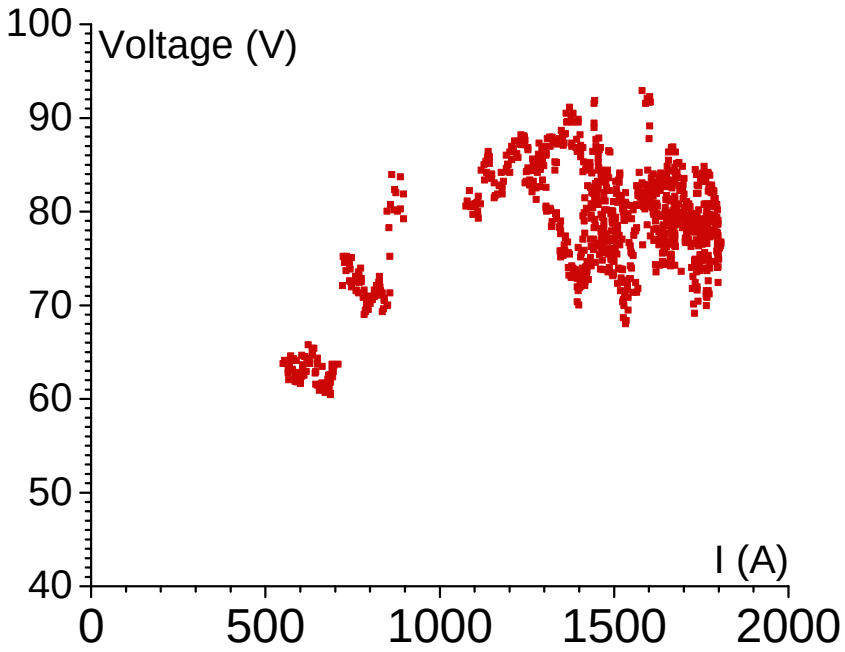

Figure 3.8: Current–voltage characteristic of the moving arc compiled from the experimental data set.

agation of the arc along the electrodes may be caused by a discontinuous displacement of one of the two roots. In this experimental investigation, the "jumping mode" of the anode and/or the cathode roots was not observed. To confirm this observation, experiments recorded with high-speed imaging at a frame rate up to 50 000 fps was performed and showed a continuous displacement of the arc. Although other experimental studies report on a continuous displacement of the cathode attachment while regular jumps of the anode root occur, the authors used a different electrode geometry [Teste 95]. Discussions based on the images from a high-speed video camera give information only in the propagation direction. In reality the electric arc mainly moves in the longitudinal direction, but there are small fluctuations in the transverse direction. These fluctuations may be the reason for the noisy voltage signal recorded for higher currents. However, this interpretation requires further investigations.

3.3.2 Experimental study with AC arc – Zodiac Aero Electric

Since the main interest of this work was to investigate the arc behavior in conditions close to those in the typical electrical distribution system of an aircraft, the aim of this section is to give a sufficiently comprehensive overview of arc behavior in such a situation. Depending on the position of the distribution system in the network, a variety of powering conditions exist, for instance 115 V, 230 V at different frequencies. In this work, just a few sets of operating parameters are considered:

- The inter-electrode distances were fixed at 5 mm or 8 mm between the aluminium electrodes.
- An alternating current waveform at a locked frequency of 420 Hz or 760 Hz was used.
- The whole system was powered with a voltage of 115 V or 230 V. Consequently, the short-circuit arc current is defined with respect to the impedance of the whole system delivering a maximum current ranging from 400 A to 2 kA.

The arc fault was initiated by a FOD placed between the electrodes. Additional details about the whole electrical system typically used in aircraft is beyond the scope of this work and will not be documented. Only the experimental results concerning the electrical arc are reported below. Experimental data of several parameter sets are presented in detail, particularly those that highlight the originality of the study. To the best of our knowledge, arc propagations along rail electrodes with respect to alternating current conditions have not been clearly reported in the literature. Starting from this point, the rest of this section is organized in four sets as follows:

	Voltage	Frequency	Gap
Set 1	230 V	420 Hz	5 mm
			8 mm
Set 2	230 V	760 Hz	5 mm
			8 mm
Set 3	115 V	420 Hz	5 mm
			8 mm
Set 4	115 V	760 Hz	5 mm
			8 mm

To ensure repeatability of the results, each condition was measured at least three times. For the sake of readability, the following systematic structure was adopted to present the results:

- Electrical waveforms of the arc.
- Time evolution of the position of the cathode and anode roots.
- Sequence of frames from the high-speed imaging recording.
- Time evolution of the cathode and anode root velocity.

Set 1: arc in aeronautical conditions, 230 V**,** 420 Hz

The arc current and arc voltage waveforms are presented in figure 3.9 (a). As mentioned earlier,

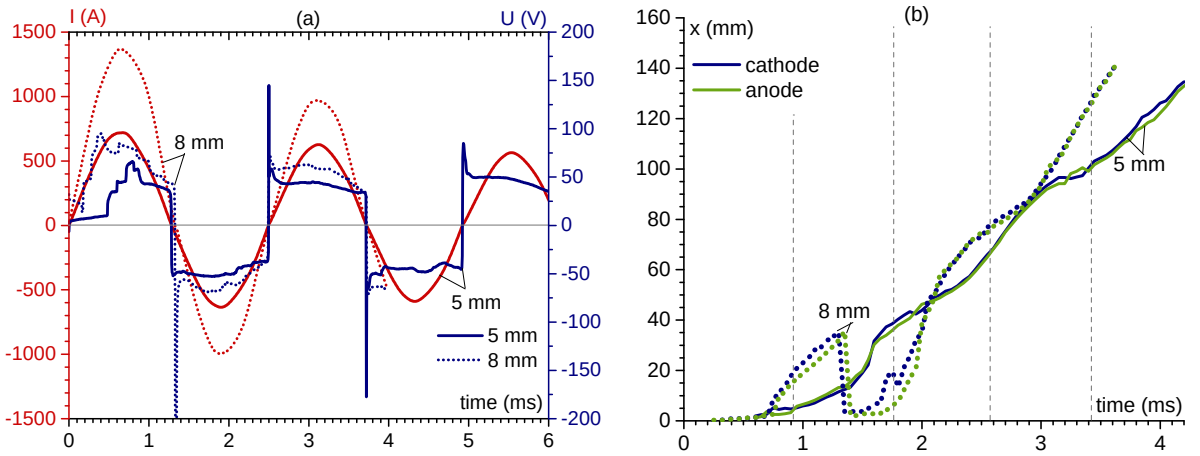

Figure 3.9: Parameter set 1, 230 V at 420 Hz with $h = 5$ mm and $h = 8$ mm electrode gap. (a) Waveforms of the arc current and arc voltage; (b) Time evolution of the cathode and anode attachments position.

at any time the current value is imposed by the load itself, i.e. the bus-bars construction, the internal circuit of the power supply unit as well as wires and coupling devices between the

source and the busbars. The maximum current value is 1350 A for the shorter arc and 700 A for the 8 mm arc. The arc voltage has overshoots when the arc current crosses zero and remains approximately constant during the half period.
The dynamic of the arc root displacement is shown in figure 3.9 (b). The root positions are defined with the same method as in the previous experiments: the maximum of the arc intensity near the cathode and anode are considered as the attachment positions. The vertical dashed lines on the graph (figure 3.9 (b)) correspond to the time point when the arc current crosses zero. For $h = 5$ mm, the arc propagates in the same direction and both roots move simultaneously. This is well identified in the sequence of images shown in figure 3.10. For the longer arc ($h = 8$ mm), *re-striking* of the arc takes place when, after one current period, the arc moves back to its initial position. This can be observed on the images of figure 3.11. However, on the arc voltage there are no significant fluctuations which could indicate re-striking.
For both distances, the cathode and the anode attachments are observed. At the time point where the arc current approaches zero, the cathode and the anode jets are very clearly distinguished. When the current is higher than 50 A, the arc has the shape of a uniform column and in some cases the so-called "nose" occurs. Similar to the work published in [Zeller 01], the formation of this specific arc shape with an elongation near the electrode is observed randomly. This is evidenced near the cathode at $t = 4.25$ ms and $t = 4.45$ ms and for the anode at $t = 1.75$ ms and $t = 1.95$ ms in figure 3.10.
The arc is initiated by inserting a FOD between the electrodes (here an piece of thin aluminum wire). It was found that re-striking of the arc most probably takes place when the rest of the FOD is soldered to the electrodes and continues to evaporate. This triggers the creation of a localized volume of higher electron and ion density while burning increases the probability of breakdown when the arc current crosses zero.
The arc root propagation velocities are displayed on figure 3.12 with error intervals resulting from numerical differentiation artifacts. A value of zero was assigned to the arc propagation velocity when re-striking takes place (figure 3.12 (b)). The vertical dashed lines on the graphs are associated with the time point when the arc current crosses the zero value. With a good correlation, the maximum arc speed is achieved when the arc current value is around its maximum. One can see that both the acceleration and deceleration of the arc are well correlated with the arc current frequency.

Set 2: arc in aeronautical conditions, 230 V, 760 Hz

The arc current and arc voltage waveforms are presented in figure 3.13 (a). The maximum value of the current was 400 A for a gap $h = 5$ mm and 700 A for a gap of $h = 8$ mm. The arc root displacements are shown in figure 3.13 (b). In this case, *re-striking* was not observed in any

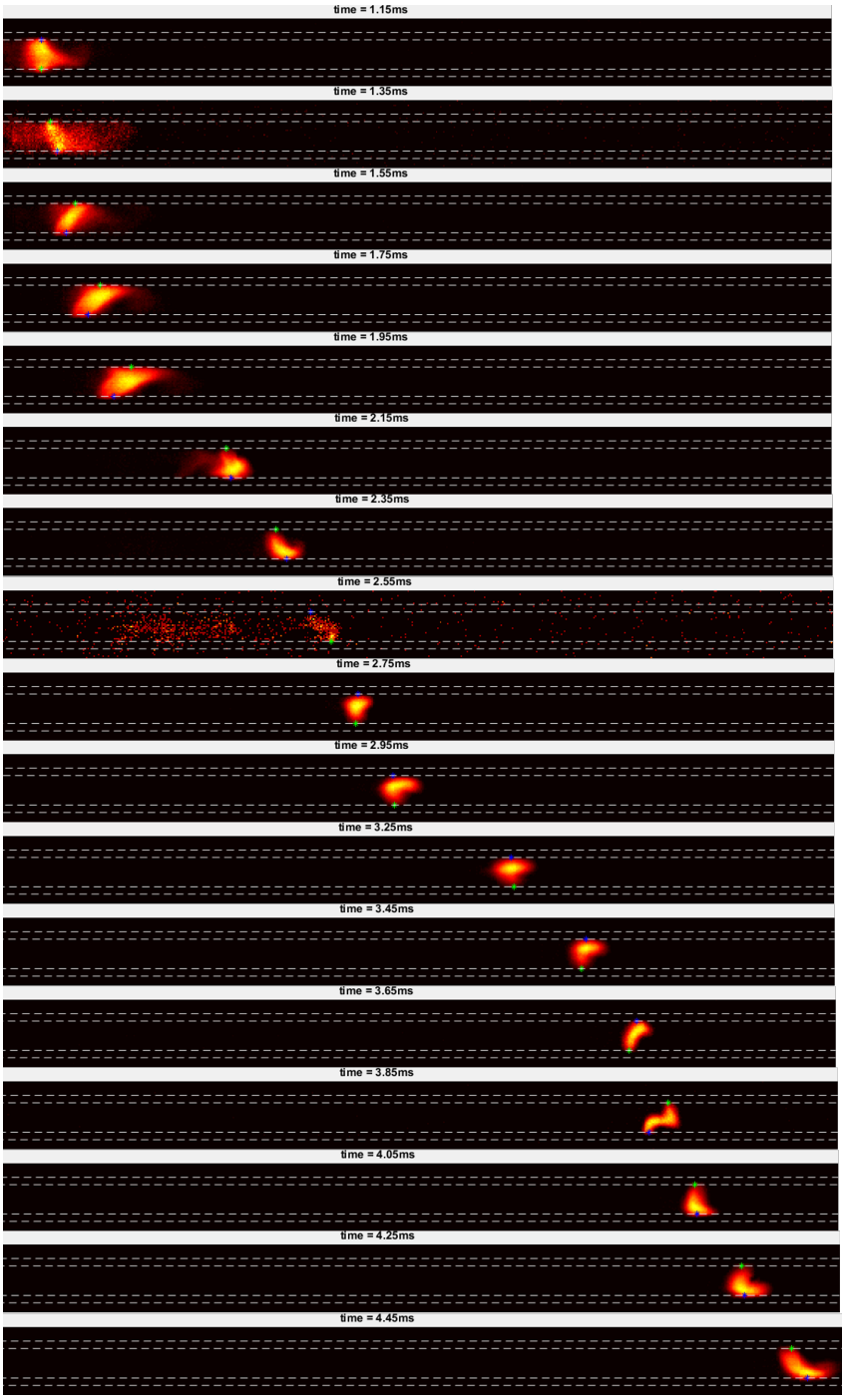

Figure 3.10: Parameter set 1, 230 V at 420 Hz with $h = 5$ mm. Sequence of frames from high-speed video imaging of the propagating arc. On each frame, the blue ($\ast$) denotes the cathode attachment while the green ($\ast$) indicates the anode attachment.

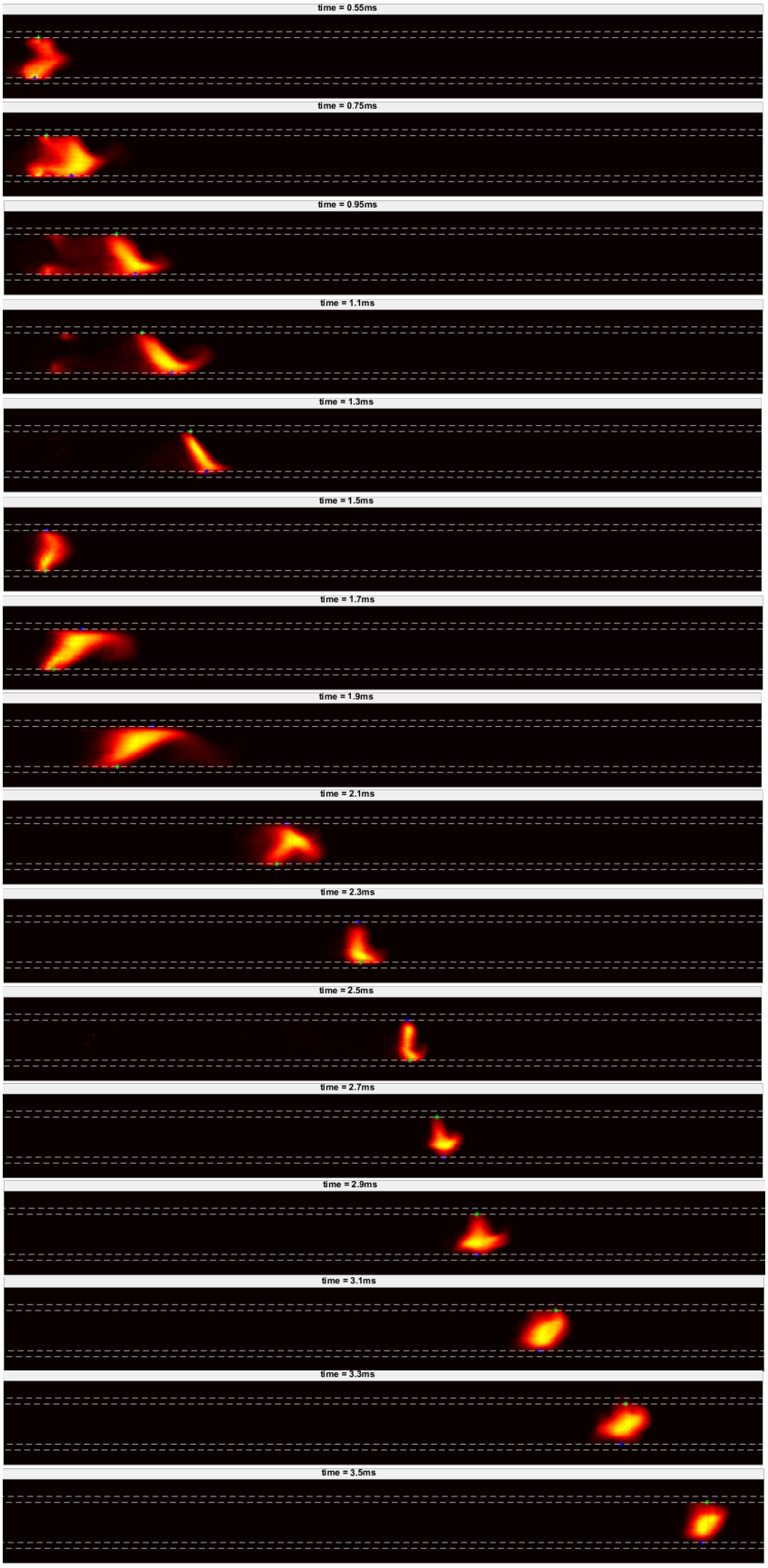

Figure 3.11: Parameter set 1, 230 V at 420 Hz with $h = 8$ mm. Sequence of frames from high-speed video imaging of the propagating arc. On each frame, the blue (⚹) denotes the cathode attachment while the green (⚹) indicates the anode attachment.

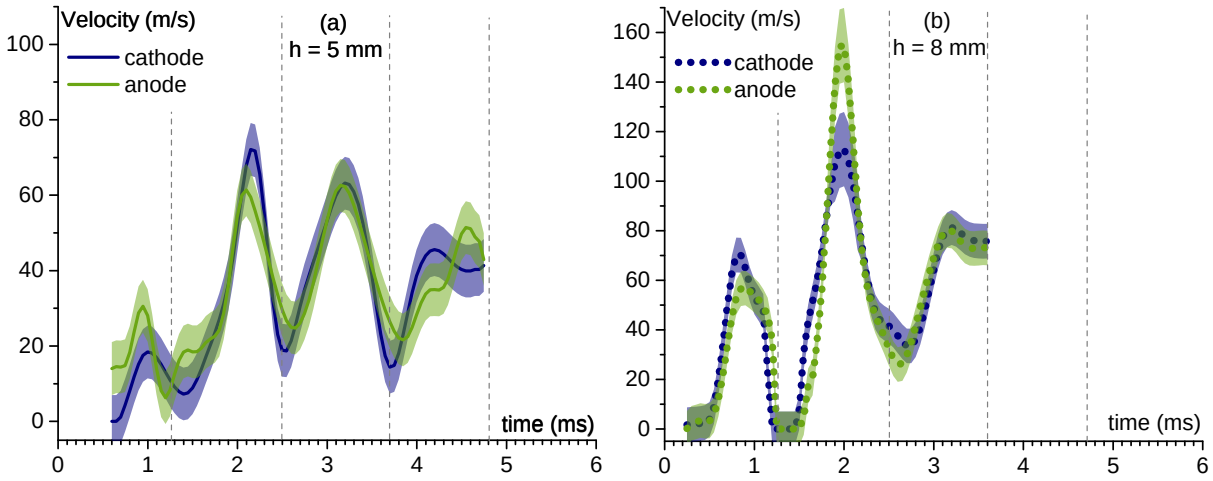

Figure 3.12: Parameter set 1, 230 V at 420 Hz. Temporal evolution of the cathode and anode root velocities for (a) $h = 5$ mm and (b) $h = 8$ mm electrode gaps.

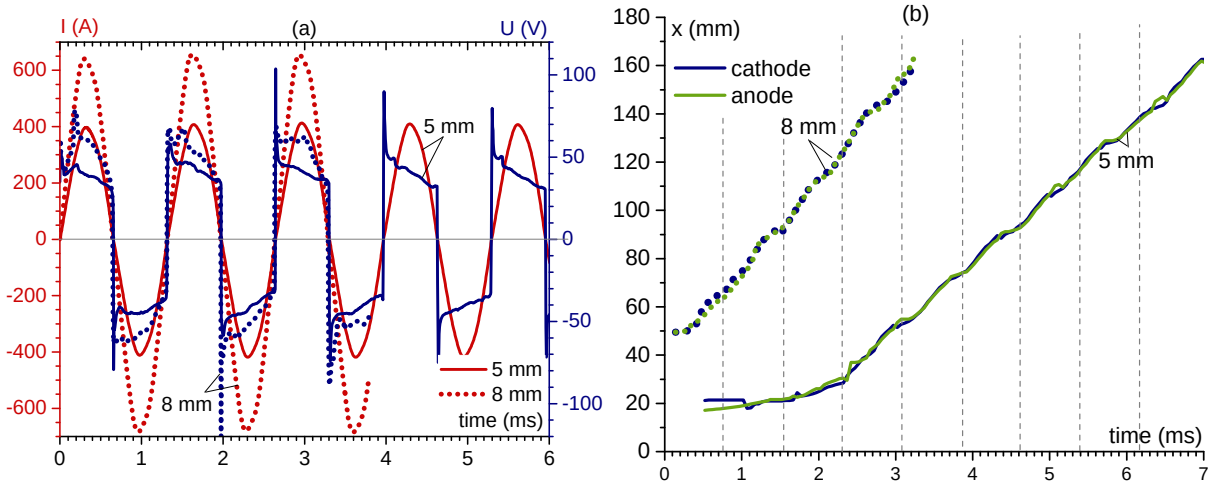

Figure 3.13: Parameter set 2, 230 V at 760 Hz with $h = 5$ mm and $h = 8$ mm electrode gap. (a) Waveforms of the arc current and arc voltage; (b) Time evolution of the cathode and anode attachments position.

measurements. The arc column is in most cases a vertical shape in comparison to the previous experimental set; however, with the smaller arc elongation the arc "nose" is not observed for all the conditions. The arc root displacement velocity is presented in figure 3.16. The minimum arc speed occurs when the arc current crosses zero and vice-versa. The arc acceleration and deceleration dynamic correlates with the discharge frequency. However, in this case, it can be seen that for some current values, the arc speed reaches a limiting propagation speed of about 40 m/s (figure 3.16 (a)) and 50 m/s (figure 3.16 (b)) for currents of 400 A and 700 A respectively.

Set 3: arc in aeronautical conditions, 115 V**,** 420 Hz

The arc current and arc voltage waveforms are presented in figure 3.17 (a). The maximum value of the current was 2.2 kA for a gap $h = 5$ mm and 1.8 kA for a gap of $h = 8$ mm. The arc root displacements are shown in figure 3.17 (b). In this case, restriking is observed for the arc with the biggest gap. On the images from the high-speed video camera shown in figure 3.19, this phenomenon is easily identified at $t = 1.25$ ms. The arc current in this set of experimental data is significantly higher than in set 1 and set 2. Therefore the strong cathode or anode jets together form the arc column and the existence of a "nose" is more likely to be observed. Again, the formation of this feature near the cathode and near the anode occurs rather randomly. This experiment also showed significant arc jumps and even the existence of several attachments to a single electrode at the same time.

Set 4: arc in aeronautical conditions, 115 V**,** 760 Hz

The arc current and arc voltage waveforms are presented in figure 3.21 (a). The maximum value of the current was 1.4 kA for a gap $h = 5$ mm and 900 A for a gap of $h = 8$ mm. The arc root displacements are shown on figure 3.21 (a). For the distance of 8 mm re-striking is more likely. During the arc propagation, the existence of several attachments was observed, for example at $t = 0.6$ ms (figure 3.22) and $t = 2.2$ ms (figure 3.23). It can be seen that the arc "jumps" alternately between several attachments to the electrodes. When the previous attachment disappears, the newest one continues to move in the propagation direction. The arc propagation velocities are shown in figure 3.24. One can see a good correlation between moments when the arc current and the arc velocity are maximum. However, as in the previous cases, the arc speed during the current zero period has values which are different from zero. It is only in the case of re-striking that the arc velocity is considered to be zero.
The various experimental conditions investigated in the Zodiac facility give a good overview of the electric arc phenomena taking place in AC conditions. A typical arc behavior observed in all these cases is the following: the arc moves in the same direction regardless of the electrode polarity. This particularity will be described in detail in the next chapter. A good correlation

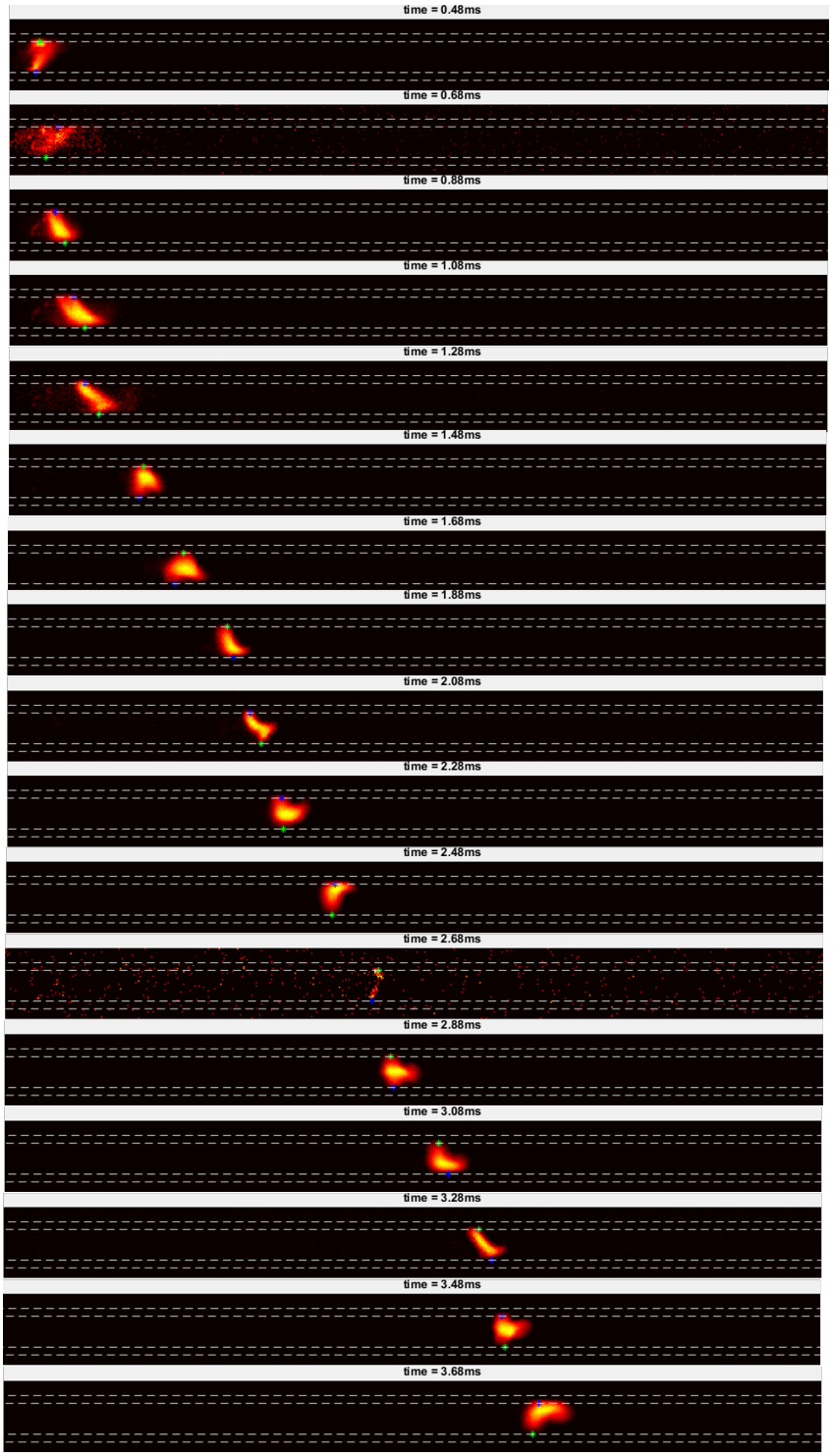

Figure 3.14: Parameter set 2, 230 V at 760 Hz with $h = 5$ mm. Sequence of frames from high-speed video imaging of the propagating arc. On each frame, the blue ($\ast$) denotes the cathode attachment while the green ($\ast$) indicates the anode attachment.

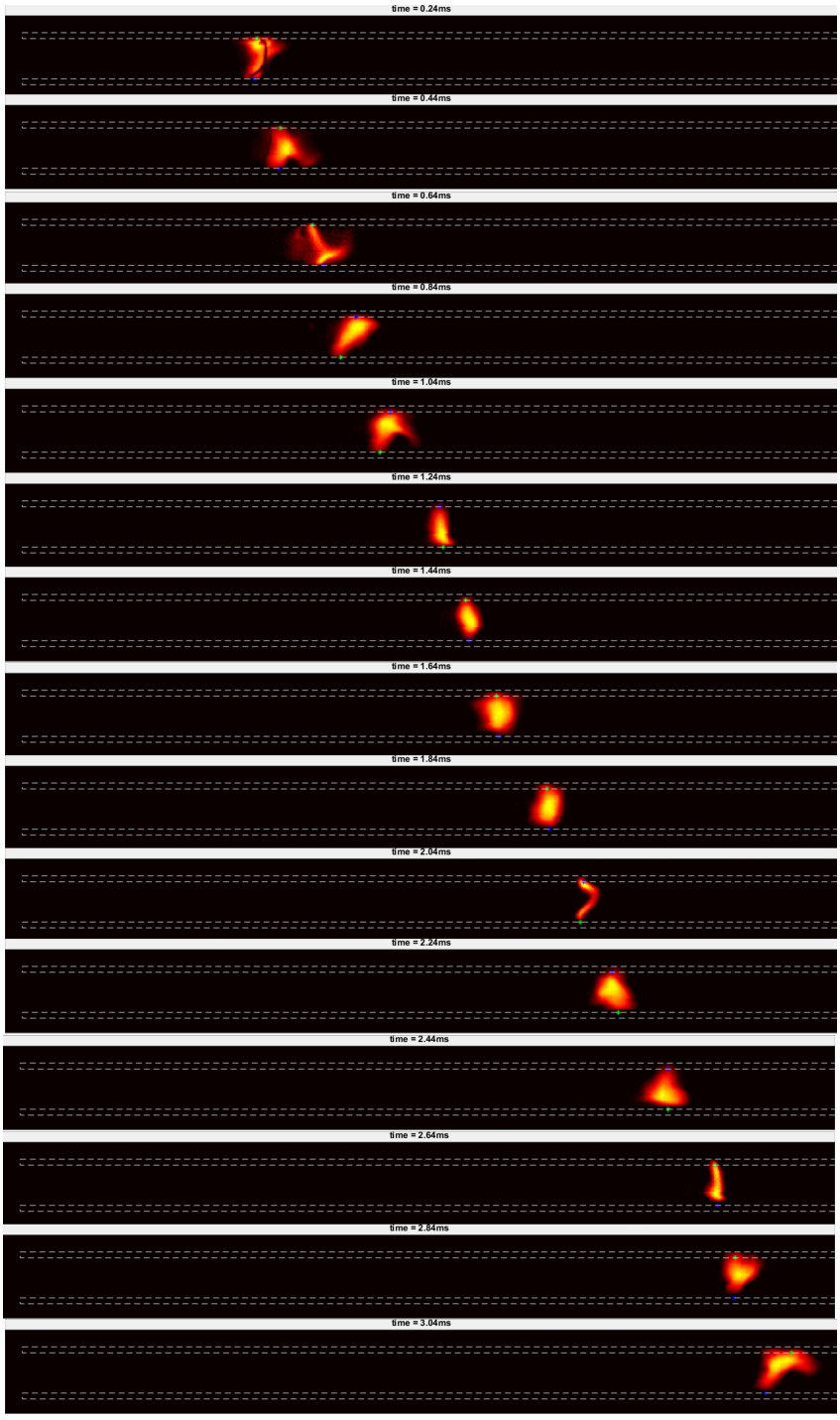

Figure 3.15: Parameter set 2, 230 V at 760 Hz with $h = 8$ mm. Sequence of frames from high-speed video imaging of the propagating arc. On each frame, the blue (⚹) denotes the cathode attachment while the green (⚹) indicates the anode attachment.

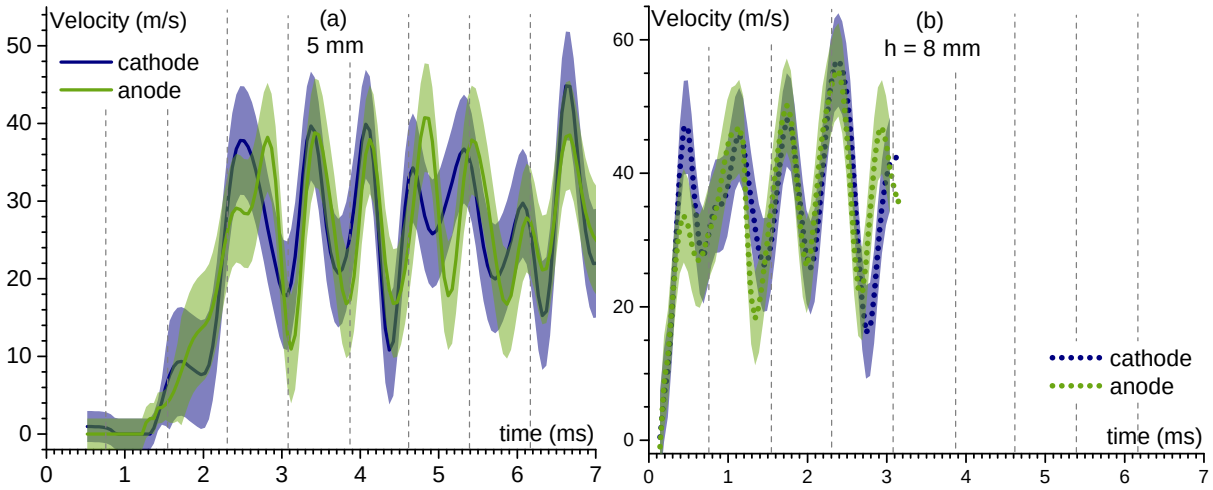

Figure 3.16: Parameter set 2, 230 V at 760 Hz. Temporal evolution of the cathode and anode root velocity for (a) $h = 5$ mm and (b) $h = 8$ mm electrode gaps.

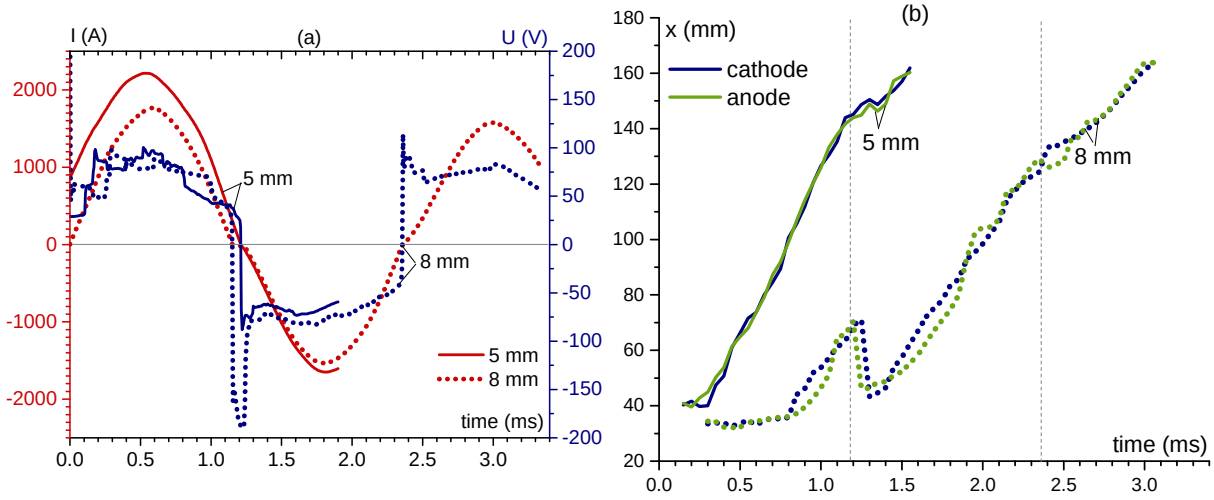

Figure 3.17: Parameter set 3, 115 V at 420 Hz with $h = 5$ mm and $h = 8$ mm electrode gap. (a) Waveforms of the arc current and arc voltage; (b) Time evolution of the cathode and anode attachments position.

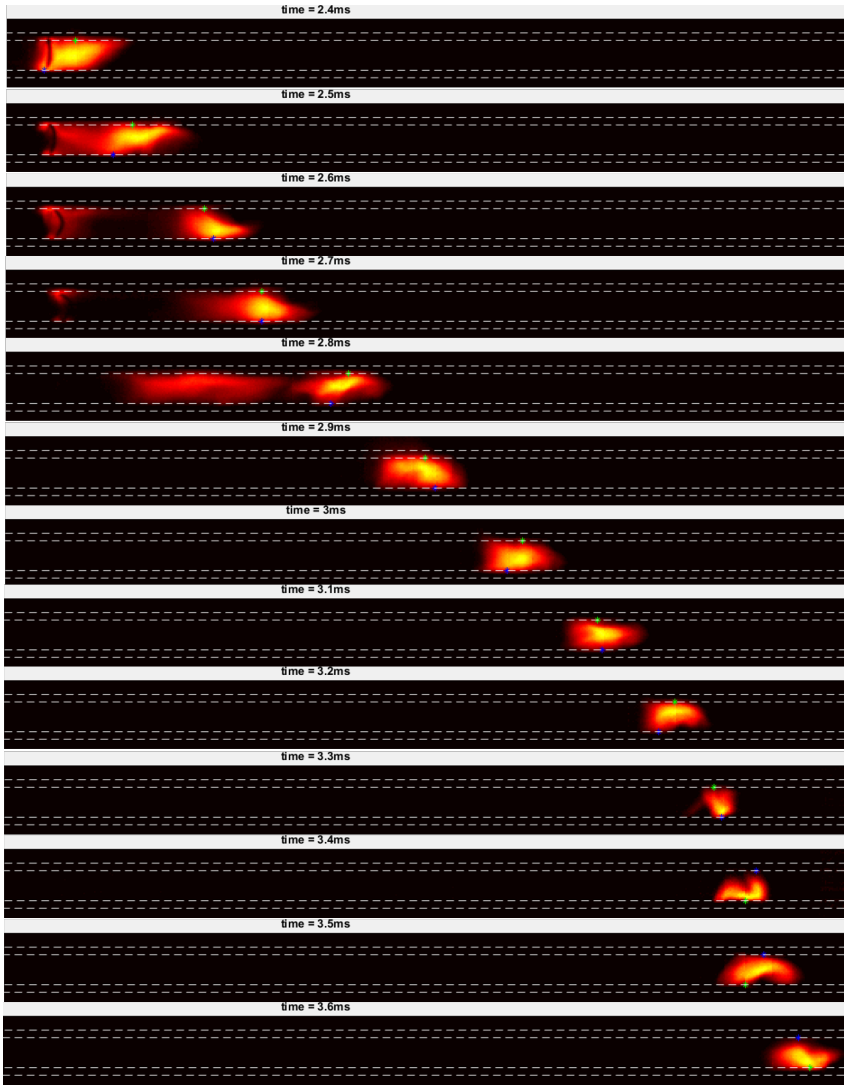

Figure 3.18: Parameter set 3, 115 V at 420 Hz with $h = 5$ mm. Sequence of frames from high-speed video imaging of the propagating arc. On each frame, the blue (⚹) denotes the cathode attachment while the green (⚹) indicates the anode attachment.

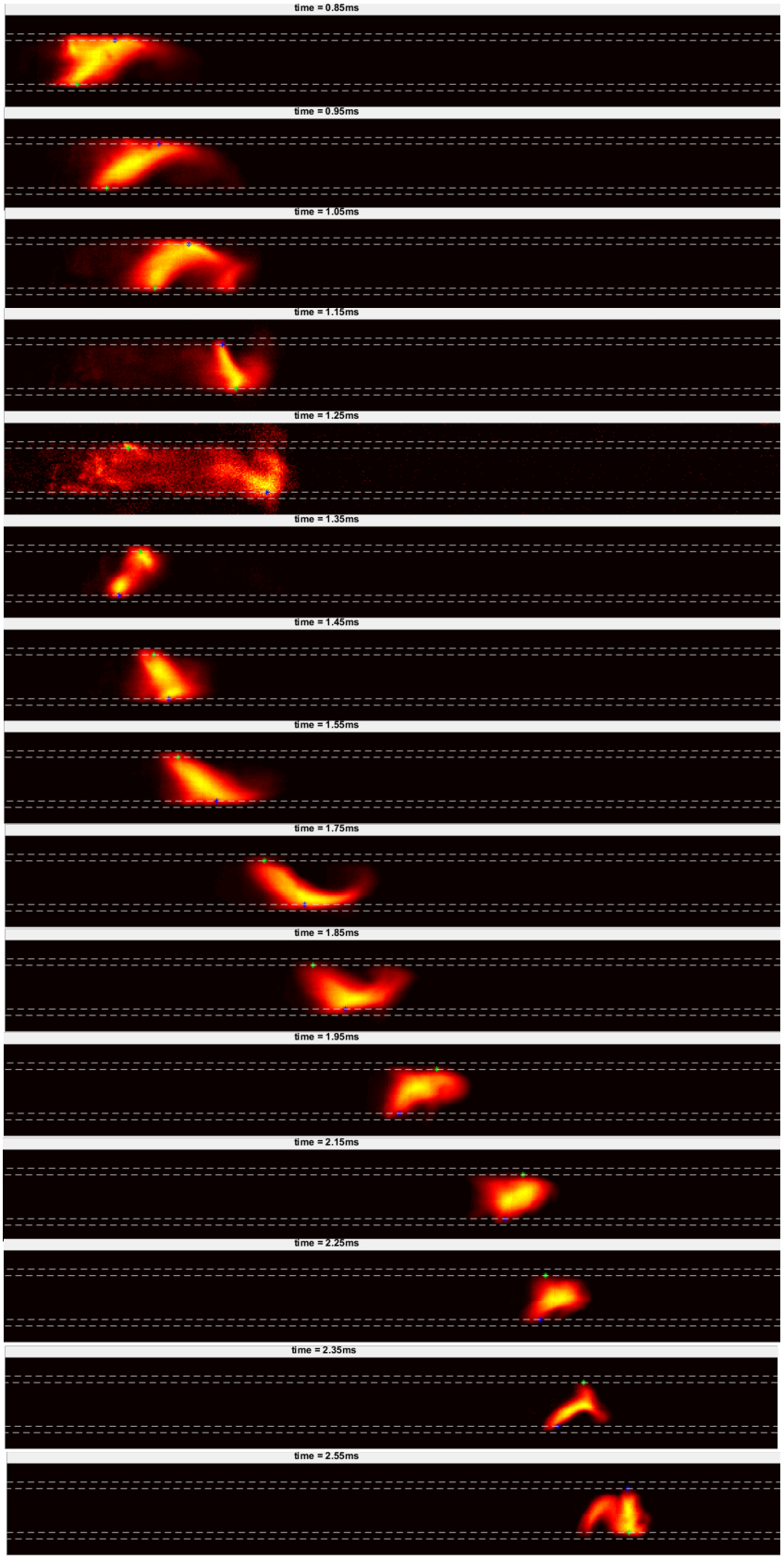

Figure 3.19: Parameter set 3, 115 V at 420 Hz with $h = 8$ mm. Sequence of frames from high-speed video imaging of the propagating arc. On each frame, the blue ($\ast$) denotes the cathode attachment while the green ($\ast$) indicates the anode attachment.

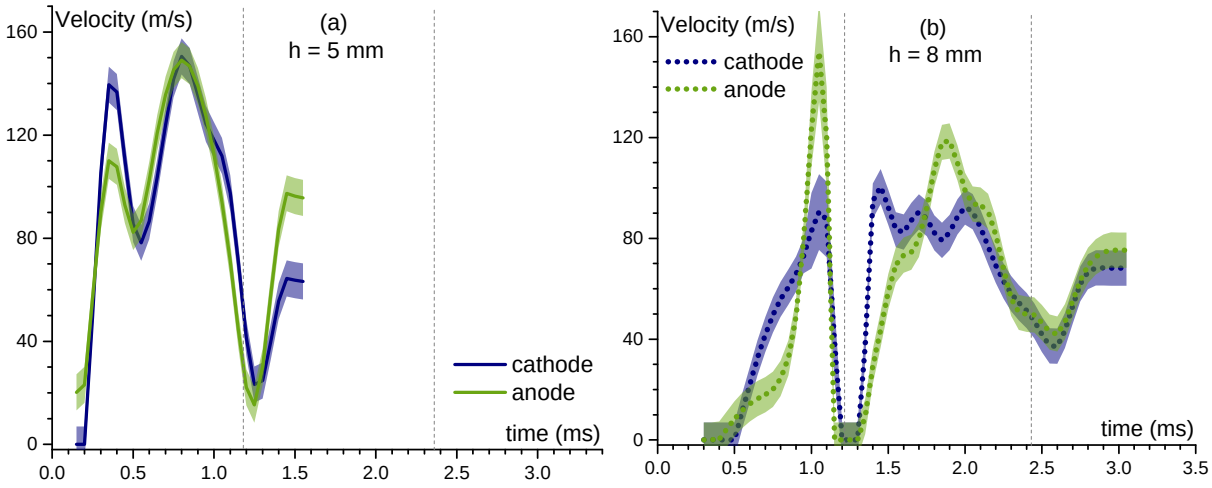

Figure 3.20: Parameter set 3, 115 V at 420 Hz. Temporal evolution of the cathode and anode root velocity for (a) $h = 5$ mm and (b) $h = 8$ mm electrode gaps.

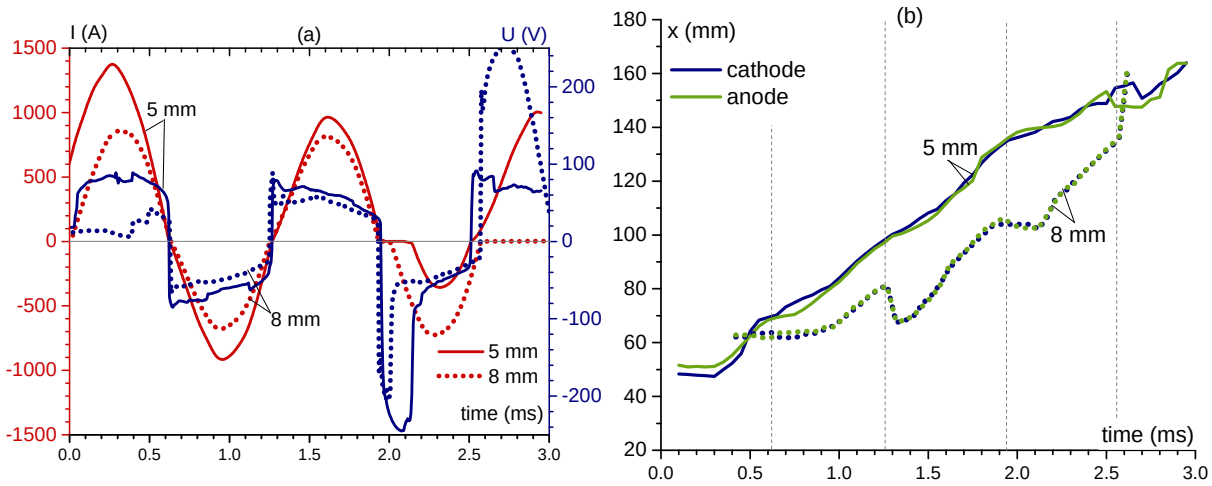

Figure 3.21: Parameter set 4, 115 V at 760 Hz with $h = 5$ mm and $h = 8$ mm electrode gap. (a) Waveforms of the arc current and arc voltage; (b) Time evolution of the cathode and anode attachments position.

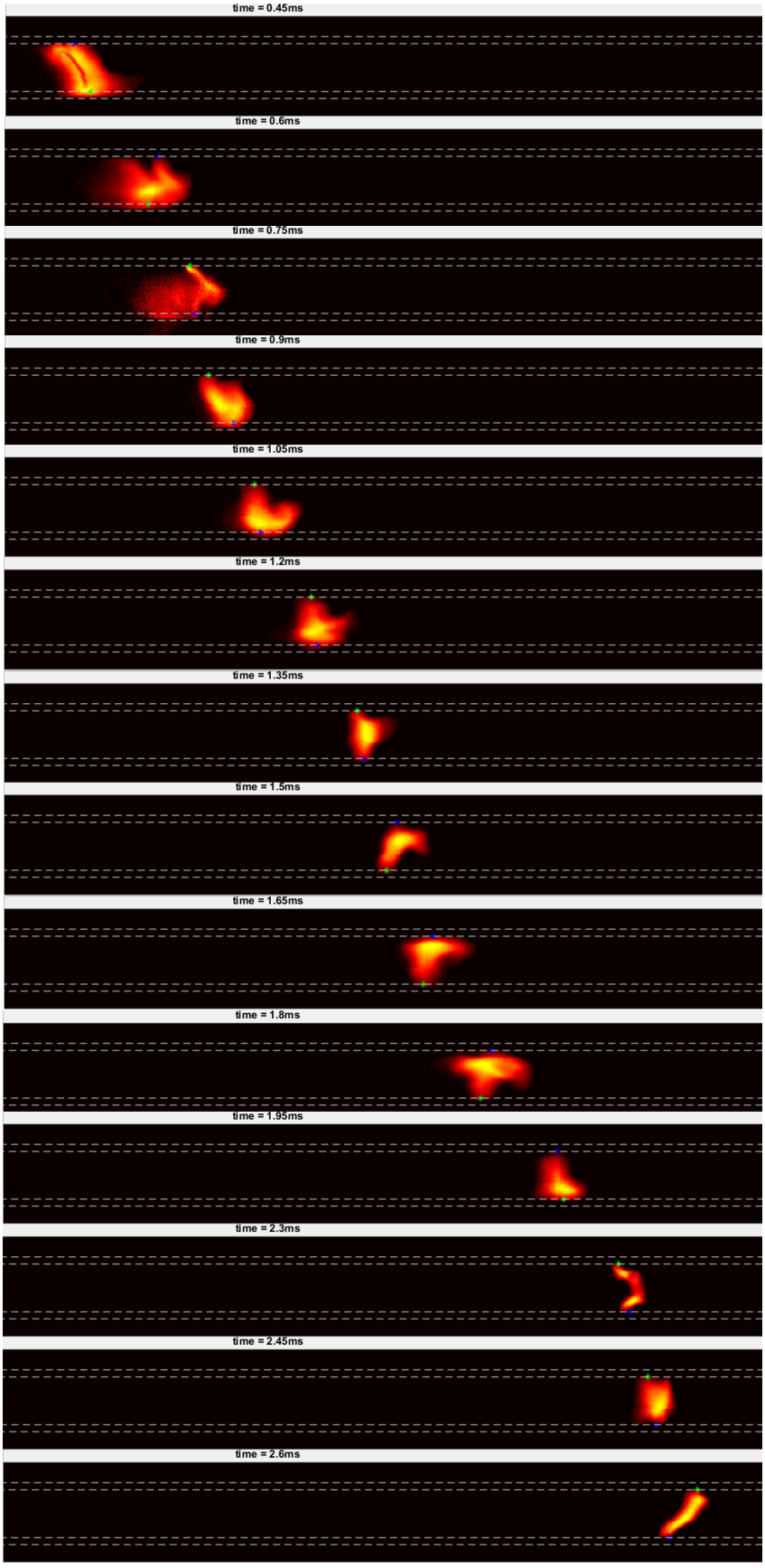

Figure 3.22: Parameter set 4, 115 V at 760 Hz with $h = 5$ mm. Sequence of frames from high-speed video imaging of the propagating arc. On each frame, the blue ($\ast$) denotes the cathode attachment while the green ($\ast$) indicates the anode attachment.

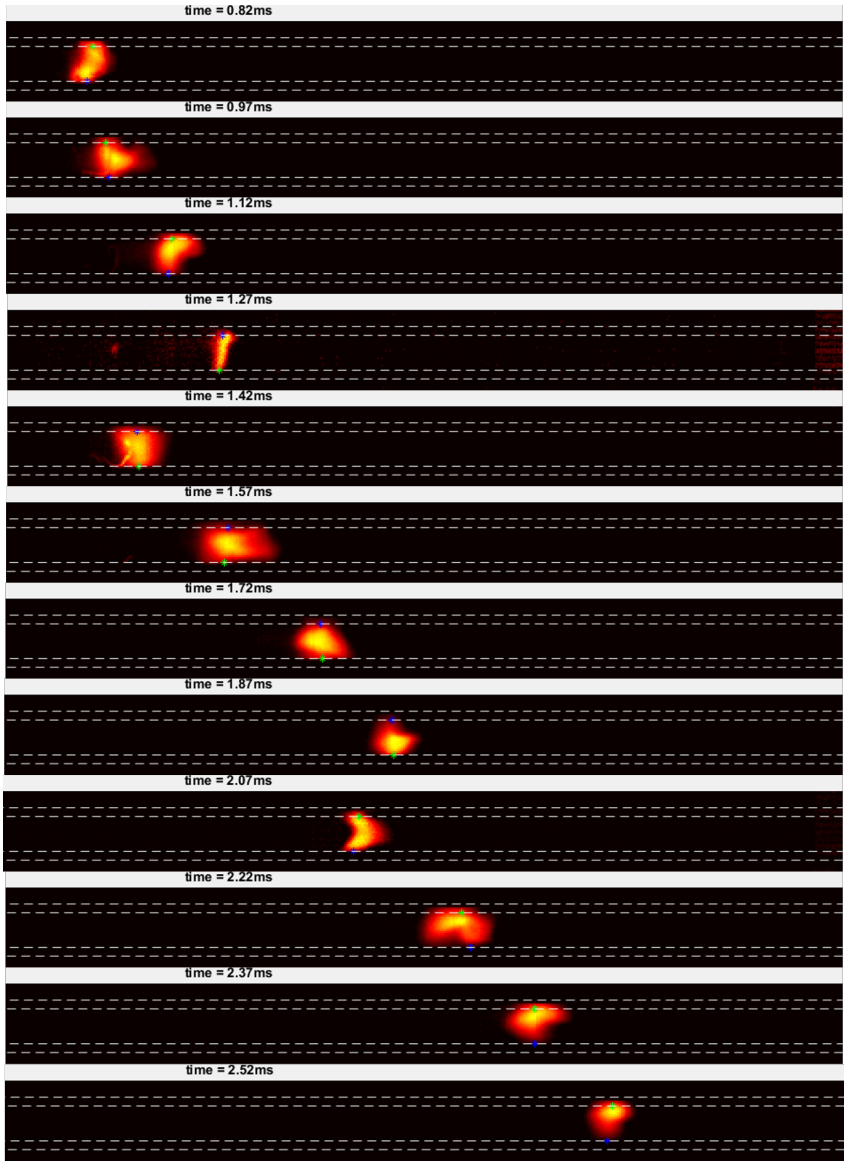

Figure 3.23: Parameter set 4, 115 V at 760 Hz with $h = 8$ mm. Sequence of frames from high-speed video imaging of the propagating arc. On each frame, the blue ($\ast$) denotes the cathode attachment while the green ($\ast$) indicates the anode attachment.

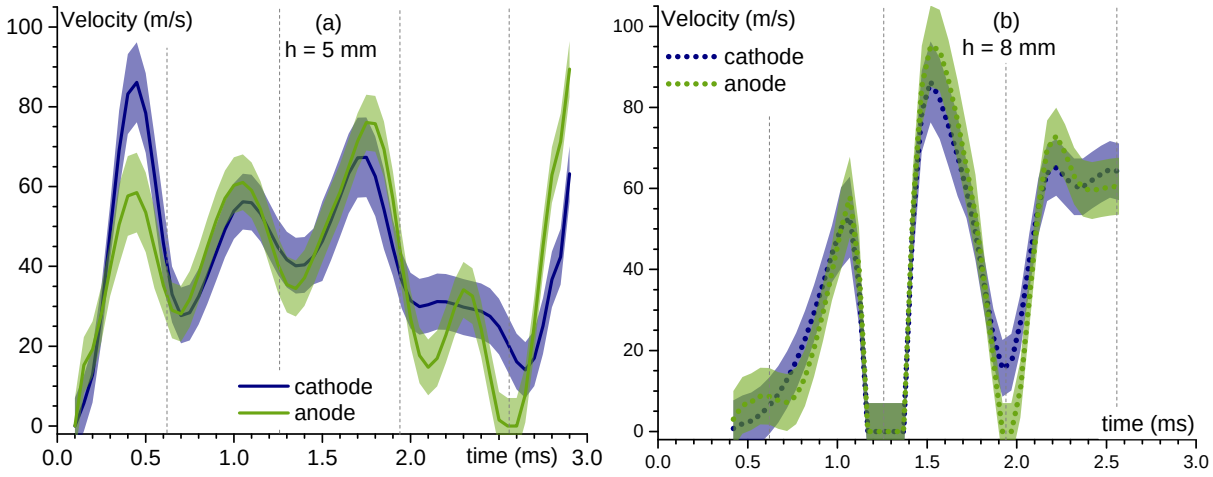

Figure 3.24: Parameter set 4, 115 V at 760 Hz. Temporal evolution of the cathode and anode root velocity for (a) $h = 5$ mm and (b) $h = 8$ mm electrode gaps.

between the arc current frequency and the acceleration and deceleration of the electric arc was found. The most critical time point is when the arc current crosses zero and the arc voltage is high. However, even at the time moment when the arc current is null, the experiments show that the cathode and anode attachments continue to move. This is most likely due to inertia or some hydrodynamic effects of the arc column. More specific investigations are necessary to gain better insight into this reproducible phenomenon.

3.4 Conclusions

The experimental investigations of an electric arc reported in this chapter enable a thorough comparison with the numerical simulation outcomes. For the record, the latter is the essence of the present PhD thesis. The valuable data gathered throughout the experiments are of significant interest to confirm, refine, tune and then validate the mathematical description of the moving arc model. From this point, predictions of the model will also be checked experimentally. Although the experimental data have been reported rather briefly in this chapter, the main features of an electric arc displaced between bus-bars have been evidenced.

The luminance of the arc on the high-speed video images enables the immediate identification of the arc and its geometrical shape. The existence of the cathode and anode attachments in so-called *spot mode*, i.e. the constriction of the arc near the electrodes, were observed for all the excitation regimes. For some conditions, the existence of several simultaneous cathode attachments was observed. Near the cathode and the anode attachment, jets are formed: the cathode and the anode one. Both jets result from the action of the self-induced magnetic field of the arc near the cathode and the anode spots. In the case of several attachments, respectively

several simultaneous jets are formed. These jets –head to tail– form the arc column.
During the propagation of the whole electric arc (the roots together with the column) away from the power source, experimental data show a displacement always in the same direction regardless of the electrode polarity imposed by the AC excitation. The displacement of the whole arc seems homogeneous, i.e. the cathode and the anode attachments move at approximately the same speed as the arc column.
Regarding the experiment performed in the GREMI laboratory (AC pulse current 50 Hz), the shape of the arc clearly resembles two jets head-to-tail forming the arc column. In the conditions at Zodiac (AC current), the presence of the jets is not clear. However, the so-called arc "nose" was observed in most cases. The existence of this phenomenon was identified on both the cathode and the anode side. With an increase in the arc current, this arc shape becomes more pronounced. It can be due to the formation of one jet that is more intense than the other and potentially hits the opposite electrode. The strength of the jet is determined by the size of the cathode or the anode spot radius and is self-induced by the arc magnetic field. Due to imperfections on the electrode surface and the existence of roughness, it is possible to obtain different cathode/anode spot radii even for the same current conditions. This phenomenon is coupled with the material properties of the electrode and requires further detailed investigations.
Concerning the GREMI experimental sets with a pulsed current in the range from 700 A to a maximum of 2 kA, a continuous displacement of the arc and its roots is observed. It is important to stress that no significant "jumps" of the arc are reported. The cathode and anode attachments are displaced with almost the same speed as for the arc column. On the contrary, experiments performed in AC current conditions evidence the existence of "jumping" attachments. A rapid "jump" of one of the roots will induce the elongation of the arc, giving rise to an expected prompt motion of the other root. The elongation of the arc is more prone to develop for shorter inter-electrode gaps (5 mm and 8 mm) while in cases with $h = 20$ mm, arc elongation was rarely observed. Another favorable situation for "jumps" to appear is when there are several simultaneous cathode attachments. In such conditions, the arc roots may tend to "jump" in the direction of newer attachments, i.e. from old to new in the direction of the arc propagation.
The re-striking phenomenon was observed only in cases of AC excitation, when the distance between $h > 5$ mm. The reason for this re-striking depends on the geometry and can be different in this case compared to the conditions in plasma torches. In this case, it was observed that re-striking occurs due to the arc initiation conditions. The sequential mechanism is the following: the arc is initiated with the presence of a FOD between the electrodes. Due to the high energy, the latter melts and evaporates within the first ms leading to the initiation of the arc which starts to displace. However, when the arc current crosses the zero value, the arc voltage experiences an overshoot, leading to another breakdown within a volume of hot gas containing

an unusually high concentration of the electrons and ions resulting from the evaporation of material from the FOD.
Except for the arc voltage overshoot, the recorded voltage waveform remains smooth during the arc displacement. However, it is important to point out that during the transient arc elongation and "jumps", random instabilities are visible on the voltage signal. However, the re-striking phenomenon could not be identified clearly on the voltage waveform, which is a very important point to consider in the conception of an arc detection procedure in aeronautic circuits.
To conclude on the results from the experiments carried out in the GREMI laboratory, these experiments provide fundamental and quantified values of the arc velocity versus the arc current. The relation between the arc velocity and the arc current is well described by a linear dependence for current below 2 kA. This linear correlation is measured for an electrode gap of 20 mm. It will likely be reproducible for shorter gaps, but with a different slope. This hypothesis requires further investigation and, in this work, it will be done numerically. A similar but rather difficult to validate trend is reported concerning the AC arc, as the speed deviation and the different excitation frequencies make the analysis more challenging. However, the main tendency has been identified: with an increase in the arc current, the electric arc accelerates up to its maximum speed correlated in time with the maximum of the arc current. Then a decrease in the arc current induces a slower deceleration which does not reach zero value (in the present work, zero speed is associated with the re-striking phenomenon).
This work provides new insights into the problem of arc propagation along rail electrodes in a wide variation of conditions. Moreover, understanding of the arc behavior helps to establish a numerical model and will support its validation.

Chapter 4

Numerical simulations of electric arc for aeronautical applications

With the continuous growth in computational power, numerical simulations of the different physical processes that take place in any industrial application have become increasingly feasible and worthwhile. Moreover, the availability of commercial software based on finite elements or finite volumes methods helps to solve even complex non-linear problems in a reasonable time. It is therefore highly interesting to investigate numerically the problem of the appearance and propagation of electric arcs in busbar distribution systems. In spite of the relevance of this topic to aircraft safety, there are currently no existing models of electric arcs in aeronautical applications. To the best of the author's knowledge, this research is the first study to offer a comprehensive model of electric arcs between busbar electrodes. The model developed has been validated with the results of the experimental investigations.
In this work, the electric arc is described in terms of a fluid model. The system of MHD equations with the assumption of LTE – which showed good agreement with the experiment in the case of a free burning arc – has been adapted to the requirements of aeronautical applications. The mathematical description of the arc is the same as in chapter 2. Some adjustments have been implemented depending on the task, such as the geometrical configuration, the boundary conditions and the plasma properties which are essential for the busbar model.
The lack of information and hypotheses concerning arc displacement within the magnetic field makes the research more complicated. The numerical simulation results shown in this chapter help to understand the arc displacement mechanisms in addition to the experimental results.

4.1 Arc displacement along the electrodes

The power of magnetic forces named Lorentz forces, where the superposition of the magnetic field and flowing current induces a mechanical force which can move the object, has been known for a long time and is frequently used in various applications. For example, this concept is implemented in the propulsion apparatus called a *rail-gun*. This device is a weapon that uses electro-magnetic forces to launch a missile. The construction is simple: the rail-gun uses a

pair of parallel conductors, or rails, along which a sliding ferromagnetic object is accelerated by the electromagnetic effect. While conventional explosive-powered military guns cannot readily achieve a velocity of more than about 2 km/s, rail-guns can launch a projectile with a velocity exceeding 3 km/s. In order to achieve such high bullet speeds, high energies in the range of 5 MJ to 50 MJ are needed, which is equivalent to a current pulse of 5 MA for a few milliseconds. Schematically, the concept of the rail-gun is presented in figure 4.1. The electric current which

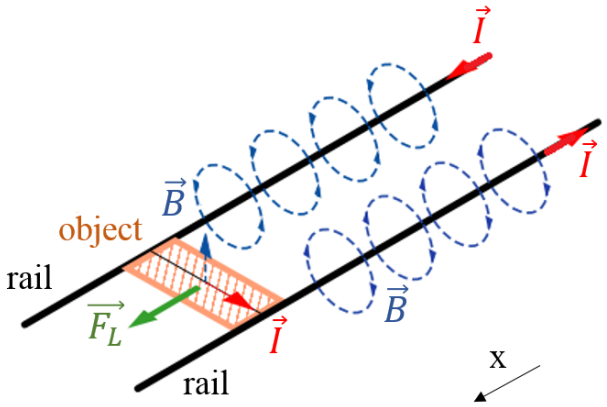

Figure 4.1: Schematic of the electromagnetically driven object system.

flows in the electrodes and armature induces a magnetic field around them. An enhancement of the overall magnetic field on the one side of the armature is generated due to the parallel arrangement of the rail electrodes involving superposition of each element. This magnetic field in the gap between the rail electrodes and the current passing through the object(armature) induces the Lorentz force which acts in the direction shown in figure 4.1. More importantly, a switch in the powered current polarity will not induce any change in the acting direction of the Lorentz force. The object will always move away from the power source. The optimization of rail-guns has been investigated by many researchers worldwide [Marshall 97, Rosenwasser 91, McNab 01]. Estimations of the speed of the projectile for different conditions have been reported in [Siaenen 11, Nosov 13, Nosov G V 13]. Theoretical research has also been carried out to estimate the object speed. Thus, the contribution of each force acting on the object can be decomposed as,

- the Lorentz force, $F_L = L_0 I(t)^2/2$, where L_0 is the effective inductance per unit length, which coincides with the running inductance of electrodes at a negligibly thin current layer. It has been documented in [Nosov 13];
- the aerodynamic force $F_{aer} = -CV^2$ which is due to the resistance of air, C is the drag coefficient and V is the object speed;

- the erosive force $F_{err} = -m_{err}V$, caused by the material of mass m_{err} eroded from the electrodes at the unit of time.

In the ideal case, when the drag forces are negligible, the main impact is the Lorentz force and the armature is continuously accelerated with the time. Then, with known rail-gun parameters ($I(t)$, L_0) and the mass of the armature, the velocity can be determined by integration of the accelerating force $V = \frac{1}{2m}\int L_0 I(t)^2 dt$. A continuous acceleration of the armature has been observed experimentally [Siaenen 11, Hundertmark 13] as well.

4.1.1 State of the art. Numerical models of the arc between rail electrodes

If, instead of the object(armature) between the rails, an electric arc occurs, the drag forces are no longer negligible while the accelerating force acting on the arcs is a Lorentz force. Electric arcs between rail electrodes were investigated in [Bobashev 10a, Bobashev 10b, Bobashev 16]. The experimental conditions used were a current pulse I_{max} in the range of ∼10 kA to 60 kA, achieving an arc displacement velocity up to several km/h. The experiments were conducted in different conditions, using various gases such as argon and helium with different electrode materials (copper and graphite). In such conditions shock waves appear and propagate together with the arc. Therefore, an additional drag force, which results from the pressure difference before and after the shock wave front, acts, $F_{sw} = p_2 A$, where p_2 is the pressure behind the shock wave and A is the channel cross section. The existence of so-called maximum velocity or saturation velocity has been shown and its value estimated. This saturation is achieved due to drag forces, therefore it is very important in the case of electric arc propagation to consider the drag forces.

Models of electric arcs between rail electrodes exist mainly due to its interest in LVCB, where similar phenomena take place. In the simplest models [Meunier 84], the evolution of the main electrical and physical parameters during the current interruption of an electric arc is computed. The arc is represented as a wire, which conducts the current and creates a magnetic field together with the rail electrodes [Meunier 83]. The movement of an arc in a gas is similar to the behavior of a solid bar for the computation of aerodynamic force.

Subsequently, the model was improved and a hydrodynamic description of the electric arc was applied while the arc plasma is assumed to be in LTE. This approach is widely accepted by the electric arc community, although there are several imperfections in such models. The arc column model is well-established for free burning arcs and can be adapted for the rail construction of the electrodes. However, the plasma-electrode interaction results from complex phenomena even for stationary free-burning arcs. In the case of an arc which displaces along the electrodes, the phenomena are different and up to now have not been well described. Another difficulty is the numerical approach for the magnetic field calculation. In order to obtain the exact value

of the Lorentz force, it is highly important to resolve the magnetic field of the arc and the rail electrodes. Necessarily, the large volume of gas around the electrodes must be considered, which can dramatically increase the computation time. A review of hydrodynamic models of electric arcs between rail electrodes is given below. The interest of this research is to understand the arc root displacement along the electrodes including the complete resolution of the magnetic field.

The propagation of an electric arc along the rails was investigated numerically in a 2D configuration and the compressible Navier-Stokes equations with the assumption of local thermodynamic equilibrium were solved for a current of 5 kA at 50 Hz in [Domejean 97, Fiévet 97] and 2.41 kA at 60 Hz in [Rachard 99]. These studies used experimental data of electrical measurements, gas temperature and pressure. The displacement of the arc was discussed in [Rachard 99] who stressed the importance of pressure forces during arc propagation as well as the limitation of the arc velocity along the rails. A significant improvement of the model was made in [Karetta 98] where a 3D hydrodynamic model of the electric arc between rail electrodes was established. The solution showed that the arc moves continuously. Cathode and anode attachments which are displaced with the same velocity as the arc centre were observed. The complications encountered during the description of arc-electrode interaction are pointed out in this work, and a method to introduce the arc root displacement along the electrodes was proposed. In order to establish plasma-electrode interaction, Neumann conditions were applied for the energy conservation, i.e. an energy flux $q = -\lambda \nabla T$ was applied in the direction from the plasma to the electrode. Dirichlet conditions with a specified current density are introduced on the cathode side. The current density was determined according to the total current and the thermal emission was calculated with the Richardson formula and an additional coefficient, which considers the electrical conductivity in the vicinity of the cathode. Calculations were done with a constant current of 1 kA. It was found that the arc root displacement velocity and the velocity of the arc centre were in agreement with the predictions of the model. It was also found that the arc speed reached its maximum of 90 m/s after 0.45 ms, after which its speed decreased due to an increase in the pressure. At the same time, an experiment was performed [Lindmayer 96] to investigate the influence of pressure on the arc propagation. The formation of an overpressure ahead of the arc in its propagation direction was reported. Improvements of the model were presented in [Lindmayer 96]. The effect of ferromagnetic material in the arc chamber was investigated in [Lindmayer 02]. The hydrodynamic model of the arc, its displacement and splitting with the blade were studied and documented in [Lindmayer 06].

Several studies adopted a similar mathematical description of the electric arc in LVCB [Yi 05, Rong 08, Rong 05, Rong 10]. The system of MHD equations – while the plasma is assumed to be in LTE – was used to simulate the arc column. For the computation of the magnetic field, the Maxwell equations for vector potential were solved in the whole calculation domain. The

detailed description of plasma-electrode interaction and the corresponding boundary conditions are not specified in these studies, but are assumed to be similar to the conditions on the anode and the cathode side used in [Lindmayer 96]. The same model was used further, but a mobile contact was implemented as in CB [Wu 06, Wu 08a, Wu 07]. The contact separation and the arc rise were studied using the numerical model. Additionally, the influence of chamber wall ablation on the arc displacement was investigated in several studies [Ma 09].

The method of arc displacement along the electrodes developed in [Swierczynski 04] differs from other approaches. Here, two roots were defined: the cathode and the anode attachment. The position of each was defined by minimization of the electric potential in the vicinity of each electrode. For the energy conservation equation, the temperature of the cathode and anode attachments was fixed at 3500 K. Calculations were performed with a constant arc current of 100 A. The anode and cathode attachment speeds ranged from 10 m/s to 20 m/s. "Jumps" of the roots were clearly identified, i.e. the roots did not displace continuously along the electrodes. Recently, the same approach for different conditions compared to experimental results was published in [Quéméneur 16]. The model showed sufficiently good agreement.

Commercial software based on finite volume methods is commonly used for such simulations. However, there is considerable uncertainty and debate about the computation of the magnetic field [Freton 11]. In the usual formalism, the Maxwell equations cannot be resolved with finite volume methods which may lead to calculation errors. Additionally, issues concerning magnetic field calculations may arise due to the big computational volume, which includes the calculation of long electrodes and their surroundings. Different approaches for the resolution of the magnetic field are used. Resorting to the Biot-Savart law [Baudoin 05] enables the magnetic field in the arc and around the rails to be calculated at a lower numerical cost than the resolution of the vector potential in the whole calculation domain, which requires including more gas around the long electrodes. Such an approach can therefore reduce the computation time. The approach based on the calculation of the magnetic field according to the Biot-Savart law in every point between the rail electrodes was reported in [Swierczynski 04] and lately successfully applied in [Quéméneur 15, Quéméneur 16]. A successful magnetic field computation using an adaptation of the Maxwell equations to resolve them with a finite volume method was precisely described in [Rondot 09a, Rondot 09b].

Current models of electric arcs displacing between rail electrodes in LVCB are capable of predicting realistic results. However, comparison with experimental data is necessary in order to validate these models.

4.2 Adaptation of the model of a free-burning arc

The literature overview on numerical simulations of arc propagation along rail electrodes shows reasonable calculation results, which are similar to the experimental observations. Therefore, it is highly interesting to apply a hydrodynamic model to describe these phenomena and resolve them numerically. Previously (chapter 2) a successful application of an MHD description for free burning arcs was described, which showed good agreement with existing work and experimental results. It therefore seemed worth adapting this model to the resolution of the problem of an arc between bus bar electrodes. Unfortunately, for various reasons, the model cannot be used in its complete form developed for a free burning arc. These reasons are as follows:

- The geometrical configuration of the arc and the electrodes needs to be extended to a 3D model. While the system of equations 2.29 - 2.35 can be applied, using the commercial software COMSOL Multiphysics®, the number of boundary conditions also needs to be extended. Specific attention must be paid to the correct resolution of the magnetic field.

- The use of metals with a low melting point such as copper or aluminium as the electrode material. The model of a free burning arc was developed under the assumption of a refractory cathode and the theory of [Benilov 95a, Benilov 02b] is valid in this case. For materials with a low melting point this theory needs to be adapted to take into account melting, evaporation of the electrode material and other processes. This is obviously not a simple task. Moreover, the processes taking place on the cathode while the arc moves along its surface can be dramatically different and the thermo-field emission is not sufficient in high currents. Therefore, the description of plasma-cathode interaction given in the original model needs to be modified.

- The model of a free-burning arc was resolved in argon at atmospheric pressure. In aeronautical conditions, however, electric arcs occur in air with atmospheric to low (0.1 bar) pressure conditions. Therefore, the gas properties need to be considered.

- Constant current conditions were used in the model of a free-burning arc. The generator of the aircraft power distribution systems (busbars) delivers AC 115 VAC and 230 VAC at frequencies ranging from 360 Hz to 900 Hz depending on the system. Hence, AC conditions must be considered in the model.

- Arc displacement mechanisms, especially near the electrodes.

Each of these problems has been solved in the present research, and their implementation is described below.

4.2.1 Geometrical adaptation of the model

The first priority issue to resolve is to consider the proper geometry which corresponds to the requirements of an aeronautical distribution system and the experiments carried out in GREMI laboratory. Slightly different geometrical configurations of the electrodes were taken into consideration. The one applied for the experiment in GREMI laboratory is shown in figure 4.2. The electrodes with a rounded cross section diameter of $d = 6\,\text{mm}$ and $200\,\text{mm}$

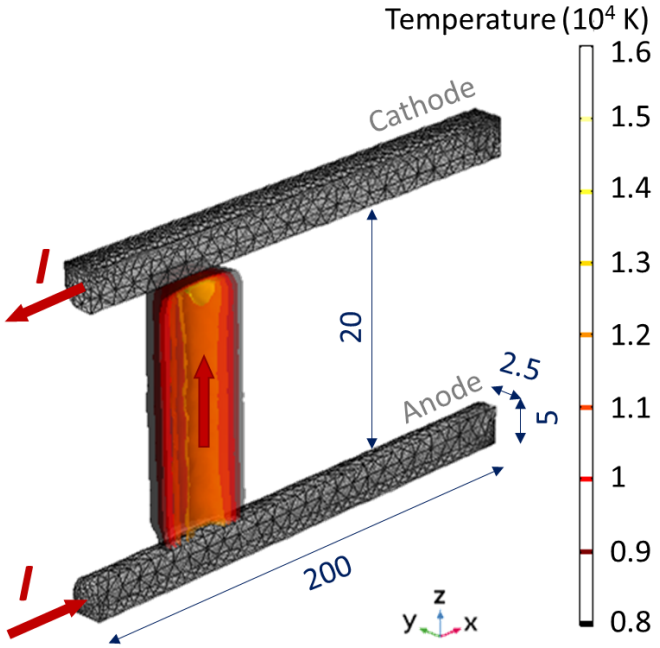

Figure 4.2: Schematic of the rail electrode assembly used for the experiment in GREMI laboratory.

long are placed side by side with a gap of $h = 20\,\text{mm}$. The inductance per unit of length can be estimated from $L_0 = \frac{\mu_0}{2\pi}\left(\ln\frac{2h}{d} - \frac{1}{4}\right) = 0.37\,\mu\text{H/m}$. The electrodes are surrounded with air at atmospheric pressure. In figure 4.2 the current flow direction is indicated: during the experiment only one current pulse is applied, therefore the cathode and anode are well identified. While this is a simplified case in comparison with the context of aircraft, it nevertheless makes it possible to tune the model and to compare its outcome with the experimental observations. Additionally, the initial temperature distribution is defined: initially a hot conductive channel is imposed between the electrodes in order to start the calculation. This initially hot channel is needed to provide initial conductance between the electrodes. In this respect, it is very similar to the experiments with FOD, which were also initially imposed between the electrodes.
The system of bus-bars applied for aeronautical conditions is similar to the one previously

reported. The cross section is rectangular 3 mm × 8 mm with a length of 20 mm. The electrode gap is 5 mm or 8 mm.

4.2.2 Magnetic field, eddy currents

The complexity of the magnetic field calculation has already been mentioned. This is particularly true for geometries where a large computational domain is required in order to resolve the magnetic field around the electrodes.

Previously, in chapter 2, it was specified that in this work the calculation of the magnetic field is based on the resolution of the vector potential $\mathbf{A}$. The latter is defined as $\nabla \times \mathbf{B} = \mu_0 \mathbf{j}$ and $\nabla \times \mathbf{A} = \mathbf{B}$. The solution must be valid for the whole calculation domain, i.e. in the rail electrodes and the gas/plasma around them. The volume of the gas (calculation domain) should be large enough to avoid edge effects. In order to confirm the precision of the numerical solution, the magnetic field induced by the rail electrodes with a constant current of 200 A was compared with the values obtained analytically. The magnetic field in the gap between the electrodes with a round cross section can be defined analytically as a superposition of the fields from the two conductors with a radius of $d/2$ as $B_y = \frac{\mu_0 I}{2\pi}\left(\frac{1}{z+d/2} + \frac{1}{h-(z+d/2)}\right)$. The comparison was done for the y-component of the magnetic field B in the gap between the rail electrodes, when the magnetic field of the arc is not considered. One can see in figure 4.3 that the analytically estimated value $B_{analytic}$ and the computed value using COMSOL Multiphysics®, B_{COMSOL}, are in good agreement. In this work, in the formulation of the Maxwell equations,

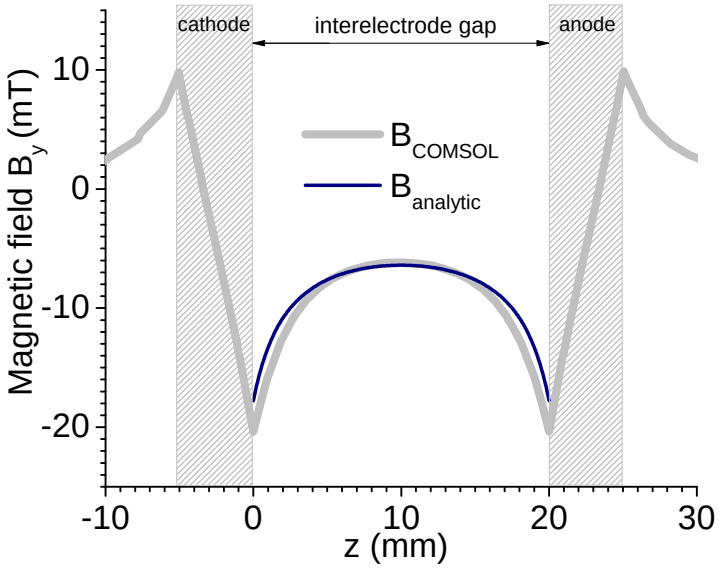

Figure 4.3: y-component of the magnetic field **B** normal to the longitudinal dimension of the electrodes.

eddy currents currents are not taken into account.

4.2.3 Plasma-electrode interaction

The description of plasma-electrode interaction becomes more complicated due to the use of electrodes with a low melting point such as copper or aluminium. The non-equilibrium processes included near the electrodes were already described in chapter 2. Here, melting and evaporation of the electrode material become important and influence the arc-electrode attachment. It is expected that these processes take place mainly in non-equilibrium conditions at the cathode and the anode layers. However, in this work the non-equilibrium effects in the layer are taken into account via current and energy transfer and the hydrodynamic model is realized only for a LTE arc column. At the same time, the arc column displacement needs to be determined; therefore, conditions on the electrodes are important. The description of the LTE arc column with each electrode is given below.

The conditions on the anode side

The description between the LTE arc column and anode established in chapter 2 can be adopted in this work. Numerically, the condition presented in 2.48 easier to apply in commercial software and was therefore used to calculate the arc between busbars. The current continuity between the LTE arc column and the anode was also verified.

The conditions on the cathode side

The description reported in chapter 2 for the LTE arc column matching with the cathode was developed for refractory material. This means that the ion current to the cathode depends only on the gas properties. The discharge current is mainly defined by thermo-ionic field emission. In the case of electrode material with significant evaporation, the ion current is high. As the ionization potential of copper and aluminium is quite low and comparable to the gas ionization potential, the ion current will be higher. This estimation requires additional knowledge and is beyond the scope of the present research.
Therefore, as the first step in the description of the LTE column and cathode, a simplified version of the matching conditions was adopted. It was observed that during the arc propagation along the electrodes, the attachment on the cathode is constricted, i.e. a cathode spot is observed. The size of the cathode attachment was defined with the arc current and using some conditions calculated in [Bade 63]. Therefore, in the model, the existence of a cathode spot is assumed, i.e. a conductive region on the cathode surface with a fixed radius. An estimation of the cathode spot radius for some materials was reported in [Bade 63, Benilov 95a], but for refractory cathodes. For the present simulations, the attachment spot radius used ranged from 1 mm to 3 mm for a wide current range from 0.2 kA to 2 kA. The temperature inside this cathode spot is assumed to be equal to the melting temperature $T_{m_{Cu}} = 1085^oC$ and $T_{m_{Al}} = 660^oC$. Obviously,

such conditions will create high temperature gradients near the cathode. This induces a gradient of plasma parameters as well which is crucial for the electrical conductivity of the plasma that is close to zero for plasma temperatures below 6000 K (figure 4.4). In such a form, current

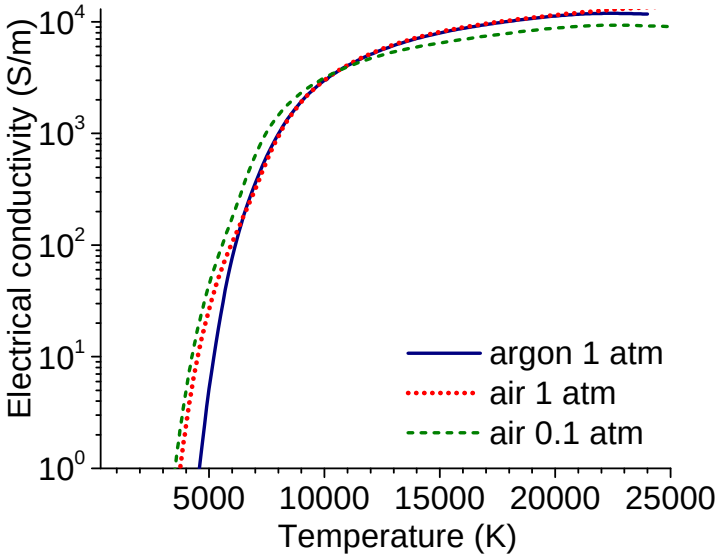

Figure 4.4: Electrical conductivity of LTE plasmas as a function of the temperature.

continuity between the cathode and the LTE column is not fulfilled. In order to establish current continuity in this region, where the temperature gradient takes place, the electrical conductivity was reasonably increased. The electrical conductivity increases significantly from 6000 K to 10 000 K and then remains nearly constant as shown in figure 4.4). Therefore, it is assumed that in the region near the cathode spot, the minimum electrical conductivity of the plasma is bounded at an equivalent value of 10 000 K. This is a necessary criterion in order to ensure both current continuity and numerical stability.

4.2.4 Arc displacement

Arc displacement along the electrodes is one of the most interesting aspects, but also an ambiguous phenomenon. The velocity of the arc is one of the parameters which can be defined from experiments using high-speed video-imaging.

The system of hydrodynamic equations is applied in the volume between the electrodes, where the arc is established. The Lorentz force, viscose forces and pressure gradient are taken into account in the Navier-Stokes equation. The arc column motion within the gap should be predicted according to the equation introduced in the model. The anode attachment is formed due to the conditions for energy and current conservation. Due to the conditions imposed on the cathode side, the position of the cathode spot needs to be defined manually. Therefore, in order to displace the cathode attachment, additional conditions need to be implemented. Two

methods to define the cathode spot position during the arc displacement were developed:
In the first method the approach similar to the one calculated in the arc column was used, i.e. the application of the momentum conservation equation with respect to all the forces acting on the near-cathode LTE plasma. The detailed description is given below.
In the second method, qualitative inputs from experiments were used based on the observations of the arc displacement. Indeed, in the conditions investigated here, the cathode and anode attachments were found to have the same propagation velocity. It can therefore be assumed that the two electrode attachments together with the arc column can be defined self-consistently. Both approaches defining the cathode attachment velocity and its position were implemented numerically together with a hydrodynamic model of the arc. A comparison of the results obtained with each method is reported below.

The conditions for the cathode attachment displacement in the first method

Since the processes take place on the cathode surface and in the non-equilibrium layer which are not described in this model, here the displacement of the cathode spot means the position of the LTE column with respect to the electrode. Therefore, the approach similar to the one calculated in the arc column can be used, i.e. application of the momentum conservation equation with respect to all the forces acting on the near-cathode plasma. Consequently, a slice of 1 mm thickness was defined in the vicinity of the cathode in order to find the average values of the plasma mass and the resulting forces acting on it. The average values of the forces acting on the arc with the mass $m_{arc} = \iiint_V \rho(x,y,z)dV$ were defined with,

- the Lorentz force:

$$F_L = \iiint_V j_y(x,y,z)B_z(x,y,z) - j_z(x,y,z)B_y(x,y,z)dV, \tag{4.1}$$

- the pressure force:

$$F_p = \iiint_V -\frac{\partial p(x,y,z)}{\partial x}dV. \tag{4.2}$$

It is assumed that the cathode attachment moves only along the x-axis (figure 4.2). The velocity of the attachment was defined according to:

$$m_{arc}\frac{dv}{dt} = F_p + F_L + Cv^2. \tag{4.3}$$

Viscous force was introduced in equation 4.3 as a typical aerodynamic drag force, which is proportional to the square of the velocity and with the coefficient C to be defined. For the arc displacement in air, this coefficient was estimated as $C = 0.85 \times 10^{-5}\,\mathrm{kg/m}$.

4.2.5 Powering of the busbar system

As the model was developed without the whole distribution system, the effects which may be induced by the external circuit were not taken into account. The current conditions were applied on the cathode and the anode was assumed to be at ground potential. Several sets of calculations are presented in this work:

- The calculation of the arc displacement with the assumption of a constant value of the current (DC). This calculation was done in order to adjust the mode and to optimize some numerical features such as the size of the calculation domain, the element size, the discretization and the stabilization methods and to estimate a reasonable computation time.
- The current pulse with a duration of 5 ms and an maximum current value ranging from 0.7 kA to 2 kA.
- Alternating current voltage (AC) which corresponds to realistic aircraft electrical systems of 115V and 230 V operating at 420 Hz and 760 Hz.

In this chapter, the simulation results are presented in order with respect to the latter conditions.

4.2.6 Calculation domain. Boundary conditions

It can be assumed that the arc propagates only in the longitudinal direction along the electrodes. Therefore, plane symmetry with respect to the XZ–plane can be assumed for all variables, except the magnetic field calculation, where the conditions $\mathbf{n} \times \mathbf{B} = 0$. This assumption is the most beneficial for the computation of the numerical solution since only half of the model is resolved, which reduces the number of finite elements and consequently the calculation time.
The calculation domain for the geometry of the experiments conducted in GREMI laboratory is illustrated in figure 4.5. The pair of electrodes 200 mm long is located in a gas volume of $30 \times 60 \times 210$ mm. To perform simulations with longer electrodes, the volume of the computational domain requires an extension in the X–axis only. The electrodes have a 5.0 mm square cross section and the inter-electrode gap is 20 mm. The edges of the electrodes are rounded as in the experimental setup.
In the busbar configuration the size of the calculation domain is $30 \times 40 \times 160$, and the size of each electrode is 3.0 mm $\times$ 8.0 mm $\times$ 15 mm. Different values of the inter-electrode gap were considered for these experiments. In spite of the slightly different geometrical configurations of the electrodes, the boundary conditions in the calculation domain were the same and are listed below:

- The plane DCHK is the plane of symmetry: symmetry conditions are applied.

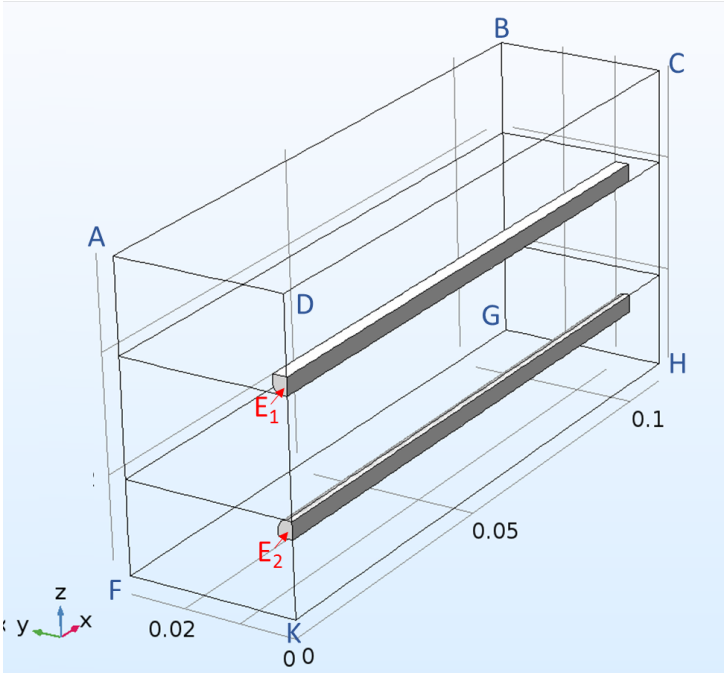

Figure 4.5: Electrical conductivity of LTE plasmas as a function of the temperature.

- On the boundary ABCD, a small inflow with a speed of 0.1 m/s is imposed. The internal temperature is set at 300 K.

- The temperature is initially set at 300 K on the boundaries ADKF, BCHG, ABGF and normal stress is set at zero, i.e. the gas can enter or exit the calculation domain.

- The temperature on the boundaries ADKF, BCHG, ABGF is 300 K and outlet conditions are imposed.

- The electrical $\mathbf{n} \cdot \mathbf{j} = 0$ and magnetic $\mathbf{n} \times \mathbf{A} = 0$ insulations are imposed on all the external boundaries of the calculation domain.

The boundary conditions applied at the interfaces between the LTE column and the electrodes are discussed above. A no-slip condition is applied on the electrode surface. The temperature at the outer electrode boundaries is set at 300 K.
At each boundary, labeled E_1 and E_2 in figure 4.5, a Dirichlet or Neumann condition is applied alternately, depending on the polarity of the power system. In the case of a cathode electrode, the current density is applied with respect to the total current. For the anode, the condition of zero electric potential is valid.

4.2.7 Numerical aspects

The numerical realization of the model was done using commercial software namely COMSOL Multiphysics®. The advantage of this software is the flexibility with which the model of the LTE arc column, the electrodes and their interactions can be implemented. It is also more convenient to apply simple changes to the electrode geometry. No additional subroutine was implemented.
The model of the LTE arc column, described in chapter 2 was adopted for the arc between busbars, although several modifications were necessary:

- the model was extended to 3D,
- the geometry of the computational domain corresponds to the experimental conditions,
- the electric arc occurs in air with 1 atm between copper or aluminium electrodes.

The mesh was specified depending on the position within the computational volume. Near the electrodes, the size of the mesh ranged from 100 µm to 500 µm, while within the electrode gap, the mesh was set at 1 mm. For the volume of gas around the electrodes, a coarse mesh with a size of 2 mm was used. An element size of 0.1 mm was imposed near the electrodes. For the discretization of the finite elements, linear basic functions were chosen.
The model was resolved using a segregated solver. Segregation was done according to the physical quantities, i.e.

- the electric potential, ϕ,
- the vector potential, $\mathbf{A}$,
- the gas pressure, p,
- the gas velocity, V,
- the plasma temperature, T,
- the cathode root displacement velocity, v_{arc}, according to equation 4.3.

Each segregated step was solved using a direct method of matrix resolution; in this problem the MUMPs method was used. Convergence towards the solution was achieved when a relative tolerance smaller than 0.001 was reached.

4.3 Results – DC current. General analysis

In this section the results of the simulations are reported first in constant current conditions (DC) with an amplitude of 200 A. This numerical experiment makes it possible to visualize the main effect of the magnetic field induced by the rail electrodes and to compare the two methods used to displace the cathode attachment. After the clarification of these primary difficulties, the model was modified to obtain results in the same conditions as in the experimental investigation.

4.3.1 Impact of the magnetic field from the rail electrodes

The electric arc powered with a constant current of 200 A and an electrode gap of 20 mm at atmospheric pressure in air was used in order to assess the strength of the magnetic field induced by the electrodes. For these simulations, the cathode attachment with $r = 1.5$ mm was fixed at one point, while no additional conditions or restriction were applied on the anode. The action of the magnetic field on the plasma can be observed on the time evolution of the temperature distribution in the arc column. The isolines of the plasma temperature are presented in figure 4.6. One can distinguish the *cathode jet* where the maximum temperature near the

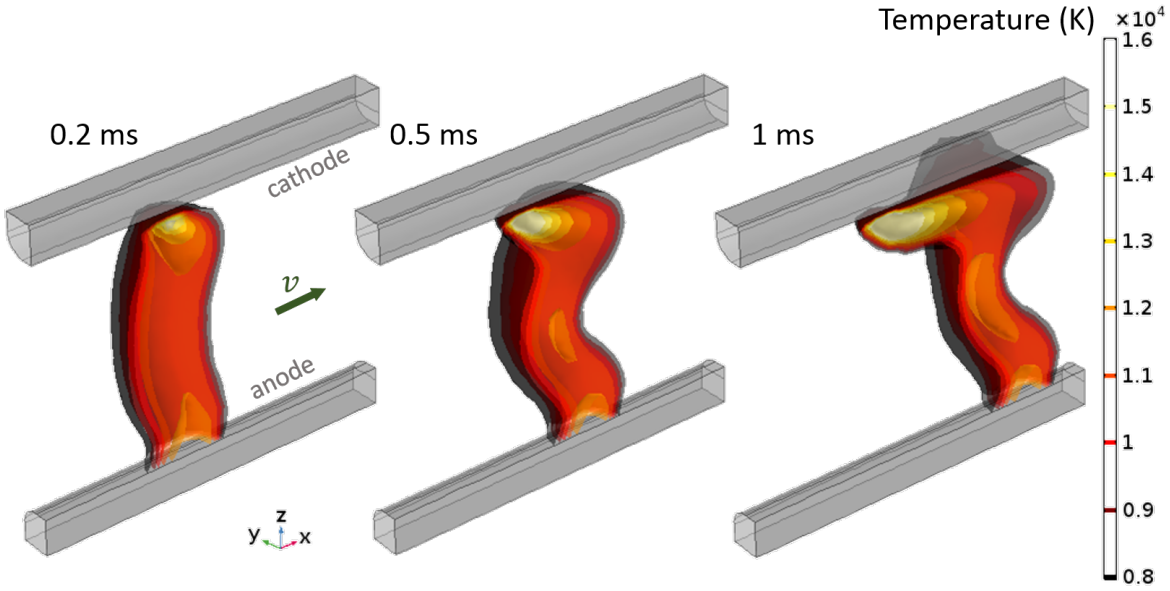

Figure 4.6: Time evolution of the temperature distribution in the arc column with DC current $I = 200$ A at 1 atm.

cathode is reached. On the opposite side of the column, the *anode jet* is identified with a local maximum of plasma temperature near the anode. Near the anode, self organized attachment is formed due to the boundary conditions adopted from chapter 2. No additional numerical re-

striction was used. The arc column and the anode attachment are displaced in the longitudinal direction under the action of the Lorentz force. This fact is noticeable in figure 4.6. After 1 ms the arc column is "blown" away from its initial position. The temperature distribution at the mid-plane longitudinal cut ($z = 10\,\text{mm}$) and near the anode longitudinal cut ($z = 19.5\,\text{mm}$) is illustrated in figure 4.7. The maximum temperature, which corresponds to the maximum

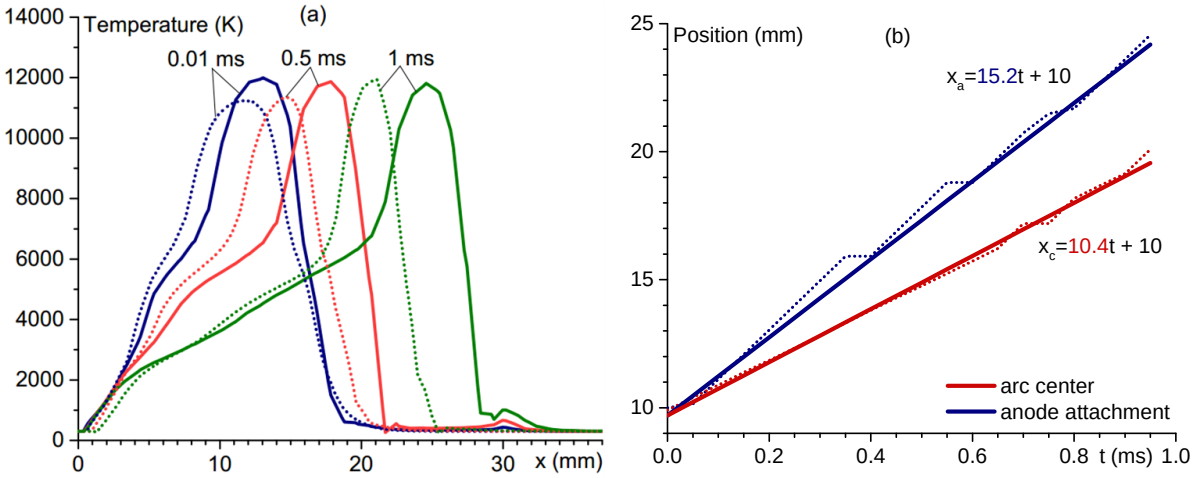

Figure 4.7: (a) Time evolution of the temperature distribution along the mid-plane longitudinal (dashed line) and near the anode (solid line) cuts. (b) Position of the temperature maximum in the mid-plane ($z = 10\,\text{mm}$) and near the anode ($z = 19.5\,\text{mm}$) with interpolation lines. DC current $I = 200\,\text{A}$ at 1 atm.

electrical conductivity, is displaced toward the longitudinal x-direction. The displacement of the temperature maximum for the arc mid-plane cut and near the anode is presented in figure 4.7 (b). The displacement of the maximum is continuous and well interpolated with a linear function in both cases. The displacement velocity of the arc center and the anode attachment were found to be 10.4 m/s and 15.2 m/s respectively.

These experiments with a fixed position of the cathode attachment allow one to see the formation and the displacement of the anode attachment and the arc column motion and deformation taking place in the cathode vicinity. The arc column displaces continuously with an almost constant velocity of ≈10 m/s to 15 m/s.

4.3.2 Displacement of the electric arc – Main features

The typical behavior of the arc column displacement between rail electrodes is described and discussed below. The time dependent solution of the model was obtained for the condition involving a constant current of 200 A with an electrode gap of 20 mm. The time evolution of the temperature distribution in the arc column according to its position between the electrodes is documented in figure 4.8. The cathode and the anode attachments form two head-to-tail jets

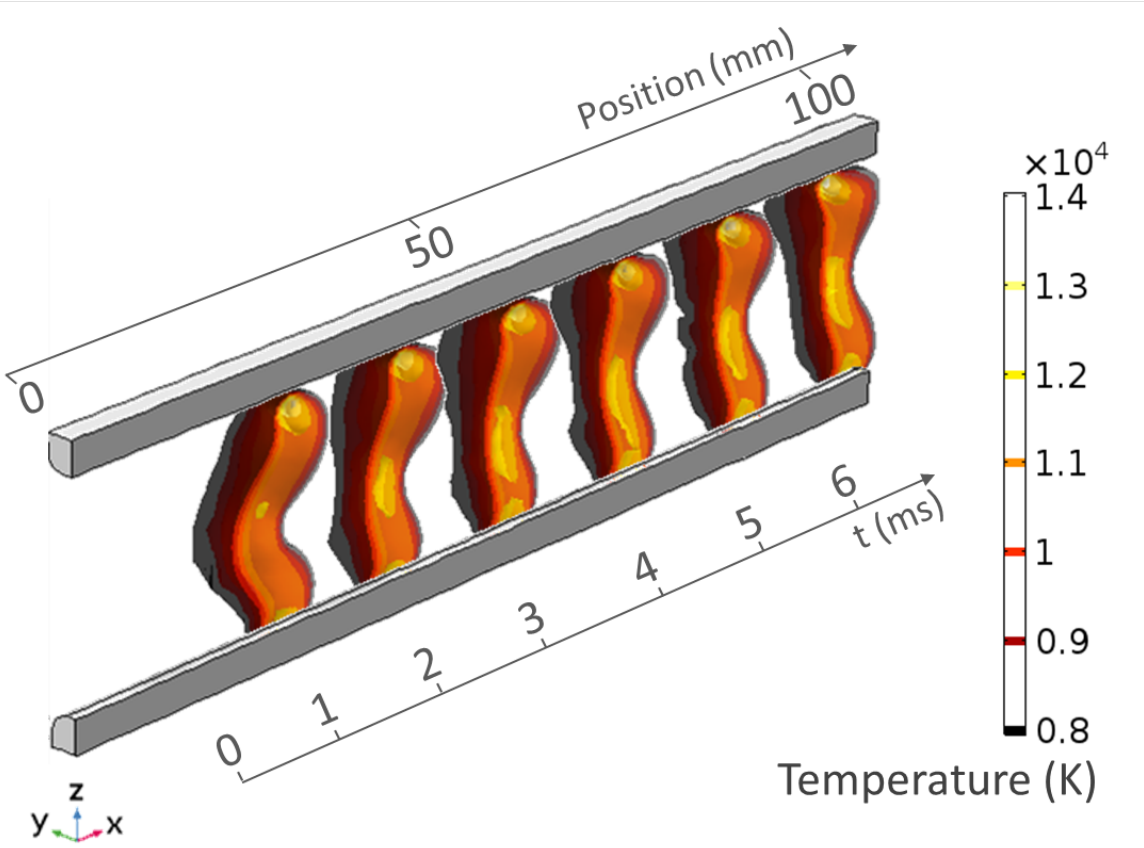

Figure 4.8: Plasma temperature isolines in the arc column at different time steps for DC current $I = 200\,\mathrm{A}$ at $1\,\mathrm{atm}$.

and move in the same direction. The maximum plasma temperature was always observed in the vicinity of the cathode while a slightly lower plasma temperature was found near the anode. The time evolution of the temperature distribution at midplane cut is presented in figure 4.9 where it can be seen that the maximum arc temperature is around 13 000 K and is displaced along the electrodes with the velocity. While the arc column moves, the gas temperature behind

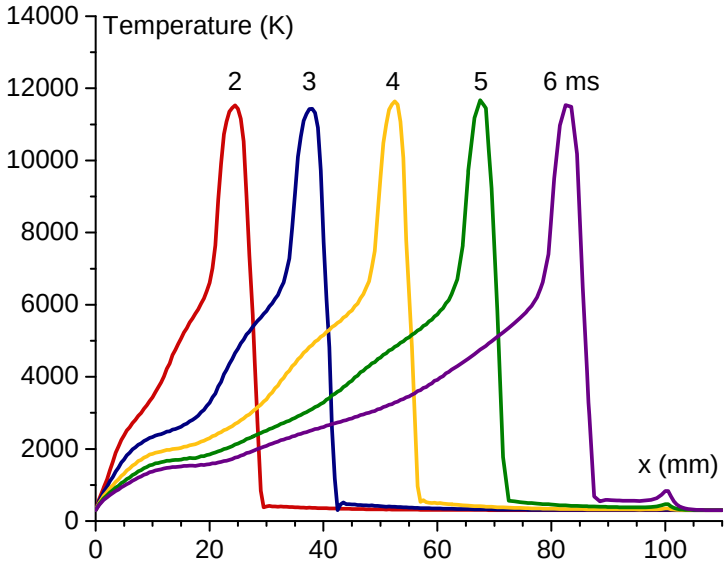

Figure 4.9: Arc column temperature at mid-plane longitudinal cut ($z = 10\,\text{mm}$). DC current $I = 200\,\text{A}$ at 1 atm.

remains rather high and cools down just due to mainly thermal conduction mechanisms. The magnitude of the velocity of the gas in the arc column does not exceed 100 m/s (figure 4.10), therefore the assumption of a laminar flow is valid. Hence, the compressible effects of the gas can be safely disregarded.

The distribution of the Lorentz and pressure $-\frac{dp}{dx}$ forces along the mid-plane longitudinal cut is presented in figure 4.11 (a). In fact, the contribution of the Lorentz force is higher than that of the pressure forces. However, it was observed that the arc achieves a constant speed from which it can be inferred that the drag force is in the same order of magnitude as the Lorentz one.

4.3.3 Comparison of the two methods describing the cathode attachment displacement

Since the anode attachment moves by the action of the Lorentz force without additional conditions, the conditions imposed on the cathode require defining the size of the cathode spot and also its position. In subsection 4.2.4 on page 136, two methods to approach the cathode attachment displacement were proposed. The first method, which is based on momentum con-

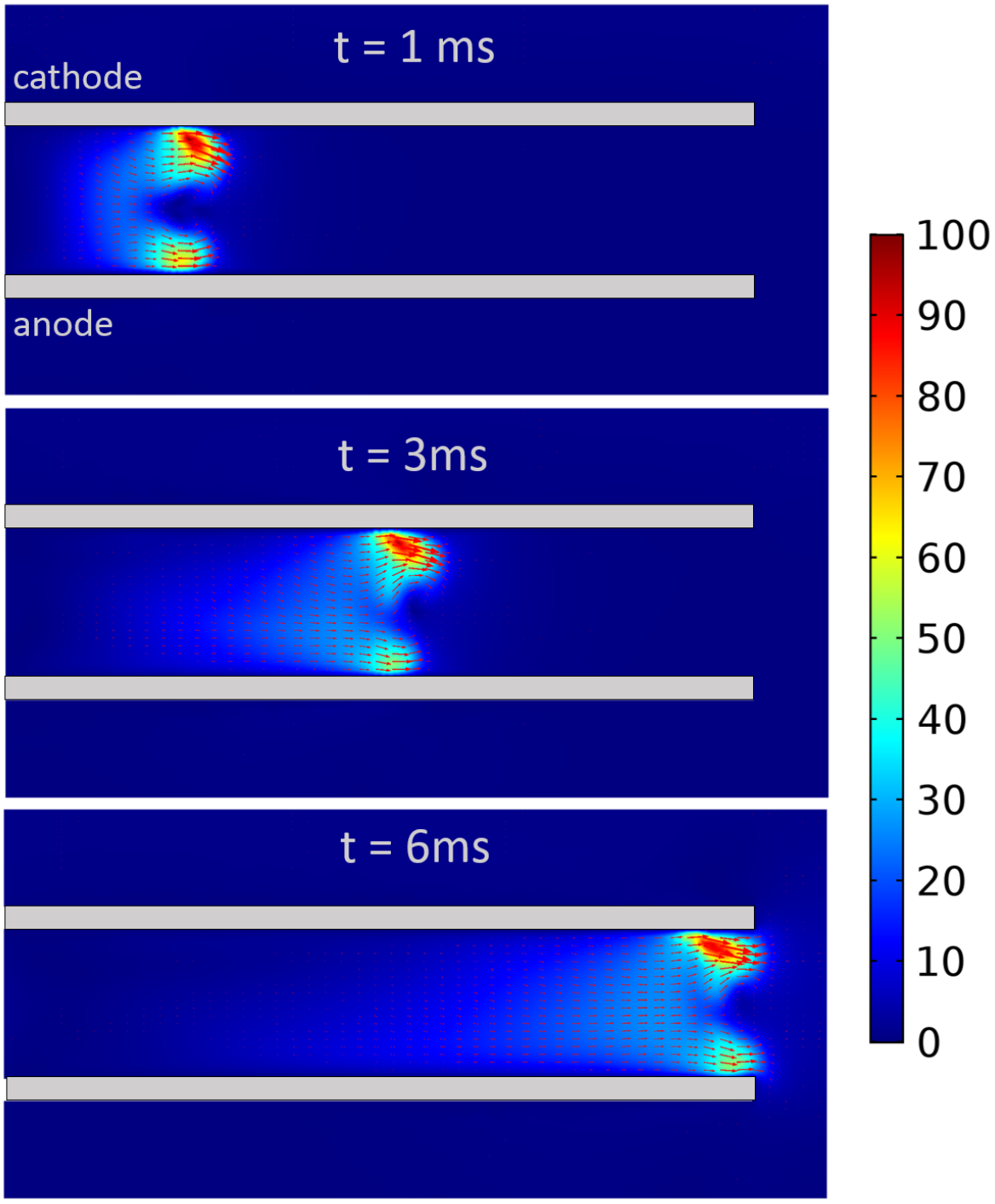

Figure 4.10: Time evolution of the velocity (in m/s) magnitude and velocity vector field. DC current $I = 200\,\mathrm{A}$ at $1\,\mathrm{atm}$.

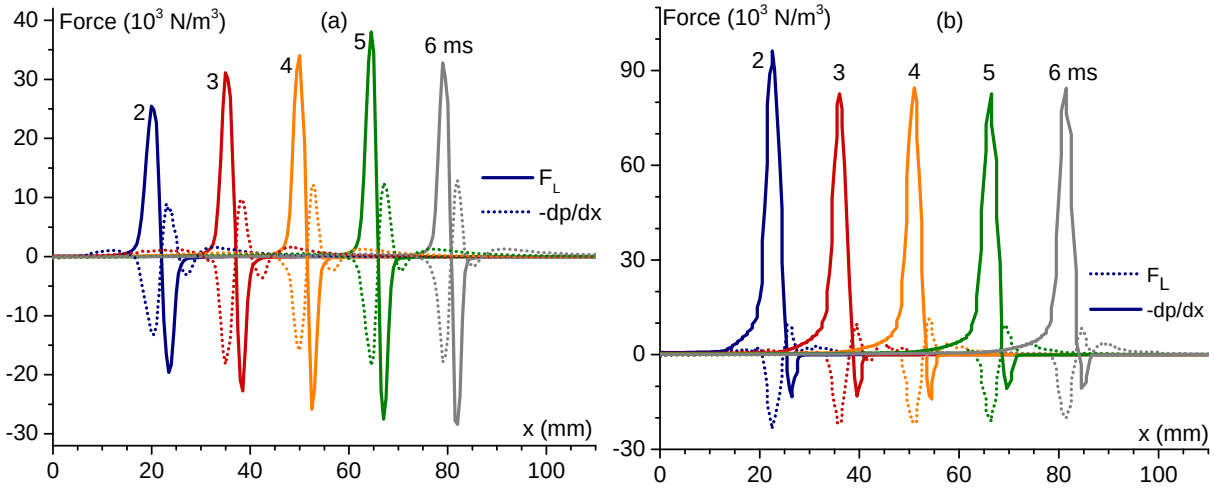

Figure 4.11: Forces (per unit of volume) acting on the plasma at (a) mid-plane longitudinal cut ($z = 10\,\text{mm}$); (b) near the anode. DC current $I = 200\,\text{A}$ at $1\,\text{atm}$. ($z = 19.5\,\text{mm}$)

servation in the near-cathode plasma, requires knowledge of the drag coefficient, which can be estimated or taken from the experimental work. The advantage of the second method is that it provides a self-consistent solution of the model. To compare the two methods, the same geometry and power parameters were used as in the previous example. The position of the cathode attachment and the anode attachment together with the position of the center of the arc were investigated according to the temperature maximum on the cathode surface, the anode surface and the mid-plane ($z = 10\,\text{mm}$). The analysis of the two methods is reported in figure 4.12. These graphs show that the velocity of the arc and of both attachments is constant around $14.5\,\text{m/s}$. Consequently, both methods lead to rather consistent results with regard to the arc propagation behavior. A reasonable explanation for this result concerns the aerodynamic drag force proportional to $\sim v^2$ which acts as the main force against the Lorentz force. The arc column voltage drop computed with the two approaches is shown in figure 4.13. The local minimum of the voltage drop occurs $0.7\,\text{ms}$ after arc ignition due to the initial temperature distribution imposed between the electrodes. Afterward, the initial temperature distribution no longer has any effect on the arc ($t > 1\,\text{ms}$). The arc voltage decreases slightly with time in the case of the first method. This is a consequence of the drag force on the cathode root which causes elongation of the arc. With the second method, the column voltage has a constant value around $30\,\text{V}$ during the arc displacement. However, within a precision of a few volts, both methods show reasonable results and can be reliably applied. In conclusion, from now on and for further simulations, the second approach was used to describe arc column displacement.

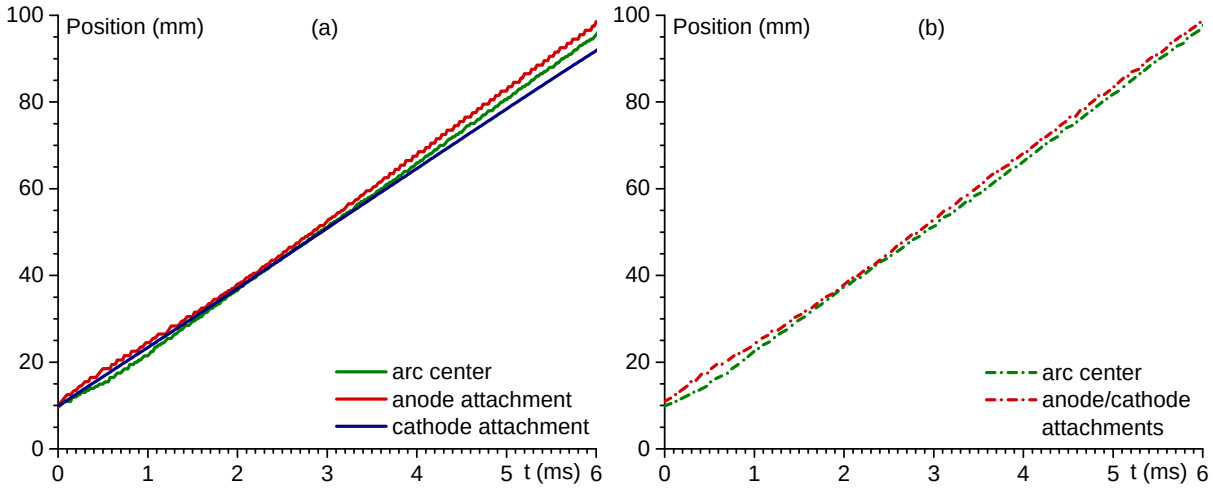

Figure 4.12: Time evolution of the position of the cathode attachment, the arc center and the anode attachments. (a) Method 1, (b) Method 2 as previously introduced in subsection 4.2.4 (page 136). DC current $I = 200\,\mathrm{A}$ at $1\,\mathrm{atm}$.

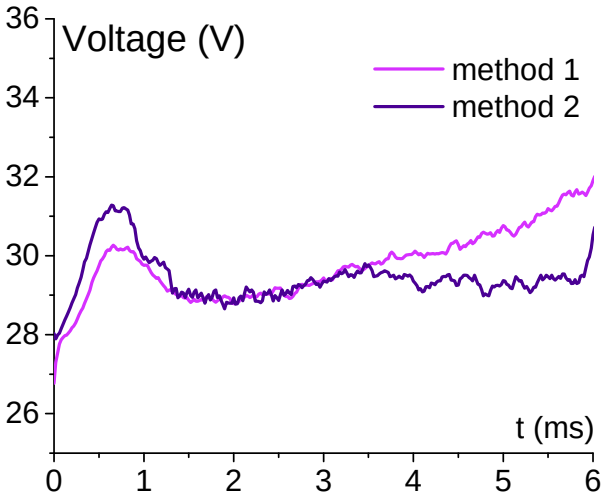

Figure 4.13: Time evolution of the temperature distribution in the arc column. DC current $I = 200\,\mathrm{A}$ at $1\,\mathrm{atm}$.

4.4 Pulsed arc – Simulations related to experiments from GREMI laboratory

Experiments were carried out in GREMI laboratory and are described in Chapter 3. Unlike the experimental protocol, where the electric arc is initiated after opening a mobile contact, in the model, the electric arc is initiated by the initial conditions of the arc temperature, i.e., by artificially enhancing the electrical conductivity locally in the electrode gap in order to provide initial conductivity between the electrodes and establish the arc column. The arc model was applied to the electrode geometry depicted in figure 4.2 on page 133. The cathode attachment displacement was implemented according to the second method introduced on page 136.

4.4.1 Outcomes of numerical simulations

To report on the results obtained by simulation, a detailed analysis is developed below for conditions with maximum currents of $I_{max} = 800\,\mathrm{A}$ and $I_{max} = 1.5\,\mathrm{kA}$. The temperature distribution in the arc column at different time points is shown in figure 4.14 and 4.15. Similar to the previous results, the cathode jet and the anode jet are formed with a maximum temperature found in the vicinity of the cathode and of the anode. In the arc center, where the latter constricts, the temperature achieves values of 16 000 K and 25 000 K depending on the current conditions. Interestingly, the intriguing arc constriction in the middle is observed for both current conditions.
The arc current and arc column voltage are presented in figure 4.16. The displacement velocity of the arc center ($z = 10\,\mathrm{mm}$) and of the anode attachment are shown in figure 4.17. The acceleration of the arc predicted within the first 0.5 ms is due to the Lorentz force. The arc velocity is then limited by the action of the drag force. In both cases, the anode attachment and the centre of the arc column move simultaneously at the same speed. One can assume a steady-state arc displacement starting around 0.5 ms after the arc initiation.

4.4.2 Comparison of numerical simulations with the experimental data

By comparing the temperature distribution in the arc with the high-speed recording images, qualitative parameters describing the arc behavior can be estimated. Two attachments are observed: the cathode jet and the anode jet. Both of them move in the same direction with almost the same speed. This was observed both in the experiment and in the model for a wide current range. In order to perform qualitative comparisons, the arc column voltage from the numerical model was compared with the total arc voltage from the experiment. In such a comparison, one should keep in mind that the numerical model does not include the cathode fall which is not a linear function of the arc current [Benilov 95b]. The compared results are summarized in figure 4.18 for arc currents below and above 1.0 kA. Surprisingly good

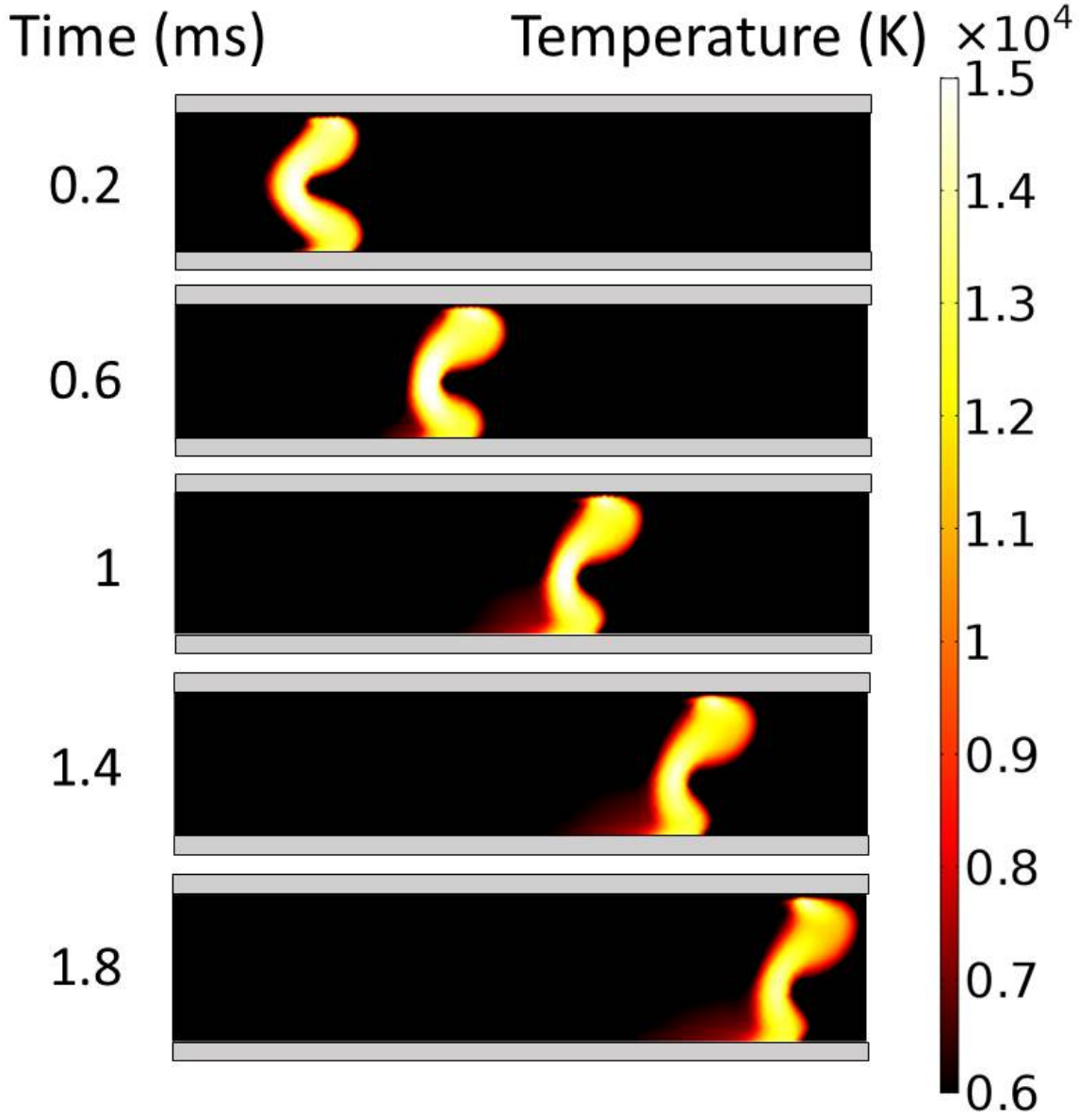

Figure 4.14: 2D temperature distribution in the arc column at multiple time points. $I_{max} = 800\,\mathrm{A}$ at $1\,\mathrm{atm}$.

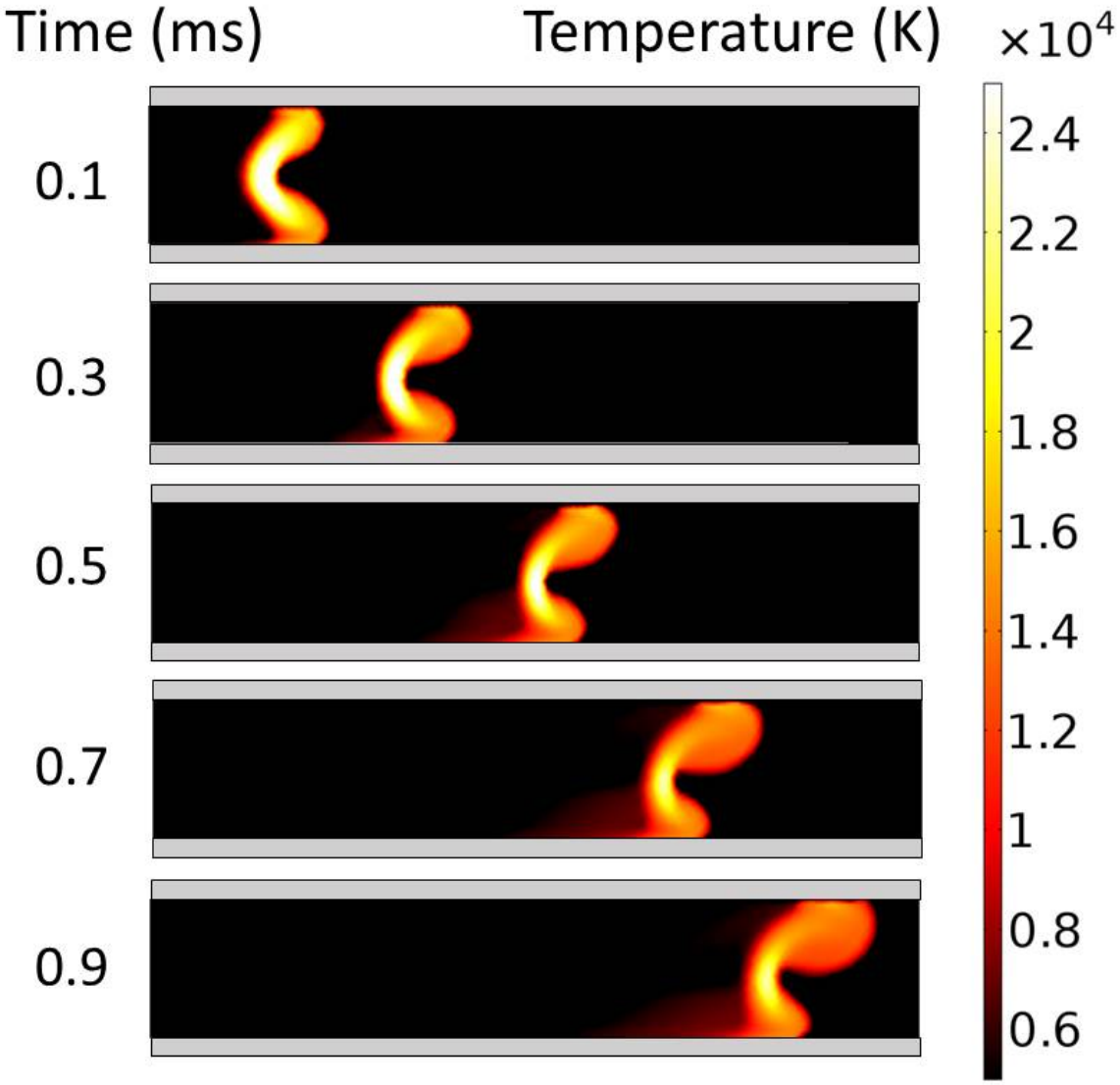

Figure 4.15: 2D temperature distribution in the arc column at different time moments. $I_{max} = 1.5\,\text{kA}$ at $1\,\text{atm}$.

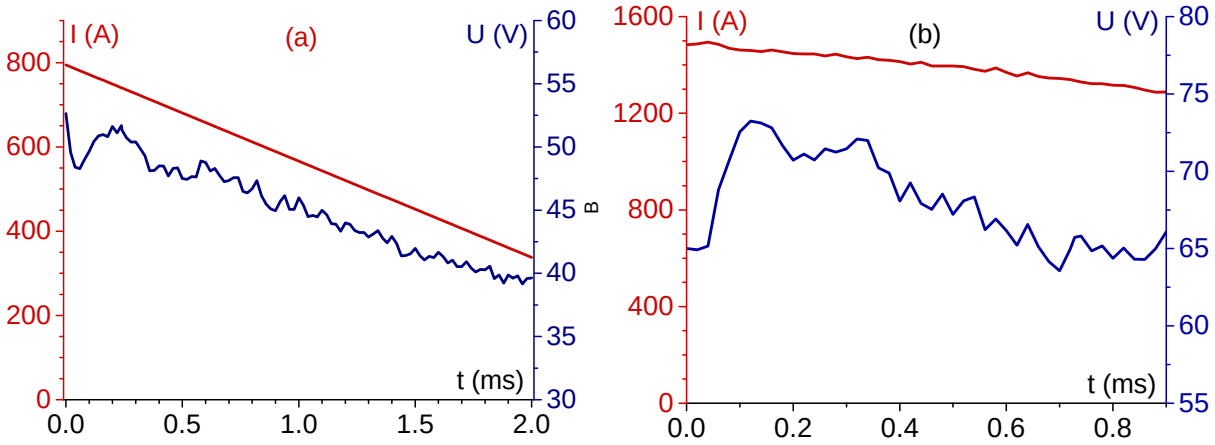

Figure 4.16: Arc current and voltage at 1 atm for, (a) $I_{max} = 800\,\mathrm{A}$ and (b) $I_{max} = 1.5\,\mathrm{kA}$.

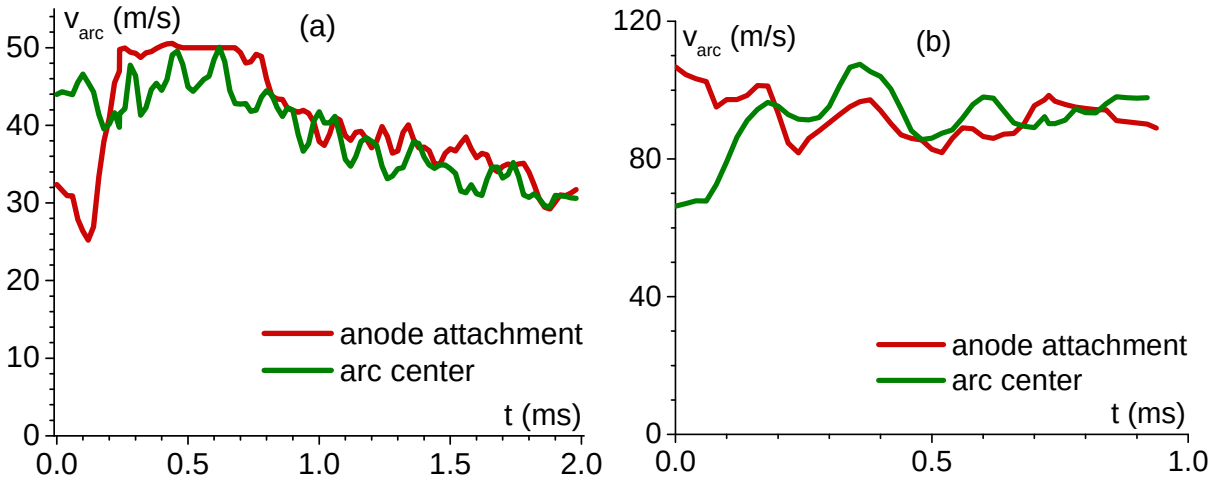

Figure 4.17: Arc displacement velocity for two current conditions, $I_{max} = 800\,\mathrm{A}$ and (b) $I_{max} = 1.5\,\mathrm{kA}$ at 1 atm.

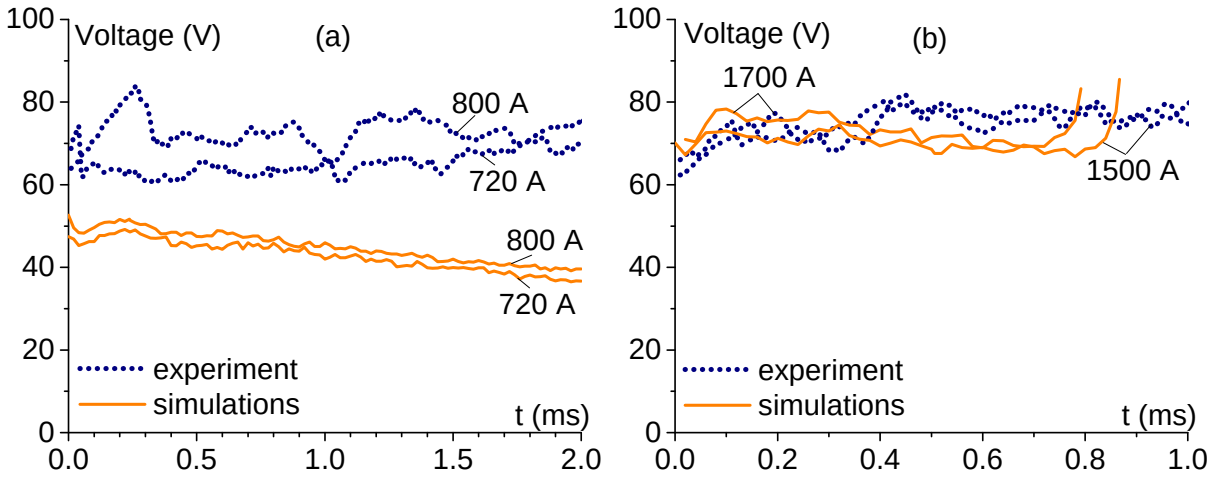

Figure 4.18: Comparison of the arc voltage recorded from the experiments with the simulated arc column voltage. (a) $I_{max} < 1.0\,\text{kA}$, (b) $I_{max} > 1.0\,\text{kA}$, at 1 atm.

quantitative agreements were found in the case of higher current. For the conditions with arc currents below 1 kA, a reasonable discrepancy was observed with a voltage difference which does not exceed 20 V. Agreement between the experiment and the simulation results for lower arc current conditions can therefore be considered satisfactory. This discrepancy is justified by the absence of a refined theoretical description of the cathode and the anode falls which are known to play a significant role at lower currents [Lisnyak 17].

Prior results of the numerical model were analyzed and very similar values of the arc velocity were found for the arc centre and the electrode attachments. For the subsequent analysis, the arc center and anode attachment velocities are evaluated from the model and will be compared with the experimental ones. The arc positions for current conditions of $I_{max} = 800\,\text{A}$ and $I_{max} = 1.5\,\text{kA}$ at atmospheric pressure are plotted in figure 4.19. In the case of lower arc current conditions, simulation results agree fairly well with the measurements obtained experimentally. The comparison for higher current conditions tends to show some tolerable discrepancies which will be discussed below. The comparison of the arc and electrode attachment velocities is based on the results presented in figures 4.20 and 4.21. The arc current decreases with time, therefore the arc speed slowly decreases from its maximum value, occurring within microseconds. The slightly "noisy" structure of the curves can be attributed to numerical effects on the calculated arc velocity. In reality, the arc displacement is smooth without significant jumps. Excellent agreement between simulation results and experimental measurements was found for current conditions below ∼1 kA (figure 4.20). While the agreement for higher arc current conditions was acceptable, the model tended to overestimate the arc velocity with values higher than 100 m/s for the most extreme conditions. In an attempt to understand these discrepancies between the model outcome and the experimental measurements, several hypotheses were formulated:

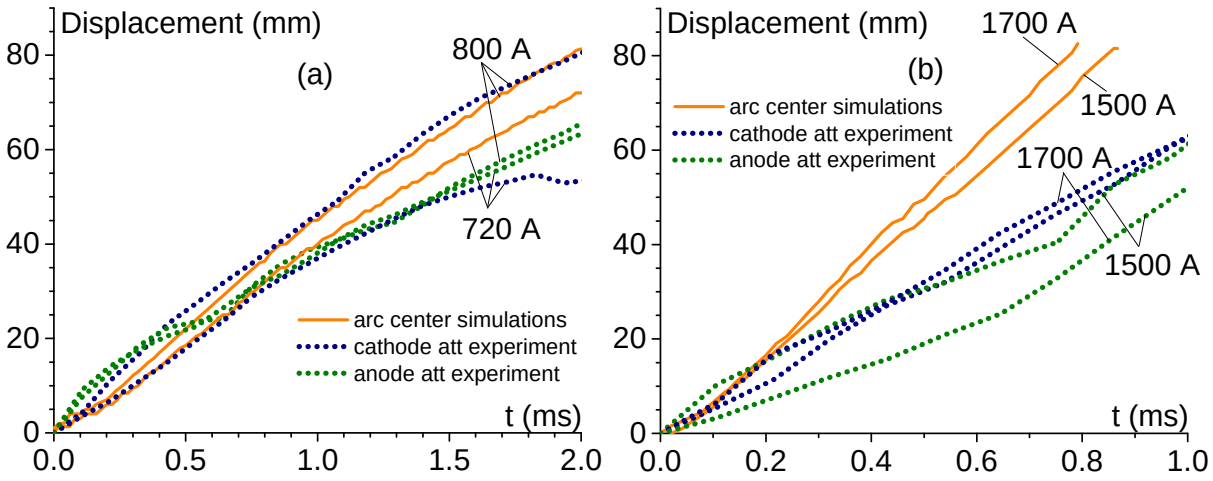

Figure 4.19: Displacement of the cathode and anode attachments (experiment) and the arc center (simulations) for (a) $I_{max} < 1.0\,\mathrm{kA}$, (b) $I_{max} > 1.0\,\mathrm{kA}$, at 1 atm.

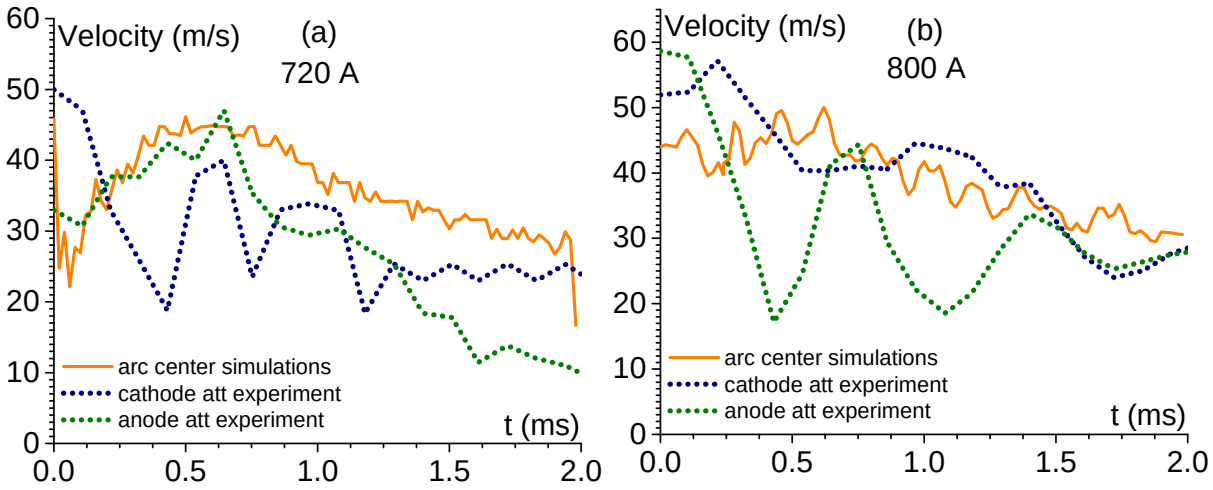

Figure 4.20: Arc cathode and anode attachments velocity (experiment) and arc center velocity (simulations) (a) $I_{max} = 720\,\mathrm{A}$ and (b) $I_{max} = 800\,\mathrm{A}$ at 1 atm.

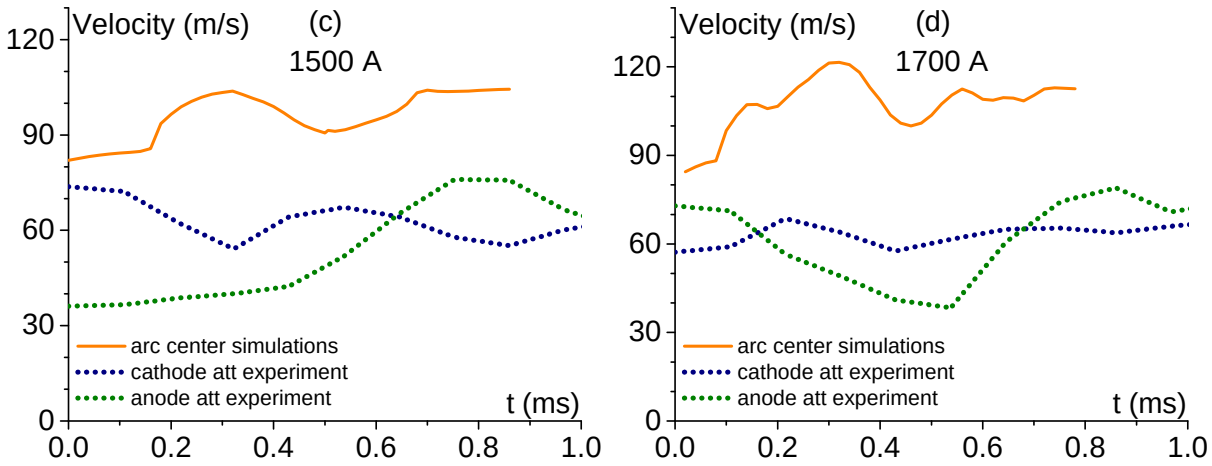

Figure 4.21: Arc cathode and anode attachment velocity (experiment) and arc center velocity (simulations) (a) $I_{max} = 1.5\,\text{kA}$ and (b) $I_{max} = 1.7\,\text{kA}$ at 1 atm.

- A simplified (or extended) implementation to describe the cathode attachment –accounting for the near-cathode non-equilibrium layer and plasma-cathode interaction– will help to compute more realistic values of the arc voltage. This improvement to the model will provide a more precise description of the cathode attachment behavior, although it should not change the arc column velocity. Therefore, additional efforts are necessary to prevent the overestimation of the arc speed for current conditions $\gtrapprox 1\,\text{kA}$.

- The MHD model of the arc column was established under the assumption of a weakly compressible fluid, i.e. $Ma < 0.3$. When the arc velocity exceeds 100 m/s, this assumption may no longer hold. Additionally, the compressibility of the fluid can change the arc behavior and the arc velocity.

- The model of the arc column adopted for the calculations does not take into account the evaporation of the electrode material. The occurrence of metal evaporation (for instance Cu, Al) can potentially have an effect on the arc behavior.

Regarding the latter hypothesis, a numerical computation was done in order to estimate the impact of metal vapor. The calculation was done with a gas composed of 99 % air and 1 % of evaporated copper. No effect was found on the thermodynamic properties, the thermal conductivity or the viscosity. However, the electrical conductivity (σ) and the *net* emission coefficient (ε_{net}) did vary for temperatures up to 9000 K, as shown in figure 4.22)[Cressault 17]. Implementing the latter properties in the model has a quantitative impact on the simulation outcome. The plasma temperature in the arc column is lower compared to simulation performed in pure air, hence, the conductive channel is wider as reported in figure 4.23. As a result, the arc column voltage is always lower in the presence of metal vapour (figure 4.24(a)). This does

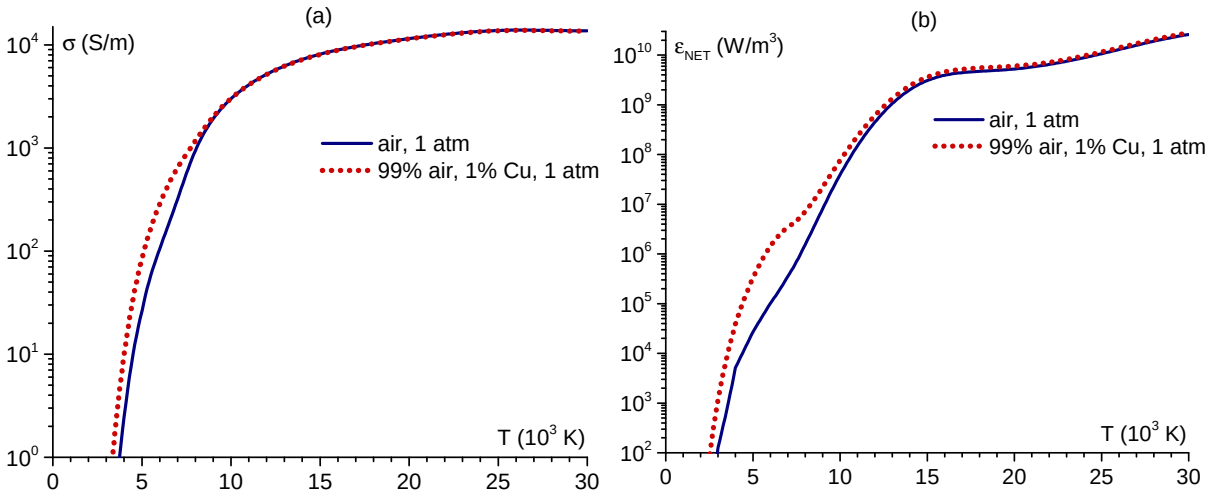

Figure 4.22: Electrical conductivity (a) and *net* emission coefficient (b) versus the temperature for a gas composition of 99 % air and 1 % vaporized copper.

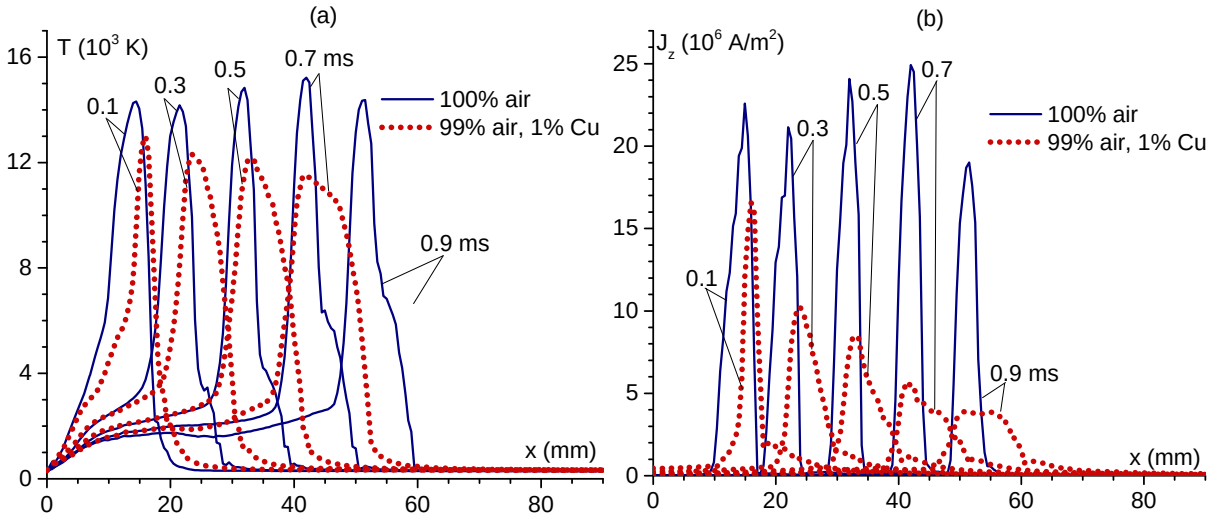

Figure 4.23: (a) Arc temperature in mid-plane longitudinal cut (z = 10 mm); (b) Current density axial component in mid-plane longitudinal cut (z = 10 mm). For pure air in 1 atm and 99% air with 1% of copper. I_{max} = 800 A.

not seem to be related with the current with regards to the investigated current range. In spite

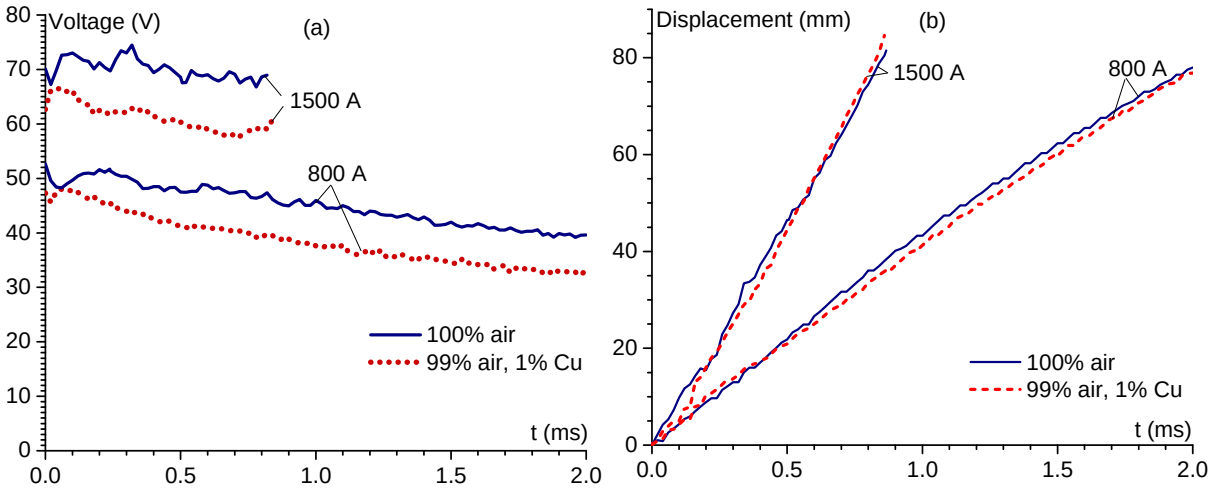

Figure 4.24: (a) Arc column voltage (b), Displacement of the arc center. For pure air in 1 atm and 99% air with 1% of copper. I_{max} = 800 A and 1500 A.

of a significant impact of metal vapour on the plasma temperature, no correlation was found with the arc displacement as shown is figure 4.24(b).

The main comparison considering a large set of experimental measurements is documented in figure 4.25. In this figure, both graphs present experimental measurements and simulation

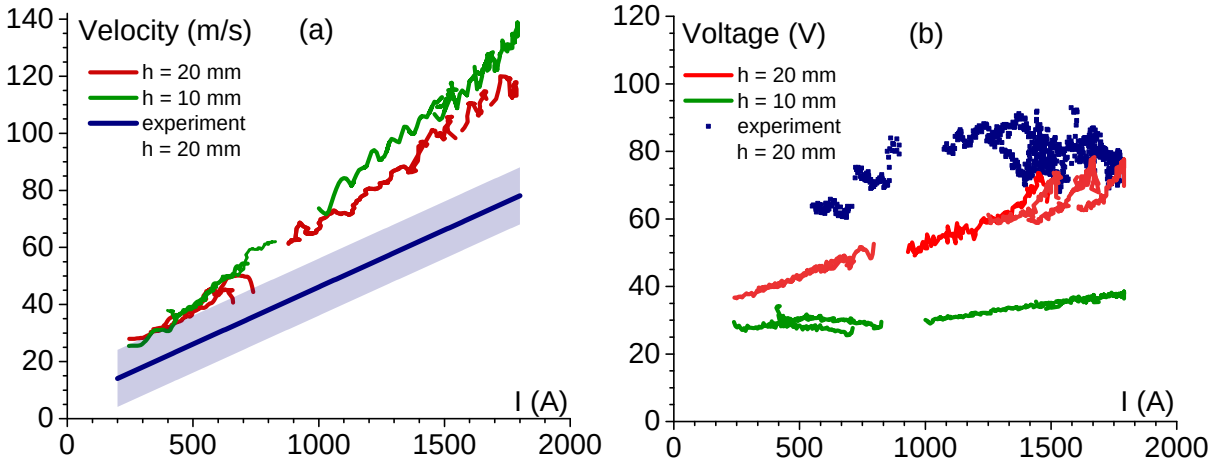

Figure 4.25: Comparison with the experiments: (a) arc cathode and anode attachments velocity (experiment) and arc center velocity (simulations); (b) the arc voltage recorded from the experiments with the simulated arc column voltage.

results of propagation velocity and arc voltage for a wide current range. A direct comparison between measurements and computed values is possible for the case of a 20 mm electrode gap. Simulation results for a 10 mm gap are also reported in order to give an idea of the arc

column behavior. A linear dependence between the arc current and the arc velocity is clearly observed experimentally and theoretically. While the slopes seems to differ slightly, leading to a reasonable overestimation of the velocity by the model –particularly for higher currents– a fairly good agreement is found. The arc voltage is also in rather good agreement between the experiment and the model. However, one needs to keep in mind that the computed values of the arc voltage column do not include the cathode and anode falls which require the additional implementation of non-linear description layers, as previously discussed.

4.5 AC arc – Simulations related to the experiments at Zodiac Aero Electric

Convincing agreements between the numerical model and the experiments were reported in the previous section, giving a credible motivation to extend the model description with additional conditions closer to the aeronautical context. To achieve this, several modifications had to be implemented in the model concerning:

- the geometrical configuration of the electrodes,
- the proper conditions applied on the cathode and anode in order to consider an alternating current (AC),
- the plasma properties, in particular the pressure which ranges from 0.1 atm to 1 atm at typical aircraft cruising altitudes.

The main difficulty concerns the numerical realization of the alternating boundary conditions at the electrodes in order to simulate an AC excitation, in particular the conditions for the current density which should be alternated with an imposed electrostatic potential, and the heat flux which should be alternated with the temperature, whether it is the cathode or anode temperature. To accomplish this, so-called Robin Conditions were applied on both electrodes. This is not straightforward in COMSOL Multiphysics®. By selecting appropriate values of stiffness matrix, one can however morph Robin conditions into acting as approximate Dirichlet or Neumann conditions. This is especially important for cases where one wants to switch between the two boundary condition types during a simulation. To create a Dirichlet condition from the COMSOL Multiphysics® predefined Neumann type, a high value of the "stiffness" needs to be assigned, for instance, a heat transfer coefficient for the energy conservation equation. In mathematical terms, this is actually a penalty implementation of the Dirichlet condition. The higher the stiffness is, the greater the accuracy of the prescribed value. Very high stiffness will harm the numerical conditioning of the stiffness matrix. For the heat transfer, issues with the

stiffness matrix can be,

$$\alpha = 10^4 \frac{\lambda}{h}, \tag{4.4}$$

where λ is the thermal conductivity and h is the finite element size. A factor 10^4 is high enough to achieve the needed value of the variable and at the same time to give numerically stable solutions. The computation and convergence of such a model is more complex and may be time-consuming. In this case, the arc temperature as boundary condition needs to be imposed with Dirichlet at T_0. Consequently, the Neumann condition is applied as

$$-\mathbf{n} \cdot (-\lambda \nabla T) = \alpha (T_0 - T), \tag{4.5}$$

where $\mathbf{n}$ is a normal vector directed from the surface where the condition is applied. Numerical outcomes of this approach give acceptable values of T_0.
In a similar way, the condition for the current density (Neumann) was transformed to Dirichlet conditions. This modification of the conditions is necessary to compute the numerical model of an AC arc with the current boundary conditions on the cathode and with an electrostatic potential at the anode set at 0 V. However, due to the complexity of the numerical calculation, particularly with the boundary conditions, the computation time is drastically increased. All other aspects of the model were kept as in the previous calculations with a pulsed arc.

4.5.1 Numerical simulation results

Before comparing the experimental results and the corresponding numerical simulations, the main particularities of the arc between the rail electrodes in AC conditions are discussed. The arc with a length of 8 mm, powered with a maximum current of $I_{max} = 600$ A at frequencies of either 420 Hz or 760 Hz was considered as a case study. The governing principles of electric arcs in alternating current conditions are poorly reported in the literature. Here, with several examples, a thorough analysis will unveil the impact of the intrinsic parameters on the arc displacement.
The arc current waveform is shown in figure 4.26 together with the voltage of the arc column. As shown, at each time point when the arc current passes at 0 A the arc column voltage exhibits a clear overshoot. The latter is due to a decrease in the electrical conductivity in the channel at this precise moment. Indeed, during each moment when ($I = 0$ A), the temperature of the center of the column is stabilized around 7000 K as shown in figure 4.27. A sequence of temperature profiles of the arc column on the longitudinal mid-plane cut is shown with a time delay of 0.1 ms. The two different colors on the graphs are related to the positive and negative amplitude of the arc current waveform. Interestingly, the temperature of the arc does not drop below 7000 K even for a current value of zero. According to figure 4.23 on page 155, at this temperature the electrical conductivity of the arc is still significantly high in the residual arc

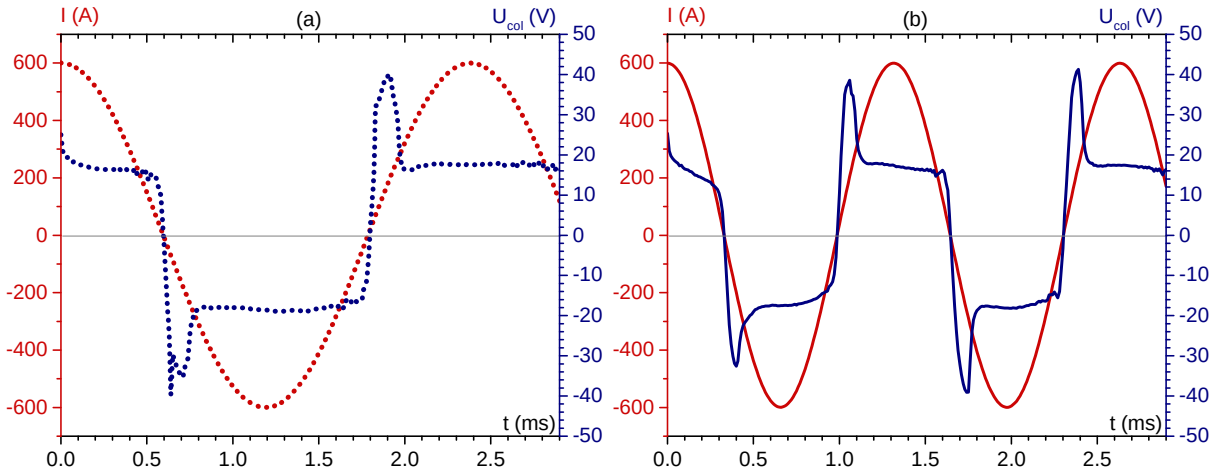

Figure 4.26: Arc current and arc voltage waveforms with $I_{max} = 600\,\text{A}$ and an arc length of 8 mm for an oscillation frequency of, (a) 420 Hz and (b) 760 Hz. The waveforms are synchronized.

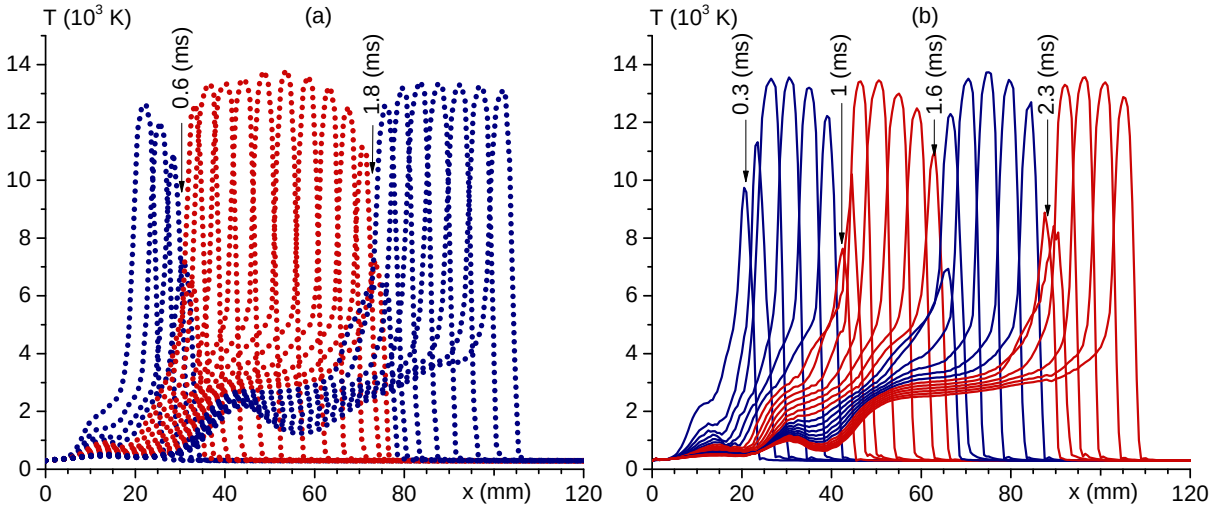

Figure 4.27: Time sequences of the arc temperature profile on the longitudinal mid-plane. $I_{max} = 600\,\text{A}$ and $h = 8\,\text{mm}$ for an oscillation frequency of, (a) 420 Hz and (b) 760 Hz. The time interval between two successive curves is 0.1 ms.

column. In other words, with a current around 0 A, the arc does not sustain, leading to the voltage overshoots. The magnitude of the voltage overshoot is still limited because of the rather low resistivity of the medium. Consequently, the next current cycle will systematically ignite a new arc within the gas channel where the conductivity is the highest , i.e. at the position of the previous arc column.

To support this argumentation, a time sequence of the arc development is depicted in figure 4.28 for the same conditions as in figure 4.27 (b) ($I_{max} = 600\,\text{A}$). At $t = 0.4\,\text{ms}$, the arc current crosses the zero value, triggering the extinction of the arc. At $t = 0.5\,\text{ms}$, the growth of the current amplitude leads to the re-ignition of the arc column at exactly the same location as the previous arc column. Furthermore, as evidenced in figure 4.28, the arc column is constricted and has a cylindrical shape. In comparison with the longer arcs investigated in the previous section (figure 4.14 on page 149), the maximum temperatures are located at different places. While in previous cases, the hottest regions were found near the cathode and near the anode, in the present case the maximum temperature of the arc is found in the center. The simulations predict a hot uniform and cylindrical shape of the highest temperature. This fact is a key factor to be considered in the case of electrodes with a low evaporation temperature and should be experimentally investigated for the same conditions.

The position of the cathode root displacement, introduced in the *second method* (see subsection 4.2.4 on page 136), is defined according to the location of the anode attachment. Thus, it is interesting to take a closer look at the time evolutions of the anode attachment and at the arc center position, plotted in figure 4.29 (a) and in figure 4.30 (a) respectively. The arc attachments and the column move in the same direction simultaneously. When the arc current equals zero, the displacement is also null. The respective arc displacement velocities are also reported for an excitation of 420 Hz in figure 4.29 (b) and for 760 Hz in figure 4.30 (b). The velocities of the anode attachment and of the arc center are displayed with error intervals resulting from numerical differentiation artifacts. The arc velocity behavior coincides with the arc current frequency: when the arc current increases, the arc accelerates and *vice-versa*. For the current of 600 A, the arc reaches a velocity around 45 m/s to 50 m/s for both frequencies 420 Hz and 760 Hz. As the result, the excitation frequency does not seem to have a significant impact on the arc displacement mechanism. Simulations with the same geometrical configuration were carried out for the DC arc regime with $I = 600\,\text{A}$ giving values of the arc speed in the range of 50 m/s to 52 m/s. In fact, the maximum arc speed for an AC excitation arc coincides with the arc speed predicted in DC conditions for the same current value.

While predictive simulations for a given current in different excitation regimes do not seem to have a significant impact on the arc velocity, other imposed parameters were considered and their influence investigated. In the context of this work, the arc velocity as a function of the electrode distance and the arc current magnitude is a key point to study. Therefore,

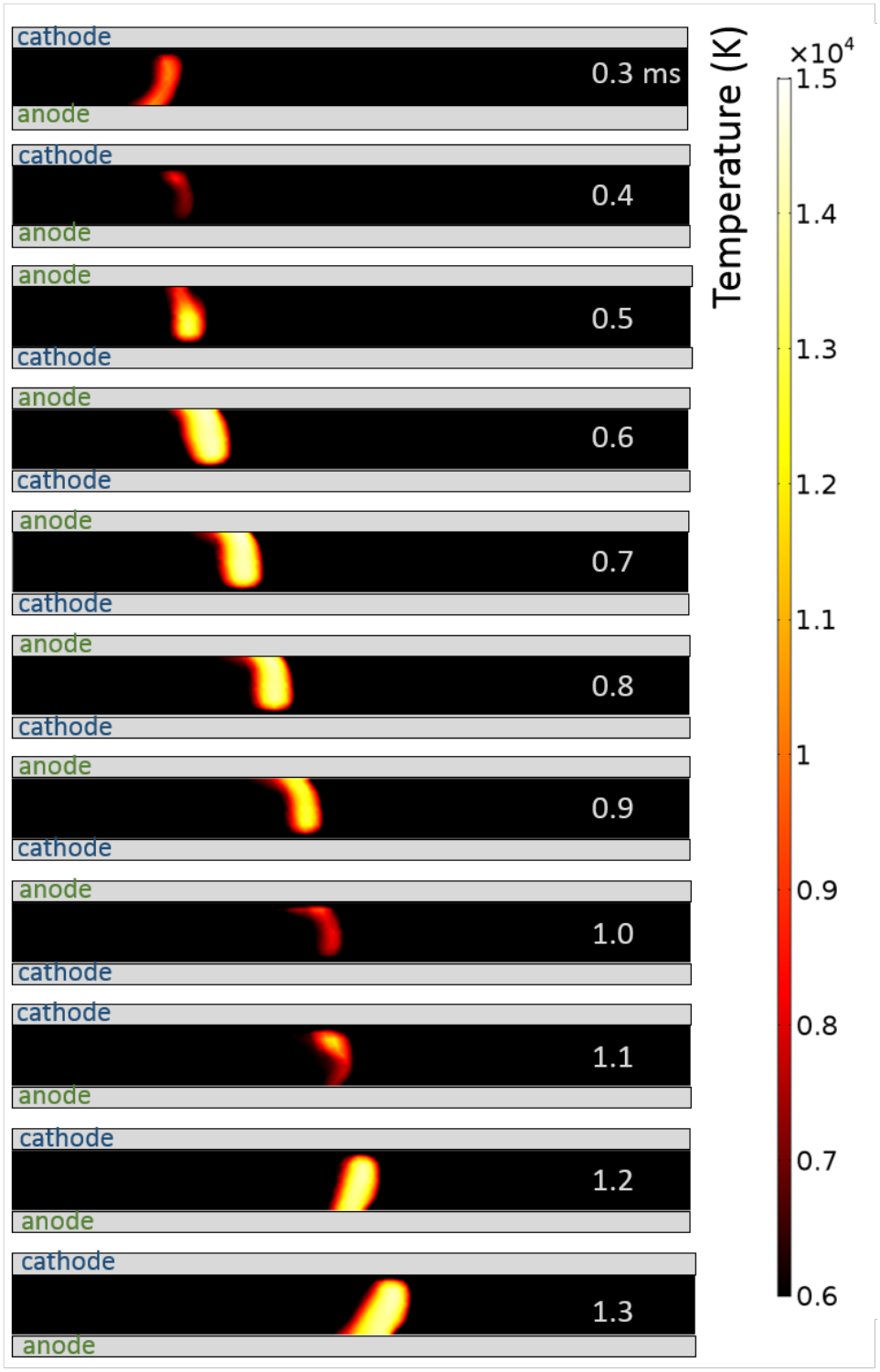

Figure 4.28: Sequence of computed 2D temperature distributions in the arc column at different time points for $I_{max} = 600\,\mathrm{A}$ at $760\,\mathrm{Hz}$,$h = 8\,\mathrm{mm}$ arc length.

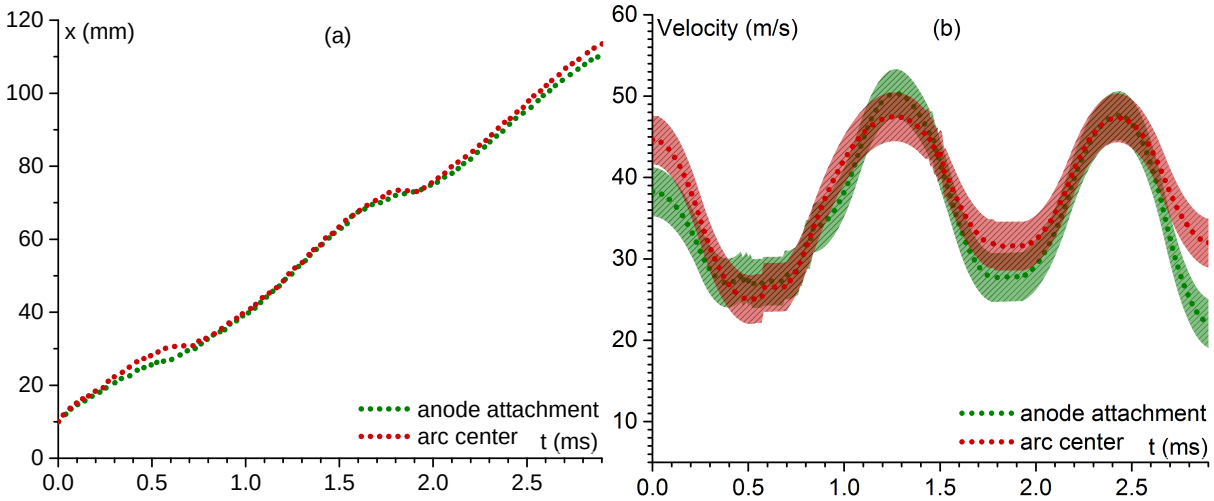

Figure 4.29: Simulation results of (a) the arc displacement and (b) the arc velocity for the conditions $I_{max} = 600\,\text{A}$ at $420\,\text{Hz}$, $h = 8\,\text{mm}$ arc length.

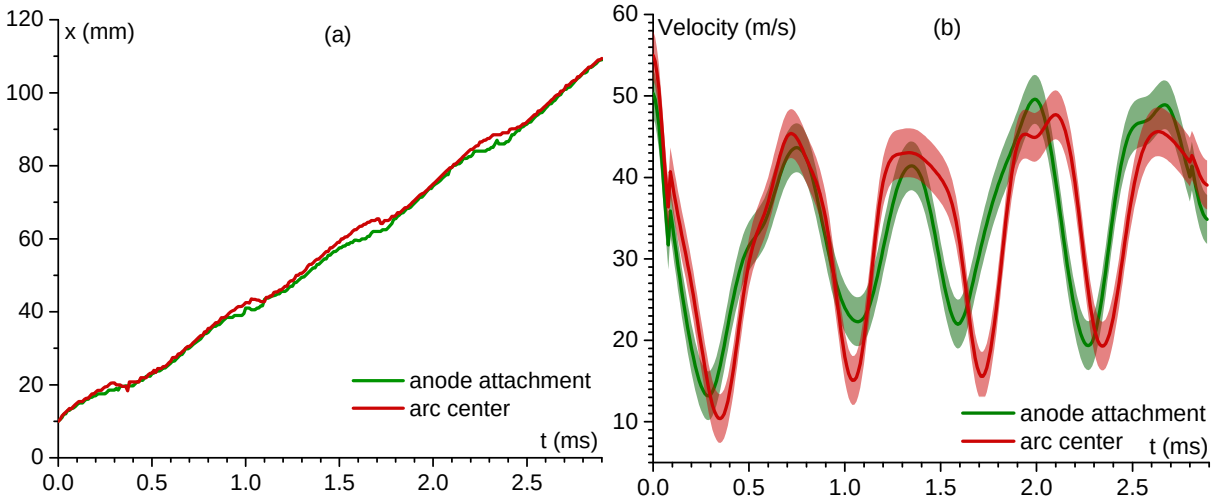

Figure 4.30: Simulation results of (a) the arc displacement and (b) the arc velocity for the conditions $I_{max} = 600\,\text{A}$ at $760\,\text{Hz}$, $h = 8\,\text{mm}$ arc length.

a parametric study was performed and is presented below. Several typical distances between electrodes are used in aeronautics. In this work, two distances were considered. Simulations for conditions with $I = 600\,\mathrm{A}$ and 760 Hz were performed for distances of 5 mm and 8 mm. As in the previous cases, the anode attachment and the arc center displacement with their respective velocities are grouped together in figure 4.31 for two inter-electrode gaps. As expected, the

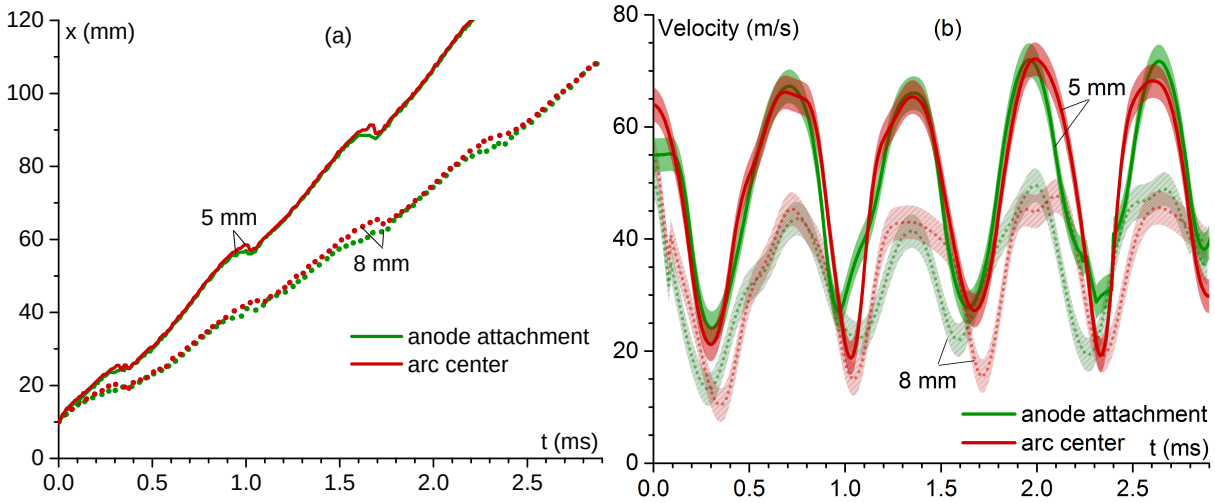

Figure 4.31: Simulation results of (a) the arc displacement and (b) the arc velocity for the conditions $I_{max} = 600\,\mathrm{A}$ at 760 Hz for $h = 5\,\mathrm{mm}$ and $h = 8\,\mathrm{mm}$.

fastest arc displacement is predicted for the shortest electrode gap. This is obviously explained by an increase in the Lorentz force with a decrease in the gap.

Simulations with the counter conditions, i.e. for a given excitation frequency and electrode gap, were computed for two different current magnitudes. The results are shown in figure 4.32 (a) for the arc displacement and in figure 4.32 (b) for the respective velocities. These results confirm that an increase in the arc current induces a clear rise in the arc column voltage (figure 4.32 (a)). Intuitively, the arc displacement velocity follows the same trend and also increases, as evidenced in figure 4.32 (b). Consequently, the arc current magnitude value has the most significant impact on the arc displacement behavior, in particular the arc velocity.

The key point of this work was to investigate the impact of low pressure on the arc displacement. Numerical simulations were performed for pressure values of 0.1 and 1.0 atm. For comparison, several parameters of the arc operated at $p = 0.1\,\mathrm{atm}$ and $p = 1.0\,\mathrm{atm}$ are shown in figure 4.33. Electrical properties of the arc are compared in figure 4.33 (a). With the current imposed, the arc column voltage decreases with the decrease in pressure. The arc temperature on the mid-plane cut is shown in figure 4.33 (b) for an arc pressure of $p = 0.1\,\mathrm{atm}$. Comparing the latter temperature profiles with those computed for $p = 1.0\,\mathrm{atm}$ (see figure 4.27 (b) on page 159) evidences a higher temperature of the arc column with a lower pressure. Keeping the same

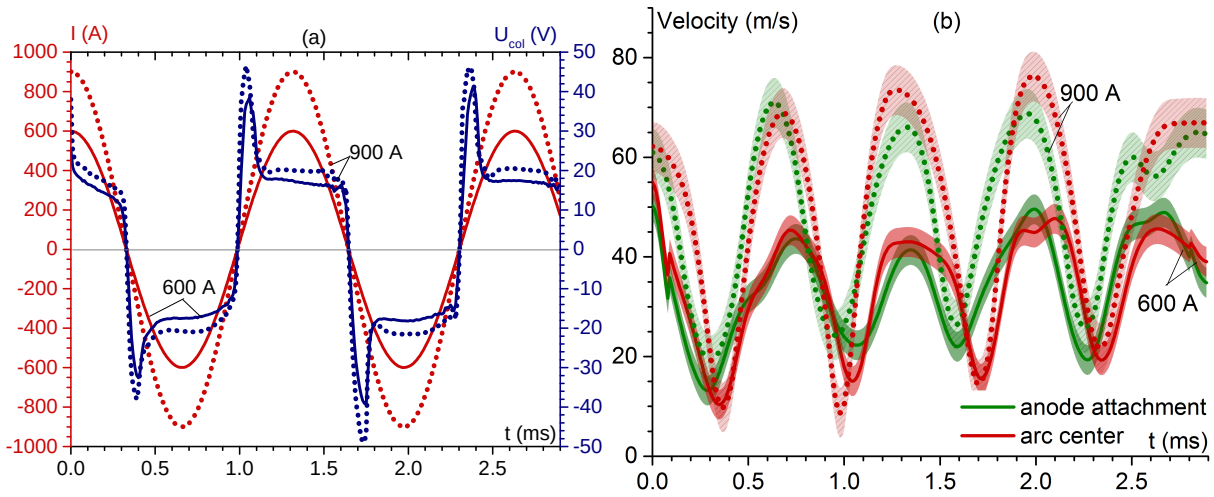

Figure 4.32: Simulation results of (a) the arc displacement and (b) the arc velocity for the conditions $I_{max} = 600\,\text{A}$ and $I_{max} = 900\,\text{A}$ at 760 Hz for $h = 8\,\text{mm}$.

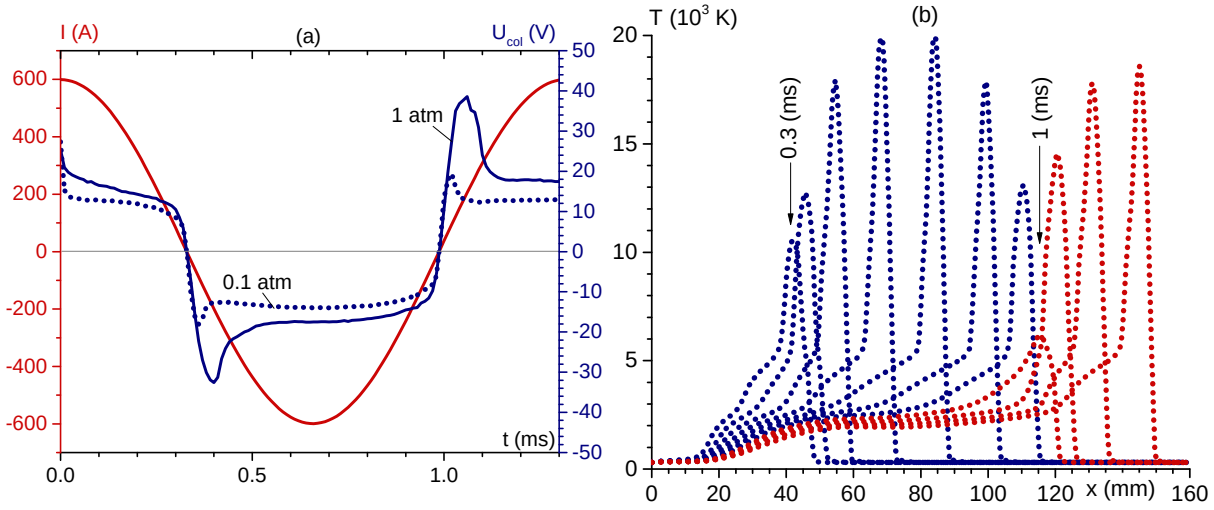

Figure 4.33: Comparison of electrical and thermal properties of the arc operated at $I_{max} = 600\,\text{A}$ at 760 Hz for $h = 8\,\text{mm}$. (a) Arc current and arc column voltage waveforms for two different pressure conditions: $p = 0.1\,\text{atm}$ and $p = 1.0\,\text{atm}$. (b) Time sequence of arc column temperature distribution on the mid-plane cut with 0.1 ms step for $p = 0.1\,\text{atm}$.

current (I_{max} = 600 A at 760 Hz) the maximum temperature reaches 20 000 K. The reason for this temperature dependence of the pressure is not clearly identified and may result from the plasma composition properties.
For the latter set of conditions, the arc root and the center position are shown in figure 4.34 (a). The arc root and the arc center reach the end of the electrode simultaneously and much faster

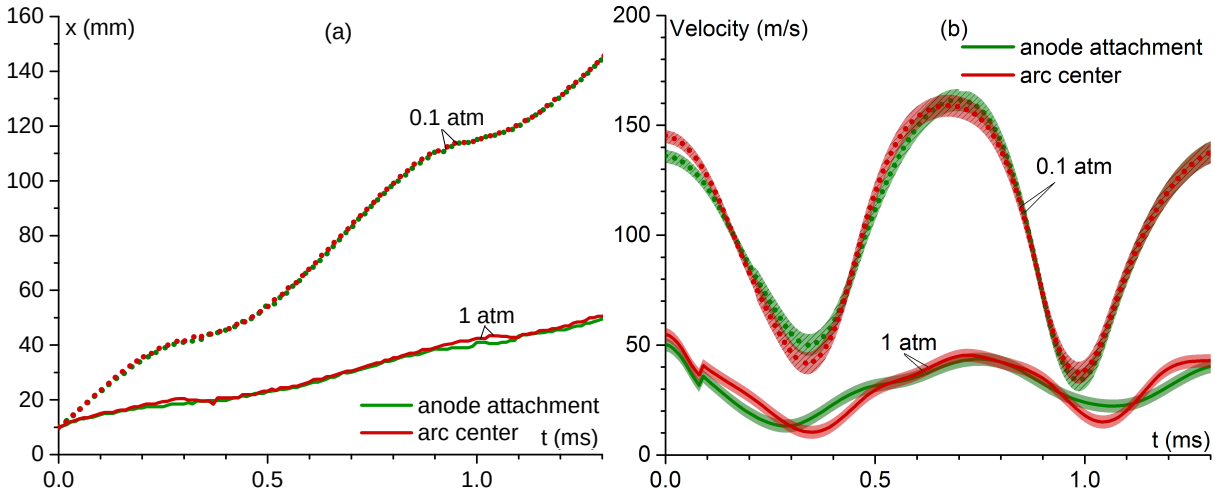

Figure 4.34: Simulation results of (a) the arc displacement and (b) the arc velocity for the conditions I_{max} = 600 A at 760 Hz for h = 8 mm and h = 8 mm at p = 0.1 atm and p = 1.0 atm.

for p = 0.1 atm than for p = 1.0 atm. As a result, the arc displacement velocity is higher for lower pressure (figure 4.34 (b)). Interestingly, the dynamic of the arc displacement is much more pronounced at lower pressure. Such a significant difference in the arc speed can be explained by the lower air density at low pressure, while the other transport parameters and thermodynamic properties do not vary significantly with the conditions around 1 atm. Consequently, for a given arc current and electrode gap, the arc velocity is mainly governed by the air density and the viscosity force. From an applications point of veiw, it can be mentioned that at lower pressure the arc displacement will be more difficult to control than at atmospheric pressure.
The model developed with the proper implementation of boundary conditions to describe alternating current conditions allows one to successfully investigate the electric arc propagation along the electrodes in a wide range of conditions such as arc current, inter-electrode distance, operating gas...

4.5.2 Comparison of numerical simulations with experimental data

It is of great interest to compare the model outcomes and the experimental measurements for arc displacement velocity and arc voltage. However, as mentioned before, *the model provides a value*

of the voltage drop only in the arc column. The comparison was done to obtain an estimation of the possible voltage drop in the near electrode regions, and involves several experimental sets of parameters with current values $\leq$1.5 kA. The results for two gaps and two excitation frequencies are grouped in figures 4.35, 4.36, 4.37 and 4.38. The data presented in the figures

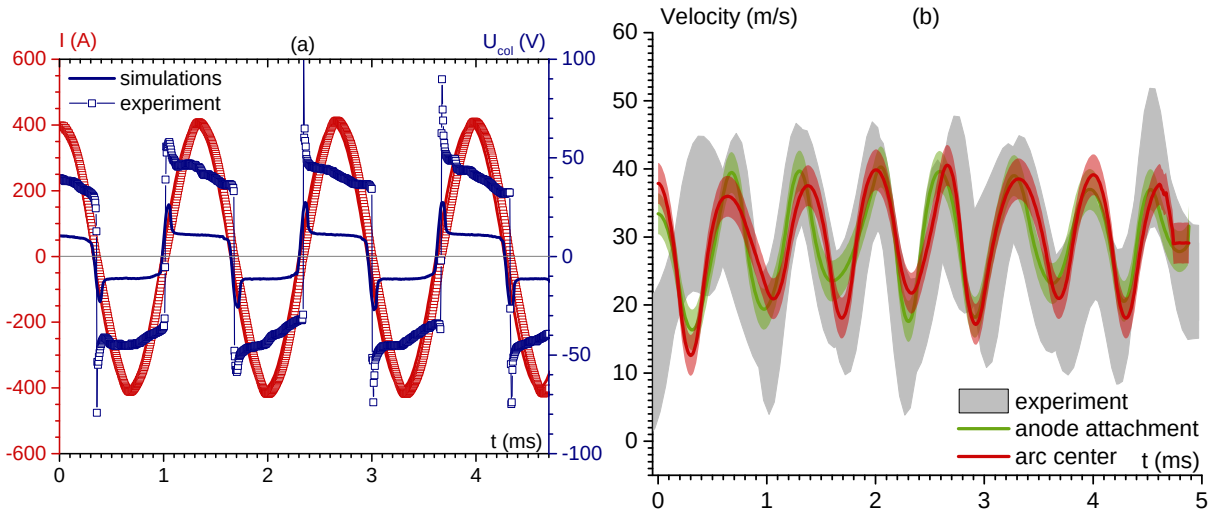

Figure 4.35: Comparison of simulation results with experimental measurements for $I_{max} = 400$ A at 760 Hz for $h = 5$ mm. (a) Arc current and arc column voltage waveforms. (b) Time evolution velocities of the anode attachment and the arc column.

are organized in such a way that current and voltage waveforms are shown on sub-figures(a) and arc velocity on sub-figures (b). The phase shift on the experimental data was rescaled for the sake of the comparison.

As expected, the arc column voltage calculated with the model is lower than in the experiments. For the cases with $I_{max} = 600$ A (figure 4.35 (a)) the measured arc column voltage was 10 V in the experimental setup while 40 V was found in the simulation results. Recall that the model does not describe the near electrode layers, which contribute to the whole arc voltage. Nevertheless, a similar trend of the arc voltage waveform can be seen, i.e. overshoots when $I = 0$ A. It should be emphasized that the time duration of these overshoots predicted by the simulations is the same as that measured in the experiments, i.e. about 1 ms. A stabilization period of the voltage follows the overshoot at a constant value. The slight decrease in the voltage magnitude when the current is about to pass zero should be pointed out. The latter feature is seen on both the experimental data and the simulation results. A small deviation of the arc current can be observed. For the arc with a current of $I_{max} = 600$ A (figure 4.36 (a)) the calculated voltage is 17 V and the experimental is 50 V. For the arc with $h = 8$ mm and current $I_{max} = 700$ A (figure 4.37 (a)), the calculated value of the arc voltage is 14 V and

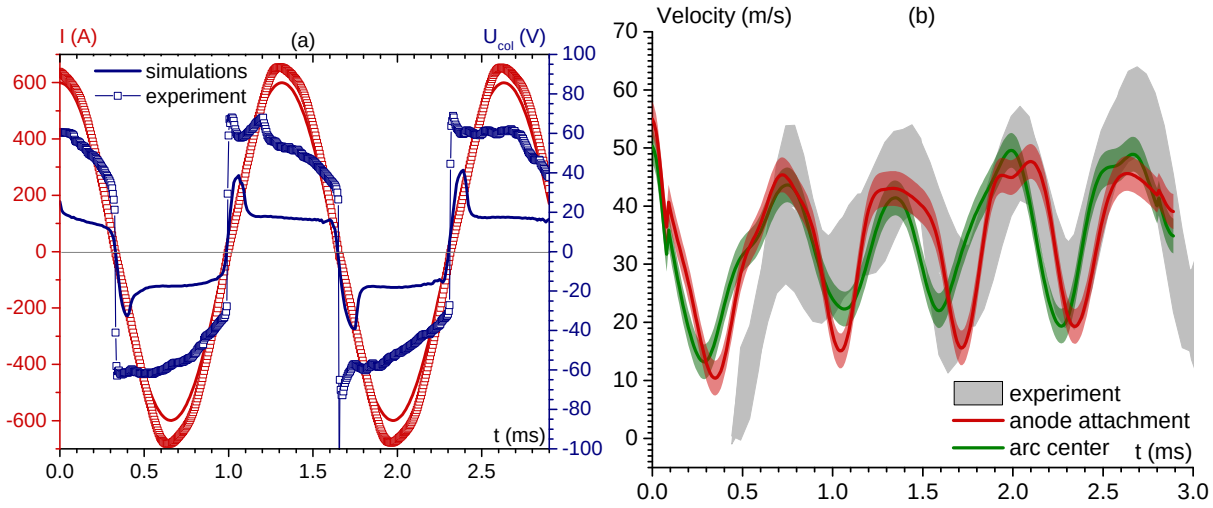

Figure 4.36: Comparison of simulation results with experimental measurements for $I_{max} = 600\,\mathrm{A}$ at $760\,\mathrm{Hz}$ for $h = 8\,\mathrm{mm}$. (a) Arc current and arc column voltage waveforms. (b) Time evolution velocities of the anode attachment and the arc column.

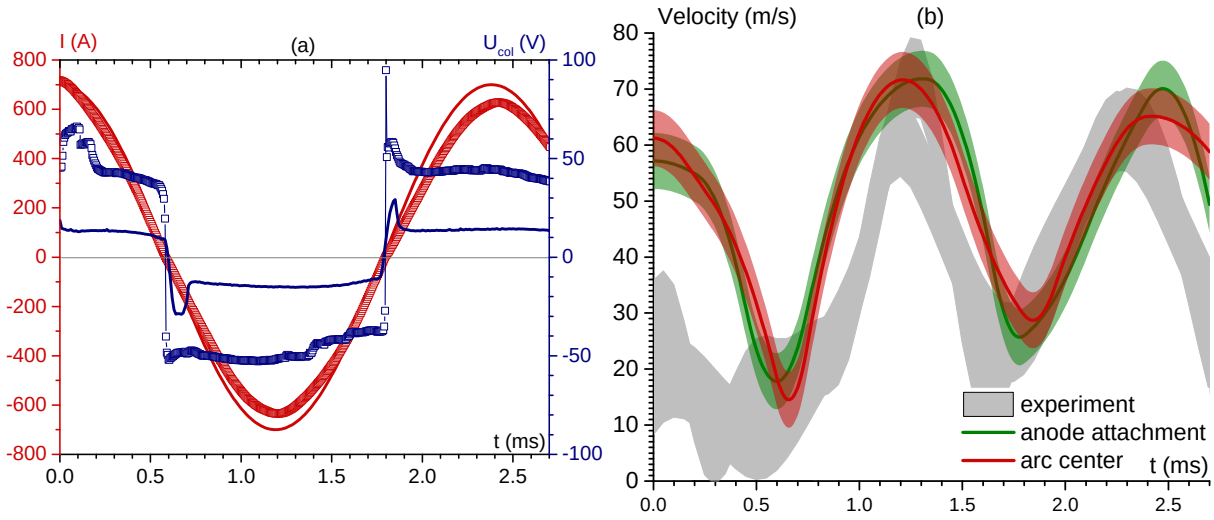

Figure 4.37: Comparison of simulation results with experimental measurements for $I_{max} = 700\,\mathrm{A}$ at $420\,\mathrm{Hz}$ for $h = 5\,\mathrm{mm}$. (a) Arc current and arc column voltage waveforms. (b) Time evolution velocities of the anode attachment and the arc column.

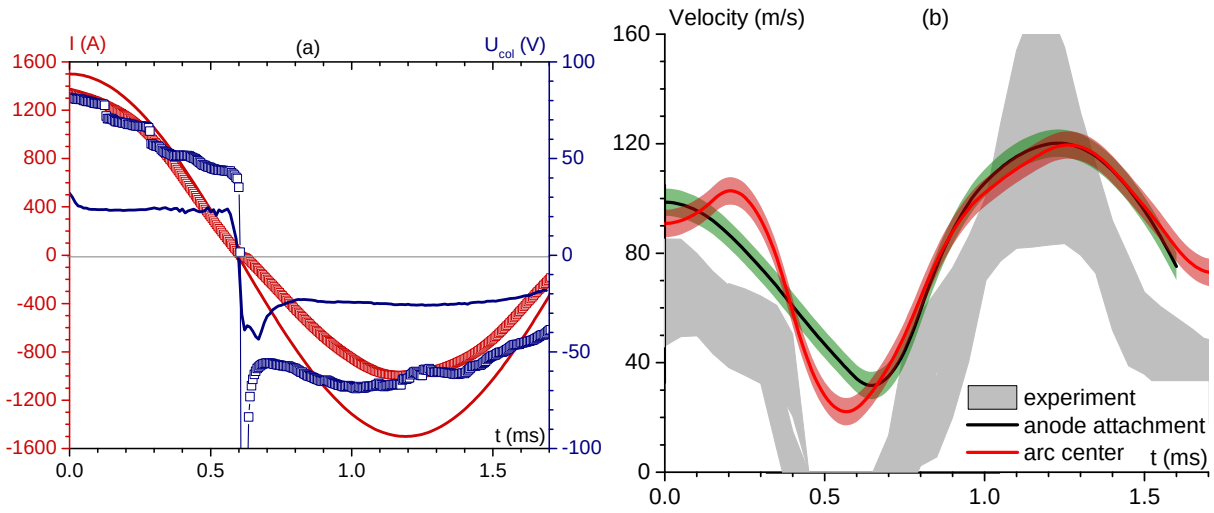

Figure 4.38: Comparison of simulation results with experimental measurements for $I_{max} = 1.5\,\text{kA}$ at $420\,\text{Hz}$ for $h = 8\,\text{mm}$. (a) Arc current and arc column voltage waveforms. (b) Time evolution velocities of the anode attachment and the arc column.

the experimental one is reduced to 44 V. For the arc current $I_{max} = 1.5\,\text{kA}$ (figure 4.38 (a)) the computed arc column voltage is 25 V while the measured total arc voltage is 65 V. The difference between the calculated values of the arc column voltage and the measured arc voltages are between 30 V to 40 V in all the cases. This discrepancy is fully attributed to the lack in the model of a proper description of the electrode layers (particularly the cathode). However, it can be noted that this deviation of the simulation results with respect to the experimental data concerns the magnitude of the voltage, while the time evolution of the voltage waveforms is well predicted by the model.

Regarding the arc behavior, the comparison will focus on the arc velocity of the arc center and of the cathode attachment. Both computed and measured velocities of the arc are plotted together. The curves corresponding to the experimental data are displayed in gray within the error interval. For all regimes with an excitation frequency of 420 Hz (figures 4.37 (b) and 4.38 (b)) and 760 Hz (figures 4.35 (b) and 4.36 (b), electrode gaps of 5 mm (figures 4.35 (b) and 4.37 (b)) and 8 mm (figures 4.36 (b) and 4.38 (b)) excellent agreement between the numerical simulations and the experiment was found. The arc displacement computed by the model, as in the experiments, accelerates when the current magnitude rises and decelerates when the arc decreases. In addition, the arc speed, even for a current value of zero in both cases, remains positive (15 m/s to 20 m/s). An exception is the re-strikes, which are observed in the experiment but not found in the simulation results. In the experiment, re-striking is identified at zero velocity as evidenced in figure 4.38 (b).

The excellent agreement on the arc velocities between the experiments and the numerical model validate the possibility of extending the model to a wide range of current regimes and of seriously considering the results of the simulations for lower pressures. Last but not least, the remarkable consistency of the simulation outcomes with the experimental measurements validates and supports the role of the present model as a predictive tool of arc behavior with respect to its limitations based on the model assumptions.

4.6 Conclusions

The aim of this work was to investigate the arc displacement between busbars for aeronautical applications by means of numerical simulations. To fulfill this goal, a thorough preparation was undertaken. The theoretical model of the electric arc was established and is described in Chapter 2 (page 43) based on a system of MHD equations. The commercial software COMSOL Multiphysics® using FEM was chosen as a tool to resolve the numerical model. A comprehensive review of the literature on the topic was also carried out. Additionally, the experimental study of the electric arc between busbars for a wide variation of conditions was performed, processed and analyzed. A compilation of this knowledge is presented in this chapter. The MHD model of the electric arc from Chapter 2 was adapted for the arc geometry between busbars in aeronautical conditions. The experimental investigations performed were compared with the simulation results.

At first glance, the phenomenon of arc displacement between rail electrodes is very similar to the so-called *railgun*. In the latter the arc object is replaced by the armature between the electrodes. The principle of the object displacement is similar: the armature and the arc column are displaced due to the Lorentz force, which appears due to the superposition of magnetic fields induced by the rails and the magnetic field from the arc/armature. Whereas the armature in the railgun accelerates continuously,in the case of an electric arc, the latter is displaced between the electrodes, drag forces becomes more important and limit the arc velocity, preventing a continuous acceleration. The value of this velocity depends on many factors, the most important being the arc current, the gap and the surrounding gas. The numerical simulation results reported in this chapter demonstrate this fact. It has been evidenced that there is no continuous acceleration of the arc for the fixed (DC) current value. For a defined couple of values of the arc current and gap, there is rather a precise limit value of the arc column velocity.

In order to obtain the arc displacement along the electrodes several requirements are satisfied in the model. For example, the magnetic field has been resolved in the arc column itself, in the electrodes and a rather large volume of gas around the electrodes in order to accurately compute the Lorentz force at each point of the gap. The MHD description of the arc column implemented allows one to calculate the arc displacement self-consistently, taking the Lorentz

and drag(viscosity) forces into account. No additional data are needed. The model is able to predict the arc displacement between the electrodes self-consistently.
The model predicts the existence of two attachments, the cathode and anode roots. Each attachment forms a jet which cross in the middle of the gap, forming the arc column. The attachments move continuously in the same direction as the arc column irrespective of the electrode polarity. The calculation results have been compared with the experimental investigations in a wide variety of conditions: pulsed DC arc and AC high frequency arc. However, different experimental facilities have been used with slightly different geometrical configurations with copper and aluminium electrodes correspondingly. It is of great interest to compare the arc displacement velocity with the experimental values for a wide range of experimental conditions. In both cases, i.e. for pulsed and AC arcs, sufficiently good agreement between simulation and experimental results was obtained. Moreover, the same tendency between the model and experiment was observed:

- With a decrease in the gap, the arc velocity increases, which was observed on the experimental measurements;
- A linear dependence between the arc velocity and the arc current was found for the pulsed DC arc regime.

However, for a pulsed DC arc with currents >1 kA, there is a noticeable difference between the model and the experiment in the arc velocity, which is less pronounced for currents <1 kA.
The model of electric arc with different frequencies at a fixed arc current and electrode gap predicts the same value of maximum and minimum velocities. It was found that for the arc with $I_{max} = 600$ A at 420 Hz and 760 Hz, $V_{arc_{max}}$ is about 50 m/s. During the propagation time of 3 ms, for both frequencies the arc was found to be in the same position. Moreover, the same value was found as for the arc powered with a DC current of 600 A.
Numerical experiments for different external conditions show that the arc displacement velocity for a fixed arc current and inter-electrode distance is defined by the plasma density and viscosity. In spite of the fact that the density and viscosity are a function of the temperature, in the temperature range 6000 K to 20 000 K, this dependence does not induce significant changes. Therefore, for high current arcs and low current arcs the arc density and the viscosity are rather similar. This fact can explain the linear correlation between the arc current and the arc velocity for the given gas pressure. It was found that for lower pressures, the arc velocity is dramatically enhanced for the same arc current and inter-electrode gap. The latter finding is one of the main achievements of the present study and one of the key points for aeronautic applications. This dramatic increase in the arc speed for lower pressures can be attributed to the finding that the arc displacement velocity is defined by the arc density and viscosity.

The arc voltage from the experiment and the arc column voltage from the numerical model were also compared. Unsurprisingly, without the implementation of the electrode layers in the model, the computed arc voltage values differ from the experimental measurements. Thus, the voltage magnitude was not considered in the comparison. However, for other features of the arc voltage waveform more promising results were obtained. The decrease and increase in the voltage with the arc current are consistent in the model. The overshoots of the arc voltage when the arc current is zero are found in the simulation results and in the measurements, and, importantly, the time duration of these overshoots predicted by the simulations is the same as that measured in the experiments, i.e. about 1 ms. Interpretation of the difference between experimental and model voltages can be associated with the sum of cathode and anode voltage falls. This sum is lower for the copper electrodes, i.e. about 20 V for currents <1 kA and 10 V for Cu >1 kA. For aluminium electrodes this sum ranges from 30 V to 40 V for the whole current range up to 1.5 kA. These values are in the expected range of the known values of cathode falls for the currents used.

The model of the arc column and its interaction with the electrodes does not take the impact of electrode evaporation into account. However, during the experiment, efficient evaporation was observed, especially in the case of aluminium electrodes. In this work, the effect of the presence of the evaporated metal in the arc column was studied. The model solutions with a gas composition of 99 % air with 1 % Cu admixture were investigated, and a significant impact on the arc temperature and consequently on the arc column voltage was found. However there was no impact on the arc displacement. It can therefore be reasonably hypothesized that the evaporation of the electrode material may affect the arc displacement velocity. In the experimental conditions used here, however, a higher evaporation rate of the electrode material can be expected. With a higher evaporation rate the impact on the gas density and gas viscosity near the electrodes and the arc center may affect the arc velocity. Moreover, the results are expected to be different for Al and Cu.

The re-striking effect observed in the experiment always occurred when the arc current crossed zero. At this moment, it is very important to consider the evaporation from the cathode and anode attachments, and the residual ionization from the previous arc, as a re-strike is highly expected when higher evaporation takes place. Since the model does not take evaporation into account, the re-striking effect could not be numerically predicted.

The main goal of this work was to study the electric arc between busbar electrodes by means of numerical simulations. The model that has been developed enables the arc parameters to be self-consistently estimated and its behavior between the electrodes to be predicted. One of the main parameters required for arc detection is the arc propagation velocity. The model provides a value of the arc velocity, and excellent agreement between the model and experimental observations was found on this point. The model was designed as a tool in which the internal parameters

- arc current, the gap, the gas pressure - can be easily changed. This flexibility will allow industrial partners to use the model as a tool to investigate arc behavior in a wider range of conditions.

There is room for improvement in the model so as to give a more precise plasma prediction. For example, the compressibility of the gas, turbulence effects, eddy currents etc. could be included. However, in the author's opinion, the most significant step is the implementation of plasma-cathode interaction for a low-melting point cathode material. Not only will this specify the cathode voltage fall, it will also shed light on the fundamental mechanism of arc displacement and answer the question of whether the cathode root displacement is continuous or discontinuous...

Chapter 5

General conclusions and outlook

Investigations into electric arcs produced by different sources have been continuously reported in the literature over the last century. To accomplish the present research, the extensive bibliography dealing with electric arcs has been reviewed in order to understand arc phenomena and develop the model which reflects physically important aspects of the electric arcs.
Developing the theoretical description of electric arcs and working on its numerical resolution provide a better understanding of the arc physics and properties. To validate the model, experimental studies are essential to observe facts and to draw conclusions which support the claims made by the author and the possible further improvement of the theoretical description of the phenomena observed.
In this last chapter, the general findings and highlights of this work are summarized and several perspectives of the research are proposed.

5.1 Conclusions

Although electric arcs have been the subject of many studies over the last 100 years, some underlying mechanisms have not been fully elucidated, leaving room for further investigations. The reason for this sustained interest is the wide range of applications involving this type of discharge, particularly in industrial processes. In comparison to cold plasmas also used in industry, the electric arc plasma is significantly different. It is characterized by high temperatures (more than several tens of thousands kelvin) and high electron densities. Due to such intrinsic properties, thermal plasmas are used in different ways. A significant amount of experimental and theoretical work has been devoted to describing electric arc plasmas, providing us with a rather general picture of this phenomenon. However, every new successful investigation triggers several new ones. The aim of this work was to significantly contribute to describing the arc phenomena resulting from an electrical fault in an aeronautical framework. It is of great interest to develop work on the combined theoretical, numerical and experimental aspects of such phenomena.
The high plasma temperature and high electron densities in the electric arc validate Saha equi-

librium, and the existence of a local thermal equilibrium (LTE) of the ionized medium can therefore be safely assumed. However, this is valid only in the arc column, where the ionization and recombination processes are in equilibrium and the Boltzmann distribution is valid for all sorts of particles. On the contrary, near the electrodes and the arc fringes, equilibrium is not satisfied. Moreover the quasi-neutrality is disturbed in a very thin layer near the electrodes.
The existence of LTE in the arc column means that magneto-hydrodynamic (MHD) equations can be used to describe the main processes in the plasma. In this approach, the plasma is presented as a gas where the electromagnetic force is the main acting force. Non-linear plasma properties and transport coefficients of the LTE arc are calculated according to the equilibrium. The MHD description involves the conservation of mass, momentum and energy in order to establish the gas flow, the current conservation and Maxwell equations governing the electromagnetic interactions. This approach has been successfully used to model thermal plasmas in recent decades, producing reasonably good results and predictions. Moreover, this approach can be implemented by using recent commercial software based on finite element or finite volume formalisms. In this work, an MHD description of the plasma was adopted to establish the arc column model. As the implementation of thermal diffusion effects in the model is important for electric arcs, this has been accomplished in the current work, unlike in other studies. The resolution of the system of MHD equations was achieved numerically using the commercial software COMSOL Multiphysics® based on the finite element method.
To describe plasma-electrode interaction, it is esential to take deviation from thermal equilibrium near the electrodes into account in the complete arc model. Particular attention must be paid to the accurate description of these zones. However, models of near electrode layers are complex and require the inclusion of more data. Moreover, their numerical realization is computationally expensive. Although the model must be physically correct, it is important to avoid complex non-equilibrium models of plasma-electrode interaction. It is known that the model of non-linear surface heating of the cathode by the plasma gives reasonable results for refractory materials. This finding was used here in order to provide the correct matching conditions for the case with a refractory cathode. In comparison to the cathode, non-equilibrium effects take place in the anode layer which were taken into account with the same method of energy and current conservation, at an anode heating voltage of 6 V. In this work, the first theoretical and numerical approach to matching the LTE model of the bulk plasma with the electrodes has been successfully developed. The model reflects reasonably and fairly the physics of the plasma-electrode interaction. The accurate matching is centered around the balance equations of the energy in the non-equilibrium near-electrode layers which separate the LTE bulk plasma and the electrodes.
The model, which contains the description of the plasma, the electrodes and the plasma-electrode interaction was developed for a geometrical configuration of a refractory rod cathode

and a flat copper anode. The matching conditions were numerically implemented in the model of the arc column and successfully computed. For instance, numerical simulation of a free-burning arc in atmospheric-pressure argon plasma is reported for a current ranging from 20 A to 200 A. The simulation results were compared with those obtained with –more sophisticated– 2T and NLTE models and with experimental data found in the literature. Good agreement between the plasma temperature in the arc column was found for current values of 100 A and higher. For lower current, for example 20 A, the deviation with NLTE models is significant. This was expected since for a current of 20 A, the assumption of thermal equilibrium in the column is questionable. The arc voltage was also compared. The arc voltage values computed by the model developed in this work agree fairly well with the values obtained by the 2T and NLTE models and with the experimental data in the entire range of arc currents from 20 A to 175 A. It is important to highlight that numerical simulations based on the conventional LTE model (i.e. disregarding the near-electrode layers) will compute arc voltages far from the physical values.
The model developed in this work, including the complete description of the plasma and its interaction with the electrodes, is a significant achievement in the field of arc simulations and provides valuable input to extend numerical models. The main advantages of this model are:

- The MHD description of the arc column assumed to be in LTE, which is simpler to establish than in 2T or NLTE;
- The matching conditions are achieved by means of boundary conditions with the LTE column;
- The mesh size near the electrodes does not have any additional requirements;
- The computation time is a couple of minutes with a single computer.

The successful realization of the model of a free burning arc meant that a similar approach could be used to establish the model of the electric arc between the rail electrodes employed in aeronautics. In this case the geometrical configuration of the electrodes comprised two rail electrodes with an inter-electrode gap of 5 mm to 10 mm made of copper or aluminum. This electrode configuration involves non-stationary arc propagation along the electrodes.
The appearance and the displacement of the electric arc between rail electrodes is a topic which is usually investigated in the context of LVCBs. Both experimental and numerical investigations have been reported in the literature. Recent models use an MHD description of the arc column in LTE and particular attention is paid to the characterization of the magnetic field between the electrodes. The plasma-electrode interaction is realized using different approaches, but no consensus has been reached yet on this aspect.

In this work, efforts were made to develop the numerical model of the arc displacement between rail electrodes in the context of aeronautical applications. This required modifying the well-established model of a free burning arc. The geometrical configuration of the electrodes and the properties of air at 1 atm and lower pressures (0.1 atm) were used. The time-dependent solution of the problem was obtained for a wide range of external parameters.

In aeronautical applications the electrodes are made of material such as copper or aluminum; hence, the processes taking place on the cathode differ from those with refractory cathodes. Thus, the model of non-linear surface heating which was used previously does not correspond to the present case. The description of the plasma-cathode interaction was therefore modified. With this modification, the position and the radius of the cathode attachment were specified. In order to realize the displacement of the cathode attachment, additional conditions are required. Two methods to achieve this were used in this work and showed similar results. Finally, the numerical model is able to predict the arc column and electrode attachment displacement self-consistently according to the MHD column description and the correct matching conditions on the electrodes.

The calculation results show that the arc column and the cathode and anode attachments displace mainly due to the action of the Lorentz force and drag forces. The numerical calculations were done in a wide range of current conditions: DC, pulsed arc (pulse duration of 5 ms) and AC arc between the electrodes with gaps of 5, 8 and 20 mm. The temperature distribution at different time moments obtained from the model showed the existence of the two attachments, the cathode and anode one, which form the cathode and anode jets that cross in the gap and form the arc column. In a wide current range it was shown that the arc and the root displacements occur in one direction with nearly the same speed. The model is capable of determining the attachment velocities and the arc center velocity. It is shown that for a DC arc, in the first couple of µs the arc accelerates and moves further away with a constant speed of 10 m/s for a current of 200 A. This effect of speed "saturation" results from the action of the drag(viscosity) force.

High-speed video imaging of the electric arc obtained from the experiment made it possible to measure the arc speed as well as simultaneously observe the arc column shape. Similar to the model, two constricted attachments near the cathode and the anode were observed. Both attachments are more pronounced for the gap of 20 mm. The short arc (5 mm) has a cylindrical shape with an elongation, the so-called arc "nose", in front of one of the electrodes. This elongation occurs randomly near the cathode or the anode and is more noticeable for higher currents.

Extensive experimental and numerical investigations of a pulsed arc with current ranging from 700 A to 2 kA showed a linear correlation of the arc displacement velocity versus the arc current. When the electrode gap decreases, the arc speed increases slightly for the same current.

Comparisons of these results with experimental data obtained for the same conditions give good agreement with a tendency to overestimate the arc velocity.
The calculation results obtained for an AC electric arc between rail electrodes showed that the arc displacement is always in the same direction, whatever the polarity. For the frequencies considered in this work, at the time moment when the arc current is zero, the arc temperature in the gap remains high enough (7000 K) to provide sufficient electrical conductivity. Therefore, re-ignition of the arc after the current reaches zero is possible due to the leftover plasma in the gap, and hence a non-zero electrical conductivity. The acceleration of the arc during the rise time of the current and its deceleration during the fall time of the current are well predicted by the model. This dynamic is in excellent agreement with the experimental data recorded in the same conditions, although the model gives more stable and reproducible values of arc velocity during each period than the experiment. The re-striking of the arc was not observed in the model, in comparison with the experiment.
Since the near-cathode non-equilibrium layer is not taken into account, the model provides only the voltage of the arc column, without accounting for the falls near the electrodes. Therefore, direct comparison with the experimental data of the full arc voltage is not meaningful but is nonetheless documented. As expected, the model finds underestimated values of the arc voltage. However, the general arc voltage waveform is well reproduced as in the experiments, with the voltage overshoots at the time point when the arc current crosses zero and an almost constant voltage during the arc period.
The model predicts the arc behavior in a wide range of external parameters. The aim of the industrial partners, i.e. to investigate the impact of the different frequencies, inter-electrode gaps and lower gas pressures, is satisfied. For example, lowering the gas pressure will increase the arc propagation speed. In another case, in the considered frequency range, the arc velocity will be mainly defined by the arc current. In spite of the complexity of the arc object, it has been shown that the arc speed is mainly defined by the arc current, the inter-electrode gap, the gas density and viscosity. This work therefore enables a generalisation of our knowledge and can be a basis on which to establish a simpler analytical model in order to predict the arc position at any time moment.
The MHD model of the electric arc assumed to be in LTE developed in this work is capable of representing the arc displacement along the rail electrodes. The same conclusion can be drawn regarding the estimation of the arc displacement velocity, which gives realistic and sufficiently precise values for the arc voltage. The overestimated arc velocity obtained from the numerical simulations may result from several factors. The model assumes a weakly compressible flow with $Ma < 0.3$ which may not be valid when the arc displacement speed is around 100 m/s or above. It has been observed numerically that for currents >1 kA, a model of compressible flow should be used. Another reason for the overestimation of the arc velocity could be that turbu-

lence effects and the dissipation energy due to turbulence are neglected. Taking into account the evaporation of the electrode material for a high evaporation rate can also have a significant effect on the arc displacement.
Last but not least, to theoretically refine the arc voltage prediction and the mechanism of cathode root displacement, the near-cathode non-equilibrium layer needs to be taken into account. For this, significant efforts must be made to describe the elementary processes near the cathode. The possible implementation of such phenomena in the model is important and several perspectives are suggested in the next section.

5.2 Outlook

Beyond the significant number of experimental and theoretical studies on electric arcs reported in the literature, questions regarding the fundamental mechanisms of arc displacement along electrodes remain open. Experimental observations by various authors have often led to different conclusions rather than a unified opinion on this topic. For instance the underlying mechanism of continuous versus discontinuous cathode root displacement is regularly discussed. While it is generally agreed that the arc motion is governed by the Lorentz force, more essential questions about how the arc moves on the electrodes and whether the motion is due to the displacement of the attachments or whether it is the attachments which follow the arc column, are still unclear. As an outlook of this work, in this section, the author would like to express her opinion concerning a hypothetical arc displacement mechanism. The idea of this hypothesis comes –partly– from previous experiments by the author in the domain of vacuum arcs with the support of more recent studies focusing on the theoretical description of cathode spot [Kaufmann 17]. In atmospheric pressures in the case of cathodes made of refractory materials, the evaporation of matter is negligible and the plasma-cathode interaction can be described as in Chapter 2, where the following processes take place on the cathode surface:

- Thermal-field emission, which is the main source of electrons from the electrode to the plasma. Usually the current density is inferred from the Richardson law for a given electrode material and temperature. The correction for the Schottky effect or field enhanced thermionic emission needs to be included.

- Back-scattered electrons, which come from the near electrode layer to the electrode.

- The ions which travel from the plasma in the vicinity of the electrode into the electrode.

- Cathode attachment can exist in diffuse (as in the case treated in Chapter 2) or spot mode; however, no significant deformation of the cathode surface has been considered.

The theoretical description of most of the latter processes has already been developed. However, for cathodes made of copper and aluminium, adjustments will be required and additional parameter estimations are necessary to establish a numerical model. The computation requires knowledge about:

- The electron and ion fluxes, which are produced by ionization of the vaporized material in the electrode vicinity.
- The existence of the cathode attachment in a spot mode. Experimental study confirms this statement and shows the existence of craters on the cathode surface. This signature from the arc attachment is formed due to intensive melting of the electrode material in the cathode spot together with the existence of the Lorentz force and the plasma pressure, which is mainly caused by evaporation of the material.

Recently, a substantial model of a single cathode spot generated in a vacuum arc showed the importance of all these phenomena. Moreover, the model was capable of predicting several stages of the spot formation: melting of the cathode surface, evaporation, deformation with the presence of the crater and extinction of the spot. The existence of sputtering material was observed. It was suggested that the new spot is created by leftover plasma from the old spot, vaporized material from the new one and evaporation from the droplets. In the case of vacuum arcs, the plasma is made of electrons, neutrals and ions coming from evaporation of the electrode. In the case of arcs ignited in gas, the plasma composition is different and together with the evaporation material, atoms and ions some come from the surrounding gas. However, it is hypothesized that similar mechanism may be the essence in the atmospheric pressure arc, which can cause the arc root displacement onto the cathode surface. An interesting perspective of the present research will therefore be developed to a more complete model including a thorough description of the latter mechanisms.

Bibliography

[Alaya 15] M. Alaya, C. Chazelas, G. Mariaux & A. Vardelle. *Arc-cathode coupling in the modeling of a conventional DC plasma spray torch.* Journal of Thermal Spray Technology, vol. 24, no. 1-2, pages 3–10, 2015.

[Almeida 08] N A Almeida, M S Benilov & G V Naidis. *Unified modelling of near-cathode plasma layers in high-pressure arc discharges.* Journal of Physics D: Applied Physics, vol. 41, no. 24, page 245201, 2008.

[Almeida 09] N A Almeida, M S Benilov, U Hechtfischer & G V Naidis. *Investigating near-anode plasma layers of very high-pressure arc discharges.* Journal of Physics D: Applied Physics, vol. 42, no. 4, page 045210, 2009.

[Almeida 17] N A Almeida, M D Cunha & M S Benilov. *Computing anode heating voltage in high-pressure arc discharges and modelling rod electrodes in dc and ac regimes.* Journal of Physics D: Applied Physics, vol. 50, no. 38, page 385203, 2017.

[Amakawa 98] T Amakawa, J Jenista, J Heberlein & E Pfender. *Anode-boundary-layer behaviour in a transferred, high-intensity arc.* Journal of Physics D: Applied Physics, vol. 31, no. 20, pages 2826–2834, 1998.

[Bachmann 13] B Bachmann, R Kozakov, G Gött, K Ekkert, J-P Bachmann, J-L Marques, H Schöpp, D Uhrlandt & J Schein. *High-speed three-dimensional plasma temperature determination of axially symmetric free-burning arcs.* Journal of Physics D: Applied Physics, vol. 46, no. 12, page 125203, 2013.

[Bade 63] W. L. Bade & J. M. Yos. *Theoretical and experimental investigation of arc plasma-generation technology. Part II, vol. 1: a theoretical and experimental study of thermionic arc cathodes.* Avco Corp., Wilmington, MA, USA, Tech. Rep. ASD-TDR-62-729, 1963.

[Baeva 12] M. Baeva, R. Kozakov, S. Gorchakov & D. Uhrlandt. *Two-temperature chemically non-equilibrium modelling of transferred arcs.* Plasma Sources Science and Technology, vol. 21, no. 5, page 055027, 2012.

[Baeva 16] M Baeva, M S Benilov, N A Almeida & D Uhrlandt. *Novel non-equilibrium modelling of a DC electric arc in argon.* Journal of Physics D: Applied Physics, vol. 49, no. 24, page 245205, 2016.

[Bastiaans 85] Glenn J. Bastiaans & Raymond A. Mangold. *The calculation of electron density and temperature in Ar spectroscopic plasmas from continuum and line spectra.* Spectrochimica Acta Part B: Atomic Spectroscopy, vol. 40, no. 7, pages 885–892, 1985.

[Bauchire 97] JM Bauchire, JJ Gonzalez & A Gleizes. *Modeling of a DC plasma torch in laminar and turbulent flow.* Plasma Chemistry and Plasma Processing, vol. 17, no. 4, pages 409–432, 1997.

[Bauchire 99] JM Bauchire, JJ Gonzalez & P Proulx. *Modelling of the plasma-particle interactions in a plasma jet.* Journal of Physics D: Applied Physics, vol. 32, no. 6, pages 675–681, 1999.

[Baudoin 05] F Baudoin, JJ Gonzalez & P Checchin. *Study of the curvature of the electrical arc in low voltage breaking devices: influence of the external magnetic field.* Journal of Physics D: Applied Physics, vol. 38, no. 20, pages 3778–3791, 2005.

[Baudry 05] C Baudry, A Vardelle, G Mariaux, M Abbaoui & A Lefort. *Numerical modeling of a DC non-transferred plasma torch: Movement of the arc anode attachment and resulting anode erosion.* High Temperature Material Processes (An International Quarterly of High-Technology Plasma Processes), vol. 9, no. 1, pages 1–15, 2005.

[Benilov 95a] MS Benilov, GG Bochkarev & BV Rogov. *Modeling of diffuse current transfer in a near-electrode layer of the high-pressure molecular plasma.* IEEE Transactions on Plasma Science, vol. 23, no. 4, pages 742–749, 1995.

[Benilov 95b] MS Benilov & A Marotta. *A model of the cathode region of atmospheric pressure arcs.* Journal of Physics D: Applied Physics, vol. 28, no. 9, page 1869, 1995.

[Benilov 98] MS Benilov & GV Naidis. *Ionization layer at the edge of a fully ionized plasma.* Physical Review E, vol. 57, no. 2, page 2230, 1998.

[Benilov 02a] MS Benilov. *Theory and modelling of arc cathodes.* Plasma Sources Science and Technology, vol. 11, no. 3A, page A49, 2002.

[Benilov 02b] MS Benilov & MD Cunha. *Heating of refractory cathodes by high-pressure arc plasmas: I.* Journal of Physics D: Applied Physics, vol. 35, no. 14, page 1736, 2002.

[Benilov 03] MS Benilov & MD Cunha. *Heating of refractory cathodes by high-pressure arc plasmas: II.* Journal of Physics D: Applied Physics, vol. 36, no. 6, page 603, 2003.

[Benilov 05] MS Benilov, MD Cunha & GV Naidis. *Modelling interaction of multispecies plasmas with thermionic cathodes.* Plasma Sources Science and Technology, vol. 14, no. 3, page 517, 2005.

[Benilov 06] M S Benilov, M Carpaij & M D Cunha. *3D modelling of heating of thermionic cathodes by high-pressure arc plasmas.* Journal of Physics D: Applied Physics, vol. 39, no. 10, pages 2124–2134, 2006.

[Benilov 08] M S Benilov. *Understanding and modelling plasma–electrode interaction in high-pressure arc discharges: a review.* Journal of Physics D: Applied Physics, vol. 41, no. 14, page 144001, 2008.

[Benilov 12] M S Benilov, L G Benilova, He-Ping Li & Gui-Qing Wu. *Sheath and arc-column voltages in high-pressure arc discharges.* Journal of Physics D: Applied Physics, vol. 45, no. 35, page 355201, 2012.

[Benilov 16] M S Benilov, N A Almeida, M Baeva, M D Cunha, L G Benilova & D Uhrlandt. *Account of near-cathode sheath in numerical models of high-pressure arc discharges.* Journal of Physics D: Applied Physics, vol. 49, no. 21, page 215201, 2016.

[Benoy 93] DA Benoy. Modelling of thermal argon plasmas. Technische Universiteit Eindhoven, 1993.

[Bini 06] R Bini, M Monno & MI Boulos. *Numerical and experimental study of transferred arcs in argon.* Journal of Physics D: Applied Physics, vol. 39, no. 15, pages 3253–3266, 2006.

[Bobashev 10a] S. V. Bobashev, B. G. Zhukov, R. A. Kurakin, S. A. Ponyaev, B. I. Reznikov & S. I. Rozov. *Parameters of an erosion carbon plasma in the channel of a railgun.* Technical Physics, vol. 55, no. 12, pages 1754–1759, Dec 2010.

[Bobashev 10b] SV Bobashev, BG Zhukov, RA Kurakin, SA Ponyaev, BI Reznikov & SI Rozov. *Generation of high-velocity plasma flows in railgun channels filled with gases of various density.* Technical Physics Letters, vol. 36, no. 1, pages 72–75, 2010.

[Bobashev 16] SV Bobashev, BG Zhukov, RO Kurakin, SA Ponyaev & BI Reznikov. *The effect of external magnetic field on plasma acceleration in electromagnetic railgun channel.* Technical Physics Letters, vol. 42, no. 3, pages 309–312, 2016.

[Bott 66] JF Bott. *Spectroscopic measurement of temperatures in an argon plasma arc.* The Physics of Fluids, vol. 9, no. 8, pages 1540–1547, 1966.

[Boulos 94] MI Boulos, P Fauchais & E Pfender. Thermal plasmas: fundamentals and applications. Springer US, 1994.

[Braginskii 65] SI Braginskii. *Transport Processes in a Plasma.* Reviews of Plasma Physics, vol. 1, page 205, 1965.

[Brice 96] CW Brice, RA Dougal & JL Hudgins. *Review of technologies for current-limiting low-voltage circuit breakers.* IEEE Transactions on Industry Applications, vol. 32, no. 5, pages 1005–1010, 1996.

[Bron OB 75] Bron OB & Sushkov LK. Plasma flows in the electric arc of switching apparatus. Leningrad: Energy, 1975. in Russian.

[Brossa 88] M. Brossa & E. Pfender. *Probe measurements in thermal plasma jets.* Plasma Chemistry and Plasma Processing, vol. 8, no. 1, pages 75–90, 1988.

[Brugeat 04] S. Brugeat & H. Coitout. *Determination of electron density in a wall stabilized Ar-CO_2 thermal plasma.* The European Physical Journal D-Atomic, Molecular, Optical and Plasma Physics, vol. 28, no. 1, pages 101–107, 2004.

[Bötticher 00] R. Bötticher & W. Bötticher. *Numerical modelling of arc attachment to cathodes of high-intensity discharge lamps.* Journal of Physics D: Applied Physics, vol. 33, no. 4, page 367, 2000.

[Bötticher 01] R. Bötticher & W. Bötticher. *Numerical modelling of a dynamic mode change of arc attachment to cathodes of high-intensity discharge lamps.* Journal of Physics D: Applied Physics, vol. 34, no. 7, page 1110, 2001.

[Cassie 39] A Morris Cassie. *A new theory of rupture and circuit severity.* CIGRE report, vol. 102, pages 2–14, 1939.

[Cayla 08] F Cayla, P Freton & J-J Gonzalez. *Arc/Cathode Interaction Model.* IEEE Transactions on Plasma Science, vol. 36, no. 4, pages 1944–1954, 2008.

[Chen 94] WLT Chen, J Heberlein & E Pfender. *Diagnostics of a thermal plasma jet by optical emission spectroscopy and enthalpy probe measurements.* Plasma Chemistry and Plasma Processing, vol. 14, no. 3, pages 317–332, 1994.

[Chen 16a] T Chen, C Wang, MR Liao & WD Xia. *Diffuse and spot mode of cathode arc attachments in an atmospheric magnetically rotating argon arc.* Journal of Physics D: Applied Physics, vol. 49, no. 8, page 085202, 2016.

[Chen 16b] T Chen, C Wang, XN Zhang, H Zhang & WD Xia. *Thermal and electrical influences from bulk plasma in cathode heating modeling.* Plasma Sources Science and Technology, vol. 26, no. 2, page 025002, 2016.

[Colombo 08] V. Colombo, A. Concetti, E. Ghedini, S. Dallavalle & M. Vancini. *Understanding Plasma Fluid Dynamics Inside Plasma Torches Through Advanced Modeling.* IEEE Transactions on Plasma Science, vol. 36, no. 2, pages 389–402, 2008.

[Cressault 04] Y Cressault & A Gleizes. *Thermodynamic properties and transport coefficients in Ar–H_2–Cu plasmas.* Journal of Physics D: Applied Physics, vol. 37, no. 4, page 560, 2004.

[Cressault 13a] Y Cressault & A Gleizes. *Thermal plasma properties for Ar–Al, Ar–Fe and Ar–Cu mixtures used in welding plasmas processes: I. Net emission coefficients at atmospheric pressure.* Journal of Physics D: Applied Physics, vol. 46, no. 41, page 415206, 2013.

[Cressault 13b] Y Cressault, AB Murphy, Ph Teulet, A Gleizes & M Schnick. *Thermal plasma properties for Ar–Cu, Ar–Fe and Ar–Al mixtures used in welding plasmas processes: II. Transport coefficients at atmospheric pressure.* Journal of Physics D: Applied Physics, vol. 46, no. 41, page 415207, 2013.

[Cressault 15] Y Cressault. *Basic knowledge on radiative and transport properties to begin in thermal plasmas modelling.* AIP Advances, vol. 5, no. 5, page 057112, 2015.

[Cressault 17] Yann Cressault. *Private communication*, 2017.

[Dabringhausen 02] L Dabringhausen, D Nandelstädt, J Luhmann & J Mentel. *Determination of HID electrode falls in a model lamp I: Pyrometric measurements.* Journal of Physics D: Applied Physics, vol. 35, no. 14, pages 1621–1630, 2002.

[Dabringhausen 05a] L Dabringhausen, O Langenscheidt, S Lichtenberg, M Redwitz & J Mentel. *Different modes of arc attachment at HID cathodes: simulation and comparison with measurements.* Journal of Physics D: Applied Physics, vol. 38, no. 17, pages 3128–3142, aug 2005.

[Dabringhausen 05b] L. Dabringhausen, O. Langenscheidt, S. Lichtenberg, M. Redwitz & J. Mentel. *Different modes of arc attachment at HID cathodes: simulation and comparison with measurements.* Journal of Physics D: Applied Physics, vol. 38, no. 17, pages 3128–3142, 2005.

[Devoto 65] RS Devoto. *The Transport Properties of a Partially Ionized Monoatomic Gas.* PhD thesis, Stanford University, CA, USA, 1965.

[Devoto 66] RS Devoto. *Transport Properties of Ionized Monatomic Gases.* Physics of Fluids, vol. 9, no. 6, pages 1230–1240, 1966.

[Devoto 67] RS Devoto. *Simplified Expressions for the Transport Properties of Ionized Monatomic Gases.* Physics of Fluids, vol. 10, no. 10, pages 2105–2112, 1967.

[Devoto 73] RS Devoto. *Transport coefficients of ionized argon.* Physics of Fluids, vol. 16, no. 5, pages 616–623, 1973.

[Dinulescu 80] HA Dinulescu & E Pfender. *Analysis of the anode boundary layer of high intensity arcs.* Journal of Applied Physics, vol. 51, no. 6, pages 3149–3157, 1980.

[Domejean 97] E Domejean, P Chevrier, C Fievet & P Petit. *Arc-wall interaction modelling in a low-voltage circuit breaker.* Journal of Physics D: Applied Physics, vol. 30, no. 15, page 2132, 1997.

[Duan 02] Z Duan & J Heberlein. *Arc instabilities in a plasma spray torch.* Journal of Thermal Spray Technology, vol. 11, no. 1, pages 44–51, 2002.

[Dzierzega 06] K Dzierzega, W Zawadzki, B Pokrzywka & S Pellerin. *Experimental investigations of plasma perturbation in Thomson scattering applied to thermal plasma diagnostics.* Physical Review E, vol. 74, no. 2, page 026404, 2006.

[Eckert 67] ERG Eckert, E Pfender & SA Wutzke. *Study of electric arc behavior with superimposed flow.* AIAA Journal, vol. 5, no. 4, pages 707–713, 1967.

[Fanara 01] C Fanara & IM Richardson. *A Langmuir multi-probe system for the characterization of atmospheric pressure arc plasmas.* Journal of Physics D: Applied Physics, vol. 34, no. 18, pages 2715–2725, sep 2001.

[Fanara 04] C Fanara & L Vilarinho. *Electrical characterization of atmospheric pressure arc plasmas.* The European Physical Journal D-Atomic, Molecular, Optical and Plasma Physics, vol. 28, no. 2, pages 241–251, 2004.

[Fauchais 97] P. Fauchais & A. Vardelle. *Thermal plasmas.* IEEE Transactions on Plasma Science, vol. 25, no. 6, pages 1258–1280, Dec 1997.

[Ferziger 73] JH Ferziger, HG Kaper & EP Gross. *Mathematical Theory of Transport Processes in Gases.* American Journal of Physics, vol. 41, no. 4, pages 601–603, 1973.

[Fiévet 97] C Fiévet, M Barrault, P Petit, P Chévrier, C Fleurier & V André. *Optical diagnostics and numerical modelling of arc re-strikes in low-voltage circuit breakers.* Journal of Physics D: Applied Physics, vol. 30, no. 21, pages 2991–2999, 1997.

[Fincke 93] JR Fincke, WD Swank, SC Snyder & DC Haggard. *Enthalpy probe performance in compressible thermal plasma jets.* Review of Scientific Instruments, vol. 64, no. 12, pages 3585–3593, 1993.

[Finkelburg 61] V Finkelburg & G Mekker. *Electric arcs and thermal plasma.* Publishing House of Foreign Literature, 1961.

[Franceries 05] X Franceries, F Lago, JJ Gonzalez, P Freton & M Masquere. *3-D visualization of a 3-D free-burning arc model deflected by external magnetic or convective forces.* IEEE Transactions on Plasma Science, vol. 33, no. 2, pages 432–433, 2005.

[Freton 03] P Freton, J J Gonzalez, F Camy Peyret & A Gleizes. *Complementary experimental and theoretical approaches to the determination of the plasma characteristics in a cutting plasma torch.* Journal of Physics D: Applied Physics, vol. 36, no. 11, pages 1269–1283, 2003.

[Freton 09] P Freton & JJ Gonzalez. *Overview of Current Research into Low-Voltage Circuit Breakers.* The Open Plasma Physics Journal, vol. 2, no. 2, pages 105–119, 2009.

[Freton 11] P Freton, JJ Gonzalez, M Masquère & Frank Reichert. *Magnetic field approaches in dc thermal plasma modelling.* Journal of Physics D: Applied Physics, vol. 44, no. 34, page 345202, 2011.

[Fridman 07] A. Fridman & Young I. Cho. Advances in heat transfer, volume 40 of *Advances in Heat Transfer*. Elsevier/Academic Press, Amsterdam, 1st edition, 2007.

[Gleizes 92] A. Gleizes, J. J. Gonzalez, M. Razafinimanana & T. Robert. *Influence of radiation on temperature field calculation in SF 6 arcs*. Plasma Sources Science and Technology, vol. 1, no. 2, page 135, 1992.

[Gleizes 05] A. Gleizes, J. J. Gonzalez & P. Freton. *Thermal plasma modelling*. Journal of Physics D: Applied Physics, vol. 38, no. 9, page R153, May 2005.

[Golant 77] VE Golant, AP Zhilinskii & IE Sakharov. *The Basis of Plasma Physics*. Atomizdat, Moscow (in Russian), 1977.

[Gonzalez 93] JJ Gonzalez, A Gleizes, P Proulx & M Boulos. *Mathematical modeling of a free-burning arc in the presence of metal vapor*. Journal of Applied Physics, vol. 74, no. 5, pages 3065–3070, 1993.

[Gonzalez 97] JJ Gonzalez, M Bouaziz, M Razafinimanana & A Gleizes. *The influence of iron vapour on an argon transferred arc*. Plasma Sources Science and Technology, vol. 6, no. 1, pages 20–28, feb 1997.

[Gonzalez 02] J J Gonzalez, P Freton & A Gleizes. *Comparisons between two- and three-dimensional models: gas injection and arc attachment*. Journal of Physics D: Applied Physics, vol. 35, no. 24, pages 3181–3191, 2002.

[Gonzalez 09] JJ Gonzalez, F Cayla, P Freton & P Teulet. *Two-dimensional self-consistent modelling of the arc/cathode interaction*. Journal of Physics D: Applied Physics, vol. 42, no. 14, page 145204, 2009.

[Gray 15] Miles D Gray, Young-Joon Choi, Jayant Sirohi & Laxminarayan L Raja. *Structure of propagating arc in a magneto-hydrodynamic rail plasma actuator*. Journal of Physics D: Applied Physics, vol. 49, no. 1, page 015202, 2015.

[Griem 63] Hans R. Griem. *Validity of Local Thermal Equilibrium in Plasma Spectroscopy*. Physical Review, vol. 131, no. 3, pages 1170–1176, 1963.

[Griem 05] H.R. Griem. Principles of plasma spectroscopy. Cambridge University Press, 2005.

[Guile 57] AE Guile & SF Mehta. *Arc movement due to the magnetic field of current flowing in the electrodes*. Proceedings of the IEE-Part A: Power Engineering, vol. 104, no. 18, pages 533–540, 1957.

[Guillot 01] S Guillot, JM Bauchire, E Le Menn, C Fievet, F Gentil & C Fleurier. *Experimental diagnostic of a low-voltage circuit breaker.* In 15$^{\text{th}}$ International Symposium on Plasma Chemistry (ISPC15), volume PO 3.75, page 1097, Orléans, France, 2001. Conference proceedings.

[Habedank 93] U Habedank. *Application of a new arc model for the evaluation of short-circuit breaking tests.* IEEE Transactions on Power Delivery, vol. 8, no. 4, pages 1921–1925, 1993.

[Haddad 84] GN Haddad & AJD Farmer. *Temperature determinations in a free-burning arc. I. Experimental techniques and results in argon.* Journal of Physics D: Applied Physics, vol. 17, no. 6, pages 1189–1196, 1984.

[Haidar 96] J Haidar & JJ Lowke. *Predictions of metal droplet formation in arc welding.* Journal of Physics D: Applied Physics, vol. 29, no. 12, pages 2951–2960, 1996.

[Haidar 99] J Haidar. *Non-equilibrium modelling of transferred arcs.* Journal of Physics D: Applied Physics, vol. 32, no. 3, pages 263–272, jan 1999.

[Hartmann 01a] R M Hartmann & J V Heberlein. *Experimental investigation of anodic arc attachment instabilities.* In 15$^{\text{th}}$ International Symposium on Plasma Chemistry (ISPC15), 2001.

[Hartmann 01b] R M Hartmann & J V Heberlein. *Quantitative investigations on arc-anode attachments in transferred arcs.* Journal of Physics D: Applied Physics, vol. 34, no. 19, page 2972, 2001.

[Heberlein 09] J Heberlein, J Mentel & E Pfender. *The anode region of electric arcs: a survey.* Journal of Physics D: Applied Physics, vol. 43, no. 2, page 023001, 2009.

[Heller 35] G Heller. *Dynamical similarity laws of the mercury high pressure discharge.* Physics, vol. 6, no. 12, pages 389–394, 1935.

[Hiraoka 97] K Hiraoka, T Shiwaku & T Ohji. *Determining temperature distributions of gas tungsten arc (TIG) plasma by spectroscopic methods.* Welding international, vol. 11, no. 9, pages 688–696, 1997.

[Hirschfelder 64] Joseph O. Hirschfelder, Charles F. Curtiss & R. Byron Bird. The molecular theory of gases and liquids. Wiley-Interscience, 1964.

[Hong 02a] D. Hong, G. Sandolache, J. M. Bauchire, E. Le Menn & C. Fleurier. *Broad band optical absorption spectroscopy investigations in a low-voltage circuit breaker*

using an ultra-bright source produced by a fast electric discharge. In IEEE Conference Record - Abstracts. 2002 IEEE International Conference on Plasma Science (Cat. No.02CH37340), pages 271–, May 2002.

[Hong 02b] D Hong, G Sandolache, K Lan, JM Bauchire, E Le Menn & C Fleurier. *A radiation source developed for broad band optical absorption spectroscopy measurements.* Plasma Sources Science and Technology, vol. 12, no. 1, page 1, 2002.

[Hong 05] Dunpin Hong, Gabriela Sandolache, J-M Bauchire, François Gentils & Claude Fleurier. *A new optical technique for investigations of low-voltage circuit breakers.* IEEE transactions on plasma science, vol. 33, no. 2, pages 976–981, 2005.

[Hsu 83a] KC Hsu, K Etemadi & E Pfender. *Study of the free-burning high-intensity argon arc.* Journal of Applied Physics, vol. 54, no. 3, pages 1293–1301, 1983.

[Hsu 83b] KC Hsu & E Pfender. *Analysis of the cathode region of a free-burning high intensity argon arc.* Journal of Applied Physics, vol. 54, no. 7, pages 3818–3824, 1983.

[Hsu 83c] KC Hsu & E Pfender. *Two-temperature modeling of the free-burning, high-intensity arc.* Journal of Applied Physics, vol. 54, no. 8, pages 4359–4366, 1983.

[Huang 08] H Huang, W Pan, Z Guo & C Wu. *Laminar/Turbulent Plasma Jets Generated at Reduced Pressure.* IEEE Transactions on Plasma Science, vol. 36, no. 4, pages 1052–1053, 2008.

[Hundertmark 13] S Hundertmark, M Schneider, D Simicic & G Vincent. *Experiments to Increase the Used Energy With the PEGASUS Railgun.* In 2013 19th IEEE Pulsed Power Conference (PPC), volume 42, pages 3180–3185. IEEE, jun 2013.

[Jenista 97] J. Jenista, J.V.R. Heberlein & E. Pfender. *Numerical model of the anode region of high-current electric arcs.* IEEE Transactions on Plasma Science, vol. 25, no. 5, pages 883–890, October 1997.

[Karetta 98] F Karetta & M Lindmayer. *Simulation of the gasdynamic and electromagnetic processes in low voltage switching arcs.* IEEE Transactions on Components, Packaging, and Manufacturing Technology: Part A, vol. 21, no. 1, pages 96–103, 1998.

[Kaufmann 17] HTC Kaufmann, MD Cunha, MS Benilov, W Hartmann & N Wenzel. *Detailed numerical simulation of cathode spots in vacuum arcs: Interplay of different mechanisms and ejection of droplets.* Journal of Applied Physics, vol. 122, no. 16, page 163303, 2017.

[Khrabry 17] A. Khrabry, I. Kaganovich, V. Nemchinsky & A. Khodak. *Investigation of a short argon arc with hot anode. Part I: numerical simulations of non-equilibrium effects in the near-electrode regions.* arXiv.org, vol. 1708.01301, 2017. arXiv: 1708.01301.

[Kirkbright 82] Gordon F Kirkbright. *Some recent studies in optical emission and absorption spectroscopy for trace analysis.* Pure and Applied Chemistry, vol. 54, no. 4, pages 769–786, 1982.

[Koyama 93] K Koyama, H Toya, Y Wada & A Hasegawa. *Arc behavior driven by electromagnetic force between rail electrodes.* IEEE transactions on magnetics, vol. 29, no. 1, pages 843–847, 1993.

[Kozakov 13] R Kozakov, G Gött, H Schöpp, D Uhrlandt, M Schnick, M Häßler, U Füssel & S Rose. *Spatial structure of the arc in a pulsed GMAW process.* Journal of Physics D: Applied Physics, vol. 46, no. 22, page 224001, 2013.

[Kühn 02] G Kühn, F Könemann & M Kock. *2D display of tungsten impurity in a free-burning arc using laser-induced fluorescence.* Journal of Physics D: Applied Physics, vol. 35, no. 17, pages 2096–2104, 2002.

[Kuiken 91] HK Kuiken. *An asymptotic treatment of the Elenbaas–Heller equation for a radiating wall-stabilized high-pressure gas-discharge arc.* Journal of Applied Physics, vol. 70, no. 10, pages 5282–5291, 1991.

[Kühn-Kauffeldt 14] M Kühn-Kauffeldt, J L Marquès & J Schein. *Time resolved Thomson scattering diagnostic of pulsed gas metal arc welding (GMAW) process.* In Journal of Physics: Conference Series, volume 550, page 012006. IOP Publishing, IOP Publishing, 2014.

[Lago 04] F Lago, JJ Gonzalez, P Freton & A Gleizes. *A numerical modelling of an electric arc and its interaction with the anode: Part I. The two-dimensional model.* Journal of Physics D: Applied Physics, vol. 37, no. 6, pages 883–897, feb 2004.

[Lago 06] F Lago, J J Gonzalez, P Freton, F Uhlig, N Lucius & G P Piau. *A numerical modelling of an electric arc and its interaction with the anode: part III. Application to the interaction of a lightning strike and an aircraft in flight.* Journal of Physics D: Applied Physics, vol. 39, no. 10, pages 2294–2310, 2006.

[Landau 69] LD Landau & EM Lifshitz. Theoretical physics. hydrodynamics. Moscow Nauka, 1969. in Russian.

[Langmuir 29] Irving Langmuir. *The interaction of electron and positive ion space charges in cathode sheaths.* Physical Review, vol. 33, no. 6, page 954, 1929.

[Li 07] He-Ping Li & M. S. Benilov. *Effect of a near-cathode sheath on heat transfer in high-pressure arc plasmas.* Journal of Physics D: Applied Physics, vol. 40, no. 7, pages 2010–2017, 2007.

[Liao 16] MR Liao, H Li & WD Xia. *Approximate explicit analytic solution of the Elenbaas-Heller equation.* Journal of Applied Physics, vol. 120, no. 6, page 063304, 2016.

[Lichtenberg 05] S Lichtenberg, L Dabringhausen, O Langenscheidt & J Mentel. *The plasma boundary layer of HID-cathodes: modelling and numerical results.* Journal of Physics D: Applied Physics, vol. 38, no. 17, pages 3112–3127, 2005.

[Lincun 08] Li Lincun & Xia Weidong. *Time-Dependent 2D Modeling of Magnetron Plasma Torch in Turbulent Flow.* Plasma Science and Technology, vol. 10, no. 3, pages 328–335, 2008.

[Lindmayer 96] Manfred Lindmayer & Joachim Paulke. *Arc motion and pressure formation in low voltage switchgear.* In Electrical Contacts, 1996. Proceedings of the Forty-Second IEEE Holm Conference on¿. Joint with the 18th International Conference on Electrical Contacts, pages 17–26. IEEE, 1996.

[Lindmayer 02] M. Lindmayer & M. Springstubbe. *Three-dimensional-simulation of arc motion between arc runners including the influence of ferromagnetic material.* IEEE Transactions on Components and Packaging Technologies, vol. 25, no. 3, pages 409–414, 2002.

[Lindmayer 06] M Lindmayer, E Marzahn, A Mutzke, T Ruther & M Springstubbe. *The process of arc splitting between metal plates in low voltage arc chutes.* IEEE Transactions on Components and Packaging Technologies, vol. 29, no. 2, pages 310–317, 2006.

[Lisnyak 17] M. Lisnyak, M. D. Cunha, J.-M. Bauchire & M. S. Benilov. *Numerical modelling of high-pressure arc discharges: matching the LTE arc core with the electrodes.* Journal of Physics D: Applied Physics, vol. 50, no. 31, page 315203, 2017.

[Lister 04] G. Lister, J. Lawler, W. Lapatovich & V. Godyak. *The physics of discharge lamps.* Reviews of Modern Physics, vol. 76, no. 2, pages 541–598, 2004.

[Lochte-Holtgreven 68] W. Lochte-Holtgreven. Plasma diagnostics. North-Holland / Wiley, 1968.

[Lowke 74] JJ Lowke. *Predictions of arc temperature profiles using approximate emission coefficients for radiation losses.* Journal of Quantitative Spectroscopy and Radiative Transfer, vol. 14, no. 2, pages 111–122, 1974.

[Lowke 97] JJ Lowke, R Morrow & J Haidar. *A simplified unified theory of arcs and their electrodes.* Journal of Physics D: Applied Physics, vol. 30, no. 14, pages 2033–2042, 1997.

[Lowke 06] JJ Lowke & M Tanaka. *LTE-diffusion approximation for arc calculations.* Journal of Physics D: Applied Physics, vol. 39, no. 16, pages 3634–3643, 2006.

[Luhmann 02] J Luhmann, S Lichtenberg, O Langenscheidt, MS Benilov & J Mentel. *Determination of HID electrode falls in a model lamp II: Langmuir-probe measurements.* Journal of Physics D: Applied Physics, vol. 35, no. 14, pages 1631–1638, 2002.

[Ma 09] Q Ma, M Rong, AB Murphy, Y Wu & T Xu. *Simulation study of the influence of wall ablation on arc behavior in a low-voltage circuit breaker.* IEEE Transactions on Plasma Science, vol. 37, no. 1, pages 261–269, 2009.

[Marković 13] Nenad Marković, Slobodan Bjelić, Jeroslav Živanić & Uroš Jakšić. *Numerical simulation and analytical model of electrical arc impedance in the transient processes.* Przegląd Elektrotechniczny, vol. 89, no. 2a, pages 113–117, 2013.

[Marshall 97] RA Marshall. *The distributed energy store railgun, its efficiency, and its energy store implications.* IEEE Transactions on Magnetics, vol. 33, no. 1, pages 582–588, 1997.

[Masquere 07] M Masquere, P Freton & JJ Gonzalez. *Theoretical study in two dimensions of the energy transfer between an electric arc and an anode material.* Journal of Physics D: Applied Physics, vol. 40, no. 2, pages 432–446, jan 2007.

[McBride 01] JW McBride & PM Weaver. *Review of arcing phenomena in low voltage current limiting circuit breakers.* IEE Proceedings - Science, Measurement and Technology, vol. 148, no. 1, pages 1–7, jan 2001.

[McBride 02] John W McBride, Kesorn Pechrach & Paul M Weaver. *Arc motion and gas flow in current limiting circuit breakers operating with a low contact switching velocity.* IEEE Transactions on Components and Packaging Technologies, vol. 25, no. 3, pages 427–433, sep 2002.

[McNab 01] IR McNab, S Fish & F Stefani. *Parameters for an electromagnetic naval railgun.* IEEE Transactions on Magnetics, vol. 37, no. 1, pages 223–228, Jan 2001.

[Mendys 11] A Mendys, K Dzierżega, M Grabiec, S Pellerin, B Pokrzywka, G Travaillé & B Bousquet. *Investigations of laser-induced plasma in argon by Thomson scattering.* Spectrochimica Acta Part B: Atomic Spectroscopy, vol. 66, no. 9-10, pages 691–697, September 2011.

[Meunier 83] G Meunier, J Sabonnadiere, J Coulomb & E Belbel. *Magnetic field computation for electric arc modelling.* IEEE Transactions on Magnetics, vol. 19, no. 6, pages 2593–2595, 1983.

[Meunier 84] G Meunier & A Abri. *A model for the current interruption of an electric arc.* IEEE Transactions on Magnetics, vol. 20, no. 5, pages 1956–1958, 1984.

[Mitchner 73] M Mitchner & CH Kruger. Partially ionized gases (wiley series in plasma physics). John Wiley & Sons Inc, 1973.

[Mitrofanov 07] NK Mitrofanov & SM Shkol'nik. *Two forms of attachment of an atmospheric-pressure direct-current arc in argon to a thermionic cathode.* Technical Physics, vol. 52, no. 6, pages 711–720, 2007.

[Modest 13] MF Modest. Radiative heat transfer. Academic press, 3rd edition, 2013.

[ModirKhazeni 15] SM ModirKhazeni & JP Trelles. *Towards a comprehensive modelling and simulation approach for turbulent non-equilibrium plasma flows.* In Proceedings of 22nd international symposium on plasma chemistry, Antwerp, Belgium, 2015.

[Moreau 06] E Moreau, C Chazelas, G Mariaux & A Vardelle. *Modeling the Restrike Mode Operation of a DC Plasma Spray Torch.* Journal of Thermal Spray Technology, vol. 15, no. 4, pages 524–530, 2006.

[Morrow 93] R Morrow & JJ Lowke. *A one-dimensional theory for the electrode sheaths of electric arcs.* Journal of Physics D: Applied Physics, vol. 26, no. 4, pages 634–642, 1993.

[Mougenot 13] J Mougenot, JJ Gonzalez, P Freton & M Masquère. *Plasma–weld pool interaction in tungsten inert-gas configuration.* Journal of Physics D: Applied Physics, vol. 46, no. 13, page 135206, 2013.

[Murphy 92] AB Murphy & AJD Farmer. *Temperature measurement in thermal plasmas by Rayleigh scattering.* Journal of Physics D: Applied Physics, vol. 25, no. 4, pages 634–643, 1992.

[Murphy 94] AB Murphy. *Modified Fowler–Milne method for the spectroscopic measurement of temperature and composition of multielement thermal plasmas.* Review of Scientific Instruments, vol. 65, no. 11, pages 3423–3427, 1994.

[Murphy 09] A B Murphy, M Tanaka, K Yamamoto, S Tashiro, T Sato & J J Lowke. *Modelling of thermal plasmas for arc welding: the role of the shielding gas properties and of metal vapour.* Journal of Physics D: Applied Physics, vol. 42, no. 19, page 194006, 2009.

[Murphy 11] Anthony B Murphy. *A self-consistent three-dimensional model of the arc, electrode and weld pool in gas–metal arc welding.* Journal of Physics D: Applied Physics, vol. 44, no. 19, page 194009, 2011.

[Murphy 14] Anthony B Murphy & Eugene Tam. *Thermodynamic properties and transport coefficients of arc lamp plasmas: argon, krypton and xenon.* Journal of Physics D: Applied Physics, vol. 47, no. 29, page 295202, 2014.

[Nagulin 15] KY Nagulin, DS Akhmetshin, AK Gilmutdinov & RA Ibragimov. *Three-dimensional modeling and schlieren visualization of pure Ar plasma flow in inductively coupled plasma torches.* Journal of Analytical Atomic Spectrometry, vol. 30, no. 2, pages 360–367, 2015.

[Nazarenko I 00] Nazarenko I. Habilitational work. Moscow, 2000.

[Nazarenko 89] IP Nazarenko & IG Panevin. *Analysis of the Near-Anode Processes Characters in Argon Arc Discharges of High Pressure.* Contributions to Plasma Physics, vol. 29, no. 3, pages 251–261, 1989.

[Nemchinskii 77] VA Nemchinskii & LN Peretts. *Anode sheath in a high-pressure, high-current arc.* Soviet Physics Technical Physics, vol. 22, pages 1868–1875, 1977.

[Nemchinsky 94] V A Nemchinsky. *Plasma parameters near a small anode in a high-pressure arc (gas metal arc welding).* Journal of Physics D: Applied Physics, vol. 27, no. 12, pages 2515–2521, 1994.

[Neumann 87] Werner Neumann. The mechanism of the thermoemitting arc cathode. Akademie-Verlag, 1987.

[Nordborg 08] H Nordborg & A A Iordanidis. *Self-consistent radiation based modelling of electric arcs: I. Efficient radiation approximations.* Journal of Physics D: Applied Physics, vol. 41, no. 13, page 135205, 2008.

[Nosov G V 13] Luss A A Nosov G V. *Determination of railgun parameters. Part 3. Computation at pereodic nonsinusoidal current.* Tomsk polytechnical university, vol. 323, no. 4, pages 166–171, 2013.

[Nosov 13] G V Nosov. *Determination of railgun parameters. Part 1. Computation at constant current densities.* Tomsk polytechnical university, vol. 323, no. 4, 2013.

[Numano 90] M. Numano. *Criteria for local thermodynamic equilibrium distributions of populations of excited atoms in a plasma.* Journal of Quantitative Spectroscopy and Radiative Transfer, vol. 43, no. 4, pages 311 – 317, 1990.

[Park 04] Jin Myung Park, Keun Su Kim, Tae Hyung Hwang & Sang Hee Hong. *Three-dimensional modeling of arc root rotation by external magnetic field in non-transferred thermal plasma torches.* IEEE Transactions on Plasma Science, vol. 32, no. 2, pages 479–487, April 2004.

[Pfender 91] E Pfender, J Fincke & R Spores. *Entrainment of cold gas into thermal plasma jets.* Plasma Chemistry and Plasma Processing, vol. 11, no. 4, pages 529–543, 1991.

[Prevosto 10] L Prevosto, G Artana, B Mancinelli & H Kelly. *Schlieren technique applied to the arc temperature measurement in a high energy density cutting torch.* Journal of Applied Physics, vol. 107, no. 2, page 023304, 2010.

[Qiang 08] Ma Qiang, Rong Mingzhe, Wu Yi, Xu Tiejun & Sun Zhiqiang. *Influence of copper vapor on low-voltage circuit breaker arcs during stationary and moving states.* Plasma Science and Technology, vol. 10, no. 3, page 313, 2008.

[Quéméneur 15] J Quéméneur, P Freton, M Masquère, JJ Gonzalez & P Joyeux. *Cathode Arc Root Movement: Models Comparison.* Plasma phys. & technol., vol. 2, 2015.

[Quéméneur 16] J. Quéméneur. *Etude des forces à l'origine du déplacement d'un arc électrique dans un disjoncteur basse-tension*. PhD thesis, Université Paul Sabatier-Toulouse III, 2016.

[Quéméneur 17] J. Quéméneur, P. Freton, J-J. Gonzalez & P. Joyeux. *Experimental and numerical study of arc commutation and restrikes in Low-Voltage Circuit Breaker*. ICPIG, 2017.

[Rachard 99] Helene Rachard, Pierre Chevrier, Daniel Henry & Denis Jeandel. *Numerical study of coupled electromagnetic and aerothermodynamic phenomena in a circuit breaker electric arc*. International Journal of Heat and Mass Transfer, vol. 42, no. 9, pages 1723–1734, 1999.

[Rahmane 95] Mohamed Rahmane, Gervais Soucy & Maher I Boulos. *Analysis of the enthalpy probe technique for thermal plasma diagnostics*. Review of scientific instruments, vol. 66, no. 6, pages 3424–3431, 1995.

[Raizer 87] Yu P Raizer. *Physics of gas discharge*, 1987.

[Ray 89] Pradosh K Ray. *Arc restrike in the rail accelerator*. IEEE Transactions on Magnetics, vol. 25, no. 1, pages 485–488, 1989.

[Redwitz 05] M Redwitz, O Langenscheidt & J Mentel. *Spectroscopic investigation of the plasma boundary layer in front of HID-electrodes*. Journal of Physics D: Applied Physics, vol. 38, no. 17, page 3143, 2005.

[Rethfeld 96] B. Rethfeld, J. Wendelstorf, T. Klein & G. Simon. *A self-consistent model for the cathode fall region of an electric arc*. Journal of Physics D: Applied Physics, vol. 29, no. 1, page 121, 1996.

[Rondot 09a] Loïc Rondot. *Modélisation magneto-hydrodynamique par la méthode des volumes finis: Application aux plasmas de coupure*. PhD thesis, Institut National Polytechnique de Grenoble-INPG, 2009.

[Rondot 09b] Loïc Rondot, Vincent Mazauric, Yves Delannoy & Gerard Meunier. *Dedicating finite volume method to electromagnetic plasma modeling: circuit breaker application*. IEEE Transactions on Magnetics, vol. 45, no. 3, pages 1262–1265, 2009.

[Rondot 14] Loic Rondot, Olivier Chadebec & Gérard Meunier. *3-D magnetostatic moment method dedicated to arc interruption process modeling*. IEEE Transactions on Magnetics, vol. 50, no. 2, pages 941–944, 2014.

[Rong 05] Mingzhe Rong, Yi Wu, Qian Yang, Guangxia Hu, Shengli Jia & Jianhua Wang. *Simulation on arc movement under effects of quenching chamber configuration and magnetic field for low-voltage circuit breaker.* IEICE transactions on electronics, vol. 88, no. 8, pages 1577–1583, 2005.

[Rong 08] M Rong, Y Wu, Y Fei, Z Sun, W Wang & X Wang. *The research of electric arc simulation in low voltage switching devices.* In Gas Discharges and Their Applications, 2008. GD 2008. 17th International Conference on, pages 9–16. IEEE, 2008.

[Rong 10] Mingzhe Rong, Fei Yang, Yi Wu, Anthony B Murphy, Weizong Wang & Jin Guo. *Simulation of arc characteristics in miniature circuit breaker.* IEEE Transactions on Plasma Science, vol. 38, no. 9, pages 2306–2311, 2010.

[Rosenwasser 91] Stuart N Rosenwasser. *Recent advances in large railgun structures and materials technology.* IEEE transactions on magnetics, vol. 27, no. 1, pages 444–451, 1991.

[Rouffet 10] ME Rouffet, M Wendt, G Goett, R Kozakov, H Schoepp, KD Weltmann & D Uhrlandt. *Spectroscopic investigation of the high-current phase of a pulsed GMAW process.* Journal of Physics D: Applied Physics, vol. 43, no. 43, page 434003, 2010.

[Sanders 84] NA Sanders & E Pfender. *Measurement of anode falls and anode heat transfer in atmospheric pressure high intensity arcs.* Journal of Applied Physics, vol. 55, no. 3, pages 714–722, 1984.

[Sansonnens 00] L Sansonnens, J Haidar & JJ Lowke. *Prediction of properties of free burning arcs including effects of ambipolar diffusion.* Journal of Physics D: Applied Physics, vol. 33, no. 2, page 148, 2000.

[Schmitz 01] H. Schmitz & K.-U. Riemann. *Consistent analysis of the boundary layer of a Saha plasma.* Journal of Physics D: Applied Physics, vol. 34, no. 8, page 1193, 2001.

[Schmitz 02] H. Schmitz & K.-U. Riemann. *Analysis of the cathodic region of atmospheric pressure discharges.* Journal of Physics D: Applied Physics, vol. 35, no. 14, page 1727, 2002.

[Schnehage 82] SE Schnehage, M Kock & E Schulz-Gulde. *The continuous emission of an argon arc.* Journal of Physics B: Atomic and Molecular Physics, vol. 15, no. 7, page 1131, 1982.

[Secker 59] PE Secker & AE Guile. *Arc movement in a transverse magnetic field at atmospheric pressure.* Proceedings of the IEE-Part A: Power Engineering, vol. 106, no. 28, pages 311–320, 1959.

[Shaw 06] BD Shaw. *Regular perturbation solution of the Elenbaas-Heller equation.* Journal of applied physics, vol. 99, no. 3, page 034906, 2006.

[Shigeta 16] Masaya Shigeta. *Turbulence modelling of thermal plasma flows.* Journal of Physics D: Applied Physics, vol. 49, no. 49, page 493001, 2016.

[Shirvan 16] Alireza Javidi Shirvan & Isabelle Choquet. *A review of cathode-arc coupling modeling in GTAW.* Welding in the World, vol. 60, no. 4, pages 821–835, 2016.

[Shkol'nik 11] Sergey M. Shkol'nik. *Anode phenomena in arc discharges: a review.* Plasma Sources Science and Technology, vol. 20, no. 1, page 013001, February 2011.

[Siaenen 11] T. Siaenen, M. G. Schneider & M. J. Loffler. *Rail Gun Muzzle Velocity Control With High Accuracy.* IEEE Transactions on Plasma Science, vol. 39, no. 1, pages 133–137, Jan 2011.

[Snyder 93] SC Snyder, GD Lassahn & LD Reynolds. *Direct evidence of departure from local thermodynamic equilibrium in a free-burning arc-discharge plasma.* Physical Review E, vol. 48, no. 5, page 4124, 1993.

[Swierczynski 04] B Swierczynski, JJ Gonzalez, Ph Teulet, P Freton & A Gleizes. *Advances in low-voltage circuit breaker modelling.* Journal of Physics D: Applied Physics, vol. 37, no. 4, page 595, 2004.

[Tanaka 03] Manabu Tanaka, Hidenori Terasaki, Masao Ushio & John J Lowke. *Numerical study of a free-burning argon arc with anode melting.* Plasma Chemistry and Plasma Processing, vol. 23, no. 3, pages 585–606, 2003.

[Tanaka 06] M Tanaka & JJ Lowke. *Predictions of weld pool profiles using plasma physics.* Journal of Physics D: Applied Physics, vol. 40, no. 1, page R1, 2006.

[Tanaka 10] M Tanaka, K Yamamoto, S Tashiro, K Nakata, E Yamamoto, K Yamazaki, K Suzuki, A B Murphy & J J Lowke. *Time-dependent calculations of molten pool formation and thermal plasma with metal vapour in gas tungsten arc welding.* Journal of Physics D: Applied Physics, vol. 43, no. 43, page 434009, 2010.

[Team 04] Lectromec Team. *The life of an aircraft wire and aircraft wire degradation.* https://www.lectromec.com/the-life-of-an-aircraft-wire-and-aircraft-wire-degradation/, 2004.

[Teste 95] Ph Teste, T Leblanc & J-P Chabrerie. *Study of the arc root displacement and three-dimensional modelling of the thermal phenomena occurring in a hollow cathode submitted to an electric moving arc.* Journal of Physics D: Applied Physics, vol. 28, no. 5, page 888, 1995.

[Thomas 15] R Thomas, DJP Lahaye, C Vuik & L Van der Sluis. *Simulation of arc models with the block modelling method.* In Submitted to the International Conference on Power Systems Transients, IPST 2015, Cavtat, Croatia, June 15-18, 2015. University of Zagreb, 2015.

[Touloukian 70] Y. S. Touloukian, R. W. Powell, C. Y. Ho & P. G. Klemens. *Thermophysical Properties of Matter - The TPRC Data Series. Volume 1. Thermal Conductivity - Metallic Elements and Alloys.* Rapport technique, (Thermophysical Properties of Matter vol 1) (New York–Washington: IFI/Plenum), 1970.

[Trelles 07] JP Trelles, E Pfender & JVR Heberlein. *Modelling of the arc reattachment process in plasma torches.* Journal of Physics D: Applied Physics, vol. 40, no. 18, page 5635, 2007.

[Trelles 08a] JP Trelles, JVR Heberlein & E Pfender. *The reattachment process in nonequilibrium arc simulations.* IEEE Transactions on Plasma Science, vol. 36, no. 4, pages 1024–1025, 2008.

[Trelles 08b] Juan Pablo Trelles, Emil Pfender & Joachim VR Heberlein. *Thermal nonequilibrium simulation of an arc plasma jet.* IEEE Transactions on Plasma Science, vol. 36, no. 4, pages 1026–1027, 2008.

[Trelles 13a] J P Trelles. *Formation of self-organized anode patterns in arc discharge simulations.* Plasma Sources Science and Technology, vol. 22, no. 2, page 025017, 2013.

[Trelles 13b] Juan Pablo Trelles. *Computational study of flow dynamics from a dc arc plasma jet.* Journal of Physics D: Applied Physics, vol. 46, no. 25, page 255201, 2013.

[Trelles 14] Juan Pablo Trelles & S Mahnaz Modirkhazeni. *Variational multiscale method for nonequilibrium plasma flows.* Computer Methods in Applied Mechanics and Engineering, vol. 282, pages 87–131, 2014.

[Valensi 10] Flavien Valensi, Stéphane Pellerin, Amar Boutaghane, Krzysztof Dzierzega, Sylwia Zielinska, Nadia Pellerin & Francis Briand. *Plasma diagnostics in gas*

metal arc welding by optical emission spectroscopy. Journal of Physics D: Applied Physics, vol. 43, no. 43, page 434002, 2010.

[Valensi 11] Flavien Valensi, Stéphane Pellerin, Amar Boutaghane, Krzysztof Dzierzega, Nadia Pellerin & Francis Briand. *LTE Experimental validation in a gas metal arc welding plasma column.* Contributions to Plasma Physics, vol. 51, no. 2-3, pages 293–296, 2011.

[van der Mullen 90] JAM van der Mullen. *Excitation equilibria in plasmas; a classification.* Physics Reports, vol. 191, no. 2-3, pages 109–220, 1990.

[Veklich 13] A Veklich, A Ivanisik & A Lebid. *Laser absorption spectroscopy of electric arc discharge plasma with copper impurities.* Vestnik Kievskoi Nacionalnoi accademii, vol. 1, no. 1, pages 7–11, 2013.

[Velleaud 89] G Velleaud, A Laurent & M Mercier. *A study of the kinematics of a low-voltage breaking self-blown arc: analysis of the derivative of the anode-cathode voltage.* Journal of Physics D: Applied Physics, vol. 22, no. 7, page 933, 1989.

[Velleaud 95] G Velleaud, Dominique Pezaire, Alain Laurent, Michel Mercier & Francis Gary. *Study of the dynamics of the roots of a low-voltage break-arc.* IEEE transactions on plasma science, vol. 23, no. 1, pages 48–54, 1995.

[Wang 03] F Wang, WK Hou, S Jack Hu, Elijah Kannatey-Asibu, William W Schultz & PC Wang. *Modelling and analysis of metal transfer in gas metal arc welding.* Journal of Physics D: Applied Physics, vol. 36, no. 9, page 1143, 2003.

[Wendelstorf 00] J Wendelstorf. *Ab initio modelling of thermal plasma gas discharges (electric arcs) PhD Thesis Carolo-Wilhelmina University*, 2000.

[Wilhelm 12] G Wilhelm, R Kozakov, G Gött, H Schöpp & D Uhrlandt. *Behaviour of the iron vapour core in the arc of a controlled short-arc GMAW process with different shielding gases.* Journal of Physics D: Applied Physics, vol. 45, no. 8, page 085202, 2012.

[Window 81] B Window & G Harding. *Thermal emissivity of copper.* JOSA, vol. 71, no. 3, pages 354–357, 1981.

[Winsor 56] LP Winsor & TH Lee. *Properties of a dc arc in a magnetic field.* Transactions of the American Institute of Electrical Engineers, Part I: Communication and Electronics, vol. 75, no. 2, pages 143–148, 1956.

[Wu 06] Yi Wu, Mingzhe Rong, Jian Li & Jianyong Lou. *Calculation of electric and magnetic fields in simplified chambers of low-voltage circuit breakers.* IEEE transactions on magnetics, vol. 42, no. 4, pages 1007–1010, 2006.

[Wu 07] Yi Wu, Mingzhe Rong, Zhiqiang Sun, Xiaohua Wang, Fei Yang & Xingwen Li. *Numerical analysis of arc plasma behaviour during contact opening process in low-voltage switching device.* Journal of Physics D: Applied Physics, vol. 40, no. 3, page 795, 2007.

[Wu 08a] Yi Wu, Mingzhe Rong, Xingwen Li, Anthony B Murphy, Xiaohua Wang, Fei Yang & Zhiqiang Sun. *Numerical analysis of the effect of the chamber width and outlet area on the motion of an air arc plasma.* IEEE transactions on plasma science, vol. 36, no. 5, pages 2831–2837, 2008.

[Wu 08b] Yi Wu, Mingzhe Rong, Fei Yang, Anthony B Murphy, Qiang Ma, Zhiqiang Sun & Xiaohua Wang. *Numerical modeling of arc root transfer during contact opening in a low-voltage air circuit breaker.* IEEE Transactions on Plasma Science, vol. 36, no. 4, pages 1074–1075, 2008.

[Yang 06] G. Yang, P. Cronin, J. V. Heberlein & E. Pfender. *Experimental investigations of the anode boundary layer in high intensity arcs with cross flow.* Journal of Physics D: Applied Physics, vol. 39, no. 13, page 2764, 2006.

[Yang 07] Guang Yang & Joachim Heberlein. *Anode attachment modes and their formation in a high intensity argon arc.* Plasma Sources Science and Technology, vol. 16, no. 3, page 529, 2007.

[Yi 05] Wu Yi, Rong Mingzhe, Yang Qian & Hu Guangxia. *Numerical analysis of the arc plasma in a simplified low-voltage circuit breaker chamber with ferromagnetic materials.* Plasma Science and Technology, vol. 7, no. 4, page 2977, 2005.

[Yih 79] Stephen WH Yih & Chun T Wang. Tungsten: sources, metallurgy, properties, and applications. Plenum Publishing Corporation, 1979.

[Yongbing 02] Li Yongbing, Lin Zhongqin, Chen Guanlong, Wang Yasheng & Xi Shengyin. *Study on moving GTA weld pool in an externally applied longitudinal magnetic field with experimental and finite element methods.* Modelling and Simulation in Materials Science and Engineering, vol. 10, no. 6, page 781, 2002.

[Zeller 01] Peter R Zeller & Werner F Rieder. *Arc structure, arc motion, and gas pressure between laterally enclosed arc runners*. IEEE Transactions on Components and Packaging Technologies, vol. 24, no. 3, pages 337–341, 2001.

[Zhu 92] Peiyuan Zhu, JJ Lowke & RHNR Morrow. *A unified theory of free burning arcs, cathode sheaths and cathodes*. Journal of physics D: Applied physics, vol. 25, no. 8, page 1221, 1992.

[Zhu 95] Peiyuan Zhu, JJ Lowke, R Morrow & J Haidar. *Prediction of anode temperatures of free burning arcs*. Journal of Physics D: Applied Physics, vol. 28, no. 7, page 1369, 1995.

[Zhukov 07] Mikhail Fedorovich Zhukov & IM Zasypkin. Thermal plasma torches: design, characteristics, application. Cambridge Int Science Publishing, 2007.

[Zodiac AE 17] Zodiac AE. *Zodiac Aero Electric, Private communication*, 2017.

Appendix

The thermodynamic properties, transport coefficient and net emission coefficient used in this research are taken from the already tabulated data from [Cressault 13a, Cressault 13b, Cressault 17] . These data are shown below to give the reader a rapid access to the details. The data are presented for argon at 1 atm and air at 0.1 atm, 0.5 atm and 1 atm.

- Thermodynamic parameters are presented on figure 5.1;
- Transport coefficients are presented on figures 5.2 and 5.3;
- Net emission coefficients are presented on figure 5.4

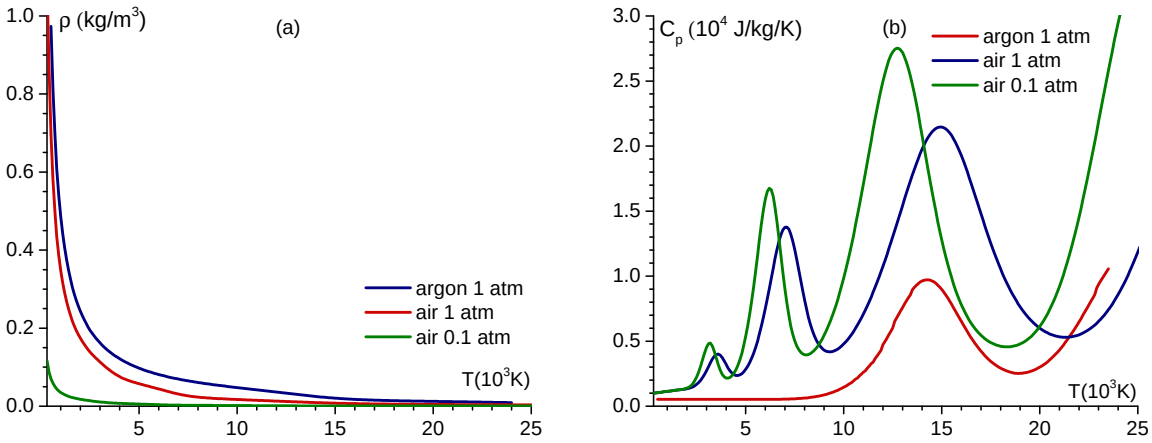

Figure 5.1: (a) Density, (b) Specific heat.

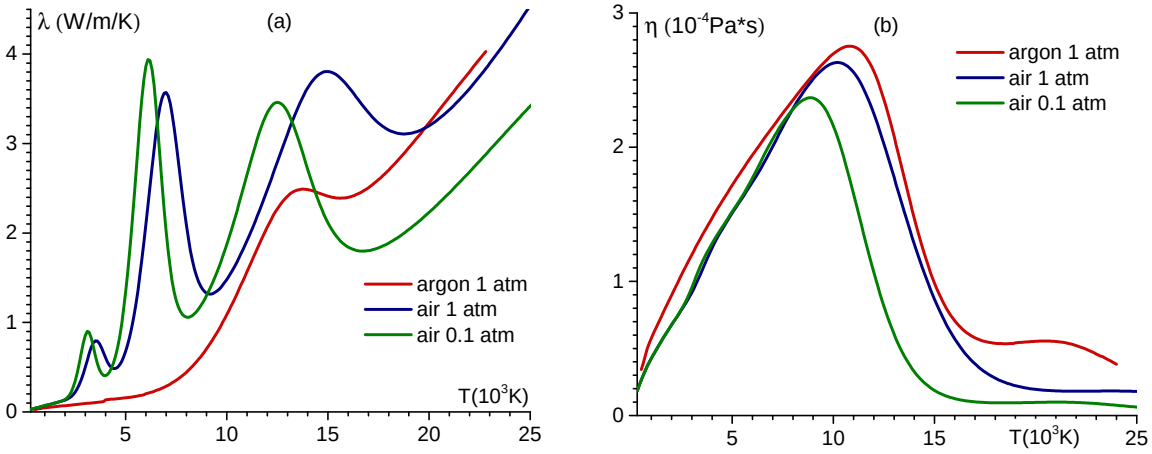

Figure 5.2: (a) Thermal conductivity, (b) Dynamic viscosity.

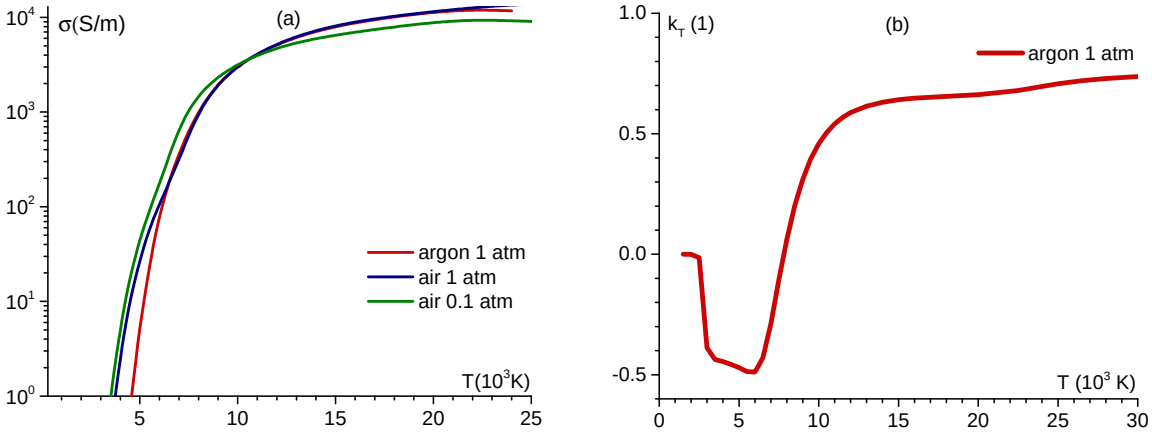

Figure 5.3: (a) Electrical conductivity, (b) Thermal diffusion ratio.

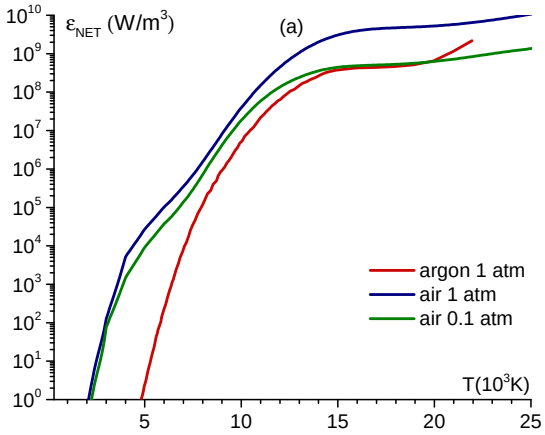

Figure 5.4: (a) Net emission coefficient.

Marina LISNYAK

Étude théorique, numérique et expérimentale d'arcs électrique continu et alternatif

L'apparition accidentelle d'un arc électrique dans le système de distribution électrique d'un aéronef peut compromettre la sécurité du vol. Il existe peu de travaux liés à cette problématique.
Le but de ce travail est donc d'étudier le comportement d'un arc électrique, en conditions aéronautiques, par des approches théorique, numérique, et expérimentale. Dans ce travail, un modèle MHD de la colonne d'arc à l'ETL a été utilisé, et résolu à l'aide du logiciel commercial COMSOL Multiphysics®. Afin de décrire l'interaction plasma-électrodes, le modèle a dû étendu pour inclure les écarts à l'équilibre près des électrodes. Ces zones ont été prises en compte en considérant la conservation du courant et de l'énergie dans la zone hors-équilibre. L'approche choisie et le développement du modèle ont été détaillés. La validation du modèle dans le cas d'un arc libre a montré un excellent accord avec les résultats numériques et expérimentaux de la littérature.
Ce modèle d'arc libre a été étendu au cas de l'arc se propageant entre des électrodes en configuration rails et en géométrie 3D. Une description auto-cohérente du déplacement de l'arc entre les électrodes a été réalisée. La simulation numérique a été faite pour des arcs en régimes DC, pulsé et AC à des pressions atmosphériques et inférieures. Les principales caractéristiques de l'arc ont été analysées et discutées. Les résultats obtenus ont été comparés avec les résultats expérimentaux et ont montré un bon accord.
Ce modèle d'arc électrique est capable de prédire le comportement d'un arc de défaut dans des conditions aéronautiques. Des améliorations du modèle sont discutées comme perspectives de ce travail.
Mots clés : plasma thermique, arc électrique, ETL, conditions hors-ETL, simulation numérique, COMSOL Multiphysics®, diagnostic des arcs.

Theoretical, numerical and experimental study of DC and AC electric arcs

The ignition of an electric arc in the electric distribution system of an aircraft can be a serious problem for flight safety. The amount of information on this topic is limited, however. Therefore, the aim of this work is to investigate the electric arc behavior by means of experiment and numerical simulations.
The MHD model of the LTE arc column was used and resolved numerically using the commercial software COMSOL Multiphysics®. In order to describe plasma-electride interaction, the model had to be extended to include non-equilibrium effects near the electrodes. These zones were taken into account by means of current and energy conservation in the non-equilibrium layer. The correct matching conditions were developed and are described in the work. Validation of the model in the case of a free burning arc showed excellent agreement between comprehensive models and the experiment.
This model was then extended to the case of the electric arc between rail electrodes in a 3D geometry. Due to electromagnetic forces the electric arc displaces along the electrodes. A self-consistent description of this phenomenon was established. The calculation was performed for DC, pulsed and AC current conditions at atmospheric and lower pressures. The main characteristics of the arc were analyzed and discussed. The results obtained were compared with the experimental measurements and showed good agreement.
The model of electric arcs between busbar electrodes is able to predict the behavior of a fault arc in aeronautical conditions. Further improvements of the model are discussed as an outlook of the research.
Keywords : thermal plasma, electric arc, LTE description, non-LTE matching, numerical simulations, COMSOL Multiphysics®, arc diagnostic.

Laboratoire GREMI – Groupe de Recherches sur l'Énergétique des Milieux Ionisés
14 rue d'Issoudun, 45067 Orléans, France